National Library of Canada

Cataloguing Branch
Canadian Theses Division

Ottawa, Canada
K1A 0N4

Bibliothèque nationale du Canada

Direction du catalogage
Division des thèses canadiennes

## NOTICE

The quality of this microfiche is heavily dependent upon the quality of the original thesis submitted for microfilming. Every effort has been made to ensure the highest quality of reproduction possible.

If pages are missing, contact the university which granted the degree.

Some pages may have indistinct print especially if the original pages were typed with a poor typewriter ribbon or if the university sent us a poor photocopy.

Previously copyrighted materials (journal articles, published tests, etc.) are not filmed.

Reproduction in full or in part of this film is governed by the Canadian Copyright Act, R.S.C. 1970, c. C-30. Please read the authorization forms which accompany this thesis.

THIS DISSERTATION HAS BEEN MICROFILMED EXACTLY AS RECEIVED

## AVIS

La qualité de cette microfiche dépend grandement de la qualité de la thèse soumise au microfilmage. Nous avons tout fait pour assurer une qualité supérieure de reproduction.

S'il manque des pages, veuillez communiquer avec l'université qui a conféré le grade.

La qualité d'impression de certaines pages peut laisser à désirer, surtout si les pages originales ont été dactylographiées à l'aide d'un ruban usé ou si l'université nous a fait parvenir une photocopie de mauvaise qualité.

Les documents qui font déjà l'objet d'un droit d'auteur (articles de revue, examens publiés, etc.) ne sont pas microfilmés.

La reproduction, même partielle, de ce microfilm est soumise à la Loi canadienne sur le droit d'auteur, SRC 1970, c. C-30. Veuillez prendre connaissance des formules d'autorisation qui accompagnent cette thèse.

LA THÈSE A ÉTÉ MICROFILMÉE TELLE QUE NOUS L'AVONS REÇUE

NL-339 (3/77)

UNIVERSITÉ D'OTTAWA
UNIVERSITY OF OTTAWA

# Part I: Rotational Hysteresis in Type II Superconducting Disks.

# Part II: Longitudinal Velocity of Flux Jumps in Axially Magnetized Type II Superconducting Wires Carrying Current.

Raymond Boyer

Dissertation submitted to the School of Graduate Studies of the University of Ottawa in partial fulfillment of the requirements for the degree

Doctor of Philosophy (Physics)

1977

© Raymond Boyer, Ottawa, Canada, 1977

## Acknowledgements

I would like to express my gratitude to my supervisor, Dr. Marcel A.R. LeBlanc for his invaluable guidance. Our daily discussions on different aspects of the research project were really appreciated.

It is also a pleasure for me to acknowledge the help received from Dr. Robert C. Smith during the writing of this thesis.

The numerous discussions with my colleagues Jean Bussière, André Lachaine, Raymond Gauthier and Jean Pierre Lorrain were greatly appreciated.

I wish to thank Miss Lise Menard for her cooperation in typing this thesis.

The financial support obtained from the National Research Council is also acknowledged.

## Abstract

This thesis consists of two separate parts reporting on two distinct projects.

### Part I

The magnetic behaviour of disks of V and VTi rotating slowly in a static magnetic field $H_o$ directed perpendicularly to the axes of rotation and along the flat faces of the disks has been investigated. The components of the average magnetic induction, $\langle B_z \rangle$ and $\langle B_y \rangle$, parallel and perpendicular to $H_o$, are monitored continuously with two orthogonal pick-up coils embracing the disk, during the evolution to the quasi-steady state and thereafter as a function of the angle of rotation of the disk.

The magnetic response of the disks has also been measured at rest as $H_o$ is slowly raised from 0 to $H_{c2}$ and subsequently cycled between $+H_{c2}$ and $-H_{c2}$. The expulsion of flux as the disks cool from $T_c$ to 4.2 K in various $H_o$ has also been determined. From these data information is extracted on (i) $j_c'$ vs B where $j_c'$ is the magnitude of the gradient of the critical B profile, and (ii) $I_R$ and $I_R'$ vs $H_o$ where $I_R$ and $I_R'$ are the surface steps operating during exit and entry of flux. This information is of intrinsic interest.

A simple but crucial picture is proposed for the evolution and final configuration of the B profiles as the disk rotates. Exploiting this model it is then possible to predict $\phi_t'$, the flux remaining in the disk and rotating in step with it as a function of $H_o$ and for several initial states. The model is pursued using (i) simple analytic approximations for $j_c'$ and (ii) the detailed data for $j_c'(B)$ and the surface steps mentioned above. The model proposed is novel and of basic significance since

it leads to a flux expulsion phenomenon independent of the rate of rotation.

Bean has proposed that the critical gradient of the B profile should be appreciably shallower where the direction of the local magnetic induction $\vec{B}(x)$ varies or rotates with distance inside the superconductor compared with the situation where $\vec{B}(x)$ is unidirectional everywhere. The present observations indicate that the gradient of B is essentially unchanged in the rotational configuration.

The simple empirical rule $d\theta/dx \approx \pm \mu_o \gamma j_c'$ is proposed to describe the rotation of the magnetic induction with depth. Using this prescription and the previously extracted data for $j_c'$, $<B_z>$ and $<B_y>$ are computed during the evolution to the quasi steady state and in this state. A good agreement is obtained with all the observations in various $H_o$ and starting with different initial states.

The model is then introduced into general expressions for $\int \vec{E}.\vec{J}\, dv\, dt$ and $\psi = \sin^{-1}(|\vec{E} \times \vec{J}|/EJ)$ which are derived from first principles. This analysis shows that this model adequately describes the energy dissipated under rotation although it does not satisfy the condition, $\vec{E} \times \vec{J} = 0$.

## Part II

The velocity of propagation of flux jumps in wires of type II superconductors carrying a transport current and axially magnetized in a longitudinal magnetic field $H_o$, has been investigated.

Two distinct mechanisms responsable for the propagation of the collapse of the superconducting state were identified: thermal coupling and electromagnetic coupling. In the thermal mode, the velocities are small since they are governed by thermal diffusion and the destruction of the superconducting state is radially symmetric. This occurs when $|\langle M_z\rangle|$ is zero or not too large and I is not too near $I_c$. When the wire is strongly axially magnetized and/or I is near $I_c$, flux avalanches occur and electromagnetic coupling determines the velocity of propagation. The velocities are large since they are not limited by the rate of thermal diffusion. Further the flux jumps are azimuthally asymmetric and follow helical trajectories along the wire.

For both modes of propagation, extensive data are presented on the dependence of the velocity on I, $H_o$ and $\langle M_z\rangle$. The helical path followed by the flux jumps is also determined as well as its dependence on the variables just enumerated.

The correspondence between $U_{fj}$, the energy dissipated during the flux jump and its velocity of propagation V is explored. The initial $B_z$ and $B_\theta$ profiles needed for the calculations of $U_{fj}$ are estimated in the spirit of the Bean-London approximation. A striking correspondence between the observed V vs I families of curves and the calculated $U_{fj}$ vs I families of curves is observed indicating that V is functionally related to $U_{fj}$. To delineate this relationship quantitatively, plots of $V_z$ and $V_z/\cos\phi$ vs $U_{fj}$ are presented where $\phi$ is the direction of advance of the helical flux jump with respect to the axis of the wire. These plots enable us to determine the threshold energy for propagation and indicate that the flux flow resistivity plays an important role in controlling V.

The assumption that the flux jumps follow helical paths corresponding to the average helical configuration of the vortices in the region where the transport current flows is pursued. A simple arithmetic average of the Bean-London approximation for the $B_\theta$ and $B_z$ profiles is used. A comparison of these estimates for $\phi$ with observations indicates that the basic idea is valid.

TABLE OF CONTENTS

PART II

TABLE OF FIGURES

# PART I

# ROTATIONAL HYSTERESIS IN TYPE II SUPERCONDUCTING DISKS

# Chapter 1

## Introduction

### 1.1 Historical Background

Several workers have investigated the mechanical response of superconducting cylinders and disks when rotated in a static magnetic field $\vec{H}$ directed perpendicularly to the axis of rotation. In these studies the axis of the cylinder or disk is chosen as the axis of rotation as shown schematically below. In all previous work, researchers have

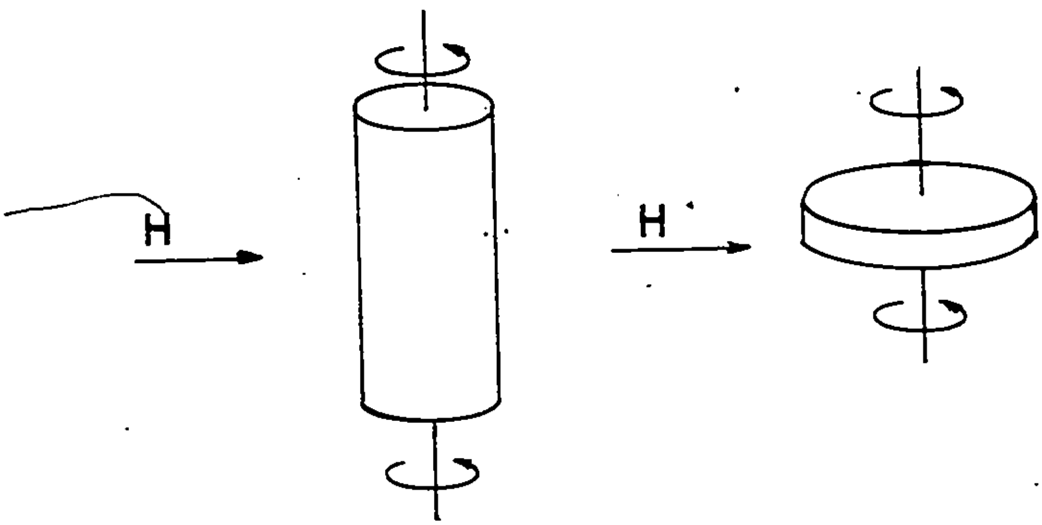


monitored the mechanical torque $\vec{\tau}$ generated by the interaction of the magnetic moment $\vec{\mu}$ of the specimen with the applied magnetic field $\vec{H}$, where

$$\vec{\tau} = \vec{\mu} \times \vec{H}.$$

By measuring the magnitude of the torque as a function of the angle of rotation of the sample or of the field $\vec{H}$, the magnitude of the magnetic moment and its direction $\theta$ with respect to $\vec{H}$ can be determined:

$$\tau = \mu H \sin \theta.$$

If the specimen is an ideal type I or type II superconductor in the perfect Meissner state, hence H at the surface of the sample is maintained below $H_c$ or $H_{c1}$, the flux expelling currents are in equilibrium with the magnetic induction in the penetration depth. These superficially-flowing currents are of course confined to the boundaries of the specimen but are not "attached" to the lattice of the sample. Thus their spatial configuration is independent of the position of the lattice and no torque should be observed. Deviations from such behaviour have then been attributed to hysteresis i.e., the trapping of flux by irregularities at the surface or in the bulk of the specimen (Condon 49; Fritz 49, 50).

If the specimen consists of an ideal (reversible) type II superconductor in the mixed state the situation is considerably more interesting and complicated. The configuration of the flux line lattice is presumably in equilibrium with the magnetic field before the rotation of the specimen begins. When the sample rotates, the interaction of the flux lines with each other and with the magnetic field will tend to maintain this equilibrium arrangement. Consequently the vortices are dragged through the lattice of the sample, and viscous forces come into play which disturb the initial configuration (Fuhrmans 76, Schafer 76). These viscous forces are velocity-dependent, so that the magnetic moment and therefore the torque generated during rotation will be functions of $\omega$, the angular frequency of rotation, as well as of $H/H_{c2}$. The data then, in principle, should shed light on the velocity dependence of the viscous forces. Unfortunately, this idealized situation is difficult to achieve in practice. In the studies performed to date, pinning forces appear to play a significant role and tend to obscure or mask the contribution of viscosity effects to the phenomena. Clearly, then in situations where the pinning forces are dominant, the observations can also yield information on the interaction of the flux lines with the pinning sites.

It is important to note that regardless of the specific purpose of the investigation it is not essential that the sample undergo continuous rotation. Several investigators have opted to study the response of the sample when it is made to oscillate at various chosen frequencies and amplitudes (Andronikashvili 67, 69, Ashimov 76).

In situations where pinning plays a major role, useful information can be obtained from measurements of the mechanical torque as a function of the angle through which the sample is rotated. The maximum torque generated is particularly sensitive to the anisotropic configuration of the pinning (Milne 72). In this context we note the classical work of Wipf (Wipf 64) on the relationship between pinning and major lattice planes in a single crystal sample.

Extensive studies have also been made using configurations which have some similarity with the arrangement just described. In order to place the present work in proper context it is worthwhile mentioning these endeavours and their basic differences with this work. The investigations of the gyromagnetic effect and of Faraday disk voltages are noted. The arrangements for these experiments are shown schematically on the following page. The crucial difference between these experiments and the present work is that here the applied magnetic field H is directed <u>along</u> the axis of oscillation or rotation.

In the experiments on the gyromagnetic effect (diagram (a) ), the applied field $\vec{H}$ varies in amplitude and in frequency. The amplitude of

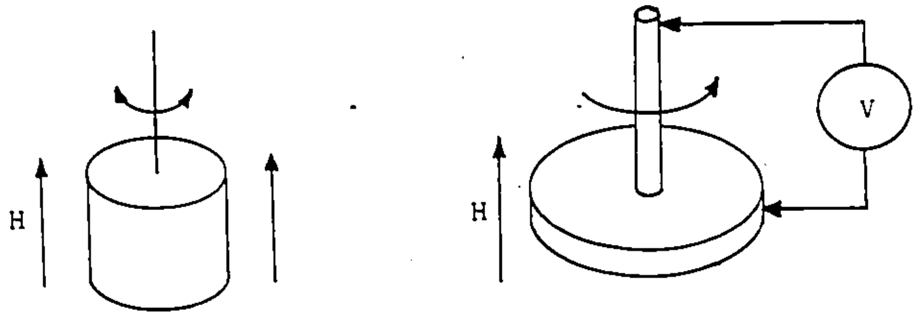


a) b)

the oscillations of the sample and their damping provides information on the ratio of the magnetic moment and the angular momentum associated with the persistent currents circulating in the superconducting specimen (usually in the form of a sphere) (Pry 52, Broer 47).

In the work on Faraday disk voltages, the superconducting sample, which may be a cylinder, disk or sphere, is rotated continuously in a stationary applied field directed as shown in diagram (b). The emf $\varepsilon$ generated between the axis of rotation and the periphery of the sample is monitored with the voltmeter V as a function of H, which determines the magnetic state of the specimen and of the angular frequency of rotation $\omega$. The emf can be written

$$\varepsilon = \int_0^R B(r)v(r)dr = \omega \int_0^R B(r)r\,dr = \omega\phi$$

where B(r) is the spatially-varying magnetic flux density and $\phi$ is the total magnetic flux threading the sample (Wexler 50, LeBlanc 66).

## 1.2 Motivational Background

In the present work it was decided to monitor the total magnetic moment of the sample "directly" or "electromagnetically". This is achieved by encircling the disk with two orthogonal pick-up coils. The experimental details are presented in the next section of this chapter. Clearly this approach is equivalent to the method of measuring the mechanical torque exploited by previous workers. It is believed that this technique is experimentally simpler than the alternative. This arrangement, however, does not lend itself readily to measurements of the frequency dependence of the phenomena. However the intention is first to concentrate on and examine the phenomena in the range of "zero" frequency or infinite period. It is believed that it is more prudent and profitable to elucidate the time-independent features of a phenomenon before undertaking a study of its more complicated time-dependent aspects.

Two limiting geometries are amenable to analysis: the long (infinite) cylinder and the disk. Attention is focussed on the latter for the following important reason. A major program of this laboratory is the study of the behaviour of type II superconductors in what is frequently referred to as the longitudinal geometry. This is the situation where the transport current is made to flow along the length of a specimen in a magnetic field which is itself applied along the length of the sample. Generally the samples have simple shapes such as ribbons, wires and hollow cylinders. Remarkable phenomena are encountered in the longitudinal geometry which contrast dramatically with those observed in the transverse case where the magnetic field is applied perpendicularly to the transport current. In particular, the critical current $I_c$ can be appreciably enhanced and hysteresis (A.C.) losses considerably diminished. It is noted that in the longitudinal arrangement, $H_s$ (the total magnetic field at the surface of the sample) oscillates in direction between $-\frac{\pi}{2}$ and $\frac{\pi}{2}$ as it changes amplitude when the conduction current undergoes full wave cycles. The situation is shown schematically in the accompanying sketch.

It is also noted that $H_s = \sqrt{H_{//}^2 + (\mu_o \, I/2\pi R)^2}$ or $\sqrt{H_{//}^2 + (\mu_o \, I/2)^2}$ for the cylinder and the wide ribbon (taken as an infinite slab) respectively. Here $\mu_o = 4\pi \times 10^{-7} N/A^2$ in SI units (this system will be used throughout the thesis) and R is the radius of the cylinder. The longi-

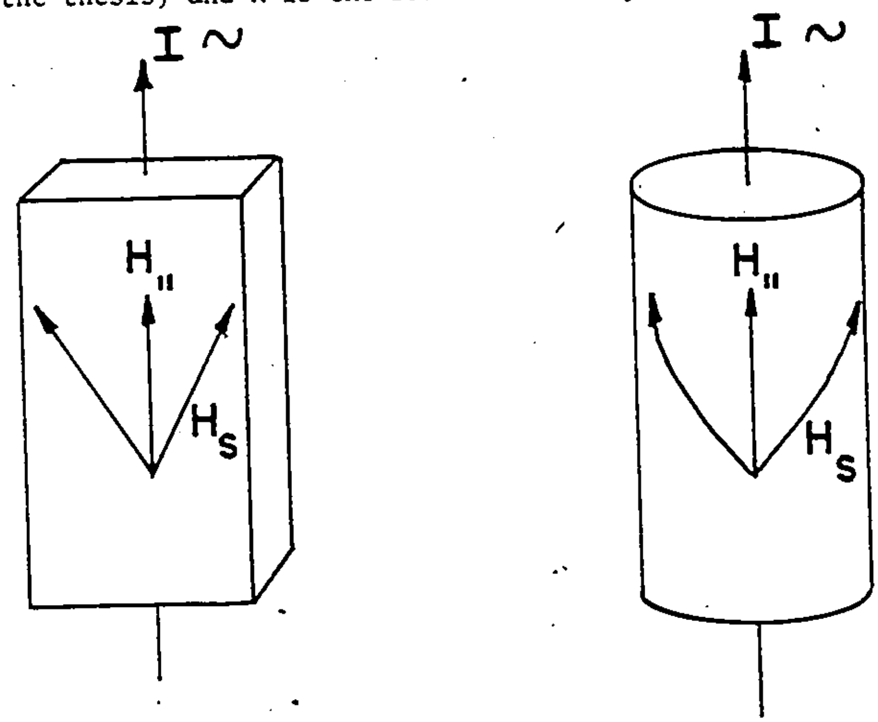


tudinal component of the external field is usually kept constant in this work. Note that for the ribbon geometry it is not necessary that the transport current be fed into the sample through leads attached to its ends and connected to a current supply. The current can be generated by induction i.e. made to flow along the ribbon by varying an externally applied transverse magnetic field $H_\perp$ directed along the flat face of the ribbon. This situation is shown schematically in the accompanying picture. In this case

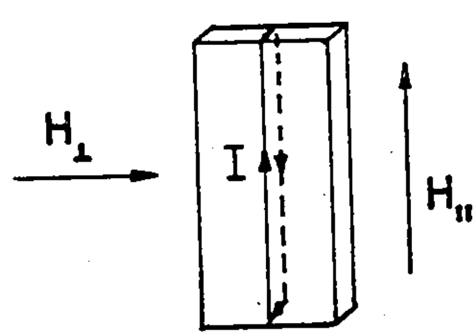

$H_s = (H^2_{//} + H^2_{\perp})^{\frac{1}{2}}$.

In all these situations, as the external magnetic field $H_s$ changes in magnitude and direction, vortices migrate into or out of the sample. Since the orientation of the external field changes with time, the vortices enter (or leave) the specimen in various directions, which also vary with time. Consequently the orientation of the rows of vortices inside the specimen varies with depth at any given time. These measurements then provide valuable information on the behaviour of a lattice of vortices where adjacent planes or rows differ in orientation as shown schematically in the diagram.

It should now be emphasized that it is immaterial whether it is the specimen or the external magnetic field which oscillates or rotates. These two situations are physically equivalent and the behaviour is expected to be identical.

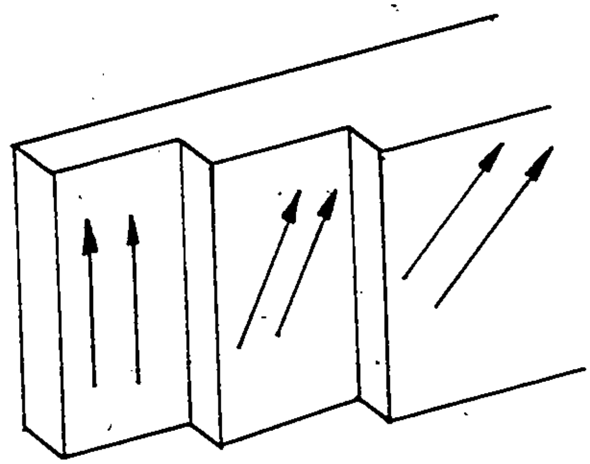

With a disk rotating (or oscillating) in a static magnetic field directed perpendicularly to the axis of rotation (or oscillation) a situation is encountered which is intimately related to work just outlined. Planes of vortices are created at the surface of the disk which differ in orientation as the disk (or the field) rotates or oscillates. The major differences between these various situations are not fundamental. For the rotating or oscillating disk, the amplitude of the field $H_s$ is kept constant whereas its transverse component generally varies sinusoidally with time in studies of A.C. losses in wires and ribbons.

Further, the change in direction can readily be made to exceed $\pi/2$ in the investigations with oscillating or rotating disks.

Since disks and cylinders are basic and simple geometries, their behaviour and the hysteresis losses they exhibit under oscillation or rotation are of considerable technological interest for applications of type II superconductors in rotating machinery and other situations where $\vec{H}$ swings in intensity and direction.

# CHAPTER 2

## Experimental Arrangement and Procedures

### 2.1 Introduction

Samples in the form of thin disks are mounted so that they can be rotated slowly and continuously or incrementally in a stationary externally applied magnetic field $H_o$ directed along the flat faces of the disk and perpendicularly to the axis of rotation. The magnetic moment of the disk as it is rotated is monitored by two orthogonal pick-up coils which embrace it and separately feed electronic amplifier-integrators driving Y axes of an $X$-$Y_1Y_2$ recorder. A signal proportional to the angle $\theta$ through which the disk is rotated drives the X axis. The magnetic behaviour of the disk is independent of the rate and manner of rotation in these investigations.

The magnetic behaviour of the disk at rest is also measured as the externally applied field is swept slowly from zero to $H_{c2}$ and subsequently cycled between $+H_{c2}$ and $-H_{c2}$. The temperature of the disk can be varied from the ambient 4.2 K of the helium bath to above $T_c$. The initial magnetic state of the disk can thus be controlled before rotation takes place. Further the expulsion of flux from the disk can then be measured (partial Meissner Effect) as it cools from $T_c$ to 4.2 K in various static applied fields $H_o$.

Pertinent details on the sample, salient features of the experimental arrangement and procedures and comments on the data are now provided.

### 2.2 Experimental Arrangement and Procedures

The magnetic behaviour under rotation of disks of two type II superconducting materials, V and VTi at 4.2 K has been investigated. The V disk samples were cut on a metal lathe from a cold-rolled sheet of high purity vanadium as it was received. The standard magnetization curves and the behaviour under rotation of a second V disk cut from the same sheet but with a smaller diameter (12 mm) have also been investigated. The main purpose of these auxiliary measurements was to determine whether edge effects played a significant role in our data. These two disks exhibited magnetization curves which overlapped within experimental accuracy. We present only the data for the wider disk, for which our measurements were more extensive. The VTi disk was also cut on a lathe from an ingot of V (75.6 at %)Ti produced by Materials Research Corporation and prepared by melting together in an induction furnace, high purity triple zone refined V and Ti starting materials. The samples were not treated in any way after cutting. Pertinent data on the two disks is presented in Table 2-1.

Table 2 -1

| Sample | Diameter (mm) | Thickness (mm) | $H_{c1}$ (tesla) | $H_{c2}$ (tesla) | $\kappa$ | Source |
|---|---|---|---|---|---|---|
| Vanadium | 19 | 0.27 | 0.0275 | 0.1650 | 2.3 | (1)T.W.C.A. |
| V(75.6 At %)Ti | 9.5 | 0.80 | 0.0075 | 2.5 | 23 | (2)M.R.C. |

(1) Teledyne Wah Chang Albany

(2) Materials Research Corporation

The values of $H_{c2}$ and $H_{c1}$ at 4.2 K are estimated from the standard magnetization curves (see Figures 3-1 and 3-7). The Ginzburg-Landau parameter $\kappa$ is evaluated from these data combined with information from the area under the estimated reversible magnetization curve and its slope near $H_{c2}$. The procedure we have followed to extract this and other information from the standard magnetization curves and flux expulsion data (cooling curve) is developed in detail in Chapter 3.

The experimental arrangement is illustrated in Figure 2-1. The electrically insulated disk is embraced by a non-inductively (bifilar) wound heater made from #38 enameled manganin wire. This sample heater assembly is placed inside two brass cups. It is thermally and electrically insulated from this metallic enclosure and rigidly held in place inside of it by mylar spacers. The two leads from the manganin heater emerge through two slots and are soldered to the brass cups. The two cups are electrically insulated from each other by a delrin ring. The electric current feeding the manganin wire heater enters the brass cups via sliding electrical contacts made from phosphor-bronze (relay) strips.

Each brass cup and its axle (axis of rotation) are an integral unit. The two brass cups are attached rigidly together. The axle of one brass cup is coupled to and rotated by a worm gear system fixed solidly inside a sample holder which is immersed in the helium bath. The sample holder is mounted inside and attached firmly to the superconducting solenoid. The worm gear system driven via a straight rotating shaft extending to and emerging from the top plate attached to the helium dewar. The shaft of a ten-turn potentiometer is coupled to the driving shaft and rotates in unison with the sample. A constant voltage is applied to the potentiometer and the central tap provides a signal which is then proportional to the angle $\theta$ through which the disk is rotated starting from a known zero setting. Further, indicator markings

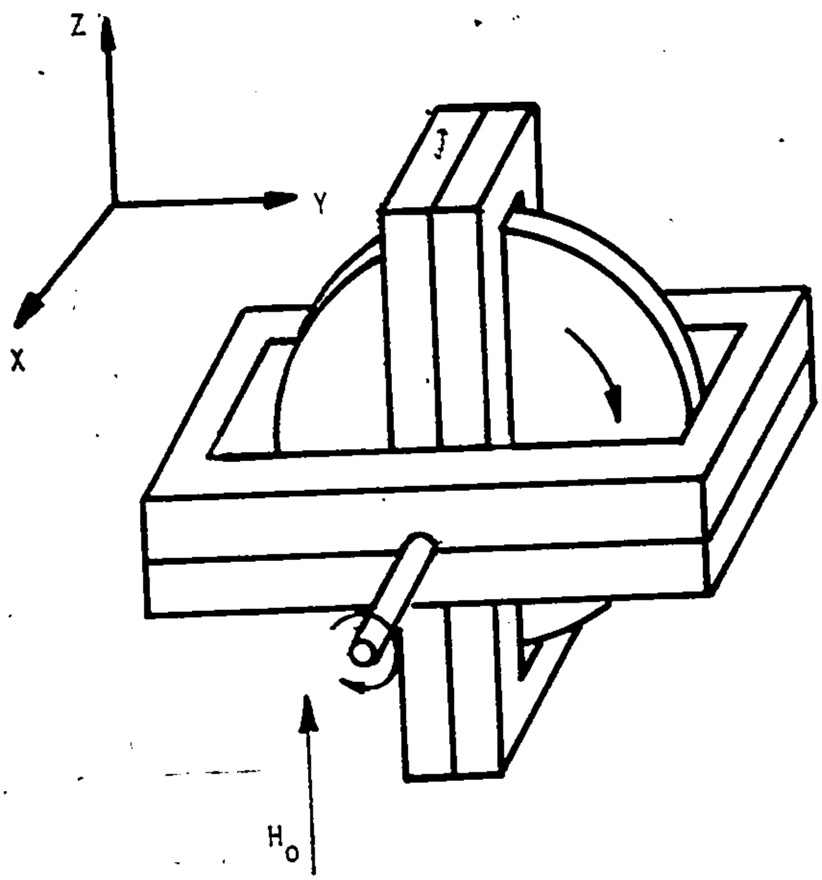


Figure 2-1 a  Experimental arrangement: System of orthogonal pick-up coils embracing the sample assembly.

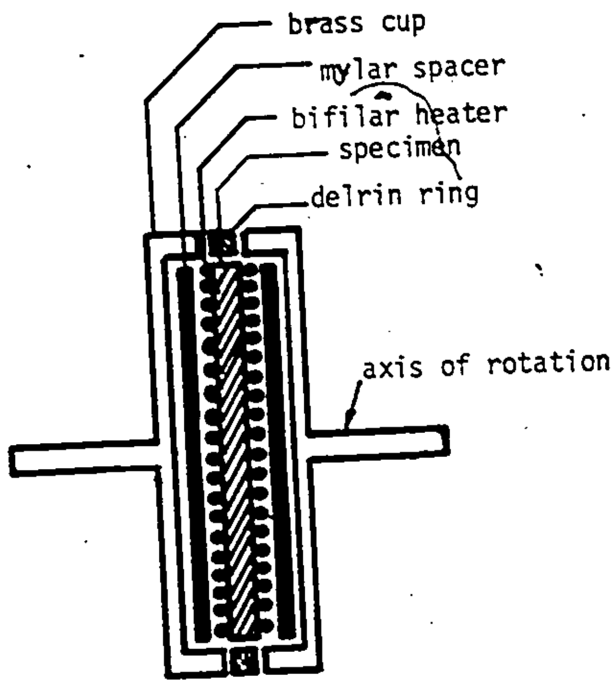


Figure 2-1 b Cross section of the sample assembly.

on the disk and other components enable us to establish the angular orientation of the disk with respect to the axis of the superconducting solenoid. This feature is important in the determination of anisotropic behaviour.

Two orthogonal pick-up coils embrace the rotating disk assembly. These pick-up coils are immobile inside the solenoid and are oriented to embrace the magnetic flux threading the sample in the directions parallel and perpendicular to the applied magnetic field. Each of these pick-up coils contain 17,000 turns of #48 copper wire. Each pick-up coil is also constructed of two halves which are separated when the sample assembly is inserted. They are then joined physically and electrically and firmly fixed in place around orthogonal diameters of the sample. The pick-up coil monitoring the magnetic moment in the direction of the applied field is connected in series opposition with a balanced pick-up coil which does not sense the field of the sample but is positioned to respond to variations of the applied field. Each of the pick-up coils separately feeds an operational amplifier-integrator (PAR Model 215) which drives the Y axes of an X-Y,$Y_2$ recorder.

In tracing standard magnetization curves, (curves where the disk does not rotate), the X axis is driven by a signal proportional to $H_o$. For measurements of the flux expulsion during cooling from $T_c$ to 4.2 K (or flux entry upon heating from 4.2 K to $T_c$) the X-axis can be driven by a signal proportional to the heater current. When monitoring the magnetic behaviour under rotation, the X axis is driven by a signal proportional to $\theta_{,}$, which is obtained from the potentiometer arrangement described before.

As is standard practice the signal along $H_o$ is calibrated on the assumption that no magnetic flux threads the specimen when $H_o$ is increased from zero to a small value with the disk initially in the virgin state (i.e. cooled from $T_c$ to 4.2 K in zero field). The magnetic field at which this signal ceases to be linear is taken to be $H_{c1}$. The signal from the second (the orthogonal) pick-up coil is calibrated in the following way. Magnetic flux is trapped by cooling the disk from $T_c$ to 4.2 K in an arbitrary field $H_o$, which is then removed. This trapped flux $\phi_t$ is a known quantity since the pick-up coil embracing it, and continuously monitoring the magnetic moment as $H_o$ is removed, has already been calibrated by the procedure just described. As the disk is now rotated (continuously or incrementally) through an arbitrary number of turns a signal from the second pick-up coil is observed which varies sinusoidally as a function of $\theta$. The amplitude of this signal is proportional to $\phi_t$, which is known. Thus the second pick-up coil and its electronic amplifying-integrating-recording system are calibrated. It should be stressed that this calibration is model independent.

The magnetic field $H_o$ is provided by a superconducting NbTi wire solenoid of 4.5 cm inner diameter, 7 cm outer diameter and 18 cm length. The axis of the solenoid is perpendicular to the axis of rotation of the sample so that $H_o$ is directed parallel to the flat faces of the disk. The applied field is estimated to be homogeneous within ±1 % over the volume of the disk sample. The possible maximum misalignment is estimated to be ± 2 degrees between $H_o$ (the z-axis) and the plane of the disk.

## 2.3 Experimental Results: Standard Magnetization and Flux Expulsion Curves.

The magnetic response of the disk specimen <u>at rest</u> as $H_o$ is raised from zero to $H_{c2}$ and subsequently cycled between $+H_{c2}$ and $-H_{c2}$ is continuously monitored. The applied field is varied smoothly and slowly to ensure isothermal conditions and to avoid flux avalanches. Typically $\mu_o dH_o/dt \lesssim 10^{-2}$ tesla per second in our work. The locus of the magnetization $\langle M \rangle = \frac{\langle B \rangle}{\mu_o} - H_o$ vs $H_o$ is referred to as the standard magnetization curve. These measurements on the V and VTi disks are presented in Chapter 3 (Figures 3-1 and 3-7) where they are analyzed in detail and information is extracted for use in the interpretation of the magnetic behaviour under rotation.

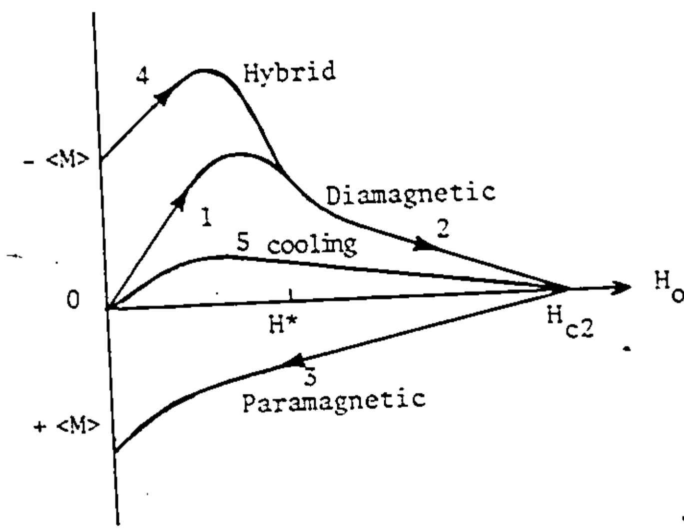


The standard magnetization curve consists of four distinct sections or branches and the reader is referred to the accompanying sketch for aid in identifying these segments and their properties. The magnetization curve as $H_o$ is initially applied with the sample in the virgin state is known as the diamagnetic curve (since $\langle B \rangle < \mu_o H_o$) and consists of two branches or sections depending on whether $H_o < H^*$ (branch 1) or $H_o > H^*$ (branch 2). According to current models, there is a central region of the sample where $B = 0$ when $H_o \leq H^*$, whereas $B > 0$ everywhere in the sample when $H_o > H^*$. The traditional practice of presenting the diamagnetic curve in the first quadrant is followed here. The magnetization curve as $H_o$ is reduced from $\pm H_{c2}$ to zero is known as the paramagnetic curve, since here generally $\langle B \rangle > \mu_o H_o$ (except in the case of semi-reversible samples where the curve may perform an excursion into the first quadrant). This branch or section is labelled as (3). The branch of the magnetization curve where $H_o$ increases in magnitude from zero to $\pm H^*$ after an excursion to $\mp H_{c2}$ is denoted as the hybrid magnetization curve, since it contains regions of magnetic induction of positive (negative) polarity surrounding regions of negative (positive) polarity. $H^*$ is the applied field, at which the hybrid branch joins the diamagnetic curve. Above $H^*$, the magnetic induction B in the sample is entirely of the polarity of $H_o$ and the hybrid configuration no longer exists.

It is found that the hybrid magnetic configuration is often particularly unstable and it is not always possible to trace out branch 4 continuously since flux jumps occur even though special precautions are taken to vary $H_o$ extremely slowly and smoothly. In such situations various stratagems can be exploited to map out the envelope of this branch, at least approximately. Such stratagems were not necessary with the present samples although special care had to be taken during the sweep of $H_o$ through this region.

As the sample cools from $T_c$ to the final temperature (4.2 K in this work) in a static applied field, flux is expelled and a diamagnetic moment develops. This expulsion of flux is impeded by pinning in the body and at the surfaces of the specimen; hence the diamagnetic moment which arises is frequently referred to as the partial Meisner Effect. This convenient and frequently used label is evidently a misnomer since above $H_{c1}$ the flux expelled, even by the ideal type II superconductor, corresponds to only a fraction of the flux permeating the sample in the normal state. The fraction of flux which is expected to be expelled in the ideal case has been calculated by Abrikosov (1957) and is known as the Abrikosov diamagnetism. The correct but more cumbersome expression for flux expulsion in the non-ideal case should then be the "partial or imperfect Abrikosov diamagnetic effect". The diamagnetic magnetization which occurs during cooling from $T_c$ in various static fields $H_o$ contains important information and constitutes an integral part of the standard magnetic behaviour characterizing a specimen. This curve is often denoted "the cooling curve" and it is labelled branch (5) in the above sketch and in the data. The measurements of this curve for the V and VTi disks are presented in chapter 3 (Figures 3-2 and 3-8) where it is analyzed together with the other branches which it complements. Unfortunately many workers fail to include this curve and branch 4 in their characterization of a specimen.

## 2.4 Experimental Magnetization Curves under Rotation.

The variation of the components of the magnetization with θ (the angle of rotation of the disk) as the disk rotates in a static applied field $H_o$ is now considered. $H_o$ is directed along the z-axis and the axis of rotation is the x-axis. Let $<B_z>$ and $<B_y>$ represent the instantaneous average magnetic induction components along the z and y axes respectively. It is stressed that $<B_z>$ and $<B_y>$ are spatial averages of the components of $\vec{B}(x)$ over the thickness X of the disk. The components of the magnetization are defined by the relations

$$<M_z> = \frac{<B_z>}{\mu_o} - H_o \quad \text{and} \quad <M_y> = \frac{<B_y>}{\mu_o} \qquad (2\text{-}1)$$

The disk is rotated slowly and smoothly, typically at the rate of one turn per minute. The rate of rotation has been varied by factors of about 4. No change in the resulting curves was observed. It is stressed that the rotation need not be continuous and can be accomplished incrementally (stepwise). Of course, the instantaneous rate of rotation dθ/dt during each increment $\Delta\theta$ is then kept small. The components of the magnetization do not vary with time when the rotation is interrupted in this way. This provides further evidence that viscous effects play no role in the phenomena observed.

A representative set of recorder tracings is reproduced in Figure 2-2. The curves are displaced vertically for convenience of viewing. The data shown in Figure 2-2 was obtained after cooling the V disk in the magnetic field $H_o$ indicated at the extreme right along each curve. This field is maintained constant in magnitude and direction as any given pairs of curves is mapped out. For the data shown in Figure 2-2, the initial magnetic moment (the flux expulsion diamagnetism $\mu_o\langle M_z\rangle_{ex}$) is small. It can readily be obtained from examination of Figure 3-2. In the actual measurements the initial magnetization can also be determined by the vertical motion of the pen recorder as the sample cools from $T_c$ before the rotation begins. The lower set of curves in Figure 2-2 is presented again in Figure 2-3 as graphs of $\langle B_z\rangle$ vs $\theta$ instead of $\mu_o\langle M_z\rangle$ vs $\theta$, since the former may be easier to visualize. The horizontal dashed lines indicate $\langle B_z\rangle = 0$ for the corresponding curves.

Figures 2-2 and 2-3 must now be interpreted. Attention is first focussed in the upper three curves of Fig. 2-3. Note that here $H_o < H^*$; the amplitude of the oscillations decreases with increasing $\theta$. Eventually (this is more evident in the continuation of these curves to larger $\theta$ values) the amplitude of the oscillations stabilizes and subsequently $\langle B_z\rangle$ oscillates at constant amplitude about a mid-level or base-line. The height of this base-line or "D.C. Component" can be evaluated in a variety of ways. In particular, an average of $\langle B_z\rangle$ can be taken over one, two or more cycles in the range of large $\theta$. Let $\langle\overline{B_z}\rangle$ denote this

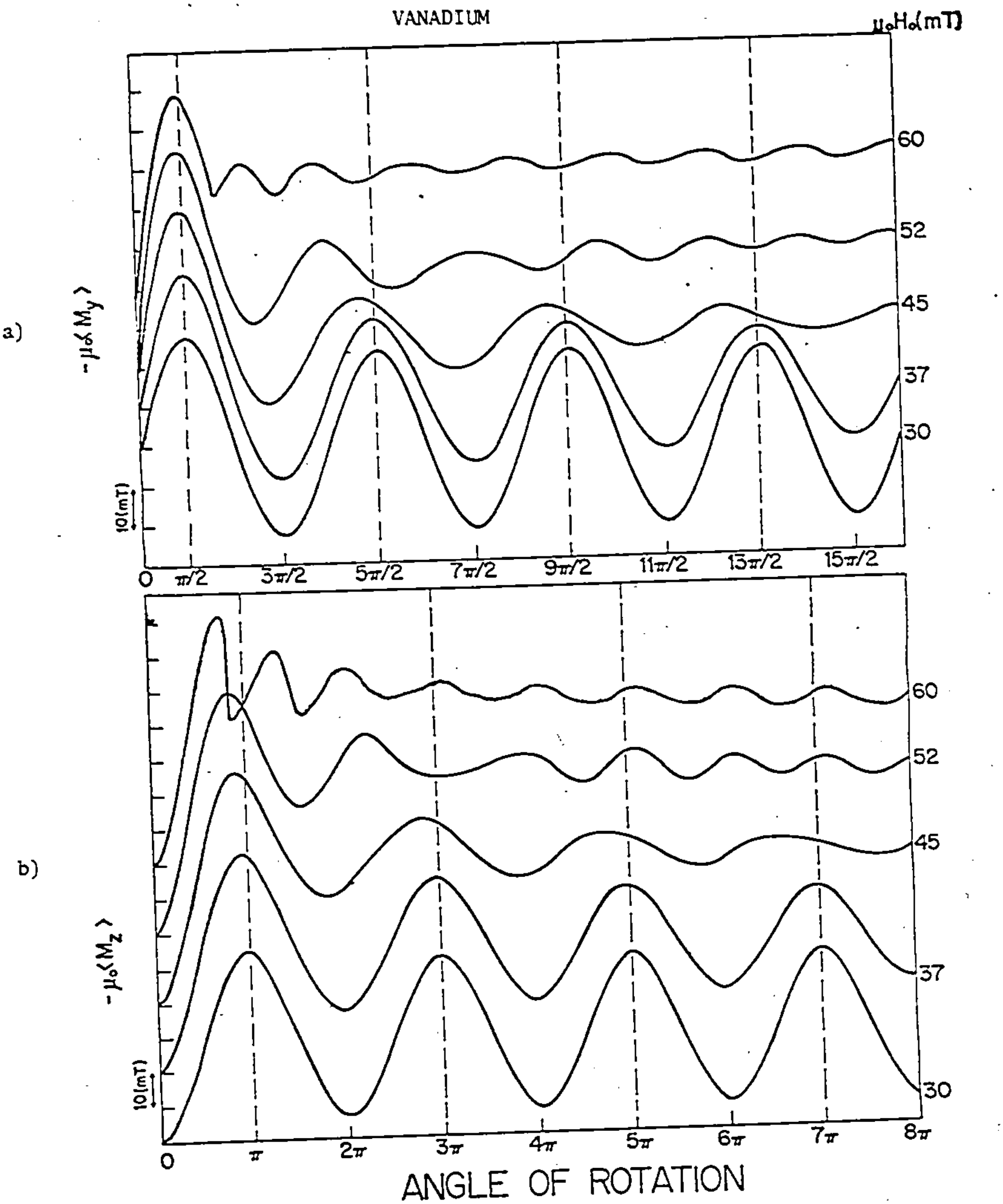


Figure 2-2 Experimental variation of the components $\langle M_y \rangle$ and $\langle M_z \rangle$ of the magnetization with the angle of rotation $\theta$ and for several applied fields $H_o$. The disk was initially cooled in the field $H_o$.

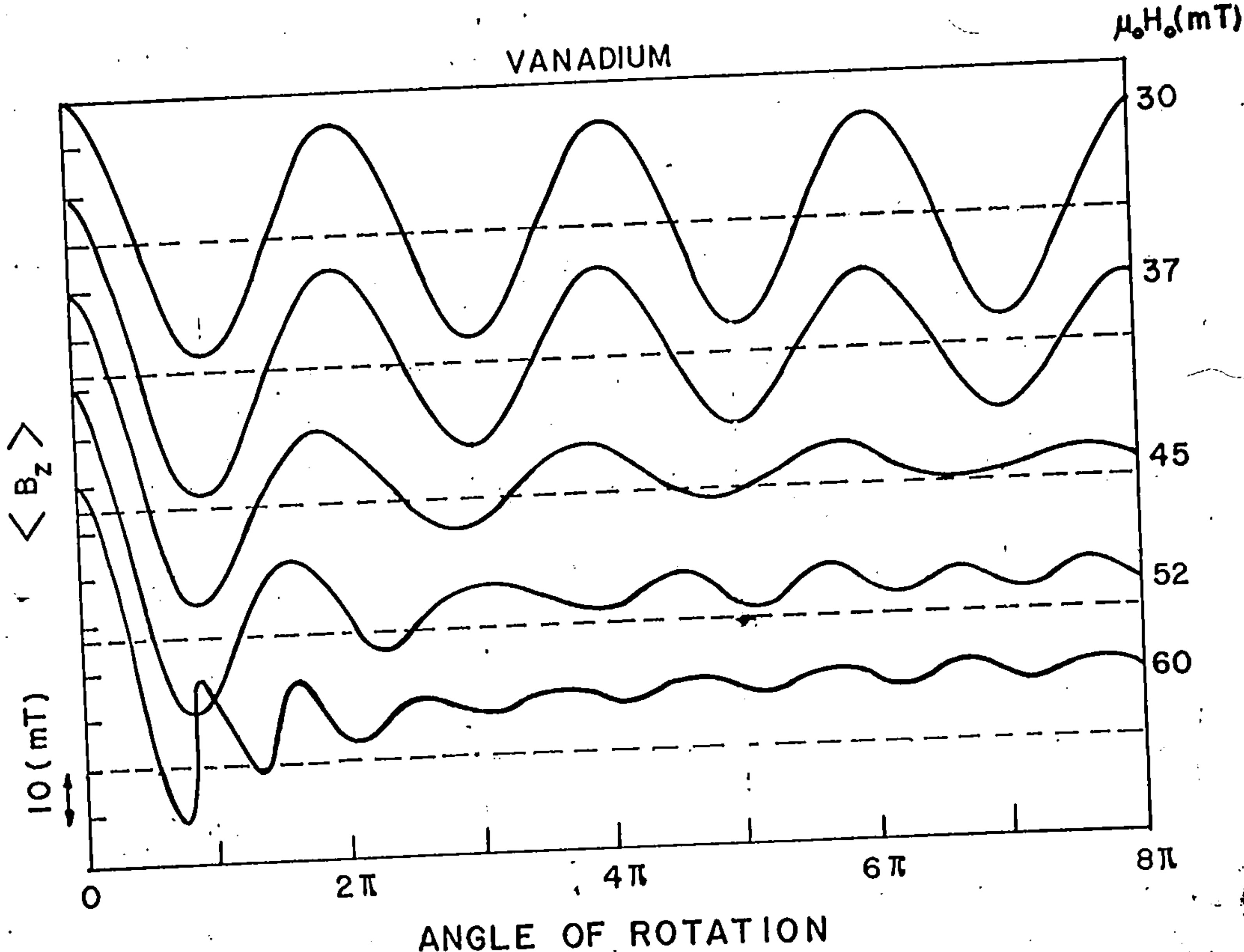


Figure 2-3  Experimental variation of the component $\langle B_z \rangle$ of the magnetic flux density with the angle of rotation $\theta$ and for several applied fields $H_o$. The disk was initially cooled in the field $H_o$.

average per cycle, and note that $\overline{\langle B_z \rangle}$ is increasing monotonically with $H_o$ for all of the curves in Figure 2-3. (Following Bean (Bean 1970) the behaviour when the amplitude of the oscillations has become constant is called the quasi-steady state.) The base-line or D.C. component $\overline{\langle B_z \rangle}$ is a measure of the z-component of the "fraction" of the configuration of the magnetic induction $\vec{B}(x)$ which is not rotating with the disk in a quasi-steady state. Turning now to part (a) of Figure 2-2 showing $\langle B_y \rangle$ vs $\theta$ it is seen that a base line or D.C. component $\overline{\langle B_y \rangle}$ is evident, and can also be obtained for each value of $H_o$ from the data at large $\theta$. Thus $\overline{\langle B_y \rangle}$ is a measure of the y-component of the "fraction" of the configuration of the magnetic induction $\vec{B}(x)$ which is not rotating with the disk in the quasi-steady state. In chapter 5 a model is developed which quantitatively reproduces the data obtained on $\overline{\langle B_z \rangle}$ and $\overline{\langle B_y \rangle}$ vs $H_o$ for the V and VTi disks.

The lower 2 curves of (a) and (b) of Figure 2-2 are now examined. Note that in the quasi-steady state (range of large $\theta$):

a) The oscillations of $\langle M_y \rangle$ and $\langle M_z \rangle$ have a period of $2\pi$. Also, the oscillations of $\langle M_y \rangle$ are shifted by $\pi/2$ with respect to the oscillations of $\langle M_z \rangle$. Hence these oscillations are in step with the rotation of the disk.

b) The amplitude of the oscillations of $\langle M_y \rangle$ and $\langle M_z \rangle$ are equal for corresponding $H_o$.

c) The direction of the oscillating (rotating) $\langle B_z \rangle$ $(\theta)$ and $\langle B_y \rangle$ $(\theta)$ extrapolated to $\theta = 0$ corresponds to the direction of $H_o$.

These considerations indicate that in the quasi-steady state there exists a quantity of flux $\phi_t'$ which is trapped in the disk and rotates with it. This quantity of flux can be appreciable in view of the magnitude of the signals it generates as it sweeps in and out of the orthogonal pick-up coils. From the present observations of the amplitude of the stabilized oscillatory signals $<B_z>$ and $<B_y>$ vs $\theta$ a quantity is determined as a function of $H_o$ which is denoted by $<B>_{rot}$. Further, this quantity is found to depend strongly on the initial magnetic state of the disk,(that is, on whether the locus of its initial magnetization lies on branch 3, 4 or 5 of the standard magnetization curve). In Chapter 4 the curves of $<B>_{rot}$ vs $H_o$ obtained for the V and VTi disks under rotation starting with different initial magnetic states will be presented and quantitatively interpreted.

Figure 2-4 shows curves of $<M_y>$ and $<M_z>$ vs $\theta$ generated by the model developed in chapters 4 and 5. These theoretical curves should be compared with the corresponding experimental curves shown in Figure 2-2. Evidently, the model proposed here can describe the evolution to the quasi-steady state as well as the behaviour in the quasi-steady state quite satisfactorily.

## 2.5 Anisotropy of Pinning

Inspection of the upper two curves of (a) and (b) of Figures 2-2 and 2-4 reveals that the theoretical curves at high fields ($H_o > H^{**}$) exhibit a plateau in the quasi-steady state, whereas the experimental curves continue to oscillate. It is also noted that these oscillations have a period of half the period of rotation of the disk. Furthermore, in Figure 2-2 the phase of these oscillations is shifted with respect to the rotation of the disk.

These residual or parasitic oscillations can be attributed to anisotropy in the pinning (bulk and surface) of the disk. This explanation

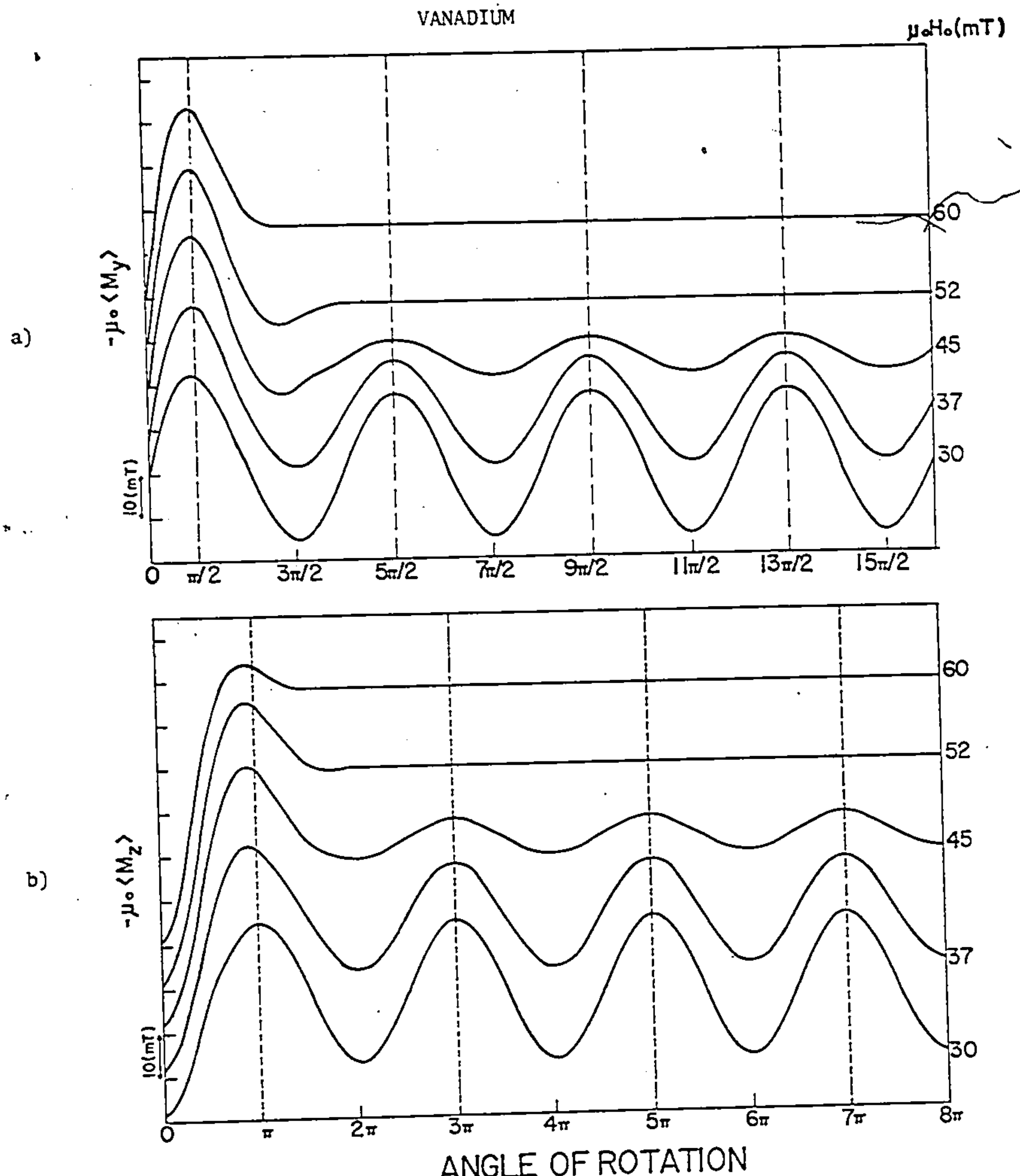


Figure 2-4 $\langle M_y \rangle$ and $\langle M_z \rangle$ versus the angle of rotation θ for several applied fields $H_o$ as calculated with the model developed in chapters 4 & 5. The initial field profiles correspond to the situation where the disk is cooled in the field $H_o$.

is consistent with the observation that the period of these residual oscillations is half that of the disk. The magnetic moment will be large whenever $\theta_p$, the direction of strong pinning in the disk, is parallel (or antiparallel) to $H_o$, and will be smallest when $\theta_p$ is perpendicular to $H_o$. The direction of $\theta_p$, however, need not necessarily coincide with the direction of $H_o$ when the sample becomes superconducting and the rotation begins, unless precautions are taken to ensure that this is the case. Consequently the phase shift can be decreased or increased from 0 to $\pi/2$ by varying the initial orientation of the disk. It has indeed been verified that the phase shift varies in step with changes in the initial orientation of the disk.

To explore and evaluate the pinning anisotropy the remanent magnetic moment generated by reducing $H_o$ from near $H_{c2}$ to 0 with the disk at rest has been measured as a function of the orientation of the disks. These results for the V disk are presented in Fig. 2-5. This curve provides an unambiguous measure of the anisotropy of the bulk pinning since $I_R = I_A = I_B = 0$ when $H_o = 0$. (These terms and associated concepts will be explained in the next chapter.) It is noted that the period of the anisotropy is indeed $\pi$, as expected. Further the magnitude of the oscillations in Figure 2-5 is consistent with the magnitude of the residual oscillations in Figure 2-2, bearing in mind that $j_c'$, the gradient of the B profile, varies with B.

It is not too surprising that the pinning in the V disk is anisotropic, since the sheet from which the sample was cut, was not annealed after cold rolling. The direction of maximum pinning coincides with the direction of cold rolling. It is surprising, however, that the VTi disk should also display anisotropic pinning behaviour. This disk was cut on

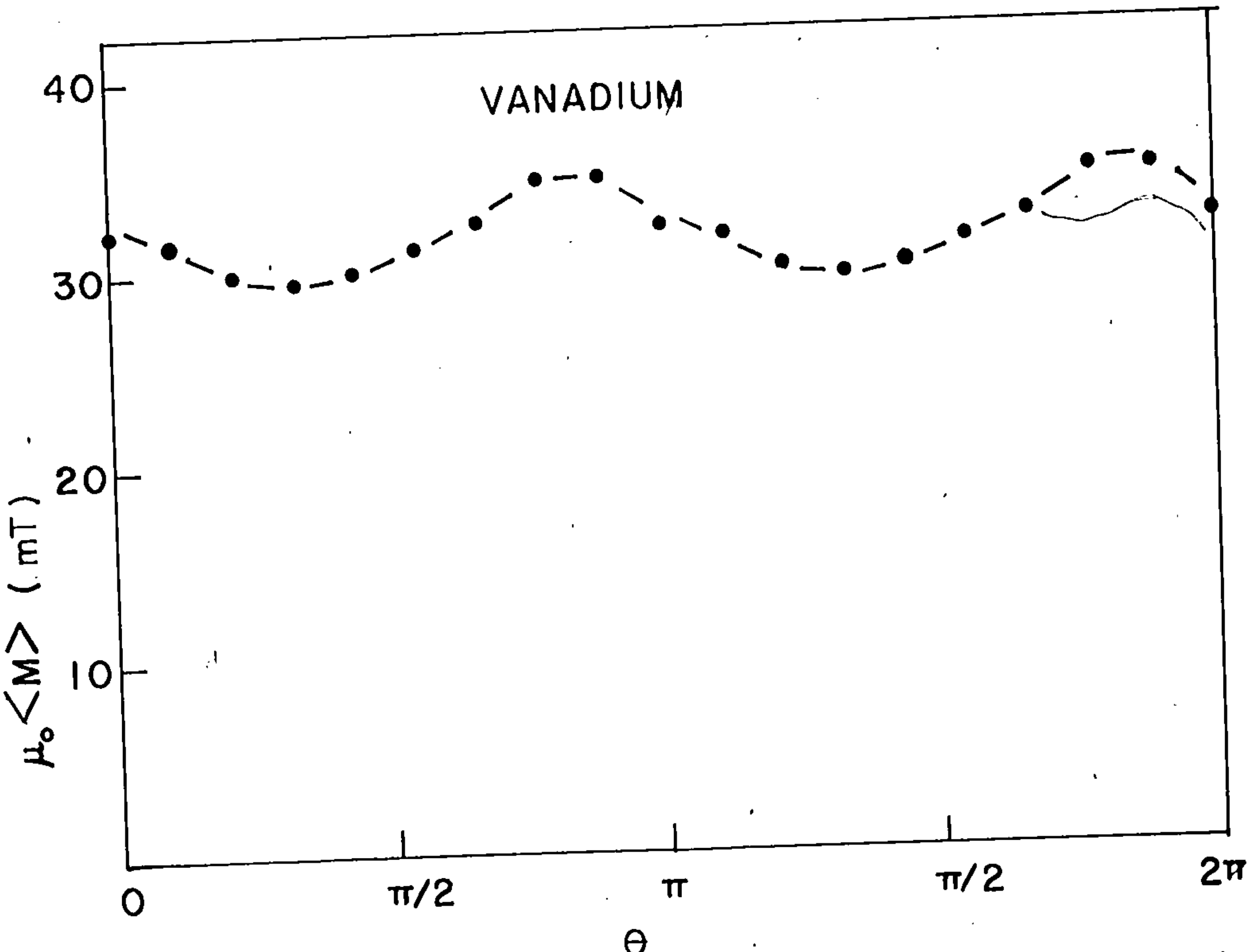


Figure 2-5 Maximum remanent magnetic moment in zero field versus θ, the direction in which the field was applied. It illustrates the pinning inisotropy.

a lathe from an ingot, so that no preferential orientation should arise from this step in the fabrication. It is conceivable that the manner of preparation of the ingot produced a preferential orientation of the grains. A microscopic study of the structure of the specimen has not yet been undertaken.

These oscillations, although annoying (since they introduce undesirable complications) do not significantly affect the final results. This feature is taken into account in the measurements in the following way. The standard magnetization curves and the flux expulsion curve presented and analyzed in the next chapter were measured with $\theta_p$ directed at $45^o$ to $H_o$, and thus at an orientation of intermediate pinning. Furthermore, the magnetic behaviour under rotation was monitored with the disk initially oriented with $\theta_p$ also at $45^o$. This approach, in the light of the model developped in Chapter 4, ensures that the B-profiles in the central region are properly characterized. The anisotropy, however, will play a role, although not an appreciable one, in the configuration of the magnetic induction $\vec{B}(x)$ in the active region (the shoulders of the B profiles). Consequently this may perturb the dimensions of this region. However, since the $\vec{B}(x)$ configuration spans several radians, especially at low fields, the effect of the anisotropy should average out.

## 2.6 Flux Jumps

The phenomenon of flux jumps considerably restricted the range of the measurements, since a reliable quasi-steady state cannot be achieved under these circumstances. With due care, the standard magnetization curves were obtained without interference from flux jumps. The rotation of the disk, however, readily leads to unstable configurations of magnetic induction which abruptly collapse (partially or totally) i.e. flux jumps or avalanches occur. Flux jumps are encountered in the range of applied fields for which the average magnetic flux density <B> is near the maximum of the pinning function (see Figures 3.6 and 3.12), and their magnitude increases rapidly with the pinning strength. This feature has been a determining factor in the selection of samples, since the ideal sample for testing the model presented in Chapter 4 is one with a minimum of surface steps in the B profiles (these being very difficult to evaluate precisely) and weak pinning properties to minimize flux jumping. The second criterion being more imperative than the first one, it was necessary to choose samples in the class of type II superconductors which can be called "partially" or "semi"- reversible type II superconductors although the appreciable magnitude of the surface steps displayed by these samples rendered the analysis of the results more laborious as we will see in the next chapter.

# Chapter 3

## Analysis of the Standard Magnetization Curves

### 3.1 Introduction

Three major contributions to the magnetic behaviour of irreversible type II superconductors have been identified and investigated. These are equilibrium diamagnetism, bulk pinning and the surface barrier. These three basic ingredients account for the main features of the magnetic response of hysteretic type II superconductors subjected to an external magnetic field $\vec{H}_o$ which does not rotate as it varies in intensity. The locus of the magnetic moment as the field $H_o$ is (i) raised from zero to $H_{c2}$ or a high value if $H_{c2}$ is excessively large (ii) subsequently decreased to zero and (iii) increased again in the opposite direction is referred to as the standard magnetization curves. In this chapter an outline of these three basic concepts exploited in the interpretation of these curves is given. In order to proceed to an analysis of the evolution of the magnetic moment of the samples during rotation in a stationary field, it is necessary to determine the gradients and the surface step of the magnetic induction which these can sustain in various applied fields and previous magnetic histories in the superconducting state. The standard magnetization curves of the samples are thus examined and the desired data are extracted in the framework of these basic concepts.

### 3.2 Equilibrium Diamagnetism.

Abrikosov (Abrikosov 57) in his classical paper developed (i) a description of the macroscopic behaviour of ideal or reversible type II superconductors and (ii) a detailed microscopic picture where the magnetic flux permeating these materials consists of a two dimensional lattice or regular array of quantized flux lines. The expressions equilibrium diamagnetism, intrinsic diamagnetism and Abrikosov diamagnetism now current in the literature are used interchangeably to refer to this aspect of Abrikosov's work. In this paper he derived a relationship between the magnetic induction B and the external magnetic field $H_o$ parallel to the surface of an infinite half space. Here B represents a quasi-macroscopic average over a plane embracing several vortices. This relationship between B and $H_o$ is shown schematically in the sketches below where B vs $H_o$ and $H_o$ vs B are presented since it is sometimes useful to consider $H_o$ in equilibrium with B rather than B in equilibrium with $H_o$. The relationship between B and $H_o$ is used to define a permeability $\mu(B) = B/H_o(B)$ or equivalently $\mu(H_o) = B(H_o)/H_o$. The ratio of the upper and lower critical fields $H_{c2}$ and $H_{c1}$ is determined by the Ginzburg-Landau parameter $\kappa$ characteristic of the material.

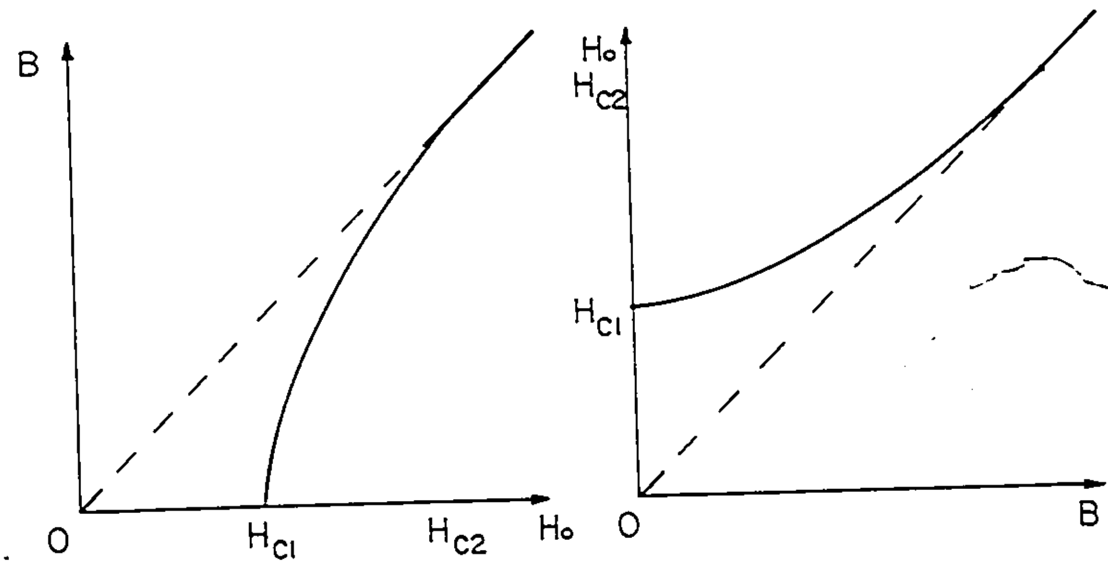

Above the critical field $H_{c1}$ and below the critical field $H_{c2}$, the magnetic induction penetrates the superconductor in flux quanta called fluxons, vortices or flux filaments. Inside a reversible type II superconductor in a uniform applied field $H_o$, the fluxons move freely in the bulk or volume of the material and assume a uniform distribution which minimizes the free energy of the superconductor. The situation which prevails is shown schematically in diagram (a) on the next page where the solid line represents B viewed on a quasi-macroscopic scale. B is a measure of the density of vortices since $B = N\phi_o$ where N is the local density of vortices and $\phi_o$ is the quantum of flux. The vertical segments of B represent the reversible flux shielding or diamagnetic surface current $\mu_o I_A$ which occupies a thin region of dimension of the penetration depth $\lambda$ where $I_A = H_o - B/\mu_o$. When $H_o < H_{c1}$, this Abrikosov surface current is identical to the Meissner current responsible for the Meissner Effect in Type I superconductors since then $I_A = H_o$. The current $I_A$ flowing at the surface ensures that the density of vortices, hence B in the bulk of the superconductor, is in equilibrium with the applied field $H_o$.

## 3.3 Bulk Pinning and the Critical State Concept.

In non-ideal type II superconductors, the motion of fluxons in the bulk of the material is impeded by imperfections and impurities. As a consequence the vortices are not free to achieve a uniform distribution. Thus the density of vortices hence B may vary considerably with position depending on the previous magnetic history of the sample in the superconducting state. Diagrams (b) and (c) on the next page show schematically the situation encountered when an infinite slab is immersed in a

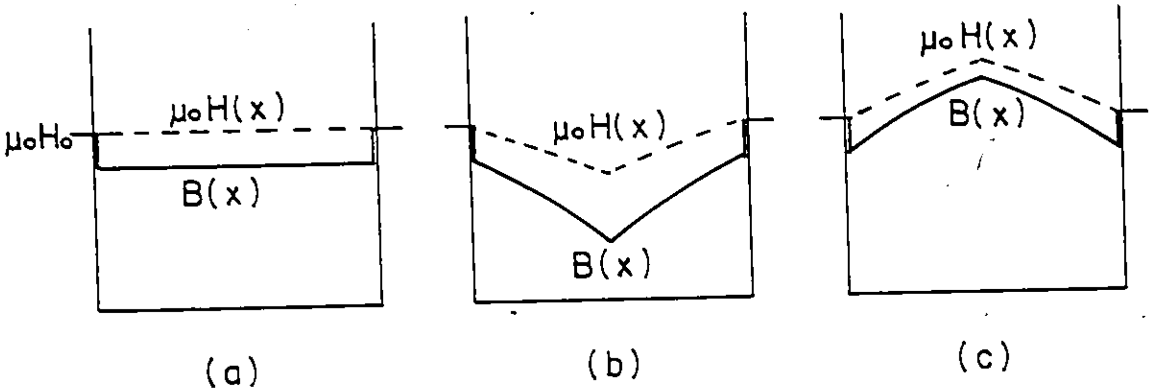


magnetic field applied parallel to its faces and where $H_o$ has increased from zero (diagram (b) ) and decreased from $H_{c2}$ or a high value (diagram (c) ).

These impurities or imperfections of the crystal lattice which hinder the migration or diffusion of flux lines in the bulk of type II superconductors are referred to as pinning sites and give rise to a pinning force when an attempt is made to rearrange or displace the lattice of flux lines threading them. It is beyond the scope of this outline to enter into the complicated interactions between pinning sites and flux lines which give rise to the pinning phenomenon. It is sufficient for our purpose to indicate that the pinning force is analogous to a friction force since it acts only when a driving force is operating on the flux lines. Further the pinning force density has been shown to depend on the magnetic induction $B/H_{c2}$ and on the temperature $T/T_c$ (Kramer 73, Campbell 72, Fietz 69).

The driving force acting on the vortices has been identified as the Lorentz force and is given in its general form by the mathematical expression

$$\vec{F}_L = [\nabla \times \vec{H}(B)] \times \vec{B} \qquad (3\text{-}1)$$

where H(B) is the value of the external field $H_o$ in equilibrium with a flux density B (Friedel 63). H(B) is obtained from the Abrikosov equilibrium condition outlined in the preceeding section. The quantity $\nabla \times \vec{H}(B)$ defines a bulk transport current density $\vec{J}$ and the Lorentz force can be written:

$$\vec{F}_L = \vec{J} \times \vec{B} \qquad (3\text{-}2)$$

The relation between the driving force acting on the vortices, and the pinning force opposing their movement at equilibrium, is known as the critical state concept. It is essentially the force equilibrium condition

$$\vec{F}_L + \vec{F}_p = 0 \qquad (3\text{-}3)$$

Note that the quantities $F_L$ and $F_p$ are forces per unit volume or force densities.

When the magnitude of the magnetic field applied to a superconductor is allowed to change, the new equilibrium field profile inside the superconductor can be obtained from solving this equation with a knowledge of the initial field profile. In particular the magnetic field profiles B (x) and H(B(x) ) or H(x) illustrated in diagram (b) and (c) can be calculated from this equation which in the slab geometry takes the form

$$B \frac{\partial H(B)}{\partial x} = \pm F_p(B, T) \qquad (3\text{-}4 \text{ a})$$

where as has been seen earlier the pinning function is a function of B and T. This picture is well supported by experimental evidence (Swartz 62, Fietz 64, Hauser 62, Silcox 63, 64, Cline 66, Druyvesteyn 64, Bode 62).

If an infinite slab of thickness X is considered and B is taken parallel to the surface of the slab and in the z direction then the quantity $(dH(B)/dx)_c$ defines a critical current density $J_c$ flowing perpendicularly to B, hence along the y axis and equation 3-4 a is simply

$$J_c B = F_p(B, T) \tag{3-4 b}$$

A pick-up coil embracing an area A of width W along the y axis and the thickness X of this slab, will monitor changes in the magnetic flux $\phi = \langle B \rangle WX$ where

$$\langle B \rangle = \int_0^X \frac{B(x)\,dx}{X} \tag{3-5}$$

with the surfaces of the slab located at $x = 0$ and $x = X$. Note that $B(x)$ can be written

$$B(x) = \int_0^x \left(\frac{dB}{dx}\right)_c dx' + \mu_o H_o \tag{3-6}$$

where the subscript c is used to indicate that the gradient of B is in a critical state wherever $J_c$ exists at a critical value.

From the magnetic response of the slab to an increase or decrease of the externally applied field $H_o$, hence from standard magnetization curves, data on $\langle B \rangle$ vs $H_o$ is obtained directly. Further, information on the sequences of $B(x)$ profiles as $H_o$ is varied can be extracted from this data and thus, ultimately, a curve of $(dB/dx)_c$ vs B can be generated for the given sample at a chosen temperature. This aspect will be developed further later in this chapter. Since $(dB/dx)_c$ is the most readily accessible quantity and also the pertinent quantity in the present analysis of magnetic phenomena under rotation, it is useful and meaningful to define an appropriate critical current density $j'_c$ as follows

$$j'_c = \frac{1}{\mu_o} \left(\frac{dB}{dx}\right)_c \tag{3-7}$$

An important feature which should be noticed here is that once $B(x)$ and its spatial derivative have been determined, it is necessary that the pinning function $F_p(B, T)$ be known also in order to arrive at $J_c$ from equation 3-4(b). Generally, however, $F_p$ for a given material is not known and cannot, at present, be derived from first principles. To proceed further in this vein, it is instructive to rewrite equation 3-4(a) as follows

$$B \left(\frac{dH}{dB}\right) \left(\frac{dB}{dx}\right)_c = \pm F_p(B, T) \qquad (3\text{-}4\ c)$$

Frequently workers have adopted the following approach. B vs H, hence dH/dB vs B or H is determined from the magnetization curve for a reversible sample of the given material. This result together with the data on B(x) and $(dB/dx)_c$ vs B for the irreversible sample are then introduced in equation 3-4(c) to obtain $F_p(B, T)$. Evidently this yields an approximation to $F_p(B, T)$ to the extent that the $\kappa$ for the irreversible sample differs from that pertaining to the reversible one. Alternatively specific forms for $F_p$ and B vs $H_o$ may be selected ab initio and their applicability verified by constructing standard magnetization curves from these ingredients until agreement with observations on a particular material is achieved. The dependence of $F_p$ and $H_o$ on B chosen in such an exercise may be analytical or graphical.

Aside from the difficulties encountered in detailed application a crucial feature or flaw remains to be elucidated in this model incorporating the concepts of equilibrium diamagnetism and the critical state. It will be seen below that the introduction of a surface barrier does not completely resolve the basic problem. The picture that was just outlined, although adequate in the range $H_{c1} < H_o < H_{c2}$, fails to account for the observations when $H_o < H_{c1}$. This aspect is now pursued.

In the context just developed, the expected behaviour of <B> and <M> is examined as $H_o$ is decreased from above $H_{c1}$ through zero to beyond $-H_{c1}$ after an excursion to $H_{c2}$ or a high value. It is noticed in the sketches below that because of the operation of equilibrium diamagnetism, B adjacent to the surfaces of the slab has diminished to zero when $H_o = H_{c1}$ where it remains as $H_o$ varies from + $H_{c1}$ to - $H_{c1}$. As a consequence, B(x) and <B> remain undisturbed during the sweep of $H_o$ between these limits. Finally B(x) undergoes a change when $|H_o|$ increasing with "negative" polarity exceeds $|H_{c1}|$ as shown in diagram (b). Since the magnetization $\langle M \rangle = \langle B \rangle/\mu_o - H_o$, throughout the range $-H_{c1} \leq H_o \leq H_{c1}$, $d\langle M \rangle/dH_o = -1$ should be observed. Diagrams (c) and (d) present the behaviour of <B> and <M> vs $H_o$ which follows from these considerations (Dunn 68, Ullmaier 66 a).

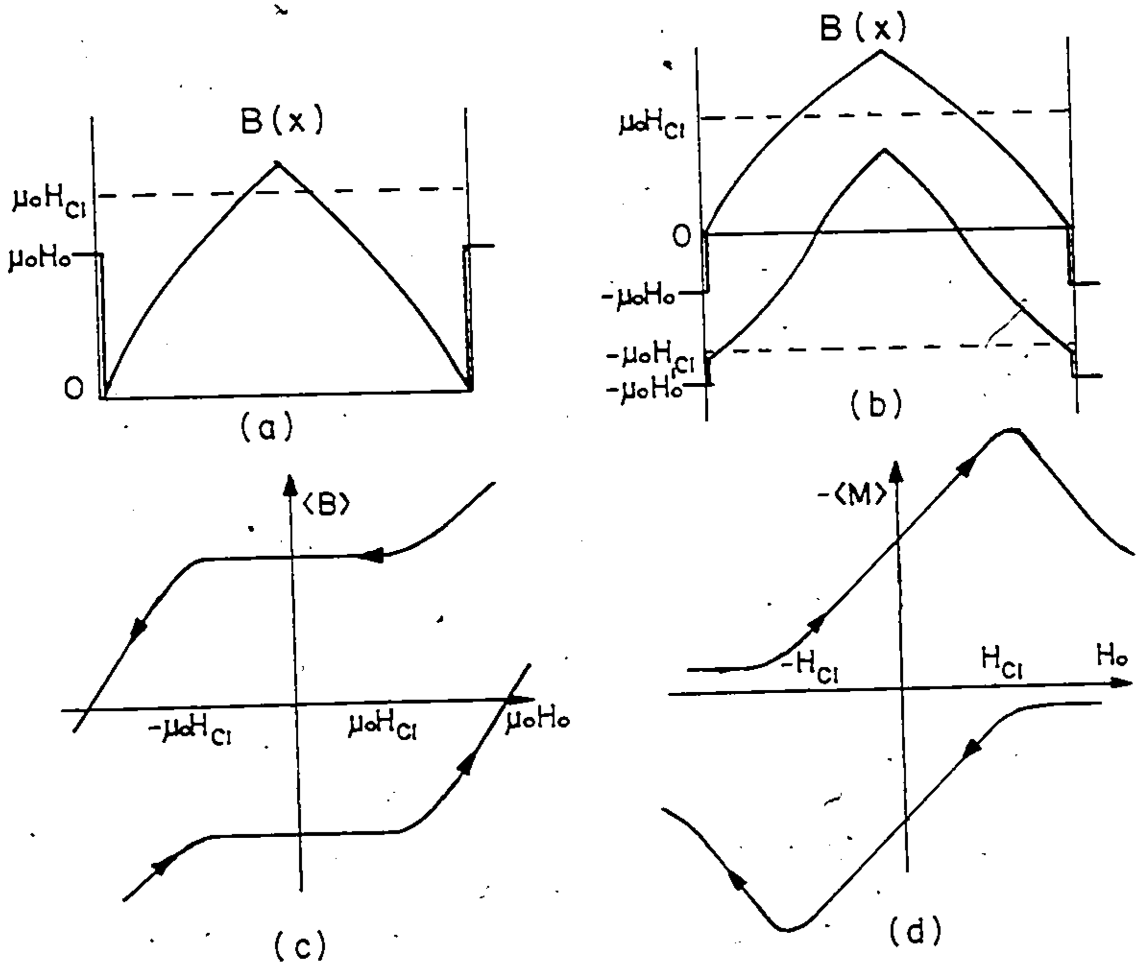


In contrast with these predictions, however, all the pertinent measurements reported in the literature as well as the ones made on the samples studied in this thesis, exhibit curves where $d\langle B\rangle/dH_o \neq 0$ and $|d\langle M\rangle/dH_o| < 1$ throughout the range $-H_{c1} \leq H_o \leq H_{c1}$ for the situation just described. Evidently something is amiss. The introduction of a surface barrier reduces but does not completely remove the discrepancy between theory and observations.

## 3.4 Surface Barrier

There is considerable evidence that the surface of type II superconductors can, under certain conditions, support an appreciable irreversible current, throughout the range $0 \leq H_o \leq H_{c2}$ (Schweitzer 67a, 67b, Swartz 65, Hart 67, Love 66, Ullmaier 66b, Chang 67, LeBlanc 67, Bussière 76). This current is irreversible since the previous magnetic history of the specimen in the superconducting state plays a role in the existence of the current, its magnitude and perhaps also in its sense of circulation. The expression, surface barrier, is also frequently used to denote this capacity of the surface to sustain irreversible currents. There is some ambiguity however in the use of the two expressions since some workers visualize that a barrier to entry or exit of flux at the surface can exist and operate with no macroscopic (free ) persistent currents circulating along the surface. In the following, the issue is ignored since it is not pertinent to the present discussion and the expression surface barrier or barrier is used because it is shorter and more picturesque than the cumbersome expression, irreversible surface current.

The origin, nature and behaviour of the surface barrier are at present shrouded in uncertainty and controversy. Only a few aspects of this intricate problem are mentioned here. The barrier has been viewed by some workers (Fink 65, Park 65) as an extension or continuation below

$H_{c2}$ down to $H_o = 0$ of the deGennes surface sheath known to exist in the range $H_{c2} \leq H_o \leq H_{c3}$, where superconductivity in the bulk has been quenched. On the other hand, various mechanisms of pinning of vortices by the surface discontinuity have been proposed (Swartz 65). In this context, Bean and Livingston (Bean 64) developed a simple image force picture to account for the observation that flux entry can be delayed beyond $H_{c1}$ but the residual (remanent) magnetic moment at $H_o = 0$ can be negligible. A layer of magnetic (ferro or antiferro) metal or one of high conductivity in intimate contact with the surface can suppress or reduce the barrier (Barnes 66). Also the barrier is depressed when the surface is pierced by the applied magnetic field (Zahradnitsky 73). In these respects, the behaviour of the surface barrier is similar to that of the surface sheath.

There are two features of the barrier which are pertinent to the present work. (i) The height of the barrier decreases as $H_o$ increases, the rate of decrease being particularly rapid in the low range of $H_o \gtrsim H_{c1}$ (Love 66, Ullmaier 66, Chang 67). (ii) The surface barrier may be semi-permeable i.e. it opposes entry of vortices much more effectively than their exit (Swartz 65, Chang 71, Rollins 67).

The effect of the barrier on the sequence of B(x) profiles is now examined as $H_o$ is decreasing from above $H_{c1}$ through zero and beyond $-H_{c1}$ after an excursion to $H_{c2}$. Let $\mu_o I_B$ and $\mu_o I'_B$ denote the height of the barrier when it opposes exit and entry of flux respectively. The barrier presumably operates in a narrow region of dimensions of $\lambda$ and is represented by a vertical line in the sketches below where the abrupt change in B due to equilibrium diamagnetism is also indicated at the surface by an adjacent vertical line drawn inside the former. B adjacent to the surfaces of the slab has diminished to zero when $H_o = H_{c1} - I_B$ where it remains as $H_o$ varies from this value to $-H'_o = -(H_{c1} + I'_B)$. As a consequence, B(x) and <B> remain undisturbed during the sweep of $H_o$ between these limits. Finally B(x) undergoes a change when $|H_o|$ increasing with "negative" polarity exceeds $|H_{c1} + I'_B|$ as shown in diagram (b). Diagrams (c) and (d) present the behaviour of <B> and <M> which follows from these considerations. Note that the main effect of the barrier is to shift the base lines and thereby introduce asymmetries in the locus

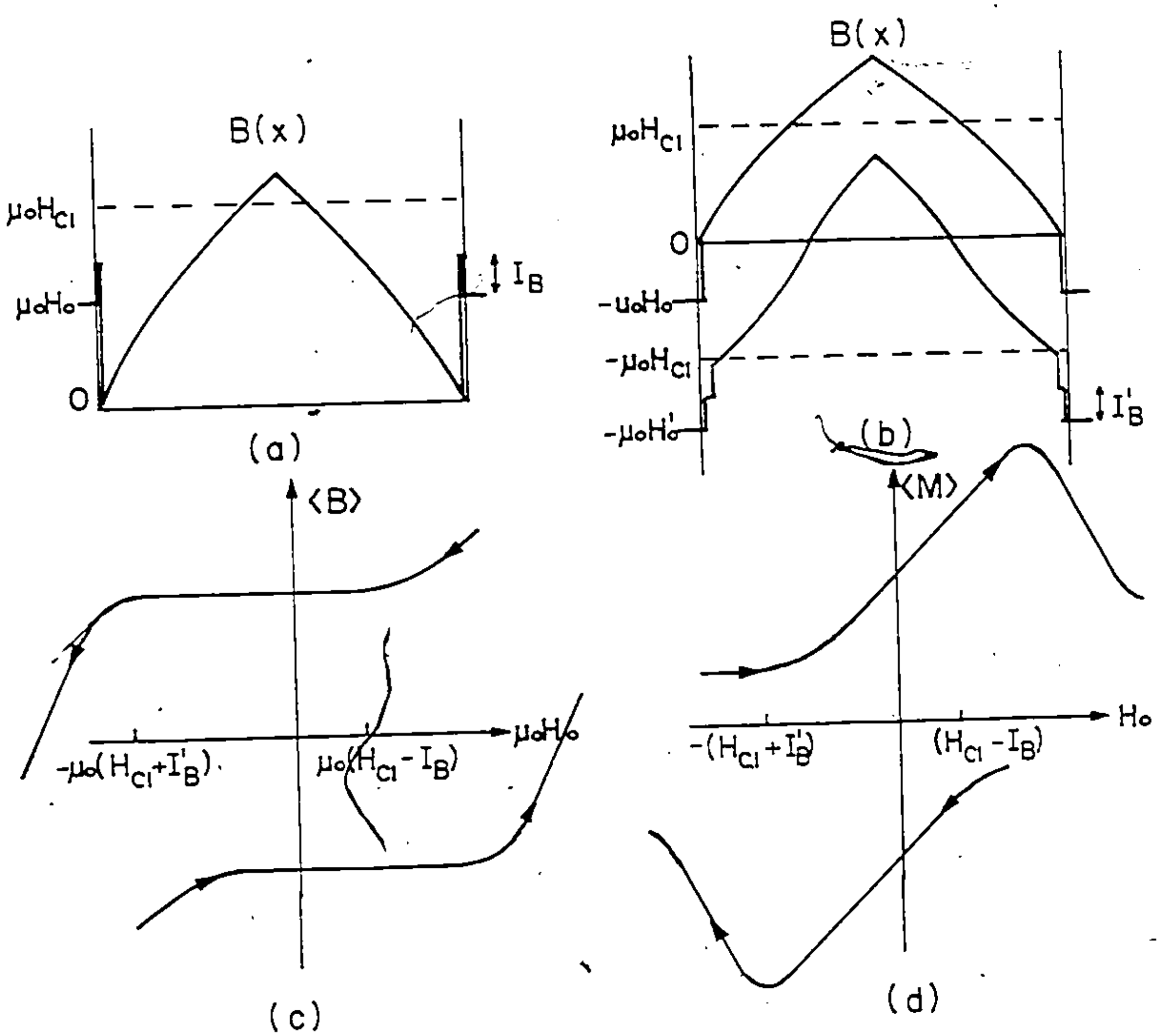

of <B> and <M> vs $H_o$. The "discontinuity" in B at the surface due to the combined operation of $I_A$ and $I_B$ (or $I'_B$) is referred to as the surface step or break.

Note that as the applied field is decreased from $H_{c1}$, flux continues to leave the specimen until $H_o = 0$ if $I_B = H_{c1}$. In this case, the base line and the asymmetry are shifted to $H_o = 0$. This also indicates that the surface step passes through a maximum and decreases to zero as $H_o$ approaches zero.

The picture just outlined satisfactorily accounts for the phenomena observed during the initial application of $H_o$ to a virgin specimen and also when $H_o$ is decreased to zero from $H_{c2}$ or a high value if it is assumed that $I_B(H_o = 0) = H_{c1}$. It can also account for the small expulsion of flux observed when irreversible samples cool through $T_c$ in a stationary $H_o$. It also describes the magnetization curve as $H_o$ increases beyond $H_{c1} + I'_B$ after a reversal of polarity. The model unfortunately fails to describe the observations in the range $0 < H_o \leq H_{c1} + I'_b$ after a reversal of polarity since experimental curves do not display a linear region with the predicted slope under these circumstances. This disparity between theory and reality is well known by most workers in the field. The problem can frequently be ignored in the interpretation of many experimental results. In the analysis of the present experimental results, however, a significant portion of the data spans this anomalous range. It has then been decided to proceed empirically and extract an "effective" surface step vs $H_o$ from the locus of the measured magnetization through this problematic region, after $j'_c$ vs B has been determined. The pertinent data are now presented. It is also indicated how $j'_c$ vs B and the surface steps vs $H_o$ are obtained from this data exploiting the model just outlined.

## 3.5 Application of the Basic Concepts.

The basic ideas just outlined are now applied to an analysis of the standard magnetization curves and to the flux expulsion measurements for the samples under study. The standard magnetization curves for the V and VTi disks are presented as solid lines in Figures 3-1 and 3-7 at the end of this chapter. The disks are immobile and the intensity of the applied field $H_o$ is varied slowly and continuously as these measurements are made. $H_o$ is directed parallel to the flat faces of the disk specimen. In these graphs the tradition of tracing the diamagnetic moment in the first quadrant is adopted. Also various sections of the locus of the magnetic moment vs $H_o$ are distinguished and labelled as follows.

Section 1. $H_o$ is increased from zero with the sample in the virgin state and raised to H* defined below.

Section 2. $H_o$ continues to increase from H* and proceeds towards and beyond $H_{c2}$ if possible.

Sections 1 and 2 are denoted as diamagnetic curves since here the average magnetic induction $\langle B\rangle < H_o$.

Section 3. $H_o$ is decreased from $H_{c2}$ or a high value to zero. This section is known as the paramagnetic curve since $\langle B\rangle > H_o$.

Section 4. $H_o$ after being reduced and traversing zero is raised again in the opposite direction to H*.

For economy of space and in keeping with established custom section 4 is presented in the first quadrant in the Figures. The curves of the magnetization coincide beyond $|H_o| >$ H* regardless of whether the sweep of $H_o$ began in zero field with a virgin sample or from $H_o = -H_{c2}$ (or a large negative value). H* is the applied field where curve 4 meets curve 1. Curve 2 is then a continuation of both these curves. Section 4 is denoted as the hybrid curve since the sample contains diamagnetic regions adjacent to the surface where $B(x) < H_o$ and a central region of trapped flux of polarity opposite to $H_o$. When $H_o$ attains $H^*$ this core of trapped flux has just been eliminated and the advancing front of the B profiles has reached the mid plane of the disk (or infinite slab).

It is noticed that curve 1 traverses a peak before $H^*$ is attained. This is a consequence of the fact that the B profiles are convex upwards as presented in the sketches. This feature follows directly from the fact that $j_c'$ diminishes as B increases.

Flux is expelled from the disks as they are cooled through $T_c$ to the final temperature T = 4.2 K in various stationary applied fields $H_o$. In figures 3-2 and 3-8 are presented the magnetization at 4.2 K resulting from this procedure. The dots in these Figures are experimental data points. It will be explained shorthly how the dashed curves are obtained. The curve defined by these data points (curve 5) are referred to as the cooling magnetization curve or cooling curve, for brevity; the sample along this curve is referred to as being in the non-magnetic state although it exhibits a small diamagnetic moment. This magnetic moment is known as the partial Meissnêr diamagnetism when $H_o < H_{c1}$ and as the partial Abrikosov diamagnetism when $H_o > H_{c1}$.

From the preceding it is seen that a sample can be viewed as existing in four different magnetic states, depending on its previous history in the superconducting state, namely: diamagnetic, paramagnetic, hybrid and non-magnetic. In chapter 4 the magnetic response of the disks to rotation will be examined for all of these interesting initial conditions or states. It is now shown how information is extracted on $j_c'$ vs B and the surface step vs $H_o$ from curves 1 through 5 presented in Figures 3-1, 3-2, 3-7 and 3-8.

It is recalled that the critical current density $j_c'$ has been defined by the relation $j_c' = (dB/\mu_o dx)_c$ (equation 3-7). Along the diamagnetic and hybrid curves the surface step is denoted by $\mu_o I_R'$ where $I_R' = (I_A + I_B')$. It is noticed that both $I_A$ and $I_B'$ flow so as to oppose entry of flux, hence in a diamagnetic sense. As a consequence B inside the sample and adjacent to the surface lies below the applied magnetic induction $\mu_o H_o$. Along the paramagnetic and cooling curves the surface step is denoted by $\mu_o I_R$ where $I_R = (I_A - I_B)$. Note that $I_B$, the surface barrier current flows to retain flux in the sample, hence in a paramagnetic sense. Since however, flux is expelled from the sample during cooling in a static $H_o$ it is inferred that $|I_A| > |I_B|$. Thus the resultant surface step or net surface current is diamagnetic along curves 3 and 5 in the Figures and B adjacent to the surface again lies below $\mu_o H_o$. It is cumbersome to indicate the magnitude of the various quantities by the conventional $||$ notation in every case. Accordingly, this notation will be used only when it is useful for clarity. Otherwise the symbols will represent the absolute values of the quantities involved.

A first rough estimate of $j_c'$ vs B and $I_R$ and $I_R'$ vs $H_o$ is obtained over the range $H^* < H_o < H_{c2}$ as follows. From inspection of diagrams (a) and (b) on the next page it is easily seen that

$$\frac{\langle B\rangle_2}{\mu_o} = H_o - I_R' - \frac{j_c'(\langle B\rangle_2)X}{4} \qquad (3\text{-}8)$$

$$\frac{\langle B\rangle_3}{\mu_o} = H_o - I_R + \frac{j_c'(\langle B\rangle_3)X}{4} \qquad (3\text{-}9)$$

where the B profile is taken as linear. $\langle B\rangle_2$ and $\langle B\rangle_3$ are the average magnetic induction in diagrams (a) and (b) respectively and are known from the corresponding magnetization curves (sections 2 and 3) since

$$<M>_2 = \frac{<B>_2}{\mu_o} - H_o \tag{3-10}$$

and

$$<M>_3 = \frac{<B>_3}{\mu_o} - H_o \tag{3-11}$$

In this first coarse evaluation, $I_R$ is taken equal to $I'_R$. This is equivalent to assuming that, the surface barriers to flux exit and entry $I_B$ and $I'_B$ are negligible compared to the Abrikosov diamagnetic current $I_A$. It is also assumed that $j'_c(<B>_2) = j'_c(<B>_3)$ for corresponding $H_o$. The sums and differences of $<M>_3$ and $<M>_2$ for corresponding $H_o$ then readily provide a first crude approximation for $j'_c(B)$ and $I_R$ (or $I'_R$) since in this context,

$$I_R = I'_R = \frac{|<M>_2| - |<M>_3|}{2} \tag{3-12}$$

and

$$j'_c(<B>) = \frac{2}{X} \{|<M>_2| + |<M>_3|\} \tag{3-13}$$

where $<B>/\mu_o \approx H_o - I_R$. Clearly this procedure overestimates $I_R$ and underestimates $I'_R$.

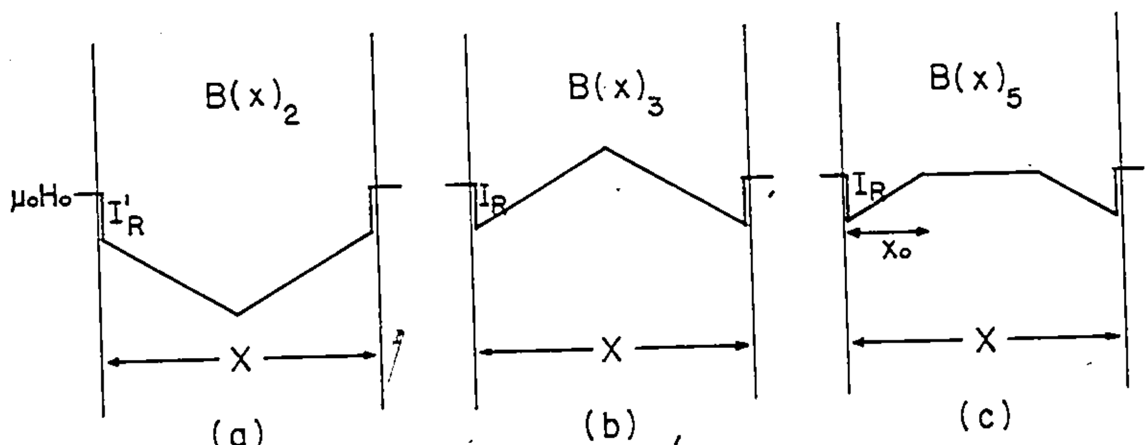

Separately another crude estimate of $I_R$ and $j_c'$ is obtained for the entire range $0 \leq H_o < H_{c2}$ using equation 3-9 and the paramagnetic magnetization curve (curve 3) together with the flux expulsion or cooling curve (curve 5) and the expression

$$\frac{\langle B\rangle_5}{\mu_o} = H_o - \frac{I_R x_o}{X} = H_o - \frac{I_R^2}{X j_c'(\langle B\rangle_5)} \qquad (3\text{-}14)$$

for the average magnetic induction $\langle B\rangle_5$ after cooling in a static magnetic field $H_o$ where again a linear B profile is assumed. Equation 3-14 can be written from inspection of diagram (c) above, noting that $x_o = I_R/j_c'$. Taking $j_c'(\langle B\rangle_3) \approx j_c'(\langle B\rangle_5) \approx j_c(\mu_o H_o)$ at corresponding $H_o$ in equations 3-9 and 3-14 the other approximation is readily obtained for $I_R$ and $j_c'(B)$ from the experimental curves for $\langle M\rangle_3$ and $\langle M\rangle_5$ vs $H_o$ since

$$\langle M\rangle_5 = \frac{\langle B\rangle_5}{\mu_o} - H_o \qquad (3\text{-}15)$$

From examination and weighting of these initial estimates a smooth graph and a table of $I_R$ vs $H_o$ and $j_c'$ vs B are constructed.

Attention is then focussed on the exact formulation

$$\langle B\rangle = \frac{2}{X}\int_0^{X/2} B(x)\,dx \qquad (3\text{-}16)$$

for $\langle B\rangle$ where

$$\frac{B(x)}{\mu_o} = H_o - I_R + \int_0^x j_c'\,dx' \qquad (3\text{-}17)$$

for the paramagnetic and the cooling curve. In the latter case $B(x) = \mu_o H_o$ in the region $x_o \leq x \leq X/2$. The integrals are performed numerically. Taking the boundary values $H_o - I_R$, hence $I_R$ as the quantities to be determined more accurately, the attention is concentrated on the experimental cooling curve progressing computationally from $H_o \lesssim H_{c2}$ to $H_o = 0$ along this curve generating a better approximation for $I_R$ vs $H_o$.

This improved table of $I_R$ vs $H_o$ is then introduced into equation 3-17 and the same procedure is undertaken with the experimental paramagnetic curve (curve 3). Again progressing along the latter curve from $H_o \lesssim H_{c2}$ to $H_o = 0$ the contribution to the integral due to $j_c'$ for the first segment $\Delta x$ adjacent to the surface is treated as the quantity to be determined more accurately and thereby generating an improved graph of $j_c'$ vs B.

Returning again to the flux expulsion or cooling curve the calculations are repeated for $I_R$ exploiting this improved version of $j_c'$ vs B. This back and forth procedure is pursued until the resulting $j_c'$ vs B and $I_R$ vs $H_o$ curves have stabilized. A computer program which accomplishes these progressive sequential computations was developed. Finally equipped with a satisfactory final $j_c'$ vs B curve the attention is then turned to the experimental diamagnetic and hybrid magnetization curves (sections 2 and 4 respectively) where

$$\frac{B(x)}{\mu_o} = H_o - I_R' - \int_0^x j_c' \, dx' \tag{3-18}$$

$I_R'$ is computed progressing along the experimental curves from $H_o \lesssim H_{c2}$ to $H_o = H^*$ for the former (curve 2) and from $H_o = 0$ to $H_o = H^*$ for the latter (curve 1). As indicated earlier in this chapter $I_R'$ vs $H_o$ along the hybrid magnetization curve is viewed as an "effective" or "empirical" surface step since the accepted picture predicts a locus of $\langle M \rangle$ vs $H_o$ in this situation which does not correspond with observations. Indeed throughout the range $0 < H_o < H^*$ along the hybrid curve, $I_R' \lesssim I_A$ is extracted from the data, whereas the model requires that $I_R' \geq I_A$. It is stressed that the flaw is not in the method of computation but in the model. Since reliable and appropriate values for $I_R'$ are required rather than idealized but inapplicable results, in order to analyze the pertinent data on the disks under rotation, no alternative is seen but to proceed as has been done in this anomalous and puzzling region of the magnetization curves.

## 3.6 Results and Conclusion

The $j_c'$ vs B, $I_R$ vs $H_o$ and $I_R'$ vs $H_o$ curves obtained for the V disk by the procedure just outlined, are presented in Figure 3-3 and 3-4. The dashed lines in Figures 3-1 and 3-2 show the final magnetization curves computed with the model described in this chapter. Obviously the agreement is very good since the quantities $j_c'$, $I_R$ and $I_R'$ were extracted from these experimental curves. In Figure 3-1 the calculated curves coincide almost perfectly everywhere and for this reason the dashed lines are plotted only along curve 1 for the portion where a small difference is observed. Although $I_R'$ does not agree with the accepted ideas which were presented in this chapter it is believed that it constitutes a reliable experimental fact. This statement is also supported by the experimental results presented in the next chapter where $I_R'$ is used in their interpretation.

When the same procedure was used to obtain $j_c'$, $I_R$ and $I_R'$ for the V-Ti disk it yielded $j_c'$ and $I_R'$ which were not well behaved. In particular, $I_R'$ was found to be negative in some range of $H_o$, that is, it was paramagnetic instead of being diamagnetic. Obviously such behaviour is not acceptable. This was not a complete surprise to us since it had been observed that this sample suffers from inhomogeneity of composition. Indeed, another sample prepared from the same ingot and studied by J.P. Lorrain, had not shown any detectable flux expulsion when cooled in a magnetic field. Consequently, the quantities $j_c'$, $I_R$ and $I_R'$ obtained using section 5 of the magnetization curve (i.e. flux expulsion) appear not to be reliable. On the other hand the other branches of the magnetization curves are comparable for different samples from the same ingot.

An alternative was then to extract from the magnetization curves (curves 2, 3 and 4) an average surface step $\bar{I}_R\,(H_o) \simeq (I_R(H_o) + I_R'(H_o))/2$ simultaneously with the corresponding data on $j_c'$. The procedure followed to obtain $j_c'$ and $\bar{I}_R$ was very similar to the one described earlier to obtain $j_c'$, $I_R$ and $I_R'$. Plots of $j_c'$ vs B and $\bar{I}_R$ vs $H_o$ are presented in Figures 3-9 and 3-10. The dashed lines in Figures 3-7 and 3-8 represent the computed magnetization curves using $j_c'$ and $\bar{I}_R$ of Figures 3-9 and 3-10. Obviously the flux expulsion data of Figure 3-8 cannot be reproduced. Presumably this is a consequence of the compositional inhomogeneity. On the other hand, the experimental results of Figure 3-7 are adequately reproduced. This then supports the assumption that the overall behaviour of this sample can be adequately described by a surface step $\bar{I}_R$ and a $j_c'(B)$.

As indicated earlier in this chapter it is also of considerable interest to determine the pinning function $F_p(B)$ for the samples. From the available data, however, only the quantity $j_c'(B) = (dB/\mu_o dx)_c$ has been extracted so far. It is relatively straightforward at this juncture to compute $j_c'B$, which is denoted by $F_p'(B)$, and the results of this computation are presented in Figures 3-5 and 3-11. Note from equations 3-4 and 3-7 that

$$j_c'B = \frac{B}{\mu_o}\left(\frac{dB}{dx}\right)_c = \frac{F_p(B)}{\mu_o(dH/dB)} = F_p'(B) \qquad (3\text{-}19)$$

Thus $F_p'(b)$ can be viewed as defining an "effective" pinning function and corresponds to the quantity frequently envisaged in the literature since many workers take $\mu_o(dH/dB) = 1$. This approximation is acceptable near $H_{c2}$ but becomes very unsatisfactory in the vicinity of $H_{c1}$. However, no accurate data are available on the variation of $I_A$ with $H_o$ hence the relationship between B and H for the present samples. Nevertheless it is of some interest to explore the semi-quantitative behaviour of $F_p(B)$ exhibited by these samples.

The following simple, useful and approximate phenomenological relationship between B and H has been proposed and exploited by Clem

$$\mu_o H = \sqrt{(\mu_o H_{c1})^2 + (kB)^2} \qquad (3\text{-}20)$$

where $k = \sqrt{H_{c2}^2 - H_{c1}^2}/H_{c2}$. The permeability $\mu$ then has the simple form

$$\mu = \frac{dB}{dH} = \frac{\mu_o H}{k^2 B} \qquad (3\text{-}21)$$

hence the slope of B vs $\mu_o H$ is $\approx H_{c2}^2/(H_{c2}^2 - H_{c1}^2) \approx 1$ near $H_{c2}$. In Figures 3-6 and 3-12 $F_p(B) = \mu_o j_c' B(dH/dB)$ are presented for the V and VTi samples. They were obtained using Clem's expression for $\mu$ together with the experimental results for $j_c'$.

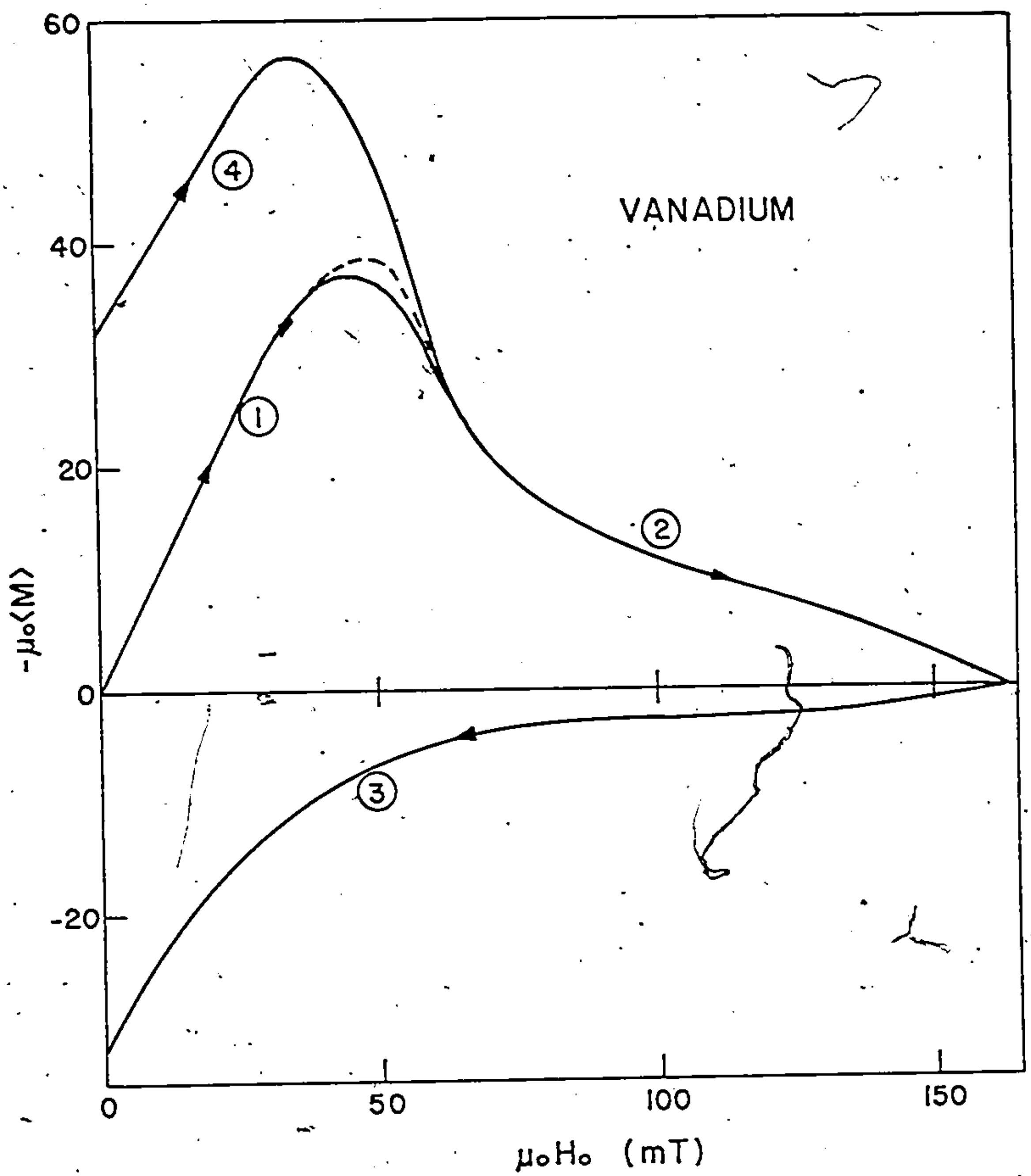


Figure 3-1 Standard magnetization curves for the vanadium sample. The calculated curves overlap almost perfectly the experimental curves except for a short length along section 1 where the calculated curve is shown as a dashed line.

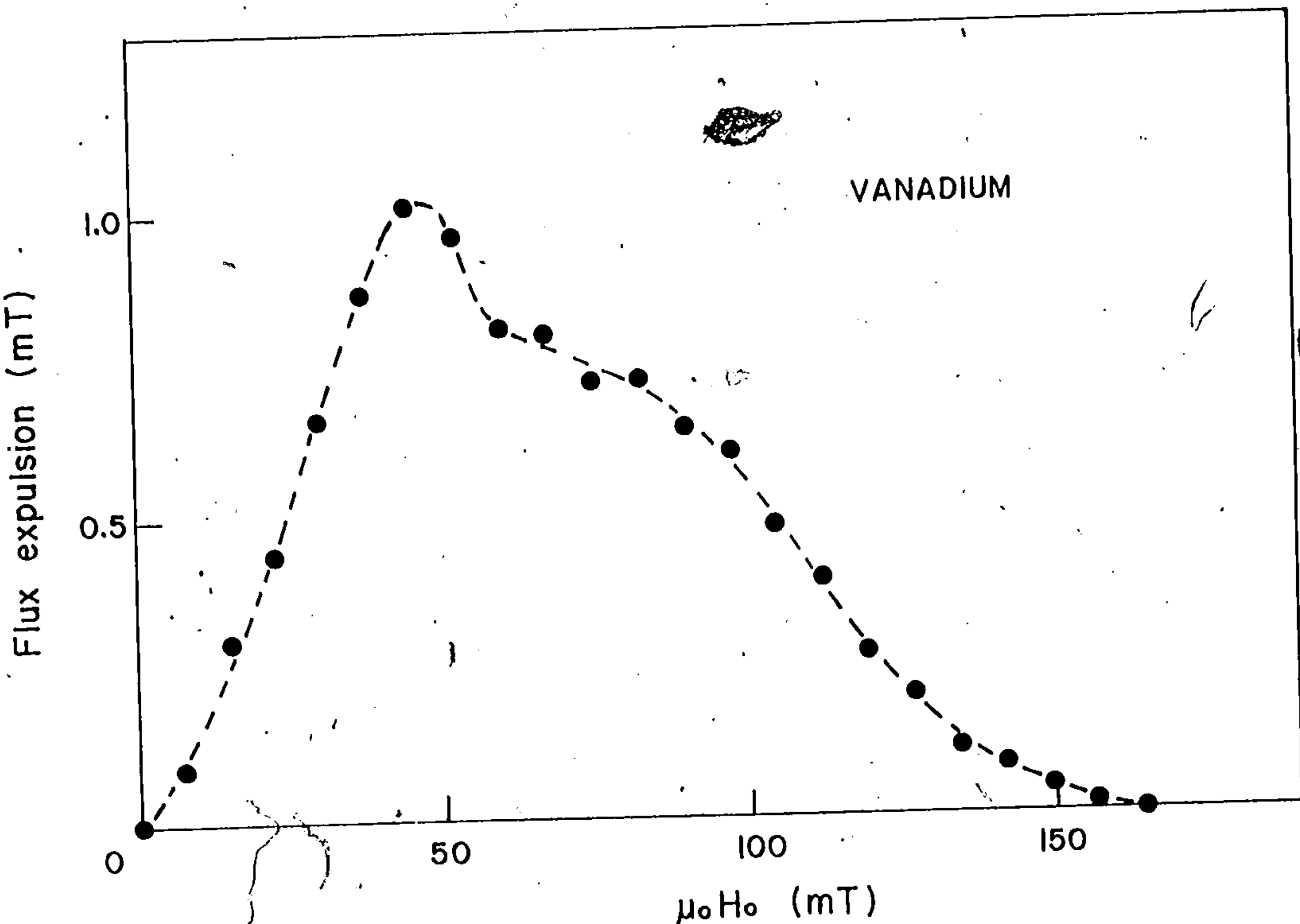


Figure 3-2. Flux expulsion upon cooling the sample in a field $H_o$. The dashed curve represents the calculated values. (vanadium sample)

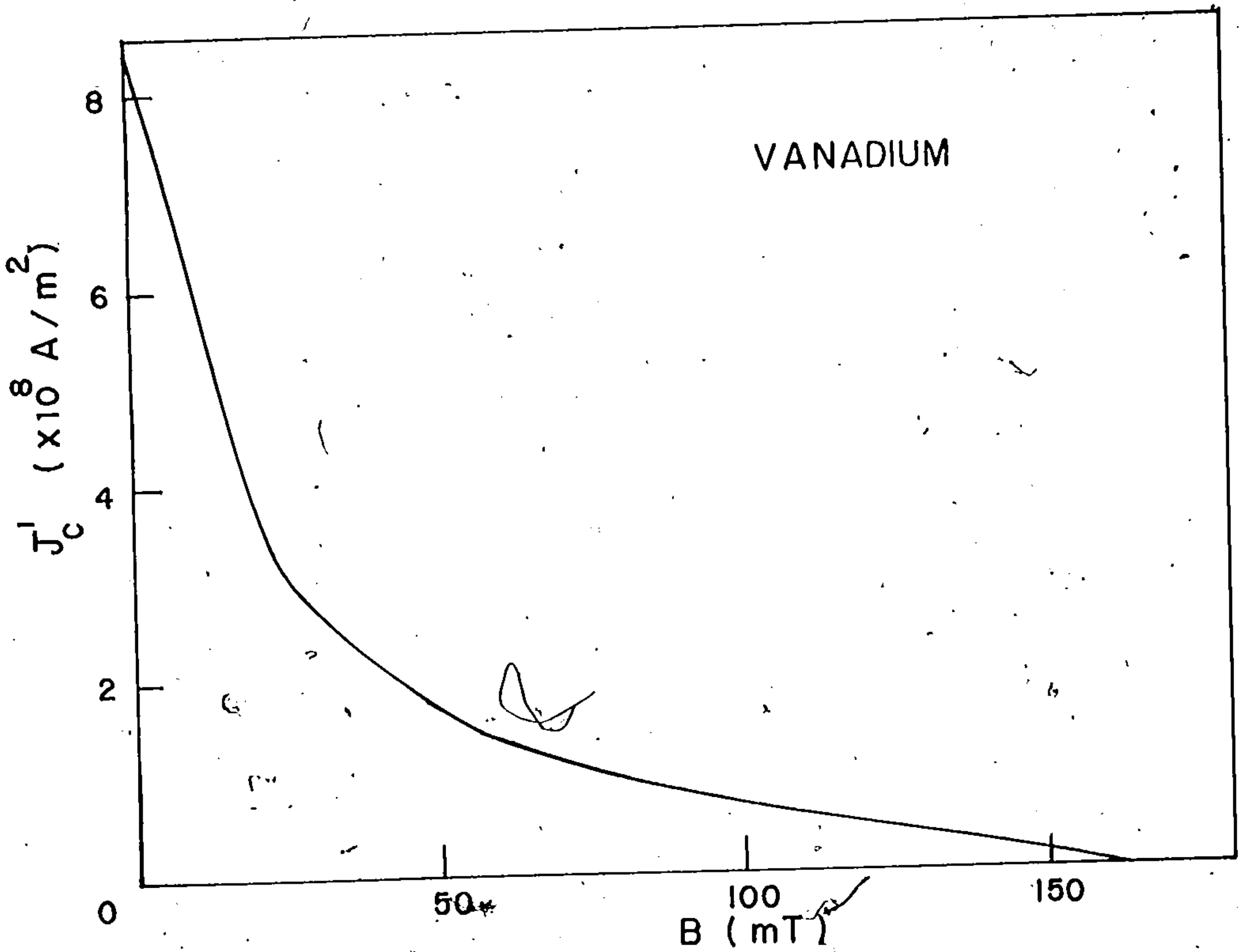


Figure 3-3 $j_c^{\prime}$ vs B for the vanadium sample.

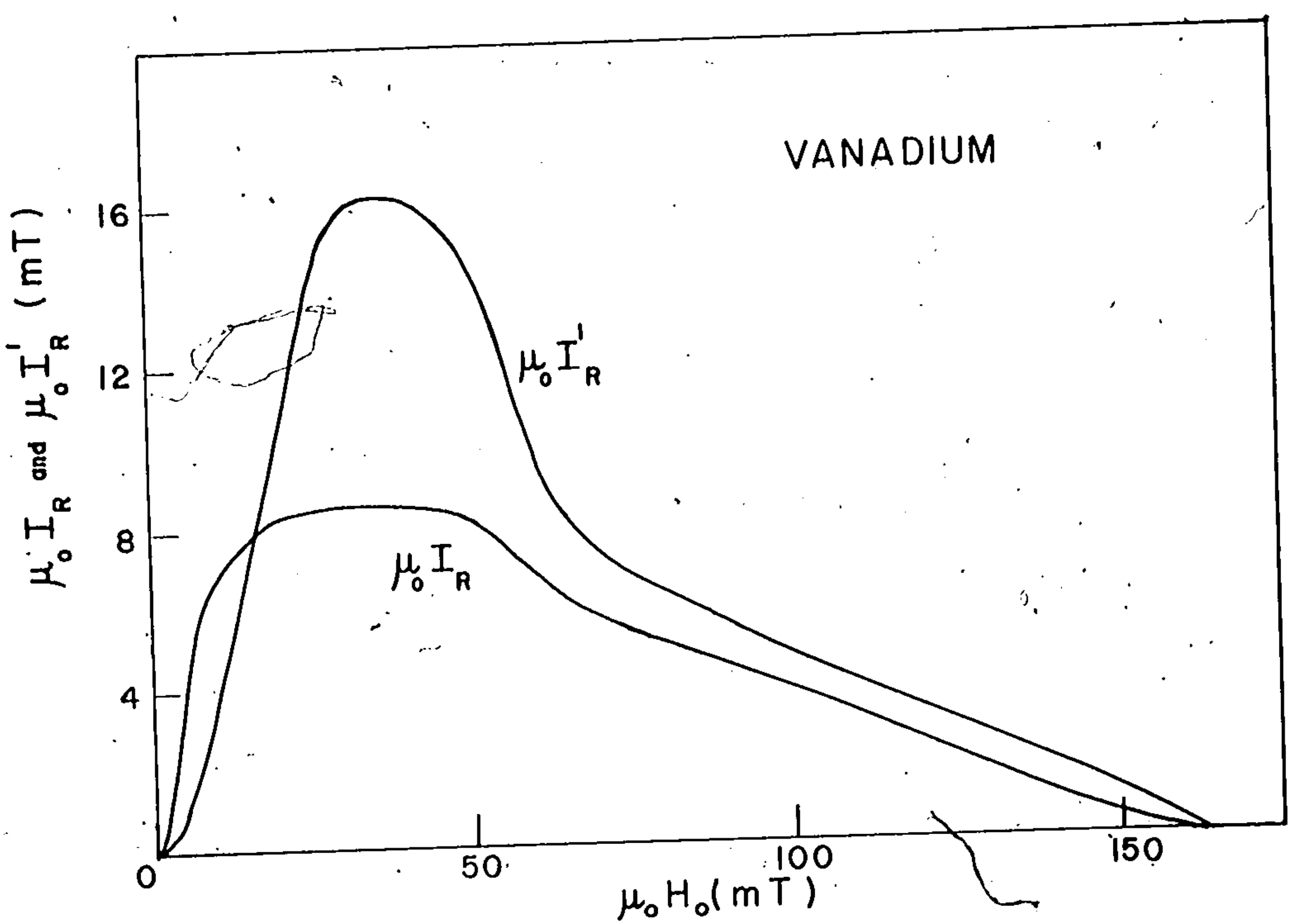


Figure 3-4 $I_R$ and $I'_R$ vs $H_o$ for the vanadium sample.

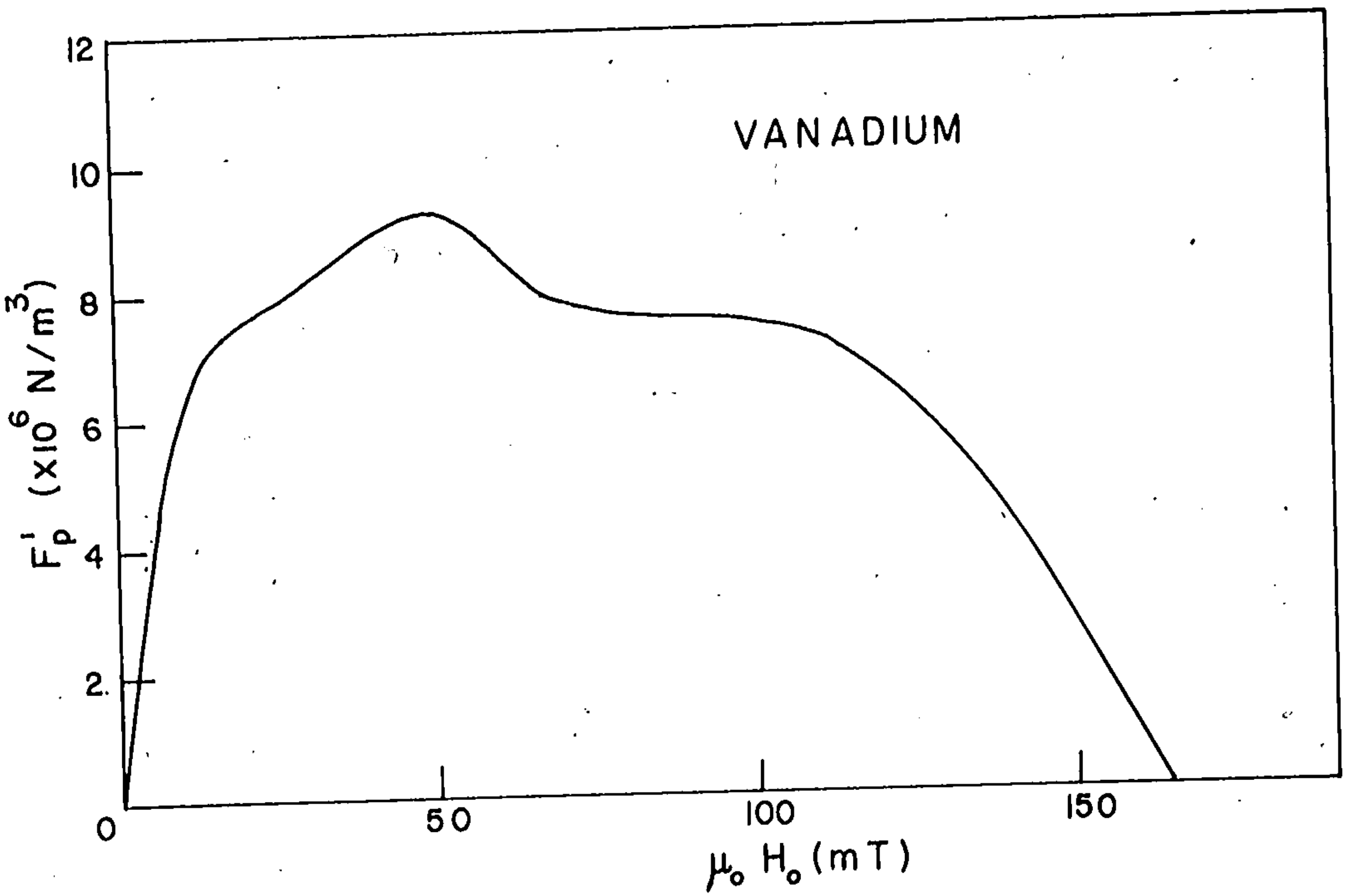


Figure 3-5 $F'_p$ vs B for the vanadium sample

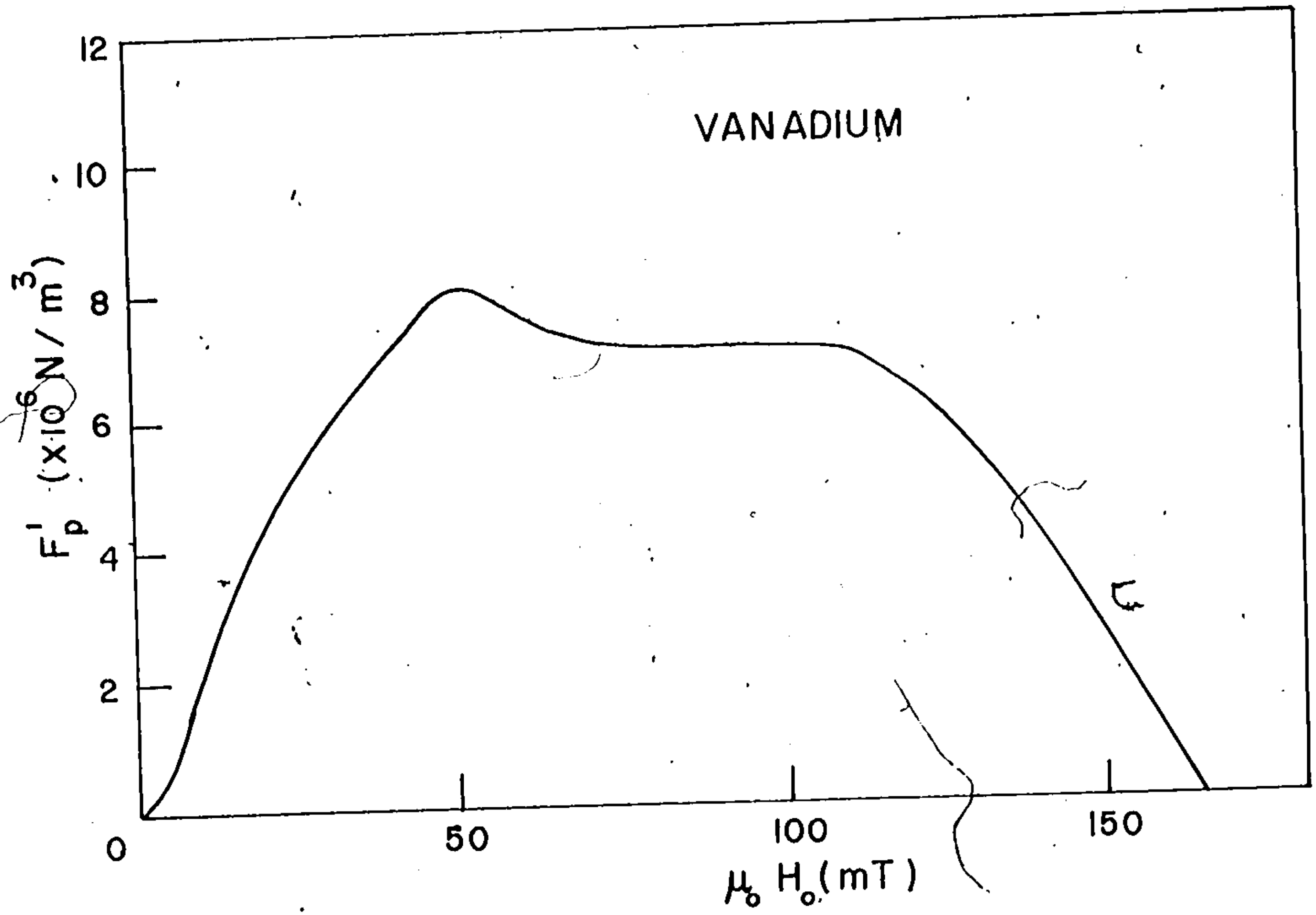


Figure 3-6 $F_p$ vs B for the vanadium sample.

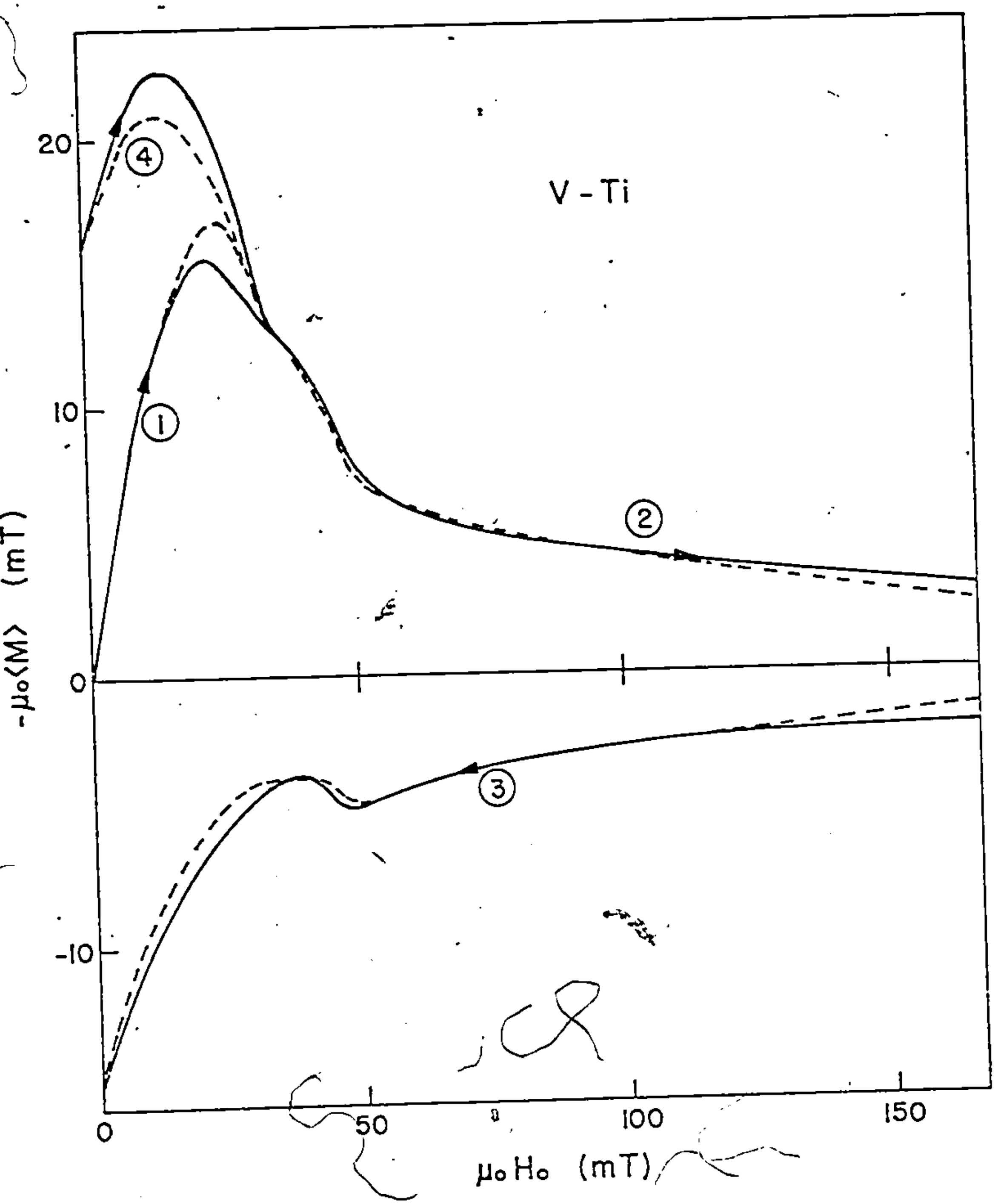


Figure 3-7 Standard magnetization curves for the V-Ti sample. The dashed lines represent the calculated curves.

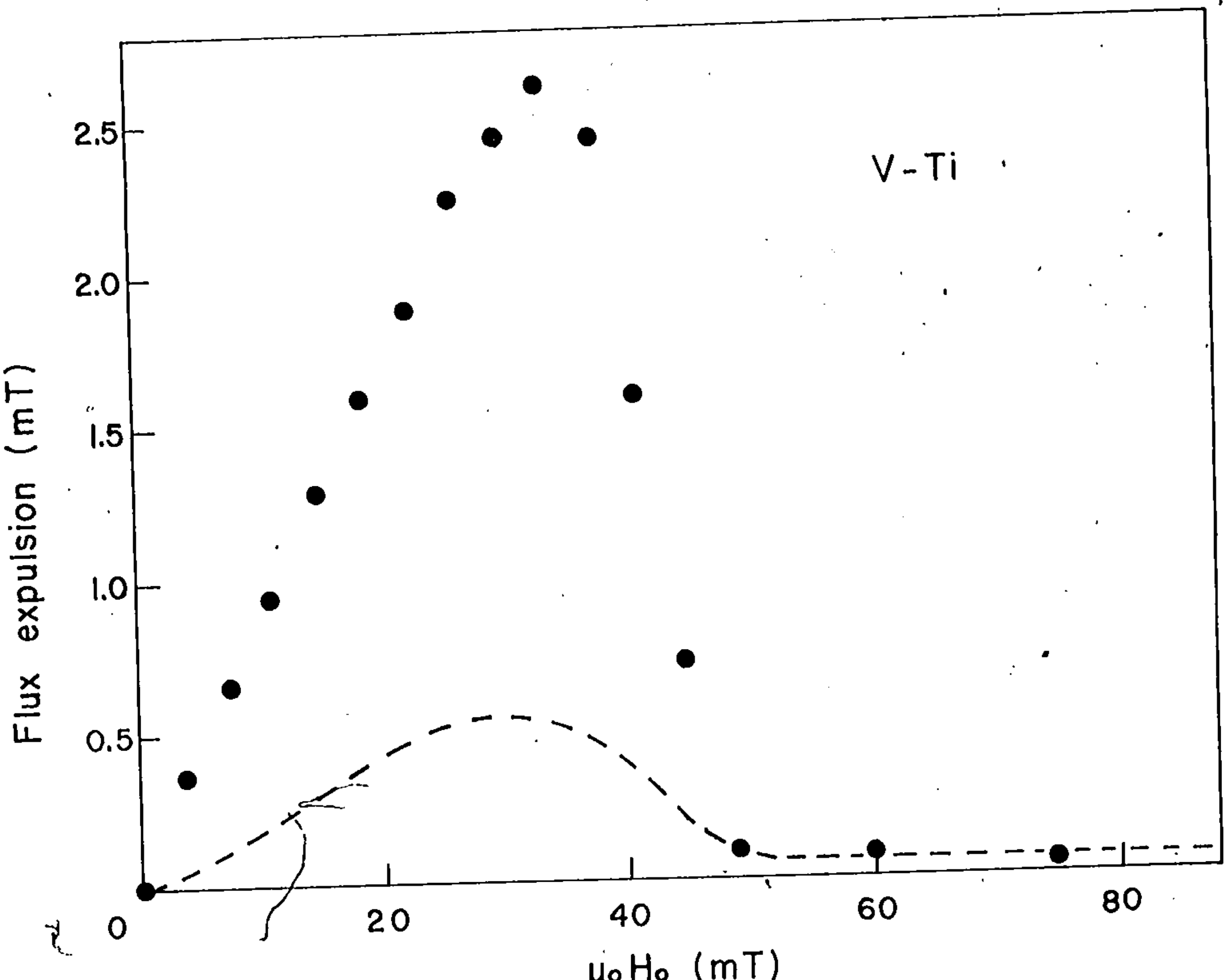


Figure 3-8 Flux expulsion upon cooling the sample in a field $H_o$. The dashed curve represents the calculated values. (V-Ti sample)

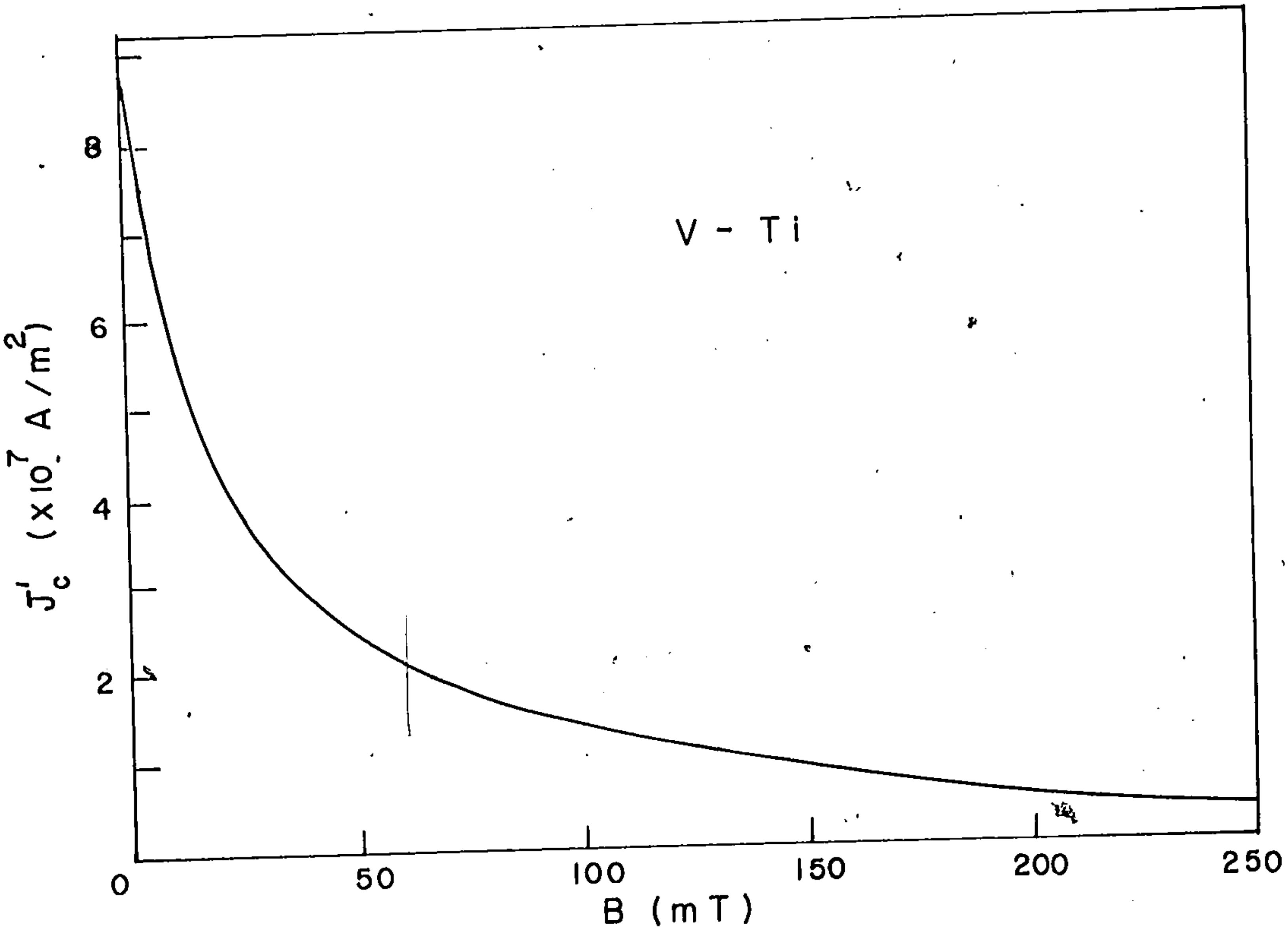


Figure 3-9 $j_c'$ vs B for the V-Ti sample

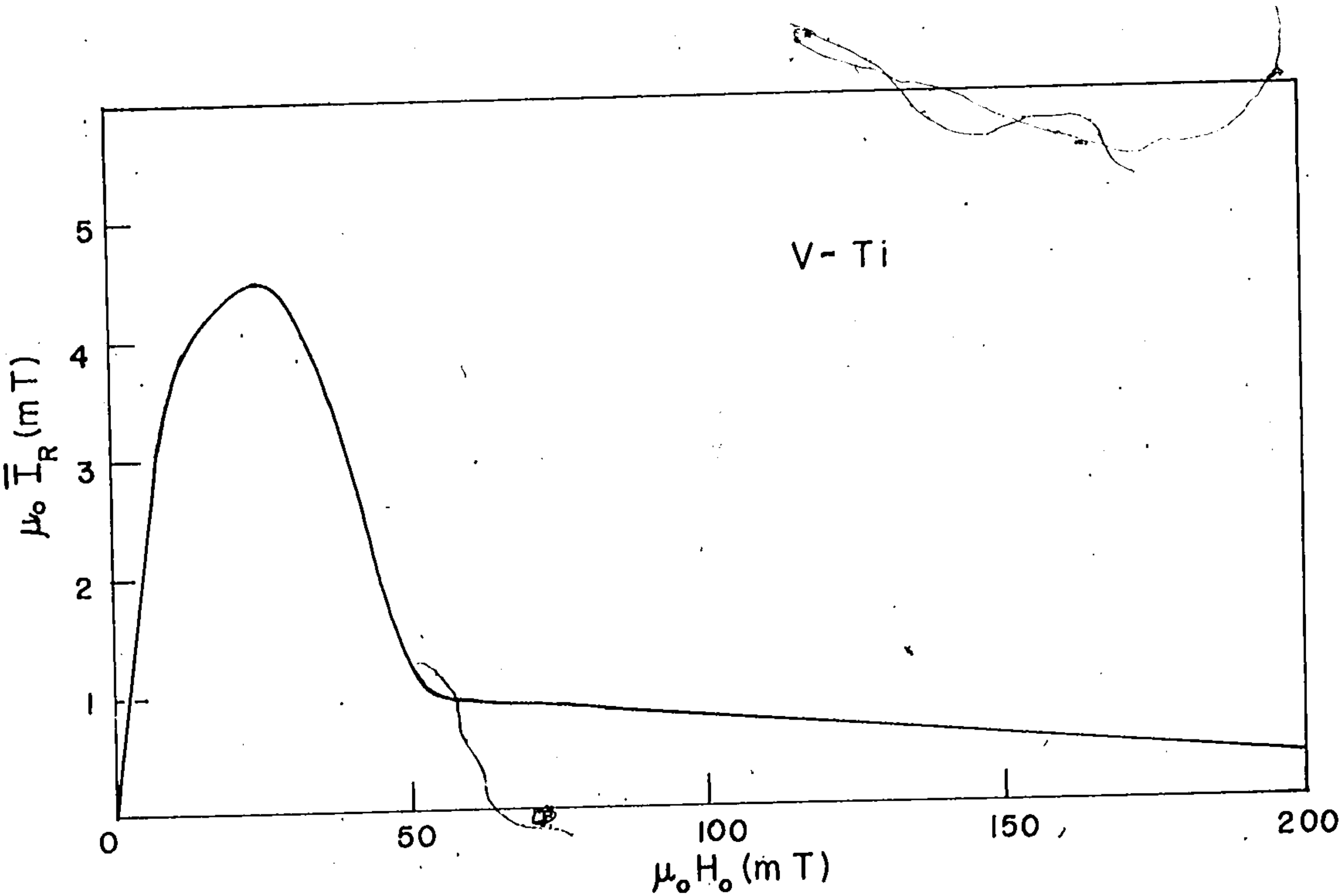


Figure 3-10 $\bar{I}_R$ vs $H_o$ for the V-Ti sample

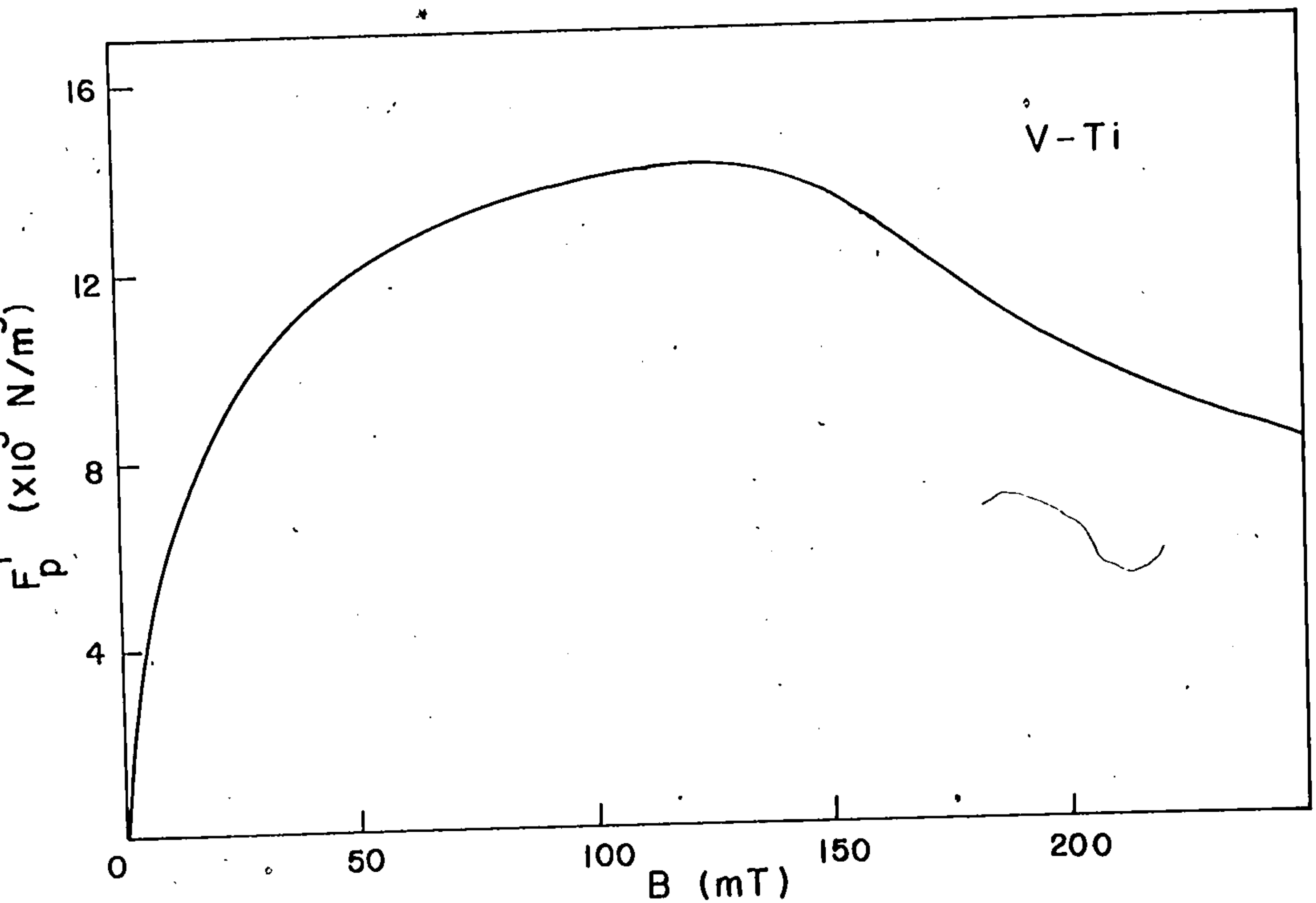


Figure 3-11 $F_p'$ vs B for the V-Ti sample

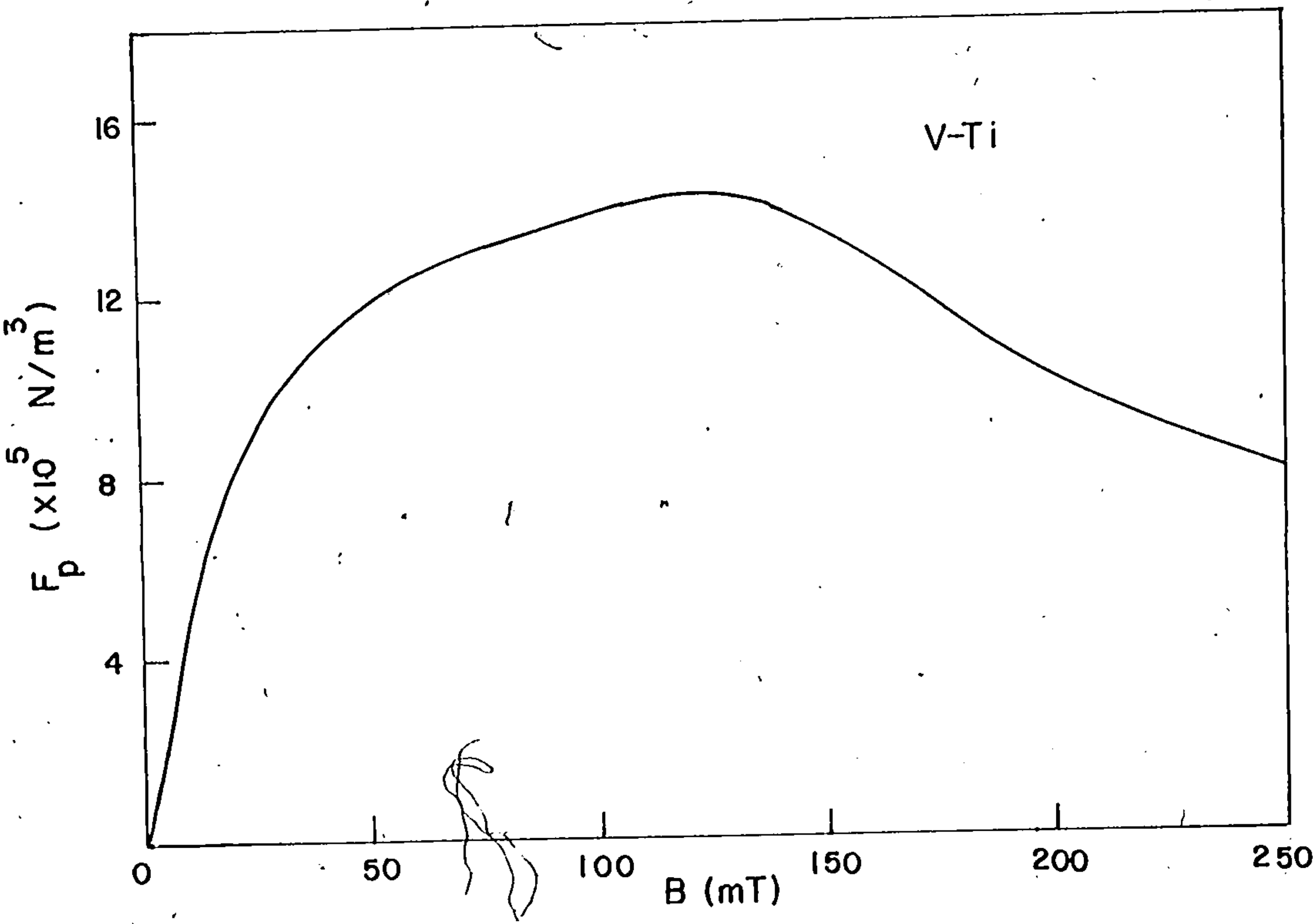


Figure 3-12 · $F_p$ vs B for the V-Ti sample.

# Chapter 4

## Rotating Disk Phenomena: Basic Model and Low Field Behaviour

### 4.1 Introduction

In the previous chapter a synthesis has been outlined of the three well established concepts of equilibrium diamagnetism, bulk pinning (critical state) and surface barrier. The magnetic response of irreversible type II superconductors in the conventional situation where the external magnetic field varies slowly in magnitude along a fixed axis can be quantitatively interpreted in this framework. This picture has been applied to glean information on the behaviour of the surface step and the configurations of the critical profiles of magnetic induction for the samples studied. The surface step is the resultant of two contributions which may aid or oppose each other;- the reversible Abrikosov shielding current and the surface barrier to entry or exit of flux. All these data are needed for a quantitative analysis of the phenomena observed when the disks are slowly rotated in a static magnetic field. In this chapter these phenomena are described and interpreted. The situation investigated where the disk rotates is physically equivalent to that encountered when the disk is held stationary and an external magnetic field of constant intensity is made to rotate. As noted earlier, this can be accomplished mechanically, by rotating the source of the magnetic field, or electromagnetically, by using two orthogonal coils and a three phase power source. Regardless of these details, it is sometimes useful to visualize the phenomena in the context of a rotating (or oscillating) magnetic field of constant magnitude. In particular, some similarities and important links are noticed between the present work and another category of investigations, namely, the study of critical currents, magnetic configurations and A.C. losses in wires and ribbons immersed in a static longitudinally applied magnetic field. The latter situations however, are perhaps more complicated than the case studied here since both the magnitude and the orientation of the external magnetic field are varying simultaneously. All of these investigations complement each other and are of fundamental interest since they provide information on the angular dependence of the interaction of non-parallel planes of flux lines. This important problem has largely been ignored by theoreticians and experimentalists until recently. It is believed that the work and analysis presented in this and the following chapter provide significant new insights towards an understanding of these phenomena.

As was indicated in chapter 1, the magnetic behaviour expected, when a disk of an ideal or reversible type II superconductor undergoes slow rotation in a static externally applied magnetic field $H_o$ directed parallel to its flat faces, is relatively straightforward. Macroscopic flux shielding (hence diamagnetic) currents flow in the London penetration depth at the surface of the disk. The magnitude and sense of circulation of these superficial reversible currents are determined by the strength and direction of the applied magnetic field. Thus these currents are not "tied" to the atomic lattice of the sample along whose boundary they circulate but are in equilibrium with and follow the applied magnetic field. Consequently, the configuration of these currents (i) remains in place as the disk rotates if the applied field is held fixed or (ii) rotates in phase or in step with the applied field if the latter rotates.

If the applied field $H_o < H_{c1}$, the magnetic induction B in the bulk or body of the superconductor is zero, except in the penetration depth region, and the disk behaves like a type I superconductor. This case has been studied experimentally in ideal type I and type II superconductors and the observations are in accord with the picture just sketched (Fritz 49, 50, Andronikashvili 67).

If $H_o$ exceeds $H_{c1}$ but lies below $H_{c2}$, the magnetic induction in the bulk of the sample is no longer zero. Now flux vortices thread the body of the specimen and viscous drag effects come into play as these vortices move through the atomic lattice of the metal when the disk or the field rotate. Presumably, if the linear velocity of the vortices is sufficiently small, these viscous effects can be made negligible and the configuration of the flux line lattice remains in equilibrium and in step with the applied field. The distortions of the flux line configuration which arise from the viscous drag as the frequency of rotation increases are of considerable interest. Clearly, the situation is more complicated if bulk pinning also enters into the picture and impedes the rotation of the flux lines. Various workers have investigated the torques generated in the mixed state when long cylinders are made to rotate or oscillate in static transverse external magnetic fields (Andronikashvili 69, Schäfer 76, Heiden 76, Fuhrmans 76, Ashimov 76). These researchers have endeavoured, with some success, to identify the contribution arising from pinning and from viscous forces in their data. This task is not easy since the dependence of both effects on the frequency of rotation and the strength of the magnetic induction is not simple.

In the present work, the frequency of rotation is extremely slow, hence viscous forces can be ignored and bulk pinning is dominant. Further, since thin disks are studied with the flat faces oriented parallel to the applied field, the demagnetization factor is negligible. Clearly, this is not the case for long cylinders in a transverse field.

It is of interest to note that the long cylinder and disk geometries bring out different aspects of the configuration of the flux line lattice. As a consequence, the conceptual framework is fundamentally different for these two situations. To appreciate this distinction it is useful to write and compare the magnetic induction vector in cartesian coordinates for each situation. The axis of rotation is taken to be directed along the x-axis and the applied magnetic field along the z-axis.

For the long cylinder

$$\vec{B} = \hat{y}\, B_y\, (y, z) + \hat{z}\, B_z\, (y, z) \tag{4-1}$$

where the $B_x$ component and the x dependence of $B_y$ and $B_z$ vanish because the cylinder is "infinitely" long in the x direction.

For the disk,

$$\vec{B} = \hat{y}\, B_y\, (x) + \hat{z}\, B_z\, (x) \tag{4-2}$$

where the $B_x$ component and the y, z dependence of $B_y$ and $B_z$ vanish because the disk has an "infinite" radius (compared to its thickness). In other words, the demagnetization factor is small and end or edge effects can be ignored. This approximation is especially valid in the present work since indeed the magnetic flux threading the "waist" of the disk is monitored. (The reader will recall from chapter 2 that the magnetic flux is measured via two pick-up coils embracing the disk along two orthogonal <u>diameters</u>, hence periphery effects do not contribute appreciably to the measurements.) It would be more difficult to justify this formulation if the data consisted of measurements of the torque since then the total magnetic moment of the entire disk is detected.

Measurements of the torques generated by rotating or oscillating long cylinders in transverse fields then lead "naturally" to information on the distortion of the flux configuration. In contrast, the present measurements on rotating disks provide data on the rotation of the flux line lattice and its intensity distribution with distance from the flat surfaces. It has been verified that end effects can indeed be ignored by repeating most of the measurements on a second disk of Vanadium cut from the same foil but where the diameter is smaller by one half. Only the data for the disk of larger diameter are presented and discussed here since these measurements were more extensive.

In this chapter the attention is focussed on the low field phenomena. Bean's theoretical investigation of rotating flux in a hysteretic type II superconductor is first summarized. Then a picture of the quasi-steady state flux configurations as well as the evolution towards the quasi-steady state is presented which explains the salient features of the present observations. The consequences of two simple analytic formulations of the presented interpretation are also developed. The model is then pursued computationally and it is shown that it accounts for the major features of all the observations in the range of low fields.

## 4.2 Bean's Model of the Rotating Disk

The rotation of planes of flux lines was first explored by Bean (Bean 70). His development is phenomenological. Further it is quasi-macroscopic since the structure of the magnetic flux density in terms of planes of vortices and their interaction does not enter in the picture. The problem in this coarse-grained context will be pursued throughout this part of the thesis.

Of Bean's paper here above mentioned only those aspects of his results which are pertinent to the present work are retained. Further, the results are translated to the situation of interest here, namely that of an infinite slab of thickness X rotating in the y-z plane in a static externally applied magnetic field $H_o$ directed along the z-axis and parallel to the faces of the slab. The infinite slab has been rotating for a long time and a quasi-steady state exists. It is a steady state since the magnetic flux configuration has ceased to evolve and is now stationary in space and in time. It is a quasi-steady state, however, since the atomic lattice of the superconducting metallic slab can be visualized as moving with respect to $H_o$ and the configuration of magnetic induction which is fixed in space. In essence, viscous effects do not enter the picture since the configuration of flux is taken as independent of the rate of rotation. Indeed the rotation can cease and the configuration of flux will remain unchanged. Thus the picture corresponds to a critical state configuration where only bulk pinning operates inside the slab. This is the situation which prevails throughout this work.

Bean, for simplicity, takes the permeability $\mu = \mu_o$, hence $\mu_o$ and B are interchangeable and the surface step $I_R = I'_R = 0$ since $I_A = 0$ and $I'_B = I_B = 0$. The critical current density $j_c = j'_c$ is assumed constant, hence independent of B, and thus the B profiles are linear. The magnetic field $H_o$ can be visualized as having been applied before the rotation began but with the sample in the superconducting state or while the slab was rotating. The end result is independent of these two choices in so far as the quasi-steady state is concerned. Bean does not explore the consequences of other possible initial magnetic states. In this thesis the effect of previous magnetic history on the evolution to the quasi-steady state and on the quasi-steady state are investigated in great detail. The present observations lead to important conclusions which will be described in this chapter.

The solutions given by Bean for the components of the magnetic induction are now presented in the context just outlined.

$$B_z(x) = \mu_o H_o \left(1 - \frac{x}{\sqrt{3}\,\delta}\right) \cos\left\{\sqrt{2}\,\ln\left(1 - \frac{x}{\sqrt{3}\,\delta}\right)\right\} \qquad (4\text{-}3)$$

and

$$B_y(x) = \mu_o H_o \left(1 - \frac{x}{\sqrt{3}\,\delta}\right) \sin\left\{\sqrt{2}\,\ln\left(1 - \frac{x}{\sqrt{3}\,\delta}\right)\right\} \qquad (4\text{-}4)$$

where $0 \leq x \leq X/2$ and the surfaces of the slab are located at $x = 0$ and $x = X$. The length $\delta$ is defined by the relation $\delta = H_o/j_c$ and $\delta \leq X/2\sqrt{3}$ for these equations to hold.

It is important to note that the front of the profile of magnetic induction (B profile) reaches the mid-plane of the slab when

$$H_o = H^* = j_c \frac{X}{2} \qquad (4\text{-}5)$$

if the field is applied with the slab stationary, whereas the B profile attains the mid-plane if

$$H_o = H^{**} = \frac{j_c X}{2\sqrt{3}} \qquad (4\text{-}6)$$

when the slab is or has been in rotation for a long time.

This feature that $H^{**} < H^*$ and indeed $H^{**} = H^*/\sqrt{3}$ is noteworthy. It is a direct consequence of the requirement imposed by Bean that the electric field, $\vec{E}(x) = \hat{y}\,E_y(x) + \hat{z}\,E_z(x)$, generated as the slab rotates, be parallel to the local total current density $\vec{j}_c(x) = \hat{y}\,j_y(x) + \hat{z}\,j_z(x)$. Since $j_c$ is assumed constant and taken to be the same for the rotating and non-rotating situations, the condition that $\vec{E} \times \vec{j} = 0$ is satisfied if the gradient of the flux density is taken shallower by a factor of $1/\sqrt{3}$ in the former case compared with the latter. This can be written

$$\left(\frac{dB}{dx}\right)_{rot} = \left(\frac{dB}{dx}\right)_c \frac{1}{\sqrt{3}} \qquad (4\text{-}7)$$

where $(dB/dx)_{rot}$ and $(dB/dx)_c$ denote the gradient of the critical B profile for the rotating and non-rotating situations respectively and $B = \sqrt{B_y^2 + B_z^2}$.

Introducing equations 4-3 and 4-4 into Maxwell's equation $\nabla \times \vec{H} = \vec{j}$ leads to

$$j_z(x) = -\frac{j_c}{\sqrt{3}}(\sin\theta + \sqrt{2}\cos\theta) \qquad (4\text{-}8)$$

and

$$j_y(x) = -\frac{j_c}{\sqrt{3}}(\sqrt{2}\sin\theta - \cos\theta) \qquad (4\text{-}9)$$

for the components of the electric current density, where

$$\theta = \sqrt{2}\,\ln\left(1 - \frac{x}{\sqrt{3}\,\delta}\right) \qquad (4\text{-}10)$$

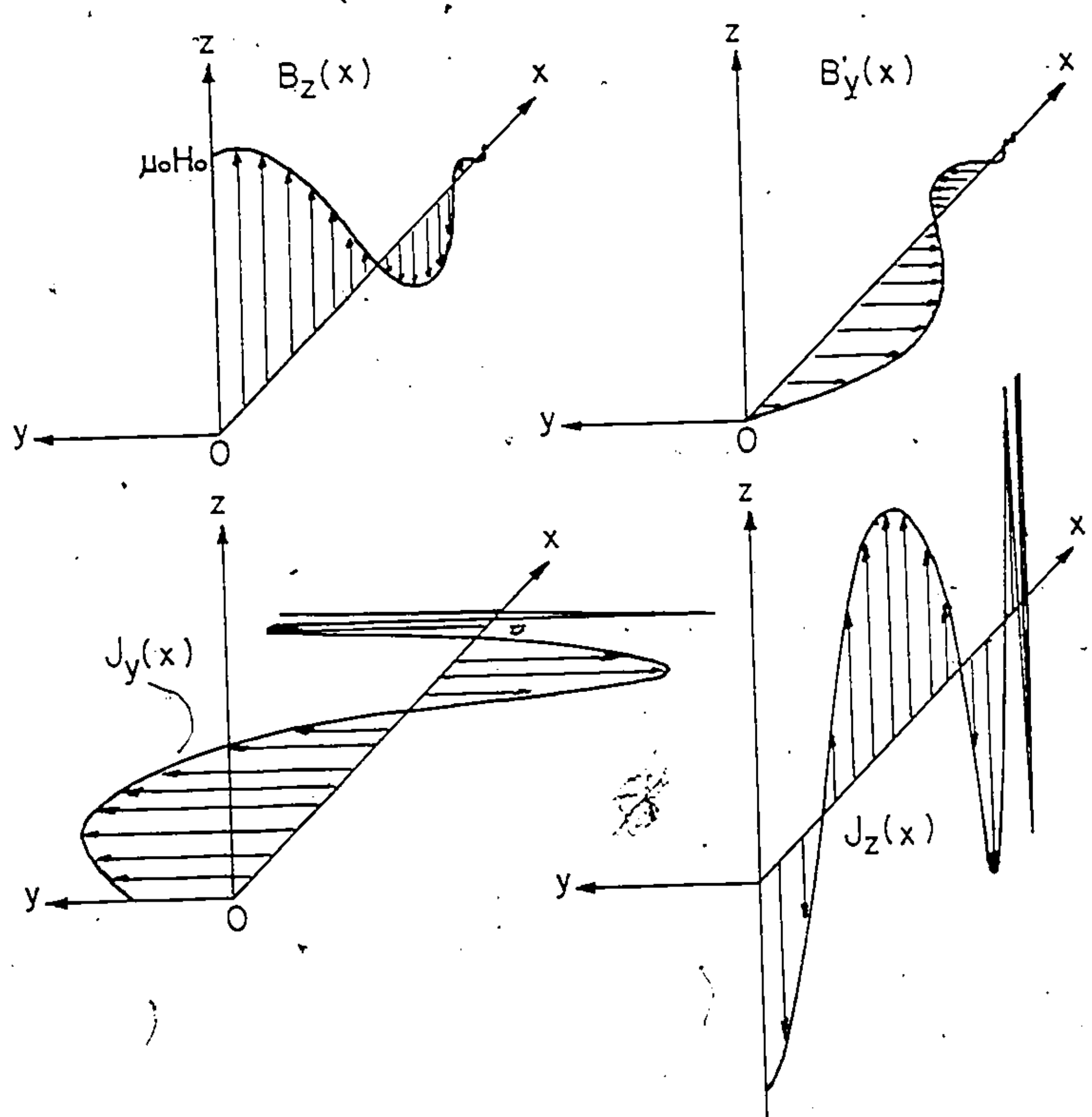

It is noticed that the current density and magnetic induction vectors are directed neither perpendicular nor parallel to each other but subtend a constant angle $\phi$, where

$$\phi = \cos^{-1}\left(\frac{|\vec{j}.\vec{B}|}{j_c B(x)}\right) = \cos^{-1}(-\sqrt{2/3}) = \pi - 35.26^{o} \qquad (4\text{-}11)$$

This situation is referred to as partially force free. The configuration of the components of the magnetic induction and the current density are shown schematically on the previous page for the case under consideration where the disk is rotating clockwise in the plane of the page. The mechanical torque, of course, acts to oppose the rotation.

In setting up this system of self-consistent expressions for $\vec{B}$, $\vec{j}$ and and $\vec{E}$, Bean assumed that the current density $\vec{j}_c$ is independent of the magnitude of $\vec{B}$ and of its orientation with respect to $\vec{j}_c$. The critical state state concept can be written

$$|\vec{j} \times \vec{B}| = j_c B \sin\phi = F_p(B) \qquad (4\text{-}12)$$

It is noticed that in equation 4-12, $j_c$ can be made independent of the magnitude of B by choosing $F_p = \alpha B$ where $\alpha$ is a constant characteristic of the material. Then, since $j_c = \alpha/\sin\phi$ and $\sin\phi = 1/\sqrt{3}$, this means that $j_c$ should be larger in the rotating case than in the non-rotating case by a factor of $\sqrt{3}$. Available experimental evidence indicates that $j_c$ is indeed enhanced in approximate agreement with equation 4-12 (Cullen and Cody 1973).

It is instructive to examine the gradient of $\theta$ which ensues from Bean's formulation. thus

$$\frac{d\theta}{dx} = \pm\sqrt{\frac{2}{3}}\ \frac{1}{\delta}\left(\frac{1}{1 - \frac{x}{\sqrt{3}\,\delta}}\right) = \pm\sqrt{\frac{2}{3}}\ \frac{\mu_o j_c}{B(x)_{rot}} \qquad (4\text{-}13)$$

where the magnetic induction profile appearing in the denominator corresponds to that existing for the rotating case. Introducing equation 4-12 into this result leads to

$$\frac{d\theta}{dx} = \pm \sqrt{\frac{2}{3}}\, \mu_o \frac{F_p}{B^2 \sin\phi} = \pm \frac{\sqrt{2}\, \mu_o F_p}{B^2} \qquad (4\text{-}14)$$

since $\sin\phi = 1/\sqrt{3}$. Lachaine (1976) and Gauthier (1976) have exploited empirical expressions for the gradient of $\theta$ similar to equation 4-14 to describe the magnetic behaviour of ribbons and wires of highly irreversible type II superconductors in situations where the external magnetic field changes orientation and oscillates while maintaining its component along the length of the samples constant.

The variation of the average magnetic induction along the z and y axes vs $H_o$ predicted by Bean's description can readily be obtained analytically. Introducing equations 4-3 and 4-4 in the definitions

$$\mu_o \langle M_z \rangle = \langle B_z \rangle - \mu_o H_o = \frac{2}{X} \int_0^{X/2} B_z(x)\, dx \qquad (4\text{-}15)$$

and

$$\mu_o \langle M_y \rangle = \langle B_y \rangle = \frac{2}{X} \int_0^{X/2} B_y(x)\, dx \qquad (4\text{-}16)$$

yields (see Dwight: Tables of Integrals and other Mathematical Data, equations 865.52 and 865.53)

$$\mu_o \langle M_z \rangle = -\mu_o H_o \left( 1 - \frac{H_o}{3H^{**}} \right) \qquad (4\text{-}17\ a)$$

and

$$\mu_o \langle M_y \rangle = \langle B_y \rangle = -\frac{\mu_o}{3\sqrt{2}} \left(\frac{H_o}{H^{**}}\right)^2 H^{**} \qquad (4\text{-}18\ a)$$

where $0 \leq H_o/H^{**} = \sqrt{3}\, H_o/H^* \leq 1$. This range is referred to as the low field range. For $H_o \geq H^{**}$ the magnetic components $\langle M_z \rangle$ and $\langle M_y \rangle$ become independent of $H_o$,

$$\mu_o \langle M_z \rangle = -\frac{2}{3}\, \mu_o H^{**} \qquad (4\text{-}17\ b)$$

and

$$\mu_o \langle M_y \rangle = -\frac{\mu_o H_o^{**}}{3\sqrt{2}} \qquad (4.18\ b)$$

These values of the applied field $H_o$ constitute the high field range and the experimental behaviour of the disks in this range will be analysed in the next chapter.

Bean's formulation provides a satisfactory account of the quasi-steady state behaviour encountered for the special case where the sample is initially in the virgin or in the diamagnetic state.

A model is required which also describes the evolution to the quasi-steady state as well as the quasi-steady state starting with a variety of different initial magnetic states for the low ($H_o < H^{**}$) and also the high ($H_o > H^{**}$) field ranges.

## 4.3 Evolution of the Quasi-Steady State from Various Initial States: Basic Qualitative Picture

The behaviour encountered as the disks are rotated has been examined starting with four basic and standard types of initial states which are denoted as diamagnetic, non-magnetic, paramagnetic and hybrid. The procedures followed to establish these initial states before the disk is rotated is now reviewed. In all cases the applied magnetic field $H_o$ is directed along the z axis and parallel to the flat faces of the disk. The axis of rotation lies along the x-axis. The measured quantities are the average magnetic induction $<B_z>$ and $<B_y>$ along and perpendicular to the stationary applied field $H_o$. It is frequently convenient to present the data in terms of the components of the average magnetization where $\mu_o<M_z> = <B_z> - \mu_o H_o$ and $\mu_o<M_y> = <B_y>$.

(i) Diamagnetic state. The disk cools through $T_c$ to 4.2 K in zero (the earth's) magnetic field, then the applied field is raised to the final value $H_o$. If $H_o < H^*$ the B profiles do not reach the mid-plane of the disk. If $H_o > H^*$, the B profiles advancing from the two flat surfaces of the disk meet at the mid-plane and $B(x = X/2) > 0$ (see diagram (a) ).

(ii) Non-magnetic state. The disk cools through $T_c$ to 4.2 K in $H_o$ which is subsequently maintained constant. The disk exhibits a small but non-negligible diamagnetic moment since flux is expelled as the disk cools (see diagram (b) ).

(iii) Paramagnetic state. The disk becomes superconducting in $H_o' \gtrsim H_{c2}$ which is then reduced to a final value $H_o$ of the same polarity as $H_o'$ (see diagram (c) ).

(iv) Hybrid state. The disk becomes superconducting in $H_o' \gtrsim H_{c2}$ which is then removed and a magnetic field $H_o$ of polarity opposite to $H_o'$ is applied. $H_o'$ is taken to be negative and $H_o$ to be positive (see diagram (d) ). If $H_o > H^*$, there is no hybrid magnetic state and the sample is in the diamagnetic state.

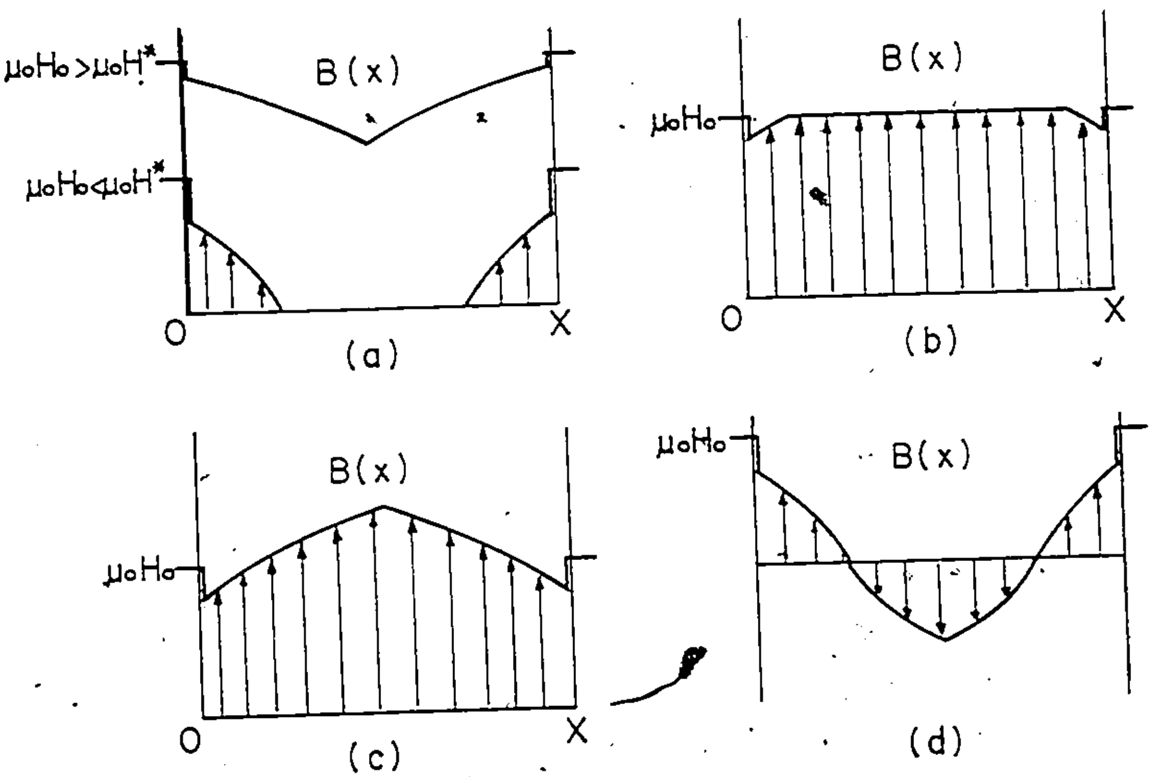

For clarity the low and the high field behaviour are examined separately.

4.4 Low Field Behaviour: Development of the Basic Model.

a) Paramagnetic and non-magnetic initial states.

To follow the picture developed for the sequence of magnetic field configurations encountered as the disk rotates it is helpful to first focus on the non-magnetic and paramagnetic initial states (diagrams (b) and (c) on the previous page). Clearly, the amount of flux threading the cross-section of the disk is considerably larger in the latter case. In both cases, this magnetic flux, which will be referred to as the trapped flux and denoted by $\phi_t$, consists of vortices pinned to the metallic lattice. Consequently it is expected that this trapped flux will tend to rotate in step with the disk. This can occur only if the paramagnetic currents, sustaining this flux and flowing transverse to it, continue to circulate and rotate in phase with this trapped flux. It is noticed that initially, before the rotation begins, the magnetic field $H_o - I_R$ also aids in supporting the trapped flux. Further, the flux retaining currents existing initially are already in the critical state. Now, consider that the magnetic field $H_o$ is removed. The edges of the B profiles must then drop to zero and the configurations of trapped flux will change as shown schematically in the sketches below.

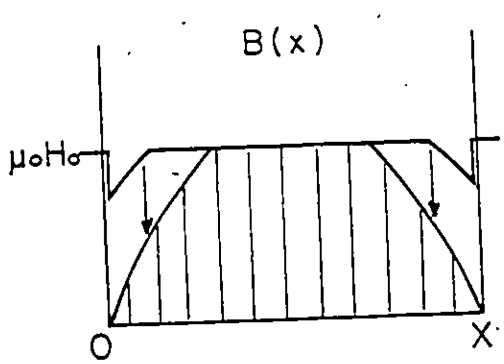


(b')

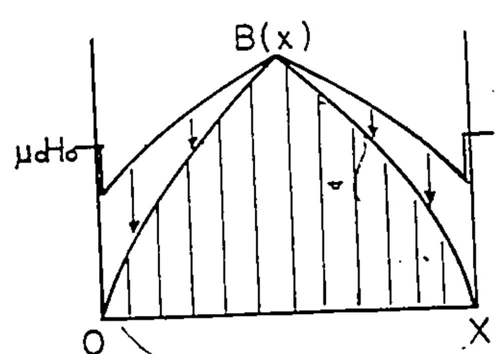


(c')

Although the magnetic field $H_o$ is not removed, its component parallel to the trapped flux is gradually reduced to zero as the trapped flux rotates by 90°. As this occurs, the presence of the applied field $H_o$, will cause flux vortices to be nucleated at the surface and penetrate into the disk unless flux shielding (diamagnetic) currents appear to oppose this occurrence.

It is assumed that when the disk is rotating, the reversible Abrikosov diamagnetic current $I_A$ continues to flow at the surface in equilibrium with and perpendicular to $H_o$. It is also postulated, for simplicity, that the magnitude of the surface barrier opposing entry or exit of flux is unchanged by the rotation. Further, it is stipulated that this barrier acts along $H_o$, hence the irreversible surface currents associated with the barrier ($I_B$ or $I_B'$) continue to flow transverse to $H_o$. These simplifying assumptions also seem quite reasonable and do not play an important role in the final results. Thus the surface steps operating in and extracted from the standard magnetizations curves in the previous chapter are retained and applied to the rotating situation.

The attention is now focussed on the flux vortices nucleated at and penetrating from the surfaces as the disk rotates. Sheets of diamagnetic (field shielding) currents induced in the bulk adjacent to the surfaces to oppose the migration of these flux vortices inward must exist at a critical value according to the critical state concept. These current sheets and the new vortices coexisting with them will also tend to rotate with the disk. Critical paramagnetic currents, however, attempting to maintain $\phi_t$ already occupy the volume adjacent to the surface where the diamagnetic currents are induced. The superposition of these rotating sheets of critical currents and rotating planes of vortices leads to

(i) a pattern of current flow consisting of successive sheets of currents directed at an angle varying with depth and (ii) a configuration of planes of vortices whose density and direction also varies with depth.

Let $x_o$ denote the distance from the surface to the edge of the profile of trapped flux $\phi_t$ oriented at an angle $\theta$ with respect to the z-axis (the direction of $H_o$). The disk, in the present context has also rotated through the angle $\theta$. The domain occupied by $\phi_t$ has shrunk to $X - 2x_o$ and the quantity of trapped flux has diminished. Consequently some of the trapped flux has in effect been expelled from the core region of width $X - 2x_o$. This is an important and inevitable consequence of the considerations which have been pursued. It is clearly impossible for the initial trapped flux $\phi_t$ to remain unchanged in the disk after a rotation of 90° unless it is stipulated, as shown schematically in the accompanying sketch,

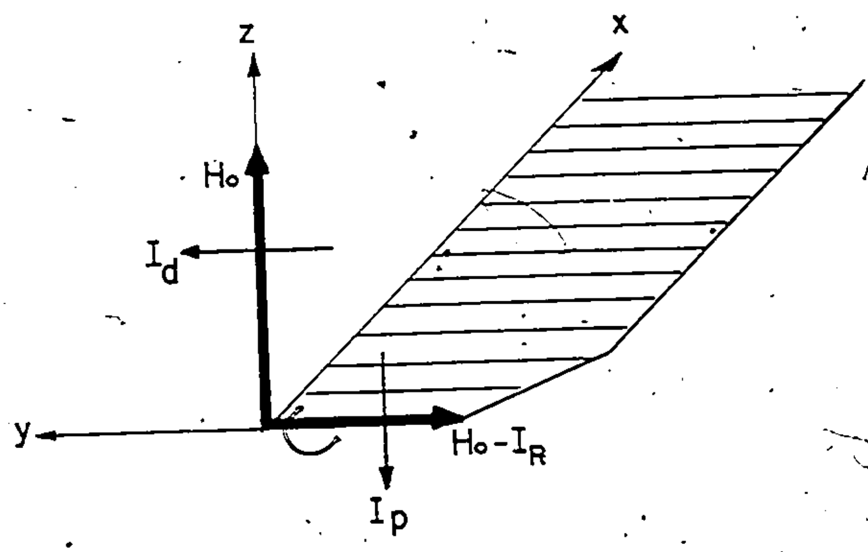


that a sheet of diamagnetic current $I_d = H_o$ flows transverse to $H_o$ at the surface and another sheet of paramagnetic current $I_p = H_o - I_R$ which rotates with the disk coexists with or is adjacent but interior to the former. Both of these arbitrary stipulations are untenable. Further they are inconsistent with the present observations. Then the only possible conclusion, which is in accord with observations, is that $\phi_t$ initially diminishes as the disk rotates. The detailed quasi-macroscopic processes coming into play as this redistribution, reorientation, migration and disappearance of the trapped vortices takes place presents an important and fascinating problem beyond the scope of this thesis. A crucial test of the macroscopic model, however, will be its ability to account for the quantity of trapped flux remaining in the disk vs $\theta$ (the angle of rotation of the disk) and in the quasi-steady state for various $H_o$ and for different initial magnetic states.

Following Bean, the region $0 \leq x \leq x_o$ where $\vec{B}$ and $\vec{j}_c$ change direction with depth is referred to as the "active" region. In the active region the current density and magnetic induction vectors are directed neither perpendicular nor parallel to each other. Indeed, as noted earlier in Bean's analysis, $\vec{j}_c$ tends to lie along but anti-parallel to $\vec{B}$. The configuration is thus partially force free and the critical density ($\vec{j}_c$ (B) ) can then be expected to be larger than occurring in standard magnetization curves for corresponding $|\vec{B}|$. This feature will be returned to later. An important result of the present considerations which is of immediate interest is that, regardless of the details of the configurations of $\vec{j}$ and $\vec{B}$, the B profile must decrease with depth in the active region. This can perhaps most readily be seen in the following ways. A succession of sheets of field shielding (diamagnetic) currents opposing the penetration of vortices nucleated at the surfaces by $H_o$ are induced by the rotation of the disk and are swept inwards as the rotation progresses. Since these induced currents oppose $H_o$ when they are generated, $|\vec{B}|$ must decrease with depth in the active region starting from the value $H_o - I_R$ just inside the surface. There is no physical basis to suggest that the currents which shield the trapped flux $\phi_t$ from the applied field $H_o$ could all flow at the surface. To the contrary it has been seen in Chapter 3 that the surface cannot support larger currents than that given by the magnitude of the surface step. Consequently the active region where B(x) decreases is not all concentrated in a thin sheet at the surface but occupies a finite region of thickness $x_o$ inside the bulk of the disk adjacent to the surface. It then results that $\phi_t$ must diminish during the initial stages of the rotation.

In agreement with Bean, it is argued that the slope of the B(x) profile in the active region $0 < x \leq x_o$ must be negative. For the time being it is not necessary to specify the spatial dependence of the gradient $(dB/dx)_c$ in the active region. Pursuing this idea it is visualized that as the rotation proceeds, hence $\theta$ increases, the width of the active region expands as its leading edges $x_o$ (and $X - x_o$) advance into the disk. Eventually, $B(x_o)$, the total magnetic induction at the front of the growing active region, decreases to zero. At this juncture, a quasi-steady state is established. Subsequently, as the disk continues to rotate ( in the same sense), the remaining trapped flux denoted $\phi_t'$, undergoes no further modifications since its outer boundaries now cease to change as it is swept around in phase with the disk. The configuration of magnetic induction in the active region also ceases to evolve and remains spatially "rigid" in the frame of the laboratory (i.e. with respect to $H_o$). The metallic lattice, of course, moves through the magnetic field configuration (the planes of vortices) at an angular velocity $\omega = d\theta/dt$, in the active region. The sequence of events is shown schematically in the sketches on the following page where for simplicity the

B-profiles are represented with constant slopes. The slope in the active region is also drawn equal in magnitude to that in the region occupied by $\phi_t$, again for simplicity. Only half the thickness of the

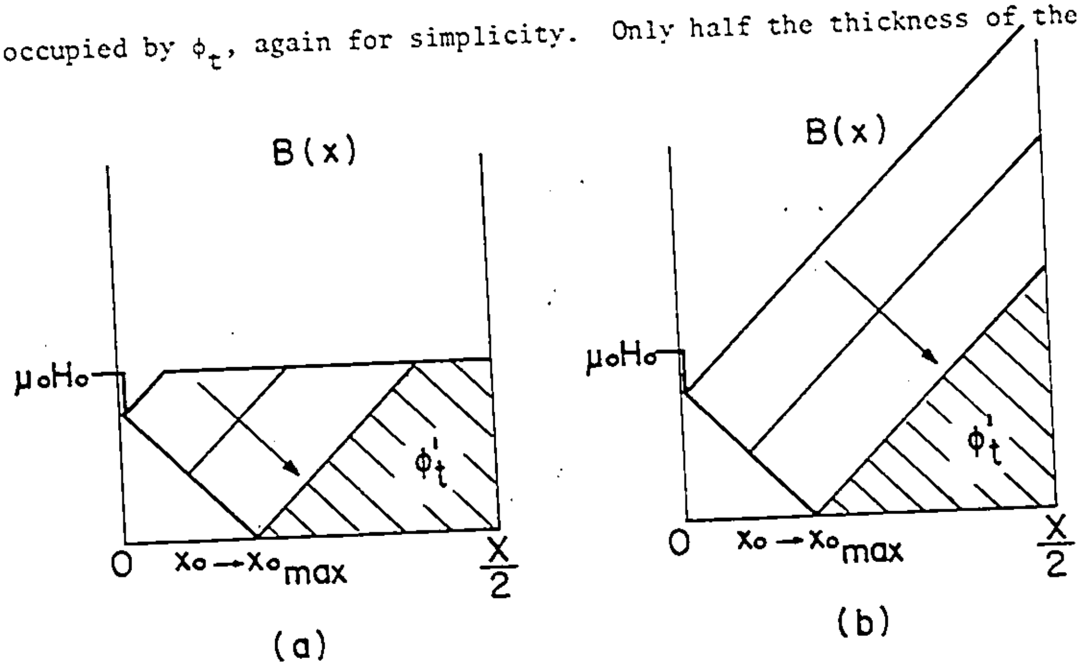


disk is shown since the two halves are symmetrical. The evolution for the non-magnetic (diagram (a)) and paramagnetic cases (diagram (b)) are presented. $x_{o\ max}$ denotes the maximum depth of penetration of the active region. The angle $\theta_{max}$ through which the disk must be rotated before the quasi-steady state is achieved will depend on the nature of the advance of $x_o$ as a function of the angle of rotation of the disk $\theta$. This aspect will be returned to in the next chapter.

According to the picture just outlined, it is expected when starting with the disk in the non-magnetic or paramagnetic state, to observe, in the quasi-steady state, a magnetic flux $\phi_t'$ rotating in unison with the disk and a steady component of magnetic induction $<B_z> = H_o - \mu_o<M_z>$ along the z-axis (the direction of the applied field $H_o$) and $<B_y> = \mu_o<M_y>$ along the y-axis (orthogonal to the applied field and to the axis of rotation). The expectations are in accord with the present observations.

and will be examined in detail shortly.

b) Diamagnetic initial state.

With the sample initially in the diamagnetic state three possibilities need to be envisaged. These are distinguished by whether $dB(x)/dx$ for the rotating case is greater, equal to or less than for the non-rotating situation (standard magnetization curves). Let $j'_{c\ rot}$ denote the former. The sequence of events for these three possibilities is shown schematically below where in sketches (a) $j'_{c\ rot} > j'_c$, (b) $j'_{c\ rot} = j'_c$ and (c) $j'_{c\ rot} < j'_c$ respectively and $\delta$ denotes the depth of penetra-

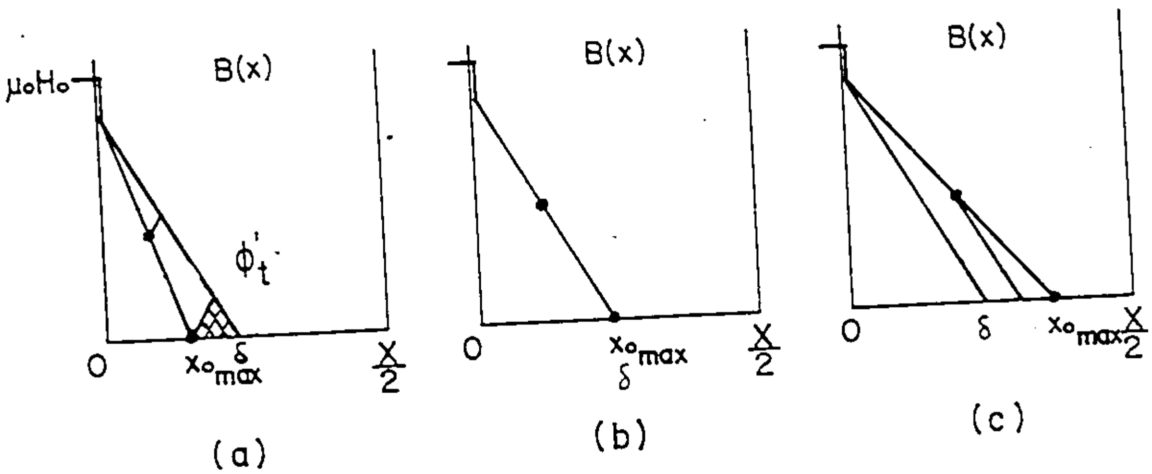


tion of the B profile in the initial diamagnetic state. The noteworthy feature is that a small residual magnetic flux $\phi'_t$ should be observed rotating in phase with the disk in the quasi-steady state, if case (a) is encountered. This residual flux $\phi'_t$ would grow with $H_o$, rise to a maximum in the vicinity of $H_o \gtrsim H^*$ and vanish at $H_o = H^{**}$. In contrast with the Bean solution, this possibility requires that $H^{**} > H^*$. No evidence has been seen for this behaviour in the present work. It is noted, for completeness, that since flux is made to leave the sample during the approach to the quasi-steady state, it would be more appropriate in this case (a), to use the surface step $I_R(H_o)$ applicable to flux exit instead of $I'_R(H_o)$ applicable when flux enters the specimen.

c) Hybrid initial magnetic state.

When the sample is initially in the hybrid magnetic state, it is again necessary to envisage the three possibilities just enumerated, namely, (a) $j'_{c\,rot} > j'_c$, (b) $j'_{c\,rot} = j'_c$ and (c) $j'_{c\,rot} < j'_c$ shown schematically below. The behaviour for the latter two cases follows in a

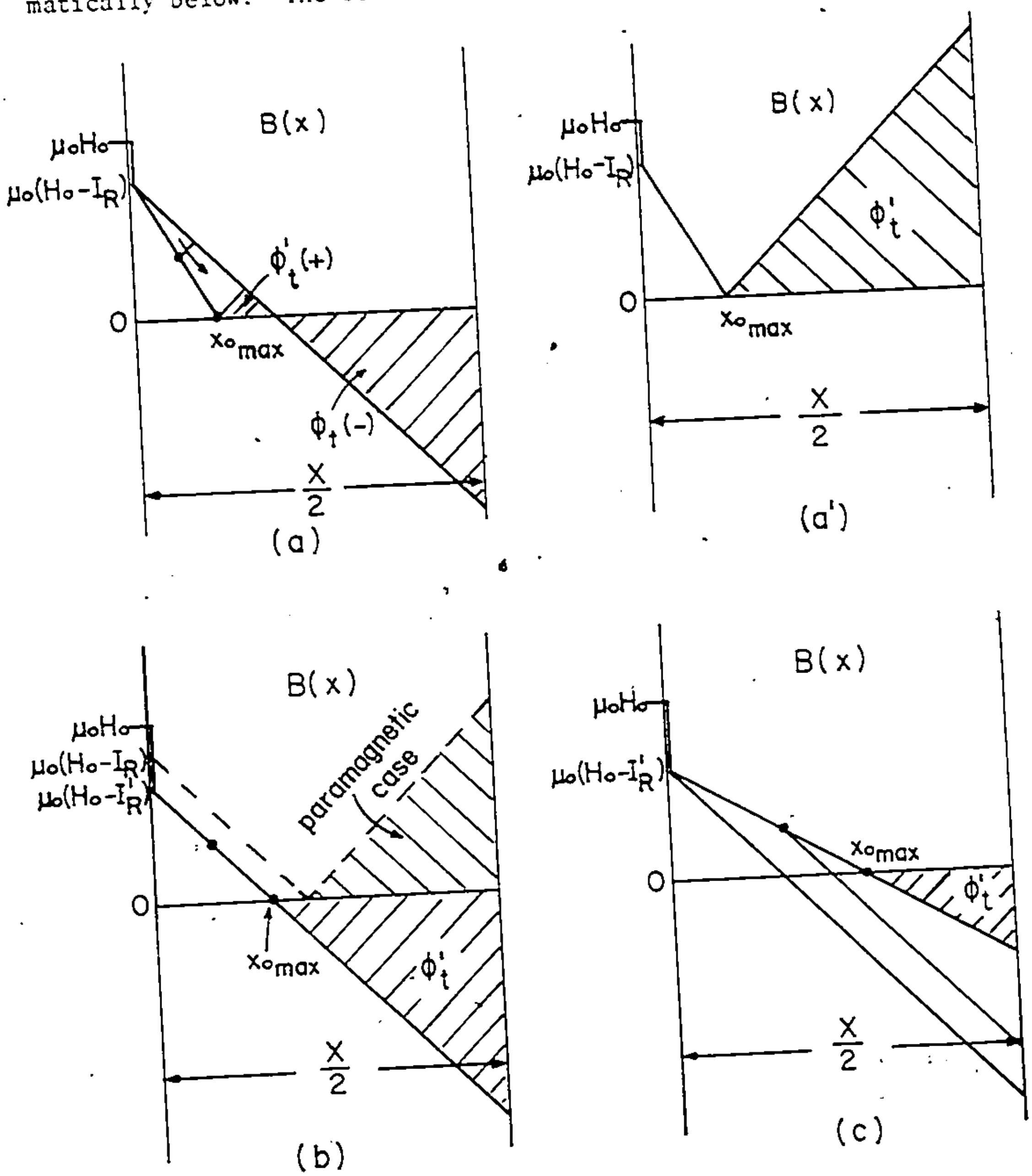

straight forward manner from the previous considerations. The graph of $\phi_t'$ vs $H_o$ for the hybrid case, however, will lie above the corresponding graphs for the paramagnetic and for the non-magnetic situations since the surface step which operates here in the hybrid case is $I_R'$ whereas it is $I_R$ which applies in the latter two cases. As has been seen in chapter 3, $I_R'(H_o)$ is generally greater then $I_R(H_o)$. To aid in visualizing this statement the quasi-steady profile for the paramagnetic case is also shown again in diagram (b). The present observations are in accord with this picture.

Case (a) again leads to interesting consequences which can readily be extracted from qualitative considerations. Firstly it is noticed that since flux is leaving the sample during the evolution to the quasi-steady state, it is appropriate here to introduce the surface step $I_R$ applicable to the flux exit situation instead of $I_R'$ as in cases (b) and (c). It is then possible to directly compare $\phi_t'$ vs $H_o$ for this case and that encountered for the paramagnetic initial state. The residual magnetic flux in the quasi-steady state for the hybrid situation is the resultant of two opposing contributions (see sketch (a))', namely $\phi_t' = |\phi_t'(-)| - |\phi_t'(+)|$. A graph of this quantity vs $H_o$ for the hybrid case must consequently lie well <u>below</u> the curve of $\phi_t'$ vs $H_o$ for the paramagnetic case. To aid in visualizing this statement again the quasi-steady state profile is shown for the paramagnetic case in diagram (a'). The present observations, however, exhibit the entirely opposite behaviour (see Figure 4-1). Therefore, from these qualitative or pictorial considerations the possibility that $j'_{c\ rot} > j'_c$ can unambiguously be eliminated. This important conclusion, of course, simplifies the problem considerably. It will be explored in some detail later in this chapter which of the two remaining options (cases (b) and (c)) prevail.

The anticipated behaviour for simple but basic cases which can be treated analytically is now examined within the framework of this model.

## 4.5 Applications of the Basic Model to Simple Cases.

The dependence on $H_o$ of the rotating magnetic flux

$$\phi_t'/XY = \langle B \rangle_{rot} \qquad (4\text{-}19)$$

remaining in the disk, in the quasi-steady state for the paramagnetic, hybrid and non-magnetic initial states is investigated. Option (b), namely, $j'_{c\ rot} = j'_c$ is considered in parallel with option (c) that $j'_{c\ rot} < j'_c$. The consequences of this model of the quasi-steady state are developed for two extreme but physically interesting pinning functions $F'_p(B) = \alpha B$ and $F'_p(B) = \alpha$. These two pinning functions are enshrined in the literature and are historically associated with Bean-London and Kim et al respectively (Bean 64, London 63, Kim 1963).

It is useful to define a quantity

$$H_1 = \int_o^{X/2} j'_c \, dx \qquad (4\text{-}20)$$

which corresponds to the magnetic field $H_o - I_R$ inside the surface when the B profile reaches the mid-plane as $H_o$ is applied from zero in the virgin state. This quantity is also the magnetic field at the mid-plane when $H_o$ is reduced to zero (where $I_R = 0$) after an excursion beyond $H_{c2}$. Thus the remanent magnetization $\langle M \rangle_r$ after $H_o$ is decreased to zero from $H_{c2}$ (or a high value) provides a direct measure of $H_1$ since

$$\langle M \rangle_r = \frac{X}{2} \int_o^{X/2} dx \int_o^{x} j'_c \, dx' \qquad (4\text{-}21)$$

a) Bean London case: $F'_p = \alpha B$, hence $j'_c = \alpha$

It is noticed that since $j'_c$ is a constant

$$\frac{B(x)}{\mu_o} = \pm \frac{H_1}{X/2}(x - x_o) \tag{4-22 a}$$

and

$$\frac{x_o}{X/2} = \frac{H_o - I_R}{H_1} \tag{4-22 b}$$

where $H_1 = \alpha X/2$ and $x_o$ is now used throughout for brevity instead of $x_{o\,max}$.

i). Paramagnetic and Hybrid Initial States.

The accompanying sketches may aid the reader in visualizing the analytical development.

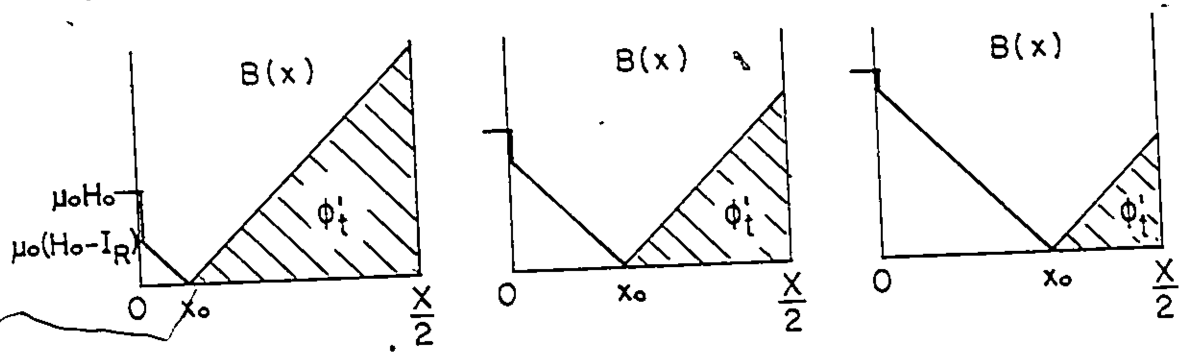


From equation 4-22 it is obtained

$$\frac{B(X/2)}{\mu_o} = H_1\left(1 - \frac{x_o}{X/2}\right) = H_1\left(1 - \frac{H_o - I_R}{H_1}\right) \tag{4-23}$$

From geometric considerations or by integration it is found

$$\frac{\langle B\rangle_{rot}}{\mu_o} = \frac{H_1}{2}\left(1 - \frac{H_o}{H_1} + \frac{I_R}{H_1}\right)^2 \tag{4-24}$$

If it is assumed that $I_R(H_o) = 0$, equation 4-24 simplifies to

$$\frac{\langle B\rangle_{rot}}{\mu_o} = \frac{H_1}{2}\left(1 - \frac{H_o}{H_1}\right)^2 \tag{4-25}$$

It is also instructive to let $I_R = kH_o$ in the range $0 \leq H_o \leq H^*$ with $k < 1$. Introducing this in equation 4-24 leads to

$$\frac{\langle B\rangle_{rot}}{\mu_o} = \frac{H_1}{2} \{ 1 - \frac{H_o}{H_1} (1 - k)\}^2 \tag{4-26}$$

which, of course, reduces to equation 4-25 if k = 0. The functional dependence of $\phi_t'$ is unchanged by k but the curve is shifted to the right as shown in the accompanying sketch.

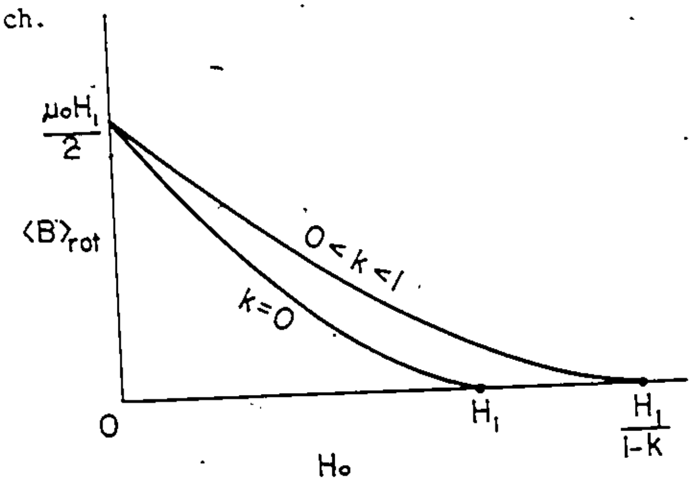


Since the corresponding experimental curves are <u>convex upwards</u> (see Figure 4-1, 4-4 and 4-5) this pinning function is clearly inadequate to describe the behaviour encountered.

It is noticed that the hybrid case is readily obtained from the above by changing the polarity of $\phi_t'$. Equations 4-24 through 4-26 continue to apply where $I_R$ is replaced by $I_R'$.

Envisaging the possibility that $j_{c\ rot}' < j_c'$, it is useful to define another quantity

$$H_2 = \int_0^{X/2} j_{c\ rot}' \, dx \tag{4-27}$$

which corresponds to the magnetic field $H_o - I_R$ inside the surface when the active region in the quasi-steady state attains the mid-plane (i.e. $H_o = H^{**}$).

It is now obtained that

$$\frac{x_o}{X/2} = \frac{H_o - I_R}{H_2} \tag{4-28}$$

Equation 4-24 must be replaced by

$$\frac{\langle B\rangle_{rot}}{\mu_o} = \frac{H_1}{2}\left(1 - \frac{H_o}{H_2} + \frac{I_R}{H_2}\right)^2 \tag{4-29}$$

and equations 4-25 and 4-26 changed accordingly. Introducing this new physical consideration does not alter the functional behaviour of $\phi_t'$ but the curves sketched above drop to zero when $H_o = H_2/(1 - k)$, where $H_2' < H_1$.

ii) Non-Magnetic Initial State.

The reader is referred to the accompanying sketches for aid in visualizing the physical meaning of the analytic expressions and their development. The dashed lines represent the initial B-profile and the solid lines, the quasi-steady state B profile. If $j'_{c\ rot} = j'_c$

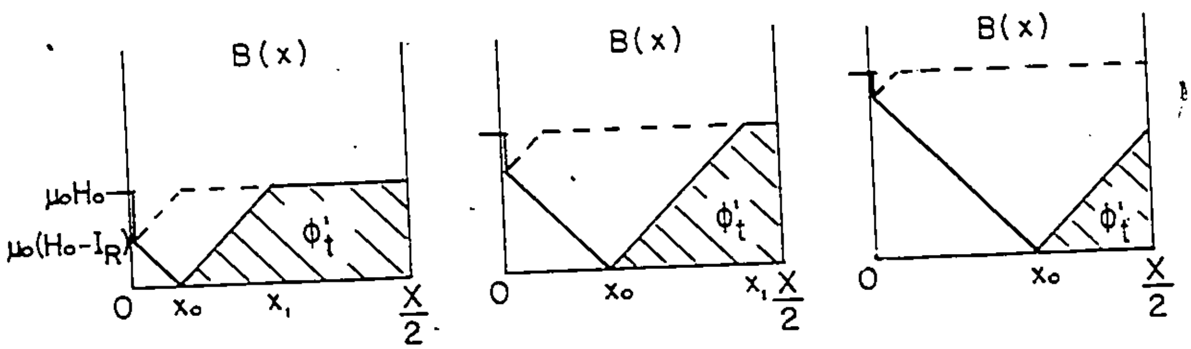


$$x_1 = \frac{H_o}{H_1}\frac{X}{2} + x_o = \frac{X}{H_1}\left(H_o - \frac{I_R}{2}\right) \tag{4-30}$$

since $x_o = X(H_o - I_R)/2\, H_1$ from equation 4-22b. Equation 4-30 applies until $x_1$ attains X/2 hence for the range $0 \leq H_o \leq (H_1 + I_R)/2$.

From geometric considerations and the above expressions or by direct integration it is obtained that

$$\frac{\langle B\rangle_{rot}}{\mu_o} = H_o\left(1 - \frac{3}{2}\frac{H_o}{H_1} + \frac{I_R}{H_1}\right) \tag{4-31}$$

For the range $(H_1 + I_R)/2 \leq H_o \leq H^*$ the same situation as was prevailing for the paramagnetic state is encountered and equation 4-24 applies.

Assuming no surface step, hence $I_R(H_o) = 0$ this simplifies to

$$\frac{\langle B\rangle_{rot}}{\mu_o} = H_o \left( 1 - \frac{3}{2}\,\frac{H_o}{H_1} \right) \tag{4-32}$$

which is valid for the range $0 \leq H_o \leq H^*/2$. The rotating flux $\phi_t'$ grows to a maximum at $H_o = H^*/3$ where $\langle B\rangle_{rot}/\mu_o = H^*/6 = H_1/6$.

Again it is instructive to assume $I_R = kH_o$ where $k < 1$. Introducing this into equation 4-31 leads to

$$\frac{\langle B\rangle_{rot}}{\mu_o} = H_o \left\{1 - \frac{H_o}{H_1}\left(\frac{3}{2} - k\right)\right\} \tag{4-33}$$

which attains a maximum value of $H_1/2(3 - 2\,k)$ when $H_o = H_1/(3 - 2\,k)$ and applies for the range $0 \leq H_o \leq H_1/(2 - k)$. Equation 4-33 joining into equation 4-26 is sketched in the accompanying diagram for $k = 0$ and $0 < k < 1$. The functional form is not modified by the k factor, although the peak and end point are shifted to the right as k hence the height of the surface are increased.

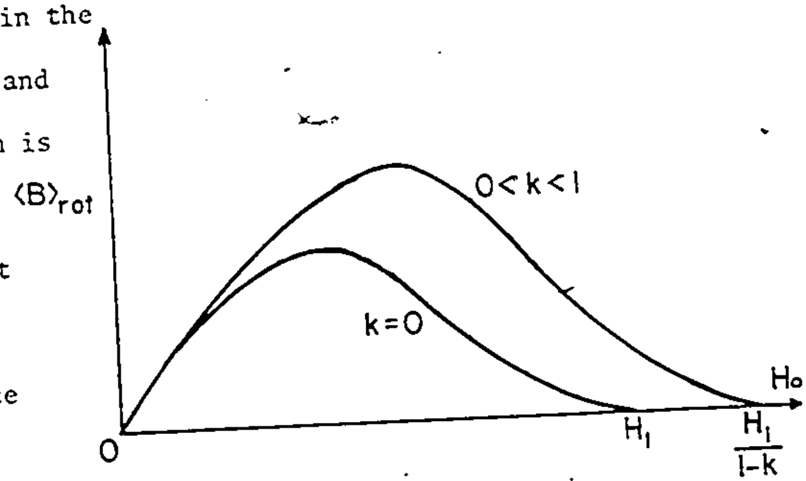


The partial Meissner effect or the amount of flux expelled in establishing the initial state can readily be evaluated and yields a diamagnetic magnetization

$$\langle M\rangle_{ex} = \frac{I_R^2}{2H_1} \tag{4-34}$$

which is parabolic if $I_R = kH_o$ and linear if $I_R = \sqrt{k_1 H_o}$.

In the context that $j'_{c\ rot} < j'_c$, hence $H_2 < H_1$ and using equation 4-29 it is found that equation 4-31 must be replaced by the equally simple expression

$$\frac{\langle B\rangle_{rot}}{\mu_o} = H_o \{ 1 - \frac{H_o}{2H_1} - \frac{(H_o - I_R)}{H_2} \} \qquad (4\text{-}35)$$

valid over the range $0 \leq H_o \leq H_1 (H_2 + I_R)/(H_1 + H_2)$. The curves sketched on the previous page then shift towards the origin as $H_2/H_1$ decreases.

b) Kim Case: $F_p' = \alpha$ hence $j_c' = \alpha/B$

Integrating $dB/dx = \pm \mu_o j_c' = \pm \mu_o \alpha/B$ leads to

$$\frac{B(x)}{\mu_o} = H_1 \sqrt{\frac{|x - x_o|}{X/2}} \qquad (4\text{-}36)$$

where

$$H_1 = \sqrt{\alpha X/\mu_o}. \qquad (4\text{-}37)$$

(Again, $x_o$ is used for brevity, instead of $x_{o\ max}$.)

Envisaging the possibility that in the active region $j_{c\ rot}'/j_c' = \beta$ where $\beta \leq 1$ is a constant it can also be written

$$\frac{B(x)}{\mu_o} = H_2 \sqrt{\frac{|x - x_o|}{X/2}} \qquad (4\text{-}38)$$

where

$$H_2 = \sqrt{\beta\alpha X/\mu_o} = \sqrt{\beta}\, H_1 \qquad (4\text{-}39)$$

It follows from equations 4-36 and 4-38 that

$$\frac{x_o}{X/2} = \left( \frac{H_o - I_R}{H_1} \right)^2 \qquad (4\text{-}40\text{ a})$$

or

$$\frac{x_o}{X/2} = \left( \frac{H_o - I_R}{H_2} \right)^2 \qquad (4\text{-}40\text{ b})$$

depending on whether $\beta = 1$ or $\beta < 1$, hence $H_2 = H_1$ or $H_2 < H_1$.

i) Paramagnetic and Hybrid Initial States.

The reader is referred to the sketch on the following page where the B profile is drawn schematically for the situation where $B < 1$.

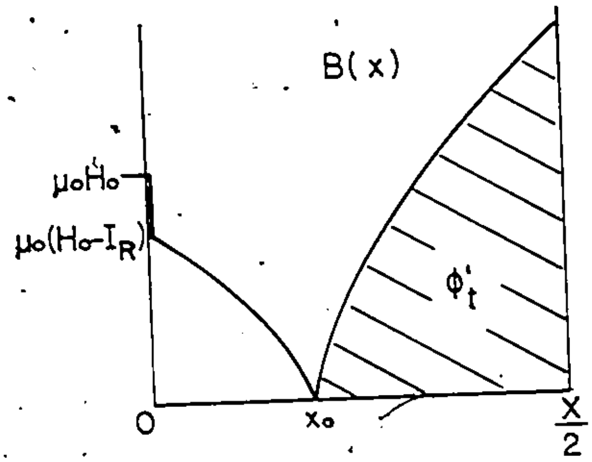


Since the special case where $\beta = 1$ can readily be obtained from the more general results by setting $H_1 = H_2$, only the latter are derived.

Integrating equation 4-36 leads to

$$\frac{\langle B\rangle_{rot}}{\mu_o} = \frac{2}{3} H_1 \{1 - \frac{x_o}{X/2}\}^{3/2} = \frac{2}{3} H_1 \{1 - (\frac{H_o - I_R}{H_2})^2\}^{3/2} \qquad (4\text{-}41)$$

where equation 4-40 (b) has been introduced.

Again it is instructive to let $I_R = k\, H_o$. Equation 4-41 then reads

$$\frac{\langle B\rangle_{rot}}{\mu_o} = \frac{2}{3} H_1 \{ 1 - (\frac{H_o}{H_2})^2 (1 - k)^2\}^{3/2} \qquad (4\text{-}42)$$

The behaviour for the hybrid magnetic state is described by substituting $I_R'$ for $I_R$ in equation 4-41 and k' for k in equation 4-42.

In Figure 4-1 equation 4-41 is displayed for $\beta = 1$ and $1/\sqrt{3}$ with $I_R = 0$. The remanent magnetization for the Vanadium disk has been used to determine $H_1$. In this Figure the experimental data are also presented for comparison.

It is indeed surprising and encouraging that the curve with $\beta = 1$ reproduces the observations so well considering the approximations involved in its formulation. The analysis of equation 4-41 will be continued later in this chapter. Clearly two curves will be generated, one for the paramagnetic and one for the hybrid initial states when $I_R\ (H_o) \neq 0$ and $I_R'(H_o) \neq 0$ will be taken into account from the results presented in chapter 3.

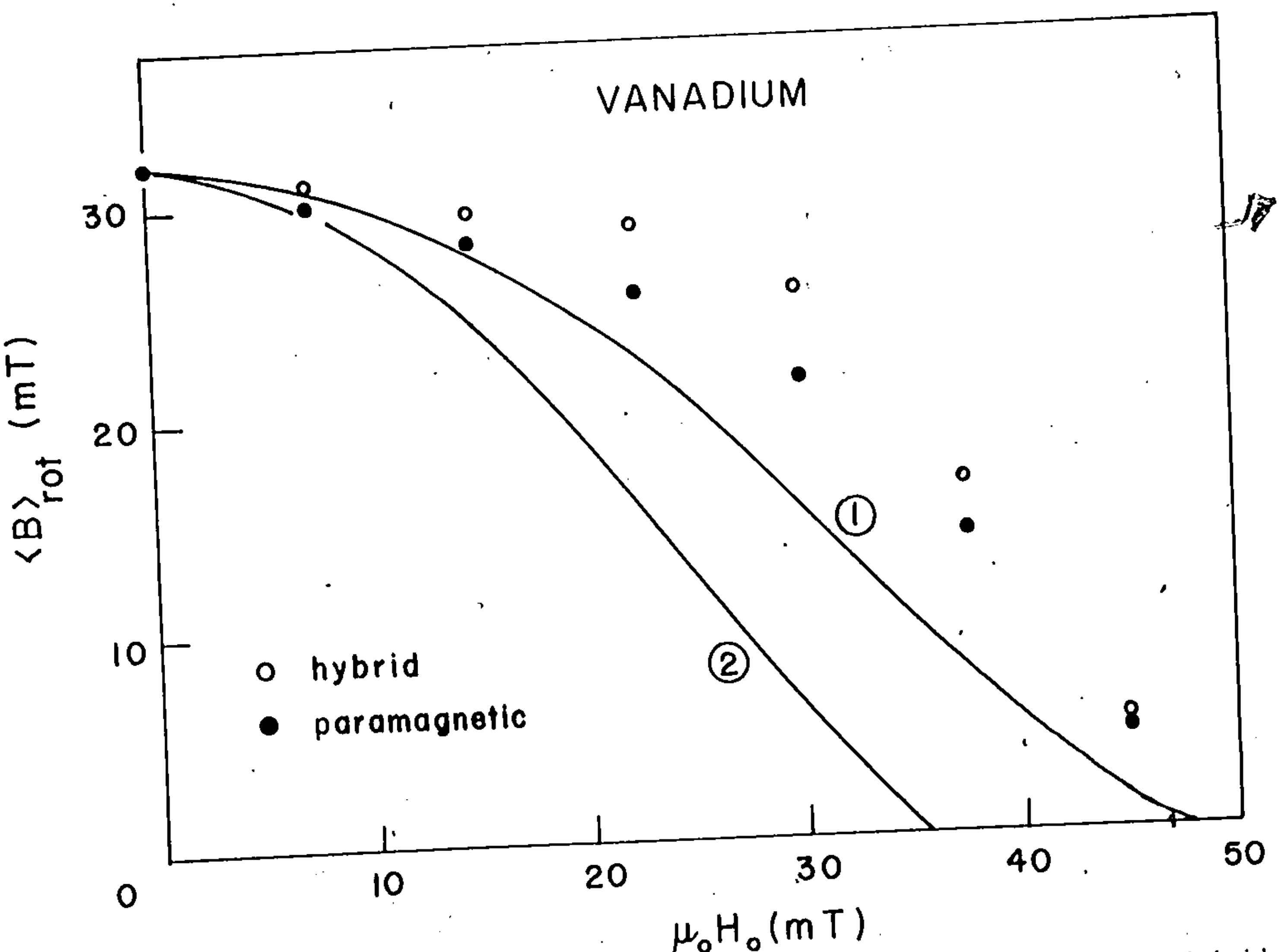


Figure 4-1 $\langle B\rangle_{rot}$ versus $H_o$. Experimental data for the vanadium disk with initial hybrid and paramagnetic field profiles. Calculated curves (Kim case: $j_c' = \alpha/B$) for $\beta = 1$ (curve 1) and $\beta = 1/\sqrt{3}$ (curve 2) and with $I_R = I_R' = 0$.

ii) Non-Magnetic Initial State.

The reader is referred to the accompanying sketch where the quasi-steady state profile has schematically been drawn for the situation where $\beta < 1$. The dashed line represents the initial B profile before rotation.

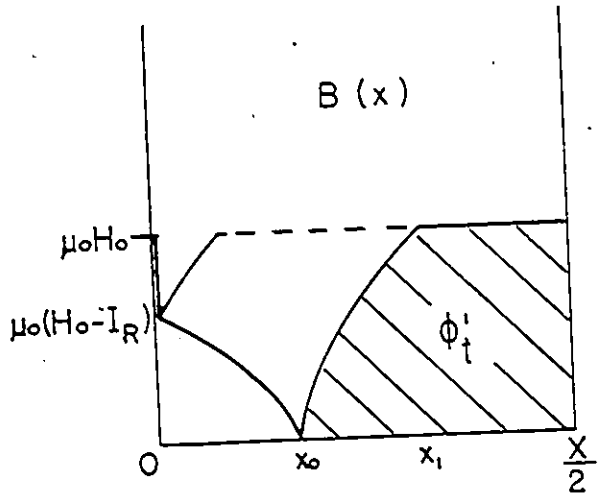


Integrating equation 4-36 gives

$$\frac{\langle B\rangle_{rot}}{\mu_o} = \frac{2}{3} H_1 \left( \frac{x_1}{X/2} - \frac{x_o}{X/2} \right)^{3/2} + H_o \left(1 - \frac{x_1}{X/2}\right). \qquad (4\text{-}43)$$

Introducing equation 4-40 b and the relation $\frac{x_1 - x_o}{X/2} = \left(\frac{H_o}{H_1}\right)^2$ which follows from equation 4-36 into equation 4-43 it is obtained that

$$\frac{\langle B\rangle_{rot}}{\mu_o} = H_o \left\{ 1 - \frac{1}{3} \left(\frac{H_o}{H_1}\right)^2 - \left(\frac{H_o - I_R}{H_2}\right)^2 \right\} \qquad (4\text{-}44)$$

which is valid until $x_1 = X/2$ hence in the range

$$0 \leq H_o \leq \left\{ \frac{H_2}{\left(\frac{H_2}{H_1}\right)^2 + 1} \right\} \left\{ \frac{I_R}{H_2} + \sqrt{1 + \left(\frac{H_2}{H_1}\right)^2 - \left(\frac{I_R}{H_1}\right)^2} \right\}$$

For the range beyond this limit up to H**, equation 4-41 applies. Again it is interesting to consider $I_R = kH_o$, at least for the initial portion of the range of equation 4-44, which then becomes

$$\frac{\langle B\rangle_{rot}}{\mu_o} = H_o \left\{1 - \frac{1}{3} \left(\frac{H_o}{H_1}\right)^2 - \left(\frac{H_o}{H_2}\right)^2 (1 - k)^2 \right\} \qquad (4\text{-}45)$$

Letting $\beta = 1$, hence $H_2 = H_1$ and $I_R = 0$ hence $k = 0$, equations 4-44 and 4-45 simplify to

$$\frac{\langle B\rangle_{rot}}{\mu_o} = H_o \{1 - \frac{4}{3}(\frac{H_o}{H_1})^2\} \tag{4-46}$$

which is valid for the range $0 \leq H_o \leq H_1/\sqrt{2}$ and which has a maximum value of $H_1/3$ at $H_o = H_1/2$.

In Figures 4-2 and 4-3 the predicted behaviour of $\langle B\rangle_{rot}$ vs $H_o$ is presented for the non-magnetic initial state exploiting the Kim pinning function with $\beta = 1$ and $1/\sqrt{3}$ and $I_R(H_o) = 0$. $H_1$ is determined from the remanent magnetization for the V and V-Ti disks to be 48 and 23.4 millitesla respectively. Again it is surprising and encouraging that this simple pinning function together with the assumption of no surface step and taking $\beta = 1$ yields approximate agreement with the data.

These results together with the behaviour shown in Figure 4-1 for $\langle B\rangle_{rot}$ vs $H_o$ for the paramagnetic (and hybrid) initial states, and obtained with the simplifying Kim approximation are most encouraging. It indicates quite strongly that the basic picture of the quasi steady profiles which has been proposed is correct. The success obtained with the Kim approximation for the V sample is perhaps not too surprising. A comparison of the actual $j_c'$ extracted for this sample from the standard magnetization curves in the range $0 < H_o \approx H_1$ is well approximated by the simple Kim relation $j_c' = \alpha/B$. As B goes to zero, the experimental $j_c'$ is of course finite whereas $j_c'$ from the Kim approximation goes to infinity. As a consequence, the B profiles, in the vicinity of $x_o$, descend too abruptly when the Kim approximation is used. From inspection of the calculated and observed curves and from consideration of the B profiles envisaged in this model it is expected to obtain better agreement for the V sample when the "real" values for $j_c'$ are used and the fact that $I_R(H_o) \neq 0$ and $I_R'(H_o) \neq 0$ is introduced.

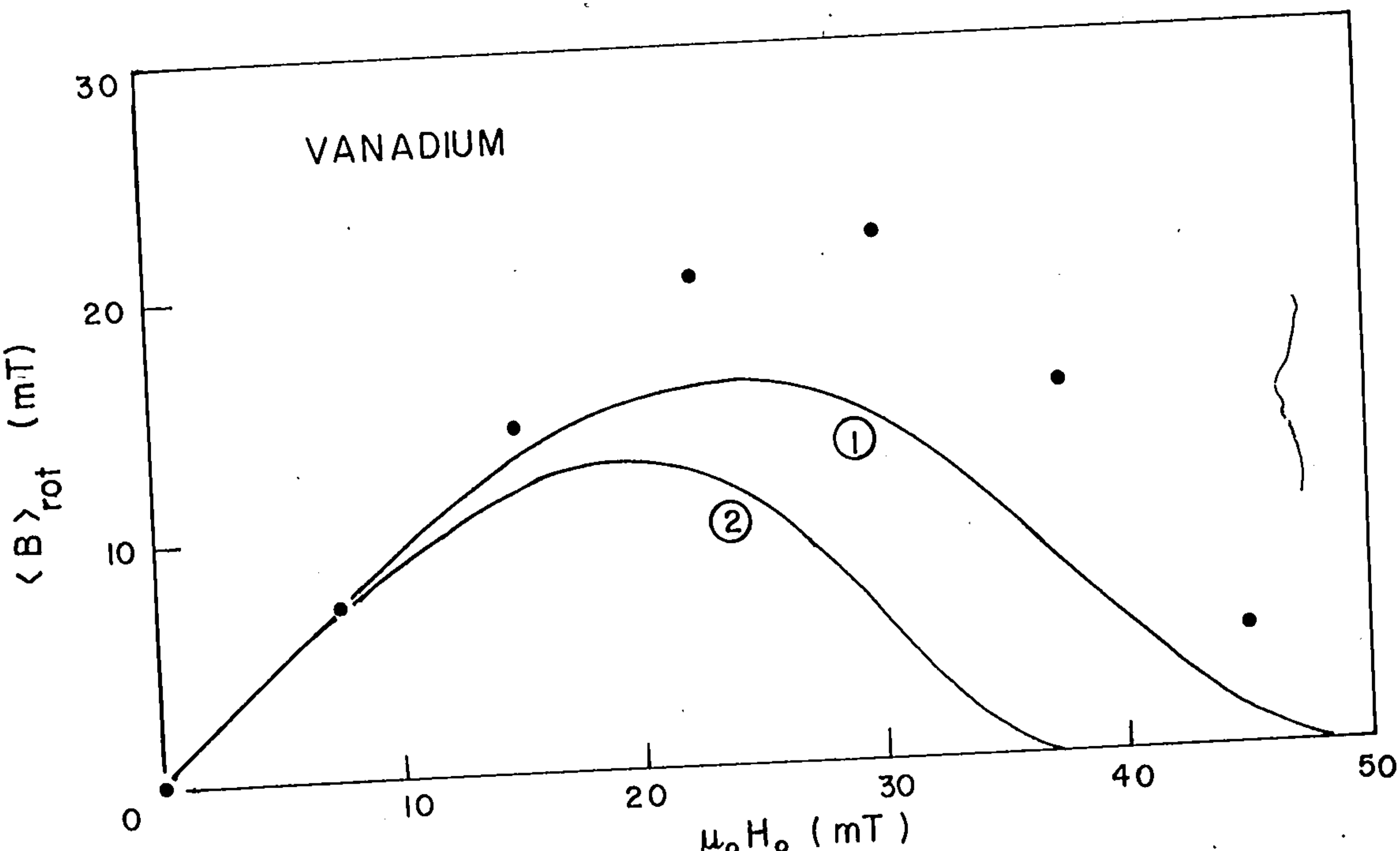


Figure 4-2 $\langle B\rangle_{rot}$ versus $H_o$. Experimental data for the vanadium disk with non-magnetic initial field profiles. Calculated curves (Kim case: $j_c' = \alpha/\beta$) for $\beta = 1$ (curve 1) and $1/\sqrt{3}$ (curve 2) and with $I_R = I_R' = 0$.

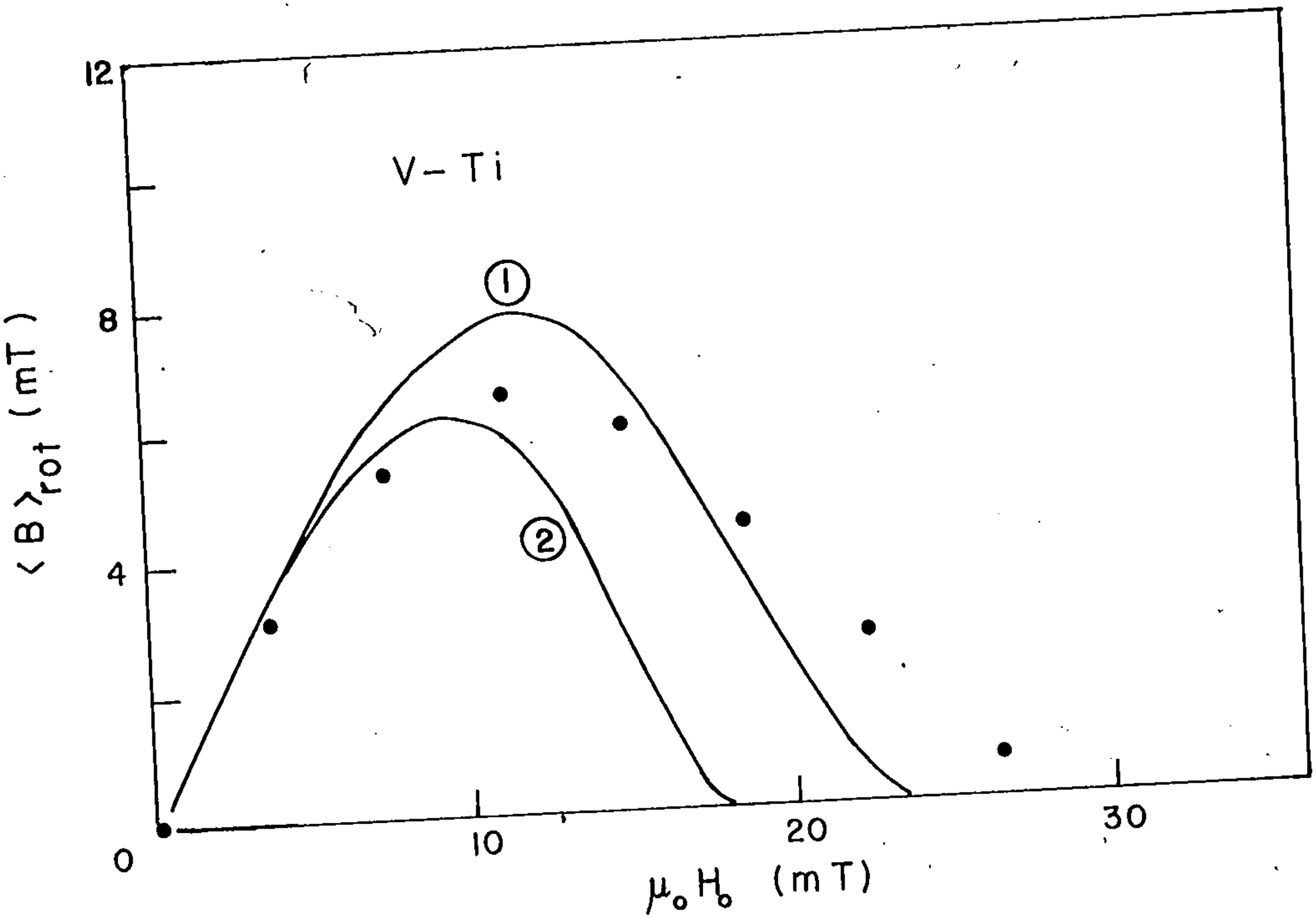


Figure 4-3 $\langle B \rangle_{rot}$ versus $H_o$. Experimental data for the V-Ti disk with non-magnetic initial field profiles. Calculated curves (Kim case: $j_c' = \alpha/B$) for $\beta = 1$ (curve 1) and $1/\sqrt{3}$ (curve 2) and with $I_R = I_R' = 0$.

## 4.6 Exact Application of the Basic Model to Quasi-Steady State: Rotating Flux in Low Field Range.

It is clear from the foregoing analysis and calculations that the basic picture presented of the quasi-steady state following upon various initial magnetic states or initial flux configurations across the thickness of the disk is essentially correct. The crucial element of the model proposed is that the B profile, in the quasi-steady state, diminishes with depth and attains zero at a distance $x_{o\ max}$ from the surface. The region adjacent to the surfaces where the orientation of $\vec{B}$ varies with depth as its magnitude declines is referred to as the active region. To evaluate the thickness $x_{o\ max}$ of the active region in the quasi-steady state it is not necessary to know how the direction of $\vec{B}$ hence $\theta$ vary with depth. To calculate the evolution to the quasi-steady state, however, a relation is required between the orientation of $\vec{B}$ with respect to $H_o$ and $\theta$ during the growth of $x_o$ to $x_{o\ max}$. This problem will be examined in the next chapter.

In order to evaluate $x_{o\ max}$ precisely it is important, however, that dB/dx in the active region, as well as the effective surface step $I_R(H_o)$ or $I_R'(H_o)$ be known accurately. Further the amount of rotating flux in the quasi-steady state is also sensitive to the B profile, hence dB/dx, in the core region, besides being dependent on the width of the core region.

In chapter 3, from a systematic numerical analysis of the standard magnetization curves for the samples, detailed curves for $j_c'$ vs B, $I_R$ and $I_R'$ vs $H_o$ were extracted. All the ingredients necessary to proceed to a numerical evaluation of $\langle B \rangle_{rot}$ vs $H_o$ for the different initial states explored experimentally are available.

The B profiles in the quasi-steady state envisaged in the model are again presented schematically below for the three pertinent flux configurations, namely (a) paramagnetic, (b) hybrid and (c) non-magnetic.

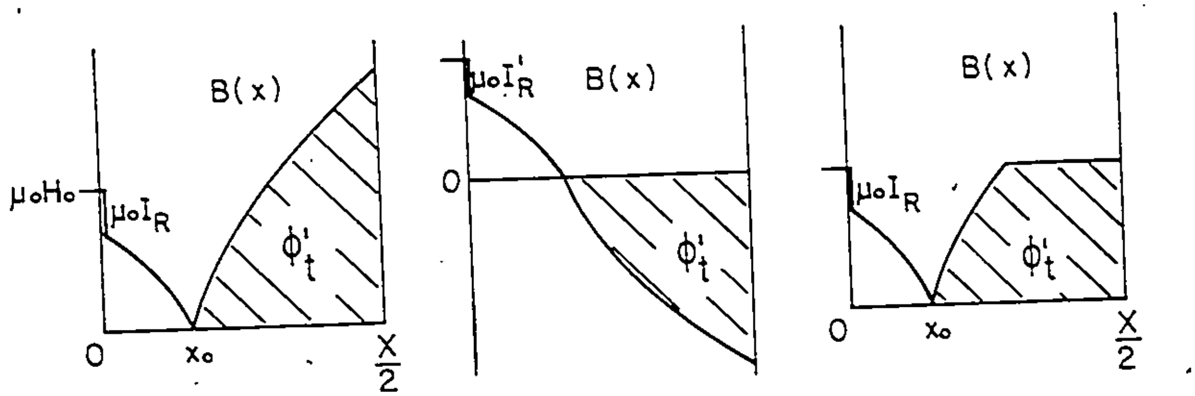


In these computations of $\langle B\rangle_{rot}$ in the active region or shoulders of the B profiles, $j_{c\ rot}' = \beta j_c'$ was adopted where $\beta = 1$ and $1/\sqrt{3}$. Bean's analysis suggests that the B profile in the active region may be shallower than encountered in the standard magnetization curves (the non-rotating situation). $\beta = 1/\sqrt{3}$ is selected simply because this value emerges in Bean's analysis (Bean 70). It has already been demonstrated earlier in this chapter that the possibility that $\beta > 1$ is inconsistent with the present observations. The results of the computations are presented in Figures 4-4 through 4-7 where again the pertinent experimental data are reproduced. Examination of these Figures reveals that the choice $\beta \simeq 1$ best corresponds with the measurements. It is noticed that the concept of a coefficient $\beta$ which is independent of B and has the specific value $1/\sqrt{3}$ is a special case developed by Bean in the framework where $j_c'$ is also independent of B. When $j_c'$ varies with B, as is generally the case, the possibi-

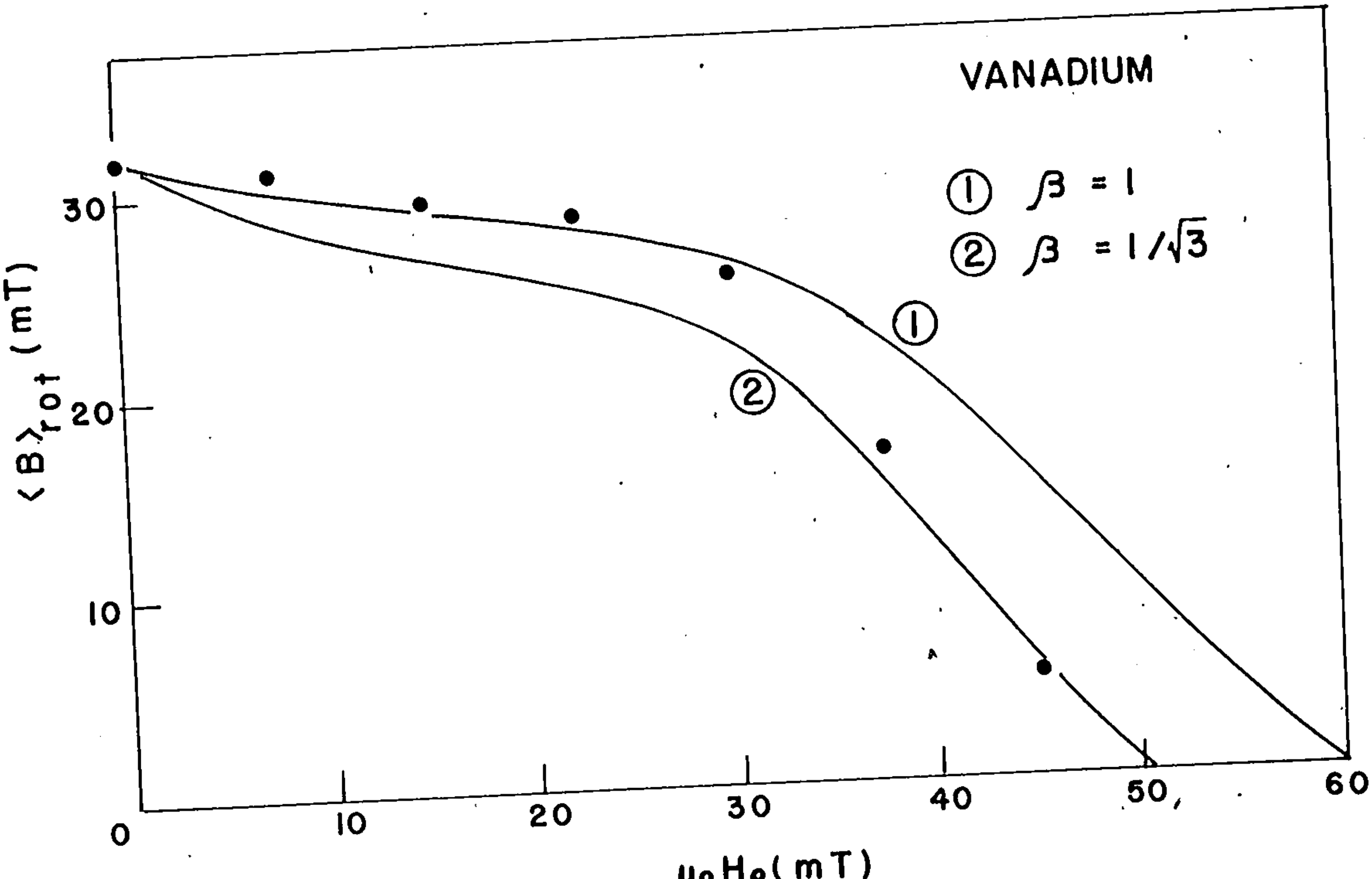


Figure 4-4 $\langle B \rangle_{rot}$ versus $H_o$. Experimental data for the Vanadium disk with hybrid initial field profiles. Calculated curves for $\beta = 1$ and $1/\sqrt{3}$, and using $j_c'(B)$ and $I_R'(H_o)$ obtained for this sample in chapter 3.

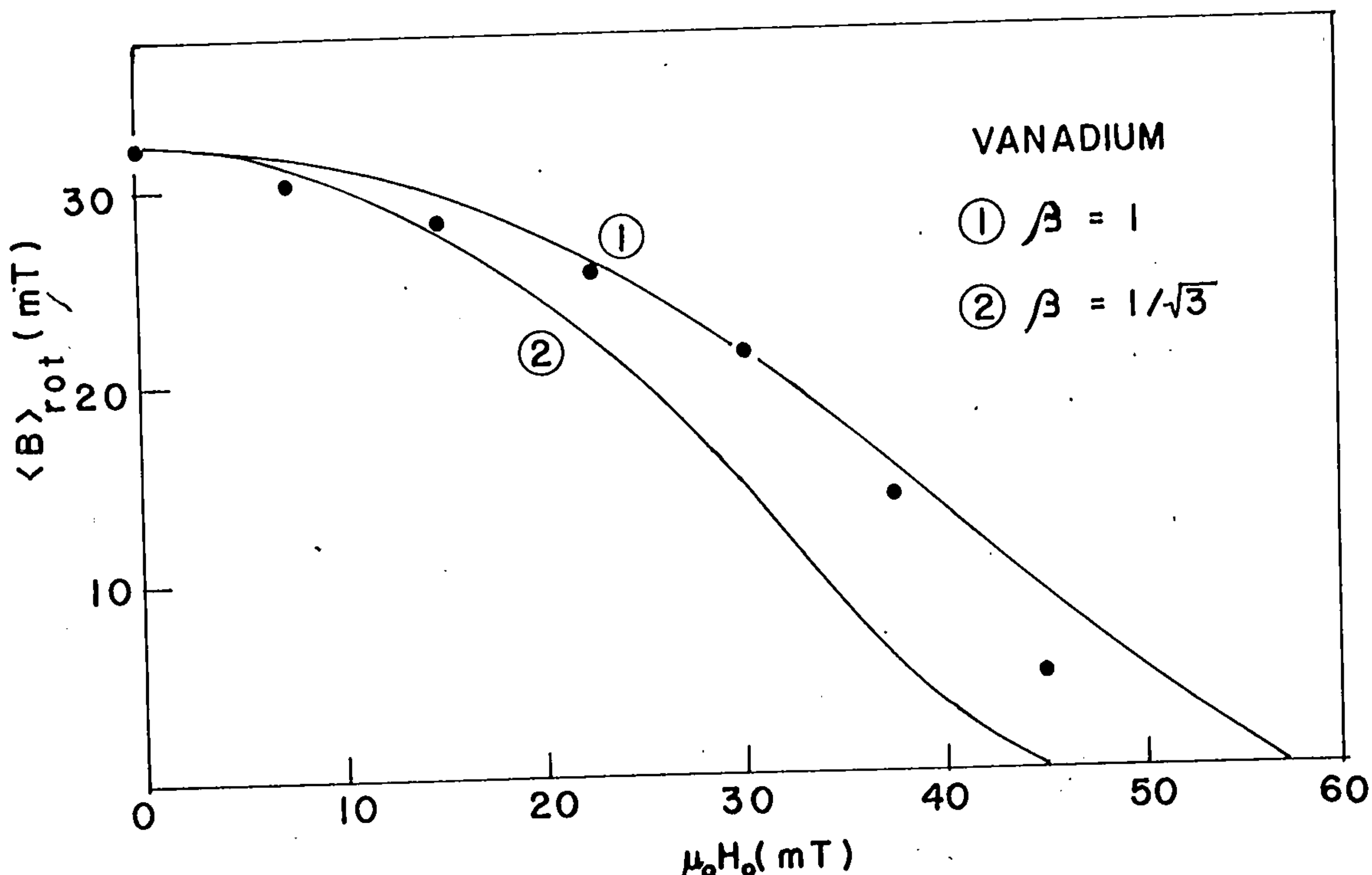


Figure 4-5 $\langle B \rangle_{rot}$ versus $H_o$. Experimental data for the vanadium disk with paramagnetic initial field profiles. Calculated curves for $\beta = 1$ and $1/\sqrt{3}$, and using $j_c'(B)$ and $I_R(H_o)$ obtained for this sample in chapter 3.

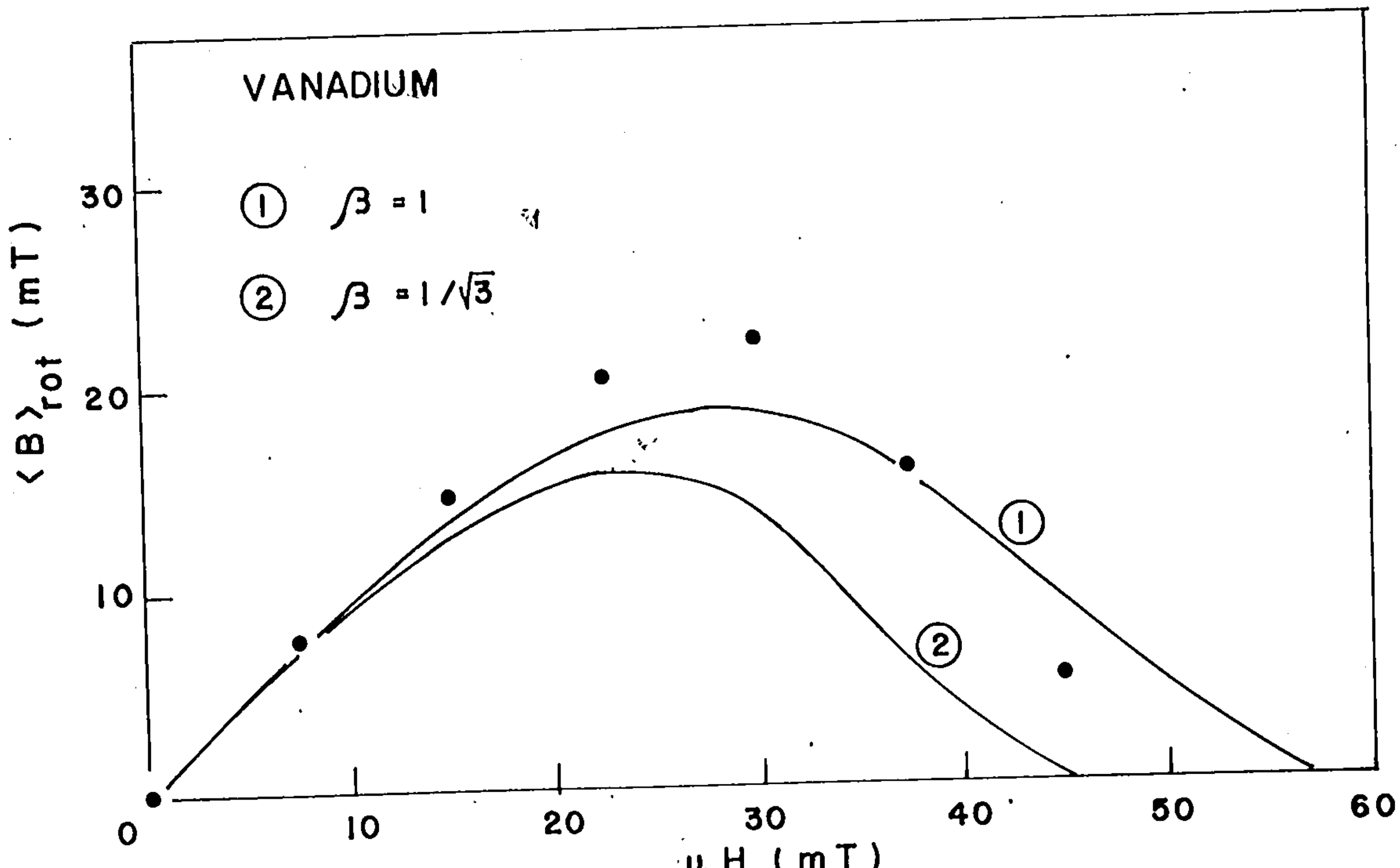


Figure 4-6 $\langle B \rangle_{rot}$ versus $H_o$. Experimental data for the vanadium disk with non-magnetic initial field profiles. Calculated curves for $\beta = 1$ and $1/\sqrt{3}$ using $j_c'(B)$ and $I_R(H_o)$ obtained for this sample in chapter 3.

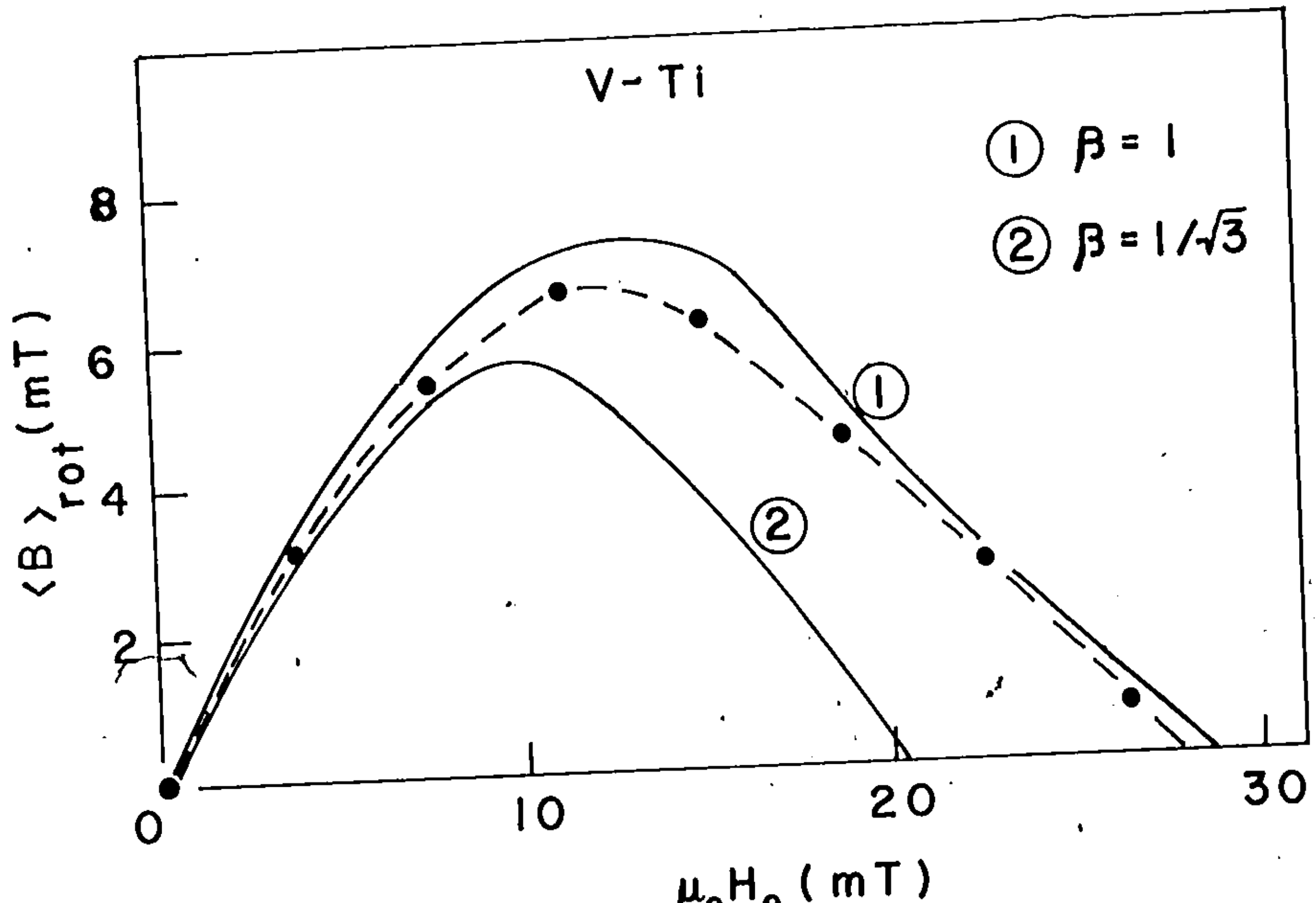


Figure 4-7 $\langle B \rangle_{rot}$ versus $H_o$. Experimental data for the V-Ti disk with non-magnetic initial field profiles. Calculated curves for $\beta = 1$ and $1/\sqrt{3}$ using $j_c'(B)$ and $I_R(H_o)$ obtained for this sample in chapter 3.

lity that $\beta$ is also dependent on B might be envisaged a priori. Fortuna-tely, the good agreement obtained with the data when $\beta \cong 1$ seems to indi-cate that this horrendously complicating aspect can be set aside.

## 4.7 Concluding Remarks

A simple model has been proposed for the B profile in the quasi-steady state of a rotating disk and during the approach to the quasi-steady state. This model leads to an accurate description of the magne-tic flux remaining in the central region of the disk and rotating with it when the quasi steady state is established regardless of the configu-ration of flux intially threading the disk. The picture requires that in many instances, some of the flux originally permeating the disk be released or expelled. This phenomenon is akin to a rotation induced Meissner Effect. It is well known that normal metallic disks rotating in a magne-tic field also expel magnetic flux and develop a diamagnetic moment along the direction of $H_o$. The flux expulsion in this case however is depen-dent on $\omega$ the angular frequency of rotation. A similar phenomenon of flux expulsion is encountered when type II superconducting cylinders are rotated in static transverse fields. Again, the diamagnetic moment along $H_o$ is frequency dependent. The expulsion of flux which is observed and described here is radically different from these phenomena since it is independent of the rate of rotation and appears undiminished in the limit approaching zero frequency. The flux expulsion reported in this chapter is an intriguing and dramatic phenomenon replete with implications about the behaviour of flux vortices and their interactions.

# Chapter 5

## Rotating Disk Phenomena:

## High Field Behaviour and Evolution to the Quasi-Steady State

### 5.1 Introduction

In the previous chapter the attention has been focussed on the quasi-steady state and particularly on the magnetic flux which rotates in phase with the rotation of the disk. According to the picture proposed and which is quantitatively consistent with all of the pertinent observations, this rotating magnetic flux occupies, in the quasi-steady state, a central region, $x_{o\ max} \leq x \leq X - x_{o\ max}$, straddling the mid-plane of the disk. The width of this central core shrinks with increasing $H_o$ and its dimensions are independent of the details of the orientation configuration of the magnetic flux in the adjacent active region or "shoulders" of the B profile. When $H_o$ exceeds a threshold value H**, this central core has vanished. Then the two shoulders of the B profile meet at the mid-plane of the disk where $B(X/2) > 0$ and the active regions occupy the entire width of the disk. This is the reason why the phenomena which is now scrutinized is labelled as the high field behaviour. This label is perhaps misleading since the active regions or shoulders exist for all fields. Below the threshold field H**, however, the active regions diminish with decreasing $H_o$. Their contribution to the detected signals is correspondingly less pronounced and tends to be overwhelmed by the rotating contribution, whereas above H**, the magnetic moment in the quasi-steady state is due entirely to the active region. In this chapter the rotation with depth of the magnetic induction in the shoulders of the B profile is examined. First the attention is focussed on the configuration in the active region for the quasi-steady state, then the behaviour is analysed during the evolution to the quasi-steady state.

## 5.2 Statement of the Model

In the active regions or shoulders of the B profile, both the orientation and the magnitude of the magnetic induction $\vec{B}(x) = \hat{y}\, B_y(x) + \hat{z}\, B_z(x)$ vary with distance from the surface. According to the picture pursued in the previous chapter, regardless of the initial magnetic state of the disk, B(x) in the active region decreases with depth and the gradient of B is dictated by the prescription

$$\left(\frac{dB}{dx}\right)_{rot} = -\mu_o \beta\, j_c' \tag{5-1}$$

where $j_c'(B) = (dB/dx)_c$ is the gradient of the B profile encountered in the non-rotating situation and extracted from the standard magnetization curves. Equation 5-1 applies to the half space between the surface located at x = 0 and the mid-plane at x = X/2; for the second half of the disk the term at the right is positive.

In the previous chapter, evidence has been presented that $\beta \cong 1$, hence this factor is not only independent of B but also of the state of rotation of $\vec{B}(x)$ with distance. Nevertheless $\beta$ is retained as a coefficient in equation 5-1 since it is desired to test further whether the data which are now examined are better reproduced by taking $\beta = 1$ or $\beta < 1$.

Quite generally it can be written that

$$B_z(x) = B(x) \cos \theta\,(x) \tag{5-2}$$

and

$$B_y(x) = B(x) \sin \theta\,(x) \tag{5-3}$$

where $\theta(x)$ is the angle subtended by the magnetic induction vector $\vec{B}(x)$

and the stationary externally applied magnetic field $H_o$.

In the quasi-steady state, the configuration of the magnetic induction $\vec{B}(x)$ in the active region is fixed or rigid with respect to $H_o$, hence with respect to the laboratory frame and the observers (the stationary orthogonal pick-up coils embracing the disk). The metallic lattice of the disk sweeps by this static configuration of $\vec{B}$ if the disk continues to rotate in the same direction. The constant (D.C.) component of the signals in quasi-steady state then provide a direct measure of the quantities $<B_z>$ and $<B_y>$ defined as

$$<B_z> = \frac{1}{X/2} \int_0^{x_{o\,max}} B(x) \cos \theta(x)\, dx \tag{5-4}$$

$$<B_y> = \frac{1}{X/2} \int_0^{x_{o\,max}} B(x) \sin \theta(x) dx \tag{5-5}$$

where $0 \leq x_{o\,max} \leq X/2$ when $H_o \leq H^{**}$ and $x_{o\,max} = X/2$ when $H_o > H^{**}$. $H^{**}$ is still used for generality, although the results presented in the previous chapter indicate that $H^{**} = H^*$. (It is also recalled that the emf from the pick-up coils are integrated hence the signals obtained are proportional to the above quantities).

To proceed further, a rule is required to determine $\theta(x)$. The following simple law is proposed.

$$\frac{d\theta}{dx} = \pm \gamma \mu_o j'_c \tag{5-6 a}$$

or equivalently

$$\theta(x) = \pm \gamma\mu_o \int_0^x j'_c (B(x'))dx' \tag{5-6 b}$$

where $\gamma$ is a parameter of the material and incorporates the coefficient $\beta$. The coefficient $\mu_o = 4\pi \times 10^{-7}$ tesla-metre/ampere is retained to maintain the convenient parallelism with equation 5-1. The choice of the + or - sign is dictated by the sense of rotation. It will now be concentrated on the half space $0 \leq x \leq X/2$.

Ultimately the validity of this empirical rule will be determined by its ability to generate results in accord with observations. It is instructive, however, to indicate the line of reasoning which led to choose this law, besides its obvious simplicity. Some of the physical implications of this formula will also be examined.

In Bean's analysis of the rotating disk, which is presented in Chapter 4 and pursued in the framework of the crude approximations that $(dB/dx)_c = \mu_o j'_c = \mu_o \alpha$ (where $\alpha$ is a constant) and $\mu = B(H)/H = \mu_o$, hence $I_R = I'_R = 0$ and $j'_c = j_c$, the following expression appeared

$$\theta(x) = \pm \sqrt{2}\, \ln \left( 1 - \frac{x}{\sqrt{3}\,\delta} \right) \tag{5-7}$$

where $\delta = H_o/\alpha$. Differentiating this leads to

$$\frac{d\theta}{dx} = \pm \sqrt{\frac{2}{3}} \; \frac{\mu_o \alpha}{B(x)_{rot}} \tag{5-8}$$

where

$$B(x)_{rot} = \mu_o H_o \left(1 - \frac{x}{\sqrt{3}\,\delta}\right) \tag{5-9}$$

and the critical B profile for the non-rotating situation is

$$B(x) = \mu_o H_o \left(1 - \frac{x}{\delta}\right) \tag{5-10}$$

The formulae are consistent with the condition that the local electric field vector generated during rotation be directed parallel to the current density vector $\vec{j}$. It is noticed that, in spite of its many crude simplifying assumptions Bean's analysis nevertheless leads to a reasonable description of the observations of $\langle B_z \rangle$ and $\langle B_y \rangle$ vs $H_o$ in the low field range $0 < H_o \leq H^{**}$.

This agreement certainly provides a strong impetus to retain the crucial features of Bean's formulae. The problem, of course, is to establish which elements are most crucial and which can be modified without undertaking the formidable task of solving this difficult problem from first principles.

It has been seen in chapter 3 that the Kim pinning function $F_p'(B) = \alpha$ satisfactorily reproduced the "low field behaviour", particularly when $B(x)_{rot}$ is chosen equal to the critical B(x) profile. Further in the Kim approximation $j_c' = \frac{\alpha_{Kim}}{B}$ . This suggests that the term $\alpha/B(x)_{rot}$ appearing in equation 5-8 could be replaced by the almost equivalent but simpler term $j_c'(B)$. There is then no justification for retaining the specific coefficient $\sqrt{2/3}$ since the latter is a consequence of the original formulation. Accordingly, an adjustable coefficient $\gamma$ is empirically introduced.

Evidently the end result of this phenomenological approach has the merit of simplicity and should perform adequately for low fields ($H_0 < H^{**}$) since it is constructed to provide approximate accord with the observations in this range. The acid test will be whether these rules (equations 5-1 and 5-6) also yield behaviour in agreement with observations in the high field range and during the evolution to the quasi-steady state. Section 5.4 will show the success of these empirical prescriptions when combined with the picture proposed for the evolution of the B profile as rotation progresses to the quasi-steady state.

## 5.3 General Discussion of the Rotational Configuration of the Model

Before proceeding to the application of equations 5-1 and 5-6 it is worthwhile to examine various basic aspects of the problem of the rotational B profile, the development of the concepts of the critical state and equilibrium diamagnetism in this special situation and the physical meaning and implications of the empirical solution.

i) The critical state and critical current density in the rotational B profile.

In the previous discussions, the formulation of the critical state and of the critical current density was relatively simple. In chapter 3, it was dealt with the standard magnetization curves where the persistent currents flow perpendicularly to the magnetic induction which is unidirectional. In chapter 4 the attention was focussed on the magnetic flux in the central region of the disk where again an internally non-rotational B profile exists. In that chapter, Bean's analysis of the rotational B profile was also presented. This analysis, however, avoids many of the complications and aspects here considered since it takes the permeability $\mu = \mu_o$ and the critical current density to be a constant, hence unaffected by B and by the rotational configuration of $\vec{B}$. Many important elements of the total picture are now reexamined in the context of the rotational B profile.

The critical state equation in vector form

$$\vec{J}_c \times \vec{B} - \vec{F}_p = 0 \tag{5-10}$$

and in scalar form

$$J_c B \sin\phi = F_p \tag{5-11}$$

is written

$$\hat{x}\,\{J_y B_z - J_z B_y \pm F_p\} = 0 \tag{5-12}$$

for infinite slab geometry or alternatively

$$B_y\left(\frac{dH_y}{dx}\right) + B_z\left(\frac{dH_z}{dx}\right) = \pm F_p(B) \tag{5-13}$$

where Maxwell's equation $\nabla \times \vec{H} = \vec{J}$ has been introduced. The capital letter J will be henceforth used for the current density (and $J_y$, $J_z$ for its components) to avoid possible confusion with

$$j_c = \left(\frac{dH}{dx}\right)_c \tag{5-14}$$

the scalar value of the gradient of the magnitude of the magnetic field where the small j will still be used. This gradient is directed along the x axis. For simplicity the + and - signs in front of $F_p$ (and $F_p'$) will be ignored except when it is useful for physical reasons. The partial derivative notation is not used since it is clear that the pertinent quantities do not vary with y and z for the infinite slab geometry here considered.

Equation 5-13 can be rewritten

$$\frac{B_y}{B}\left(\frac{dH_y}{dx}\right) + \frac{B_z}{B}\left(\frac{dH_z}{dx}\right) = \frac{F_p}{B} \tag{5-15}$$

This apparently trivial change is extremely useful as will be seen shortly and we are indebted to Dr. John Clem for drawing our attention to the idea now exploited.

According to the concept of Abrikosov diamagnetism, the vectors $\vec{H}$ and $\vec{B}$ are collinear and in equilibrium. The permeability $\mu(B)$ (or $\mu(H)$) is a scalar and therefore

$$\mu = \frac{B}{H} = \frac{B_y}{H_y} = \frac{B_z}{H_z} \tag{5-16}$$

hence

$$\frac{B_y}{B} = \frac{H_y}{H} \quad \text{and} \quad \frac{B_z}{B} = \frac{H_z}{H} \tag{5-17}$$

Introducing these considerations in equation 5-15 gives

$$\frac{H_y}{H}\frac{dH_y}{dx} + \frac{H_z}{H}\frac{dH_z}{dx} = \frac{d}{dx}\left(H_y^2 + H_z^2\right)^{\frac{1}{2}} = \left(\frac{dH}{dx}\right)_c \tag{5-18}$$

and finally

$$B(\frac{dH}{dx})_c = F_p(B) \qquad (5\text{-}19\ a)$$

or equivalently

$$j_c B = F_p(B) \qquad (5\text{-}19\ b)$$

where $j_c$ corresponds to a critical current density only in the non-rotational (unidirectional) B profile. It is stressed that equation 5-19 applies regardless of the orientation of the configuration of the current density $\vec{J}(x)$ and the magnetic induction $\vec{B}(x)$ and is valid for infinite slab geometry.

The magnitude of the critical current density $\vec{J}_c = \hat{y}\, J_y + \hat{z}\, J_z$ associated with the H profile can be written,

$$J_c = \{(\frac{dH_y}{dx})^2 + (\frac{dH_z}{dx})^2\}^{\frac{1}{2}} = \{(\frac{dH_y}{dB_y})^2(\frac{dB_y}{dx})^2 + (\frac{dH_z}{dB_z})^2(\frac{dB_z}{dx})^2\}^{\frac{1}{2}} \qquad (5\text{-}20)$$

It is now returned to the equilibrium diamagnetism concept (equations 5-16 and 5-17). A differential permeability may also be defined

$$\mu' = \frac{dB(H)}{dH} = \frac{dB}{dH(B)}$$

or equivalently

$\mu' (\hat{y}\ \Delta\ H_y + \hat{z}\ \Delta H_z) = \hat{y}\ \Delta\ B_y + \hat{z}\ \Delta\ B_z$ where $\mu'$ is a scalar function. Then

$$(\frac{dH_y}{dB_y})_x = (\frac{dH_z}{dB_z})_x = (\frac{dH}{dB})_x \qquad (5\text{-}21)$$

Consequently, equation 5-20 yields

$$J_c = \frac{dH}{dB} \{(\frac{dB_y}{dx})^2 + (\frac{dB_z}{dx})^2\}^{\frac{1}{2}} \qquad (5\text{-}22\ a)$$

or equivalently

$$J_c = \mu_o \frac{dH}{dB} J_c' \qquad (5\text{-}22\ b)$$

where

$$J'_c = \frac{1}{\mu_o} \{ ( \frac{dB_y}{dx} )^2 + ( \frac{dB_z}{dx} )^2 \}^{1/2} \tag{5-23}$$

is the magnitude of the current density $\vec{J}'_c$ associated with the B profile.

It can also be written

$$\vec{J}'_c = \hat{y} J'_y + \hat{z} J'_z = \{ \hat{y} ( - \frac{dB_z}{dx} ) + \hat{z} ( \frac{dB_y}{dx} ) \} \frac{1}{\mu_o} \tag{5-24}$$

where Maxwell's equation has been introduced in the form $\nabla \times \vec{B} = \mu_o \vec{J}'_c$.

Returning to the critical state equation 5-13 it can be rewritten

$$B_y ( \frac{dH_y}{dB_y} ) \frac{dB_y}{dx} + B_z ( \frac{dH_z}{dB_z} ) ( \frac{dB_z}{dx} ) = F_p(B) \tag{5-25}$$

Again, making use of equation 5-21 this becomes

$$\frac{1}{\mu_o} \{ B_y \frac{dB_y}{dx} + B_z \frac{dB_z}{dx} \} = \frac{F_p(B)}{\mu_o (dH/dB)} = F'_p(B) \tag{5-26}$$

Since $B = \sqrt{B_y^2 + B_z^2}$, this can be abbreviated to

$$\frac{1}{\mu_o} B ( \frac{dB}{dx} )_c = j'_c B = F'_p(B) \tag{5-27}$$

where $\mu_o j'_c = (dB/dx)_c$ is the scalar value of the critical gradient of the magnitude of the magnetic induction. Again it is noticed that equation 5-27 applies regardless of the orientation of $J'_c$ with respect to $\vec{B}$.

Introducing $J_c = \mu_o J'_c \, dH/dB$ (equation 5-22 b ) into $J_c B \sin \phi = F_p$ (equation 5-11) a critical state equation is obtained in scalar form for the B profile

$$J'_c B \sin \phi = \frac{F_p}{\mu_o dH/dB} = F'_p(B) \tag{5-28}$$

which, in vector form, becomes

$$\vec{J}'_c \times \vec{B} - \vec{F}'_p = 0 \tag{5-29}$$

Recalling the definitions $B_y(x) = B(x) \sin \theta(x)$ and $B_z(x) = B(x) \cos \theta(x)$ it is obtained upon differentiation with respect to x

$$\mu_o J'_y = -\frac{dB_z}{dx} = B \sin\theta\left(\frac{d\theta}{dx}\right) - \cos\theta\left(\frac{dB}{dx}\right)_c \qquad (5\text{-}30)$$

and

$$\mu_o J'_z = \frac{dB_y}{dx} = B \cos\theta\left(\frac{d\theta}{dx}\right) + \sin\theta\left(\frac{dB}{dx}\right)_c \qquad (5\text{-}31)$$

Introducing these expressions into equation 5-23 leads to

$$J'_c = \frac{1}{\mu_o}\sqrt{\left(\frac{dB}{dx}\right)_c^2 + B^2\left(\frac{d\theta}{dx}\right)^2} \qquad (5\text{-}32\text{ a})$$

and equivalently

$$J'_c = \sqrt{(j'_c)^2 + \frac{B^2}{\mu_o}\left(\frac{d\theta}{dx}\right)^2} \qquad (5\text{-}32\text{ b})$$

It is noted that equations 5-30, 5-31 and 5-32 are general results unrelated to the critical state and equilibrium diamagnetism concepts. Similar expressions can readily be obtained for $J_c$ and its components $J_y$ and $J_z$ starting from the definitions

$$H_y(x) = H(x)\sin\theta(x) \text{ and } H_z(x) = H(x)\cos\theta(x)$$

and using equation 5-23. The relationship between $J_c$ and $J'_c$ (equation 5-22) depends, however, on invoking the concept of isotropic equilibrium diamagnetism.

Further, it is remarked that all of the above expressions are applicable regardless of whether the rotational and unidirectional B and H profiles happen to differ as suggested by Bean. If they do differ then $H(x)$, $B(x)$, $J_c$, $j_c$, $J'_c$ and $j'_c$ in the above formulae need only be replaced by the corresponding symbol carrying the subscript rot to indicate this state of affairs. The configuration which exists, rotational or unidirectional, should be clear from the situation under scrutiny. The subscript is introduced only to express the feature proposed by Bean that the profiles may be modified and, in particular, become shallower in the rotational configuration.

Introducing equation 5-1 and 5-6 a into equation 5-30 a it is obtained that

$$J'_c = j'_c\sqrt{\beta^2 + (B\gamma)^2} \tag{5-33}$$

hence $J'_c > j'_c$ if $\beta = 1$. In other words, as expected, the critical current density associated with the B and the H profile is enhanced in going from the unidirectional to the rotational configuration when $\beta \simeq 1$.

ii) Direction of $\vec{E}$ with respect to $\vec{J}$.

The configuration of the electric currents and magnetic induction developed by Bean satisfies the condition that the electric current densities $\vec{J}_c$ and $\vec{J}'_c$ (which are identical in his case) lie along the electric field $\vec{E}$ when the disk or the configuration of magnetic induction rotate. Bean requires that $\psi = 0$ where

$$\psi = \sin^{-1}\left(\frac{|\vec{E} \times \vec{J}|}{EJ}\right) \tag{5-34}$$

The behaviour of $\psi$ which ensues from the empirical rules developed previously is now examined. The components of the electric field vector

$$\vec{E}(x) = \hat{y}\, E_y(x) + \hat{z}\, E_z(x) \tag{5-35}$$

can be found from Maxwell's equation $\nabla \times \vec{E} = -\partial\vec{B}/\partial t$ as follows. Rewriting $\frac{\partial E_y}{\partial x} = -\frac{\partial B_z}{\partial t}$ and integrating gives

$$-E_y(x) = \int_x^{x_{o\,max}} dE_y = -\frac{d}{dt}\int_x^{x_{o\,max}} B(x')\cos\theta(x')\,dx' \tag{5-36}$$

$$E_y(x) = -\frac{d\theta}{dt}\int_x^{x_{o\,max}} B(x')\sin\theta(x')\,dx' \tag{5-37}$$

since $E_y = 0$ at $x = x_{o\,max}$.

It is convenient to define

$$\langle B_y\rangle_x = \frac{2}{X}\int_x^{x_{o\,max}} B(x')\sin\theta(x')\,dx' \tag{5-38}$$

In terms of this definition

$$E_y(x) = -\frac{X}{2}\left(\frac{d\theta}{dt}\right)\langle B_y\rangle_x \tag{5-39}$$

Proceeding similarly with $\partial E_z/\partial x = +\partial B_y/\partial t$, since $E_z = 0$ at $x = x_{o\,max}$, it is obtained that

$$E_z(x) = -\frac{X d\theta}{2dt}\langle B_z\rangle_x \tag{5-40}$$

where

$$\langle B_z\rangle_x = \frac{2}{X}\int_x^{x_{o\,max}} B(x')\cos\theta\,(x')dx' \tag{5-41}$$

Using equation 5-39 for $E_y$ and 5-40 for $E_z$ together with equation 5-30 for $J'_y$ and 5-31 for $J'_z$ and making use of equation 5-22 b to convert $J'_y$ to $J_y$ and $J'_z$ to $J_z$ gives

$$|\vec{E}\times\vec{J}| = E_yJ_z - E_zJ_y = \left(\frac{dH}{dB}\right)\frac{X}{2}\left(\frac{d\theta}{dt}\right)\Big[-\Big(B\cos\theta\left(\frac{d\theta}{dx}\right) + \sin\theta\left(\frac{dB}{dx}\right)_c\Big)\langle B_y\rangle_x$$

$$+\Big(B\sin\theta\left(\frac{d\theta}{dx}\right) - \cos\theta\left(\frac{dB}{dx}\right)_c\Big)\langle B_z\rangle_x\Big] \tag{5-42}$$

Making use of 5-22 b to convert $J'_c$ to $J_c$ and equation 5-32 a for $J'_c$ together with 5-39 for $E_y$ and 5-40 for $E_z$, the denominator in the expression for $\psi$ becomes

$$EJ = \left(\frac{dH}{dB}\right)\frac{X}{2}\left(\frac{d\theta}{dt}\right)\Big[\Big\{\left(\frac{dB}{dx}\right)_c^2 + B^2\left(\frac{d\theta}{dx}\right)^2\Big\}^{\frac{1}{2}}\Big\{\langle B_y\rangle_x^2 + \langle B_z\rangle_x^2\Big\}^{\frac{1}{2}}\Big] \tag{5-43}$$

It is remarked that equations 5-42 and 5-43 are general results and that $\psi$ is independent of the rate of rotation $d\theta/dt$ and of equilibrium diamagnetism. It should be noted here that for the type I superconductor and the ideal type II superconductor below $H_{c1}$, where $d\theta/dx = 0$, hence $\langle B_y\rangle_x = 0$, equations 5-42 and 5-43 lead, as they should to $\psi(x) = -90^o$. In this case, the electric field $\vec{E}$ must be perpendicular to $\vec{J}$ since there cannot be any dissipation of energy associated with the reversible current density $\vec{J}$.

It is relatively straightforward to verify that Bean's formulation leads to $\psi = 0$ at the surface $(x = 0)$ where $\theta = 0$. This is achieved by introducing $<B_z>$ from equation 4-17 and $<B_y>$ from equation 4-18 into equation 5-42.

Introducing equation 5-1 for $(dB/dx)_c$ and equation 5-6 for $d\theta/dx$ into equations 5-42 and 5-43 leads to the following

$$\frac{|\vec{E} \times \vec{J}|}{EJ} = \frac{\{-(\gamma B \cos\theta - \beta \sin\theta)<B_y>_x + (\gamma B \sin\theta + \beta \cos\theta)<B_z>_x\}}{\{\beta^2 + \gamma^2 B^2\}^{\frac{1}{2}} \{<B_y>_x^2 + <B_z>_x^2\}^{\frac{1}{2}}} \tag{5-44}$$

where $<B_y>_x$ is positive if $\gamma$ is taken to be positive.

It is evidently a formidable task to compute the dependence on $H_o$ of $\psi$ vs x. The problem is considerably simplified when concentrating on its behaviour at the surface only where $\theta = 0$; it leads to

$$\psi(0) = \sin^{-1}\left[\frac{-\gamma B_s <B_y> + \beta <B_z>}{(\beta^2 + \gamma^2 B_s^2)^{\frac{1}{2}}\{<B_y>^2 + <B_z>^2\}^{\frac{1}{2}}}\right] \tag{5-45}$$

where $B_s = \mu_o(H_o - I_R)$ or $B_s = \mu_o(H_o - I_R')$ depending on the initial magnetic state of the disk.

In Figures 5-11 and 5-12 $\psi(0)$ vs $H_0$ which ensues from the present model is shown for the V and VTi samples with $\beta = 1$ and taking $B_s = H_o - I_R$. Since $I_R \gtrsim I_R'$ when $H_o > H^{**}$ and $I_R$ is negligible compared to $H_o$, this choice is not significant.

If we accept the condition $\psi(x) = 0$ as a necessary requirement, equation 5-44 and particularly, equation 5-45 provide a useful tool in the search for improvements to the simple and approximate empirical choice for $d\theta/dx$.

iii) Rate of Energy Dissipation

From the results developed in the previous section an expression can readily be obtained for W, the rate of energy dissipation as the disk rotates. Following the Poynting formulation it can be written

$$W = \int (\vec{E} \times \vec{H}) \cdot d\vec{A} = 2A\ E_y H_o = AX\left(\frac{d\theta}{dt}\right) H_o \langle B_y \rangle \tag{5-46}$$

where AX is the volume of the disk of area A and thickness X.

This expression leads, as it should, to Bean's result for the energy dissipation when $\langle B_y \rangle = \mu_o H_o^2 \sqrt{2}/\sqrt{3}\ J_c X$ which applies in the narrow range $0 < H_o \leq H^{**}$.

Gilchrist (Gilchrist 72) has also analyzed the problem of energy dissipation in a rotating type II superconductor in a generalized framework and obtains results which reduce to Bean's conclusion in the limit of $J_c$ constant and $H_o \leq H^{**}$.

Since the present model generates curves of $\langle B_y \rangle$ vs $H_o$ which are in good agreement with observations as will be seen shortly, it consequently provides a satisfactory account of the energy dissipation accompanying the rotation.

iv) Some Physical Implications of $d\theta/dx = \pm\mu_o \gamma j_c'$

The empirical rule

$$\frac{d\theta}{dx} = \pm \mu_o \gamma j_c' = \pm \gamma \left(\frac{dB}{dx}\right)_c \tag{5-6 a}$$

indicates that the gradient of the θ profile is proportional to the gradient of the B profile. This seems reasonable since in the regime of slow rotation, which applies in this work and where viscous forces are negligible, it is presumably the same pinning sites and pinning forces which control the orientation of the planes of flux lines as well as their migration into and out of the disk. This aspect emerges more clearly if equations 5-26 and 5-27 are used to rewrite equation 5-6 a. It yields

$$\frac{B}{\gamma} \left( \frac{dH}{dB} \right) \frac{d\theta}{dx} = F_p(B) \tag{5-47}$$

and

$$\frac{B}{\gamma\mu_o} \frac{d\theta}{dx} = F'_p\,(B) \tag{5-48}$$

These expressions suggest that the interaction between two adjacent planes of vortices separated by a distance $\Delta\tilde{x}$ and oriented at an angle $\Delta\theta$ with respect to each other gives rise to $F_t$, a turning force density or torque per unit length which tends to make them line up parallel to each other. This picture is now pursued in more detail and the two adjacent planes are labelled as 1 and 2. It is visualized that plane 1, initially parallel to plane 2 is rotated infinitesimally while plane 2 maintains its orientation. A turning force or torque per unit length, $F_t$ acting on plane 2 then arises. The pinning forces come into action and impede any rotation of plane 2 until the angle $\Delta\theta$ has increased sufficiently so that $F'_t$ equals the maximum pinning force density $F'_p$. If now $\Delta\theta$ increases further, $F'_t$ exceeds $F'_p$ and plane 2 now follows the rotation of plane 1. A third plane adjacent and initially parallel to plane 2 then begins to experience a turning force or torque and the process just described is repeated for the succession of planes. It is thus visualized a critical state situation vis à vis the relative orientation of the planes of vortices in complete analogy with the critical state concept of a Lorentz driving force $F_L$ in equilibrium with an opposing pinning force $F_p$ operating when planes of flux lines are compressed or decompressed and made to penetrate into or move out of the specimen. Viewed in this context, equations 5-47 and 5-48 constitute critical state equations $F_t = F_p$ and $F'_t = F'_p$ where

$$F_t = \frac{B}{\gamma}\left(\frac{dH}{dB}\right)\left(\frac{d\theta}{dx}\right) \tag{5-49}$$

and $$F_t' = \frac{B}{\gamma\mu_o}\left(\frac{d\theta}{dx}\right) \tag{5-50}$$

Thus $d\theta/dx$ is the critical gradient of the orientation of the planes of flux lines.

## 5.4 Application of the Model

i) The Quasi-Steady State.

As in the previous chapter, it can be proceeded analytically to explore the consequences of the empirical rules (Equations 5-1 and 5-6) using the Bean and Kim pinning functions $F_p' = \alpha B$ and $F_p' = \alpha$ respectively. The starting expressions in these two cases then become

$$\langle B_z \rangle = \frac{2}{X}\int_0^{x_{o\,max}} (B_s - \mu_o\,\alpha\beta x)\,\cos\,(\mu_o\gamma\alpha x)\,dx \tag{5-51}$$

with the Bean pinning function and

$$\langle B_z \rangle = \frac{2}{X}\int_0^{x_{o\,max}} (B_s^2 - 2\mu_o\alpha\beta x)^{\frac{1}{2}}\cos\gamma\{B_s - (B_s^2 - 2\mu_o\alpha\beta x)^{\frac{1}{2}}\}dx \tag{5-52}$$

with the Kim pinning function where $B_s = \mu_o(H_o - I_R)$ or $B_s = \mu_o(H_o - I_R')$ depending on the initial state. The expression for $\langle B_y \rangle$ follows by substituting sin for cos.

These expressions can be integrated analytically. The resulting expressions, however, are quite complicated, particularly with the more physically meaningful Kim pinning function. As a consequence, these results are not very illuminating and still require considerable computation to yield information. Further, in the range of high fields, the Bean and Kim functions need to be corrected by introducing a factor of the form $(1 - B/H_{c2})$ or a variant thereof. Now, the analytic solutions, if they can be obtained, become even more cumbersome. For these reasons this thesis is not burdened with the results which would be obtained from pursuing this avenue.

In view of the complicated non-analytical dependence of $j_c'$ on $B$ and $I_R$ (and $I_R'$) on $H_o$ it is then proceeded computationally to determine $B_y(x)$, $B_z(x)$ and $\theta(x)$, hence $\langle B_z \rangle$ and $\langle B_y \rangle$ vs $H_o$ in the shoulders of the B profiles which ensue from the model for the quasi-steady state. In Figures 5-1 and 5-2 typical configurations of $B_z(x)$ and $B_y(x)$ are shown at a low and an intermediate value of $H_o$. Figure 5-3 presents $\theta(x)$ for these two configurations. In Figure 5-4 and 5-5 is displayed for completeness and comparison, $B_z(x)$, $B_y(x)$ and $\theta(x)$ ensuing from Bean's model.

In Figures 5-6 through 5-8, $\mu_o\langle M_z \rangle = \langle B_z \rangle - \mu_o H_o$ and $\mu_o\langle M_y \rangle = \langle B_y \rangle$ generated by the present model are compared with observations for the V and VTi samples. In Figure 5-6 two calculated curves are presented for two different values of $\gamma$ illustrating the sensitivity of the model to this parameter at high field. The value of $\beta = 1$ was selected. Similarly, in Figure 5-7 the same experimental measurements are presented with two calculated curves corresponding to $\beta = 1$ and $1/\sqrt{3}$ ; $\gamma$ is kept constant ($\gamma$ = 95 rad/T). As can be seen, the calculated curves are not very sensitive to this parameter. Further as expected the experimental and calculated results are not sensitive to the choice of $I_R$ and $I_R'$ at high field consequently either one can be used for the computation.

Let $\Delta\theta_{max}$ denote the total angular variation of $\vec{B}(x)$ from the surface where $\theta = 0$ to the front of the B profile in the quasi-steady state. In Figures 5-9 and 5-10 the dependence of $\Delta\theta_{max}$ on $H_o$ is displayed for the two samples. For fields lower than $H^{**}$, $\Delta\theta$ becomes infinite.

ii) Evolution to the Quasi-Steady State.

It is a straightforward matter to pursue the picture, developed in Chapter 4, for the sequences of B profiles encountered with various initial states as the rotation of the disk begins and progresses until the quasi-steady state is achieved. As the disk is rotated and $\theta$ grows, $x_o$, the limit of the active region advances into the sample and the shoulders of the B profile expand. The equations 5-1 and 5-6 dictate the B and $\theta$ profiles in the expanding active region $0 \leq x \leq x_o$. The reader is referred to Figures 5-13 and 5-14 where the sequences of the B and $\theta$ profiles are shown schematically for the low and high field ranges with $I_R = I'_R = 0$ and the B profile is sketched as linear, for simplicity. Also, for brevity, only the sequence of events occurring for the non-magnetic (cooling) initial state are represented.

The y and z components of the $\theta$ dependent spatial average of the magnetic induction $\vec{B}$, can be written

$$\langle B_y \rangle (\theta) = \frac{2}{X} \int_0^{x_o \max} B(x)_{rot} \sin \theta(x) dx + \frac{2 \sin \theta(x_o)}{X} \int_{x_o}^{X/2} B(x) dx \tag{5-53}$$

and

$$\langle B_z \rangle (\theta) = \frac{2}{X} \int_0^{x_o} B(x)_{rot} \cos \theta(x) \, dx + \frac{2 \cos \theta(x_o)}{X} \int_{x_o}^{X/2} B(x) dx \tag{5-54}$$

where B(x) and $\theta(x)$ are again obtained from equations 5-1 and 5-6.

The new feature which appears in considering the behaviour during the evolution of the quasi-steady state is that $x_o$, the distance of penetration of the active (rotational) region is determined by the relation

$$\theta = \mu_o \gamma \int_0^{x_o} J'_c (B(x)) \, dx \tag{5-55}$$

which follows from equation 5-6 and $\theta$ is the angle through which the disk has been rotated. (Of course, the sense of rotation of the disk must not change.)

The dependence of $\mu_o\langle M_y\rangle(\theta) = \langle B_y\rangle(\theta)$ and $\mu_o\langle M_z\rangle(\theta) = \langle B_z\rangle(\theta) - \mu_o H_o$ on $H_o$ as $\theta$ increases which ensues from the model is displayed in Figure 2-4 where it may be compared with the corresponding experimental observations (Figure 2-2). These sets of experimental and calculated curves are obtained with the Vanadium disk initially in the non-magnetic (cooling) state. Comparable agreement between measurements and theory is obtained starting with the other initial states for the V and VTi disks. When $H_o \geq H^{**}$, the theoretical curves evolve until a plateau is attained whereas the experimental curves continue to exhibit small oscillations superimposed on the steady (D.C.) "background". The origin of these "residual" oscillations has been discussed in detail in chapter 2. The frequency of these "parasitic" oscillations is twice that of the signal from the rotating flux $\phi_t'$ remaining in the central core in the quasi-steady state when $H_o < H^{**}$. This and other evidence presented in chapter 2 indicate that these residual oscillations are due to anisotropy of the pinning in the bulk or volume of the disks.

## 5.5 Conclusion

A simple empirical equation has been proposed to describe the rotation of the magnetic induction $\vec{B}(x)$ as the disk rotates. This basic equation combined with the model for the configurations of the B profiles as the rotation progresses provides a satisfactory account of a variety of observations on the V and VTi disk. In particular the dependence on $H_o$ of $\langle B_z\rangle$ and $\langle B_y\rangle$, the steady components of the magnetic induction in the quasi-steady state is reproduced quantitatively and similarly is the variation of these components with $\theta$ during the approach to the quasi-steady state for the entire range of fields $0 < H_o < H_{c2}$ and starting with the disk in a variety of initial magnetic states.

Further, although the model does not satisfy the condition $\vec{E} \times \vec{J} = 0$, it accounts quite satisfactorily for the electromagnetic energy dissipated in the quasi-steady state as the disk rotates slowly (i.e. $\int \vec{E} . \vec{J}$ dv where dv is an element of volume).

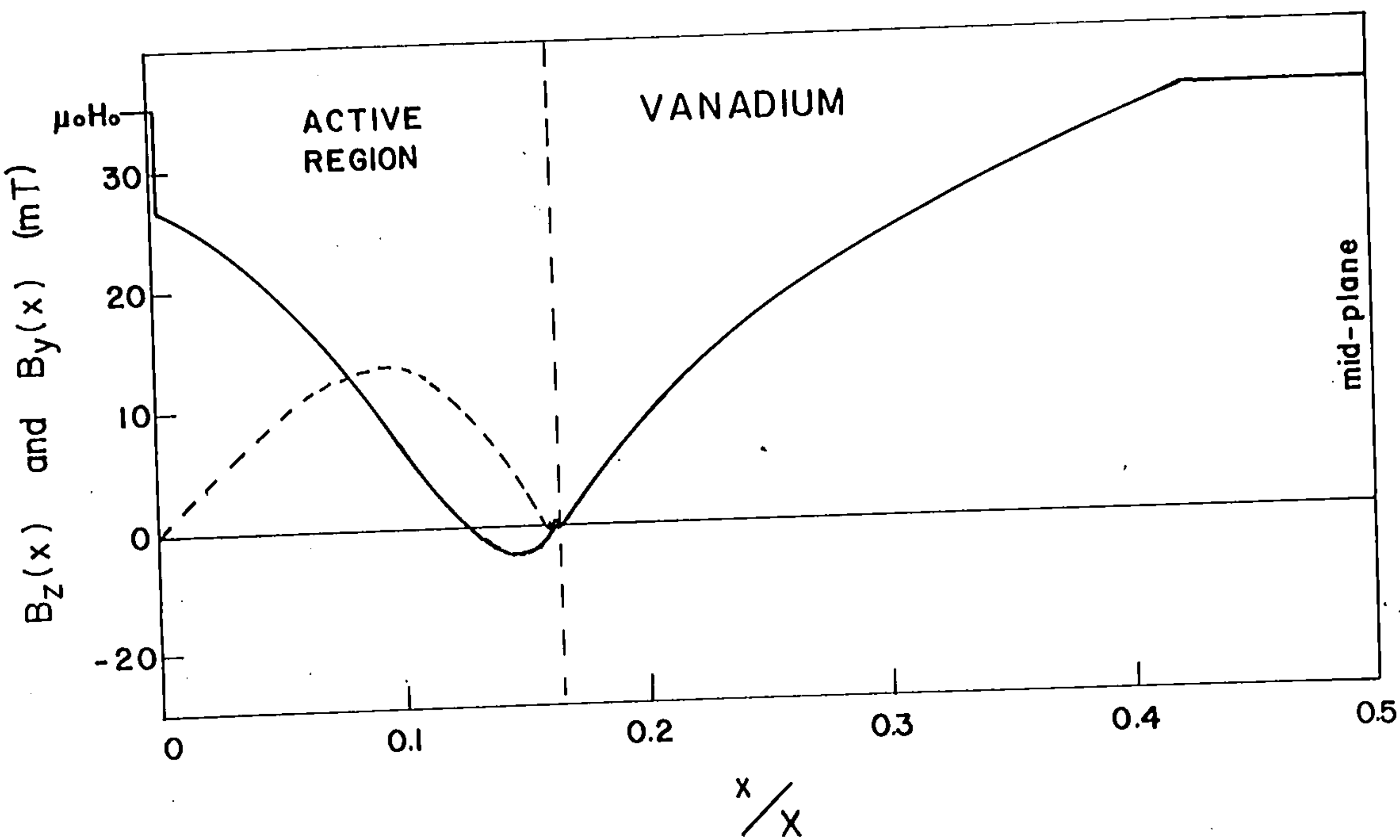


Figure 5-1 Quasi-steady state field profiles $B_z(x)$ and $B_y(x)$ for a non-magnetic initial state, for the vanadium disk ($\mu_o H_o$ = 35 mT). The value of $\beta$ = 1 and $\gamma$ = 95 rad/T as well as $j_c'(B)$ and $I_R(H_o)$ from Chapter 3 were used for computing the field profiles.

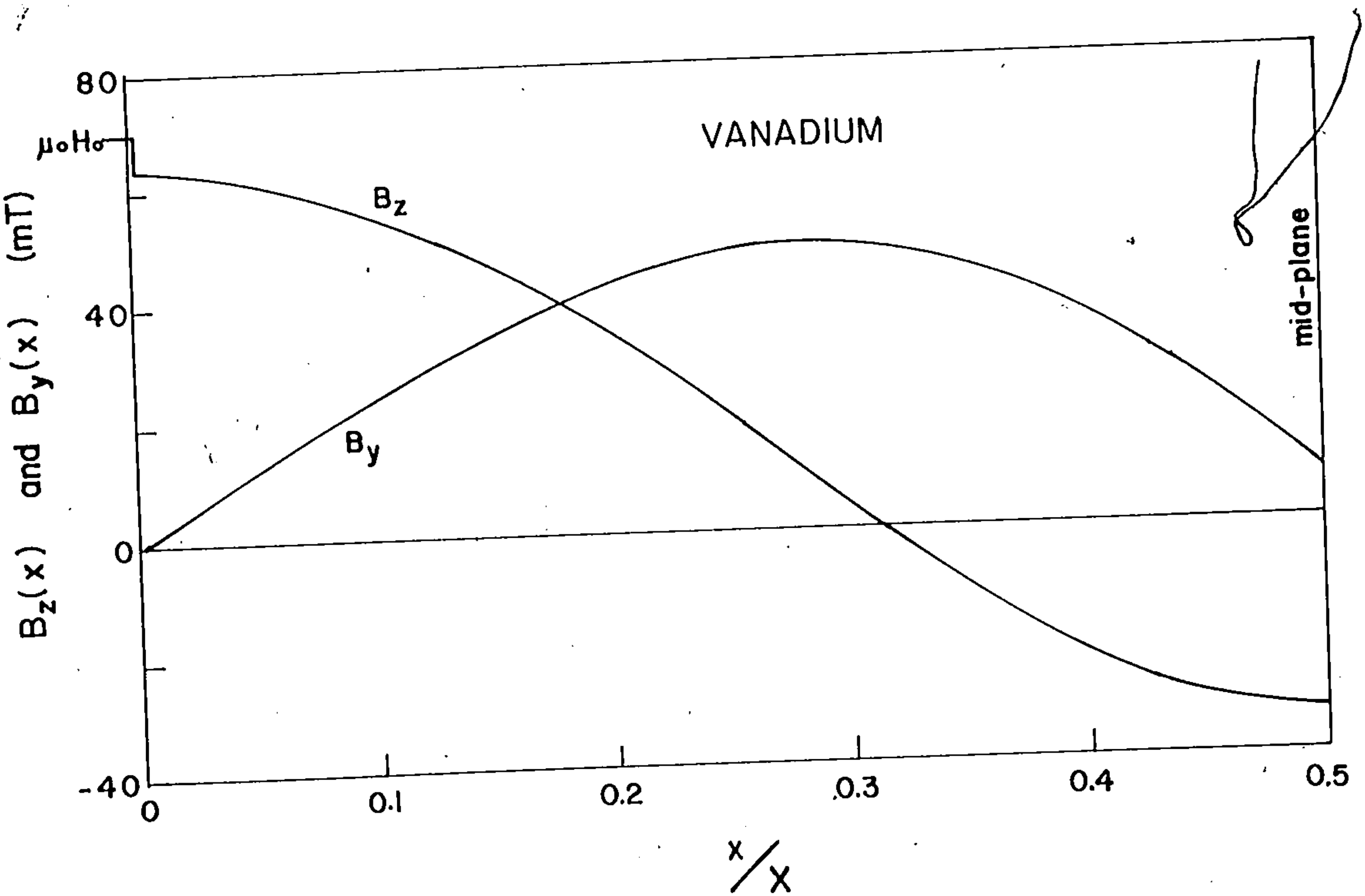


Figure 5-2 Quasi-steady state field profiles $B_z(x)$ and $B_y(x)$ for the vanadium disk after cooling in a field $H_o$ = 70 mT. The value of $\beta$ = 1 and $\gamma$ = 95 rad/T as well as the $j_c'$ and $I_R(H_o)$ from chapter 3, were used for computing the field profiles.

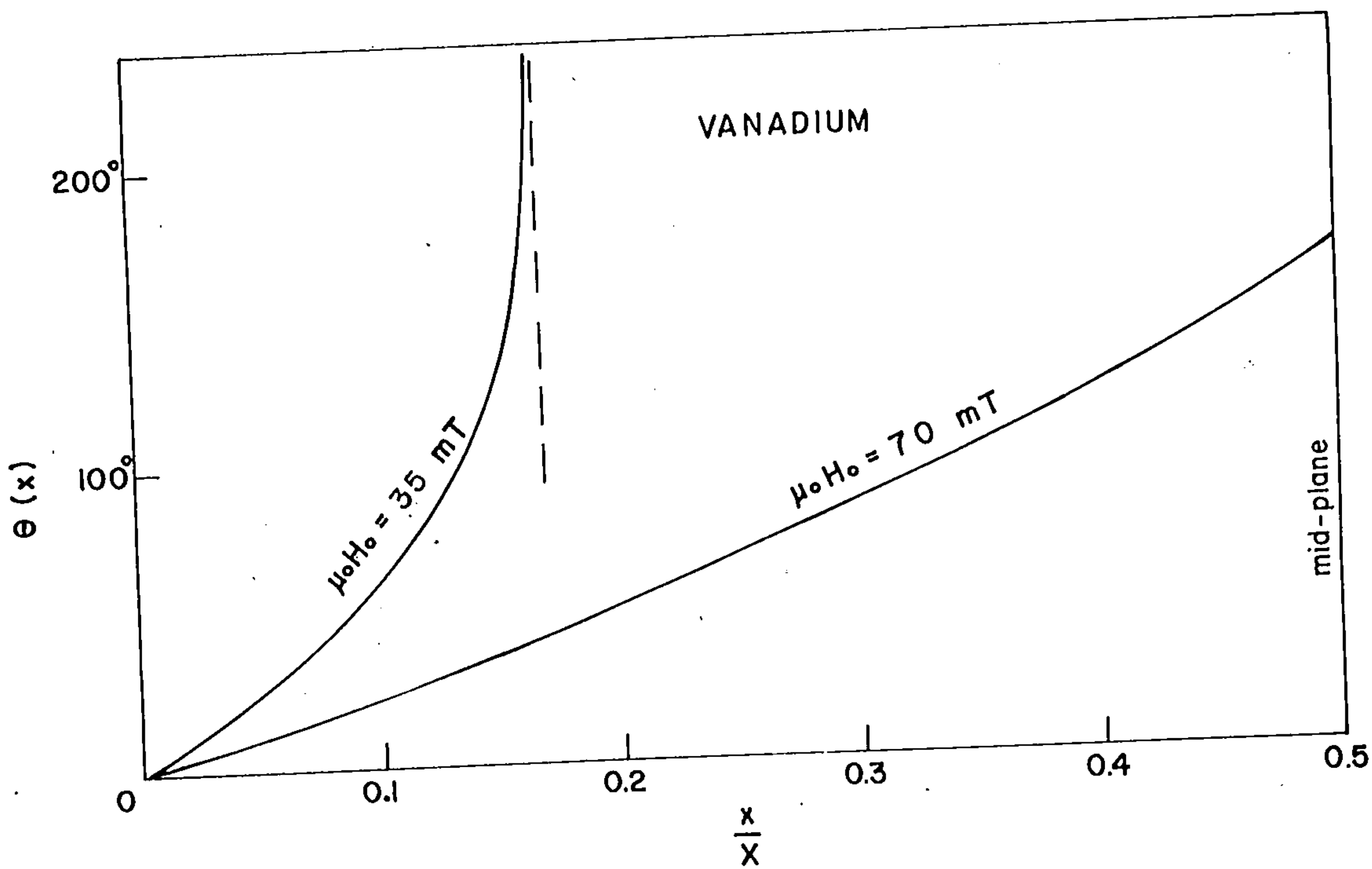


Figure 5-3 $\theta(x)$ for the two previous Figures

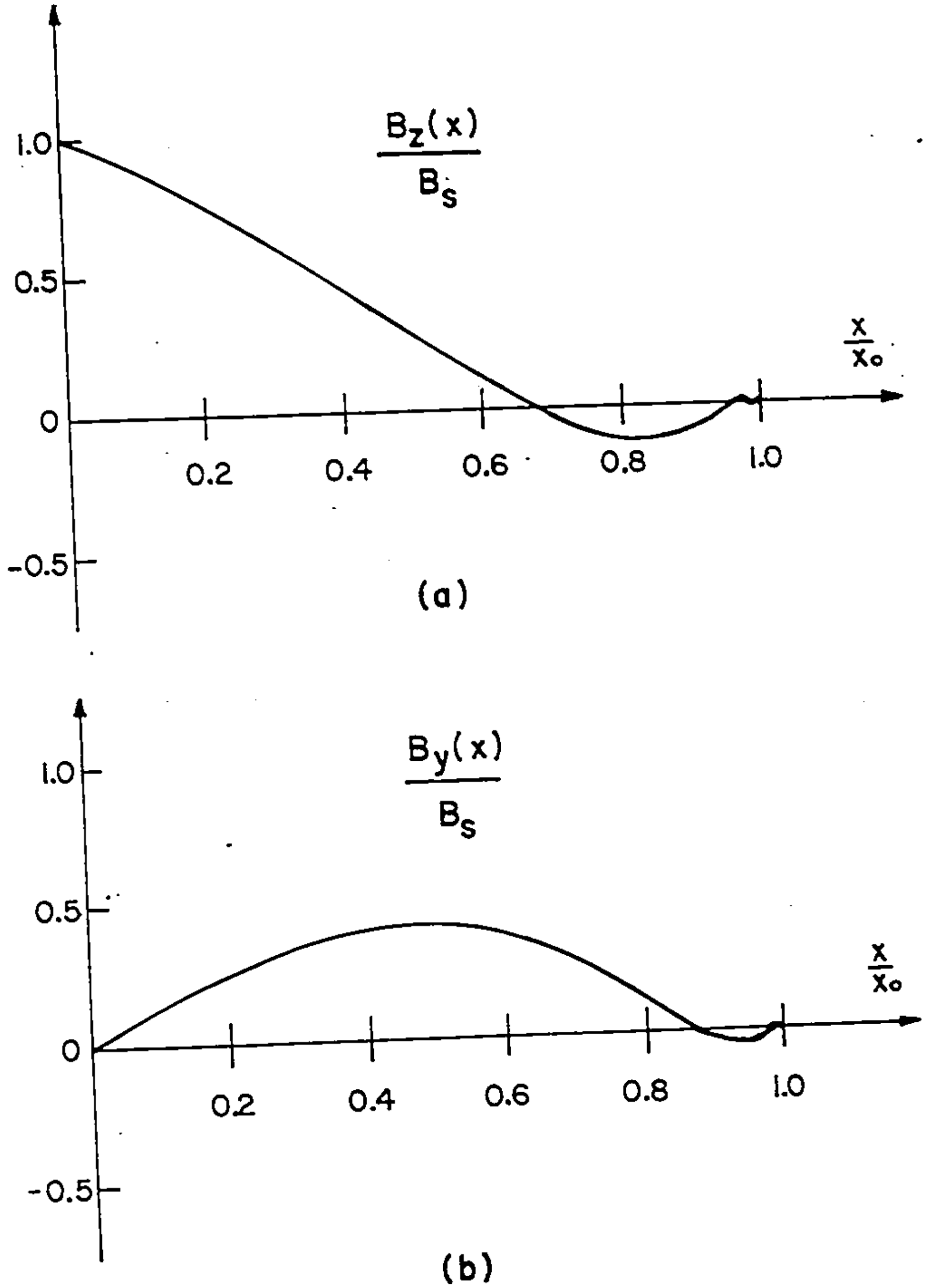


Figure 5-4 Quasi-static field profiles $B_z(x)$ and $B_y(x)$ in the active region as calculated with Bean's model. $B_z(x)$ and $B_y(x)$ are normalized with respect to the field $B_s$ at the surface.

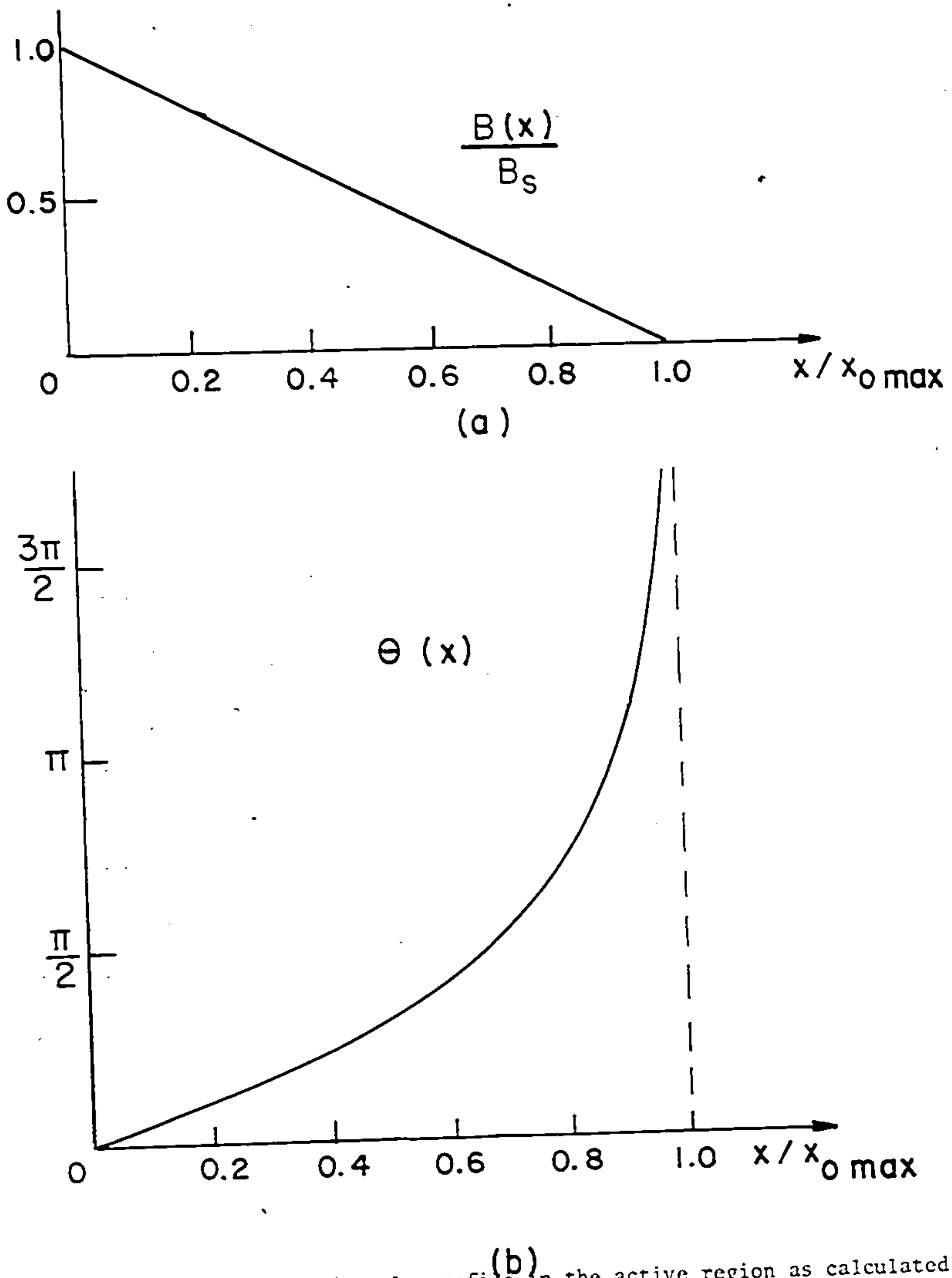


Figure 5-5 Field and angle profile in the active region as calculated with Bean's model. B(x) is normalized with respect to $B_s$, the field at the surface.

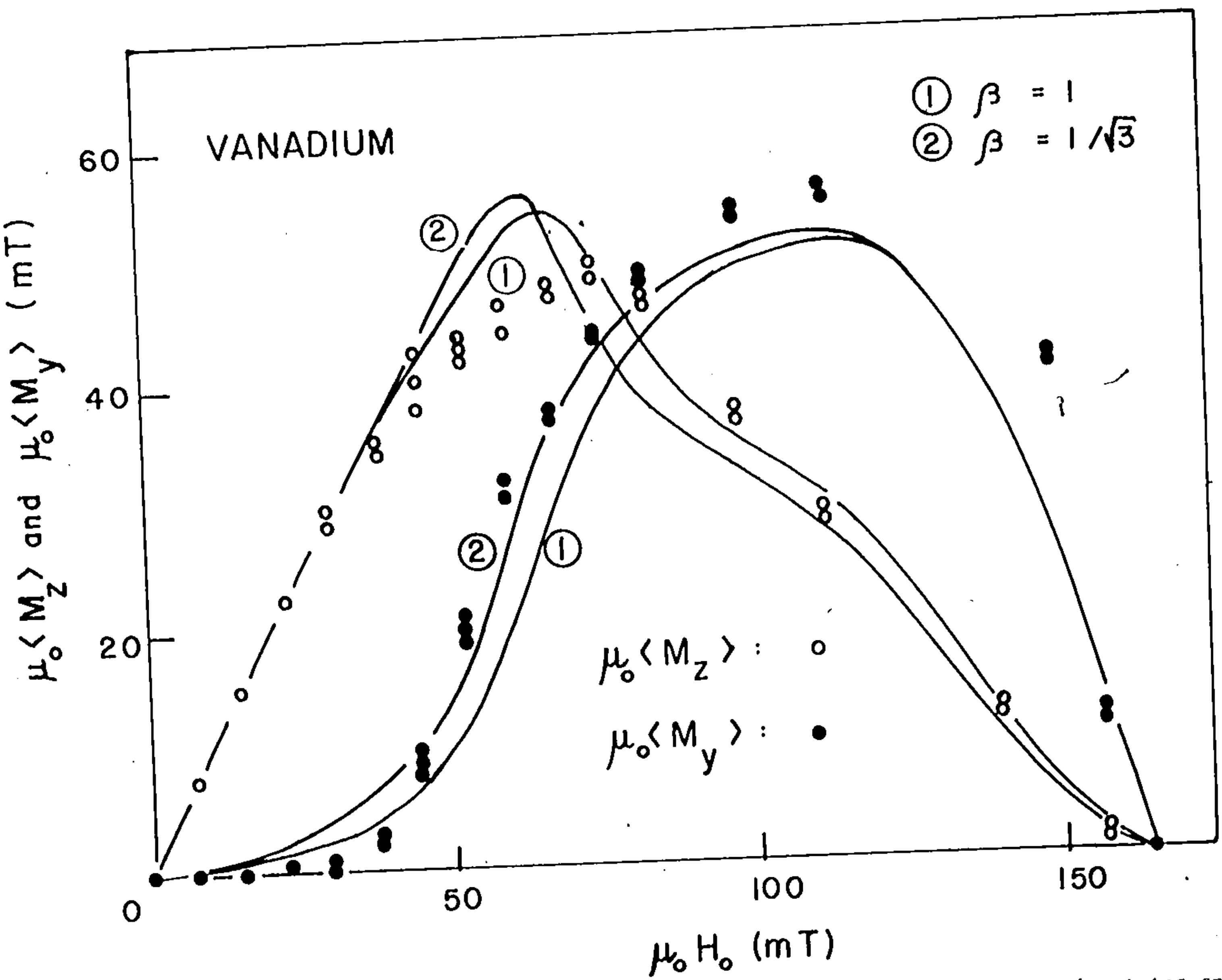


Figure 5-6 $\langle M_z \rangle$ and $\langle M_y \rangle$ vs $H_o$. Experimental data for different initial magnetic states and calculated curves for $\beta = 1$ and $\beta = 1/\sqrt{3}$; $\gamma$ is taken as 95 rad/T.

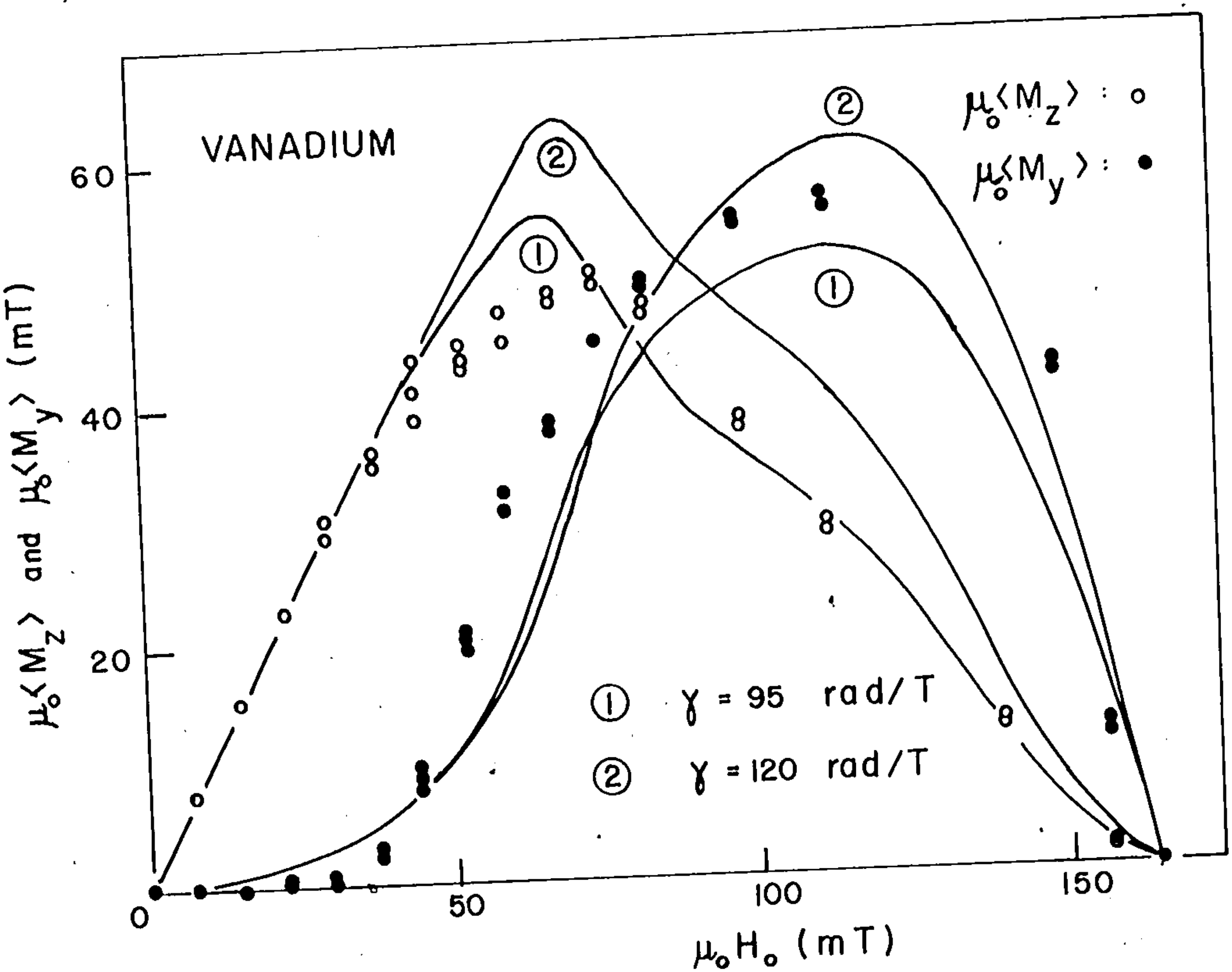


Figure 5-7 $\langle M_z\rangle$ and $\langle M_y\rangle$ vs $H_o$. - Experimental data for different initial magnetic states and calculated curves for $\gamma$ = 95 and 120 rad/T; $\beta$ = 1.

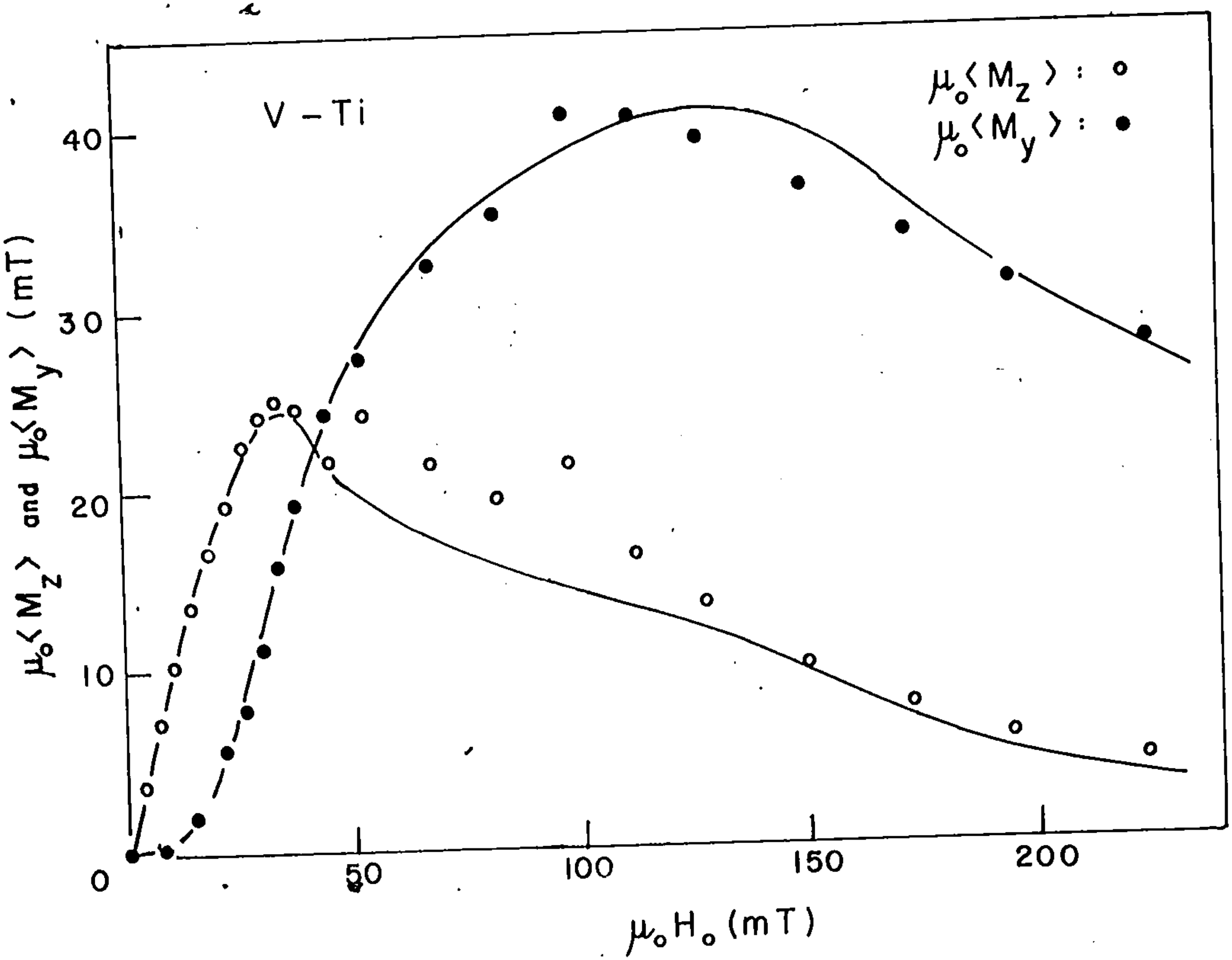


Figure 5-8 $\langle M_z\rangle$ and $\langle M_y\rangle$ vs $H_o$ for the V-Ti disk. Experimental data and calculated curves for $\beta = 1$ and $\gamma = 120$ rad/T

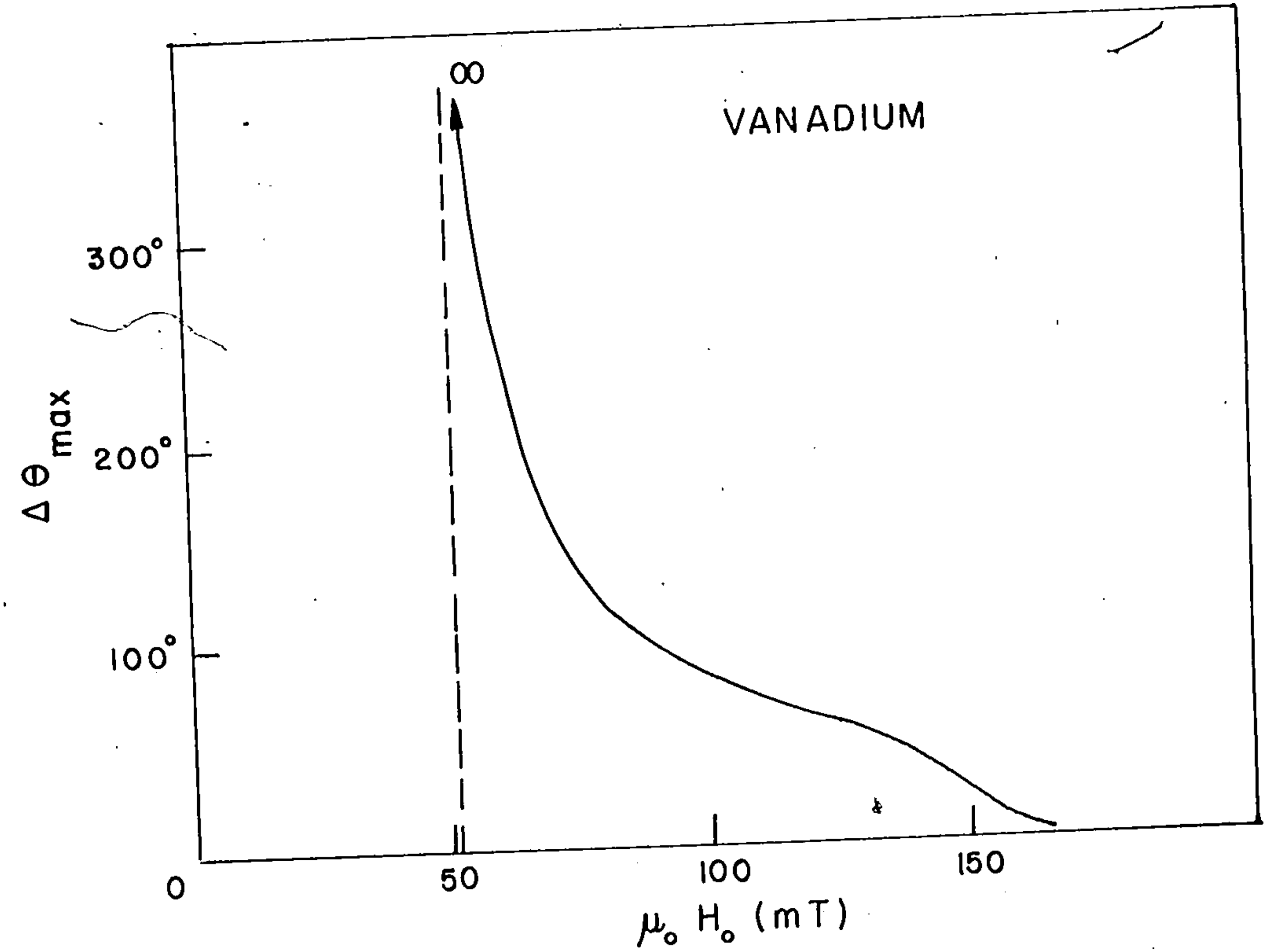


Figure 5-9 $\Delta\theta_{max}$ vs $H_o$ for the vanadium disk

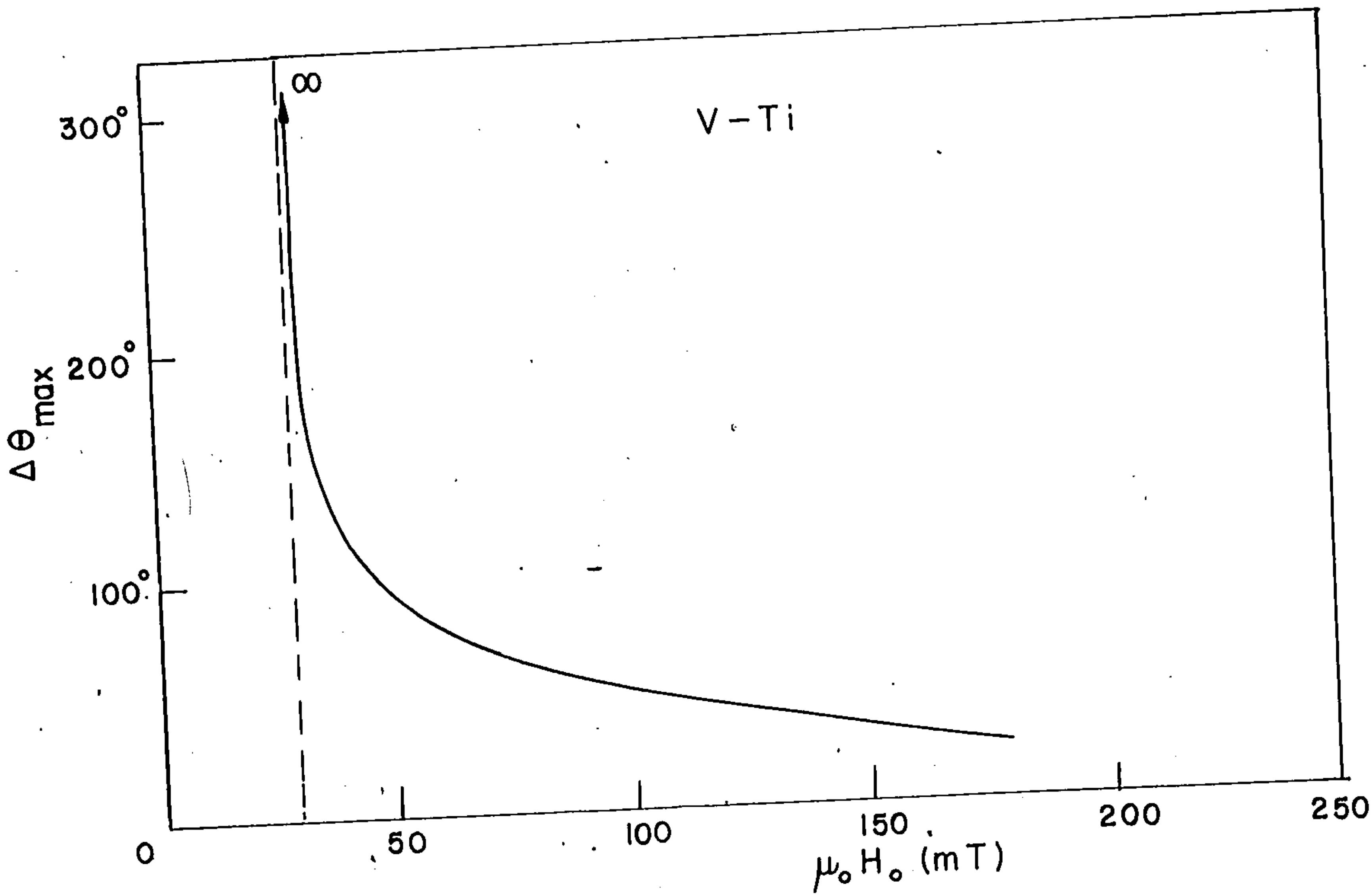


Figure 5-10 $\Delta\theta_{max}$ vs $H_o$ for the V-Ti disk.

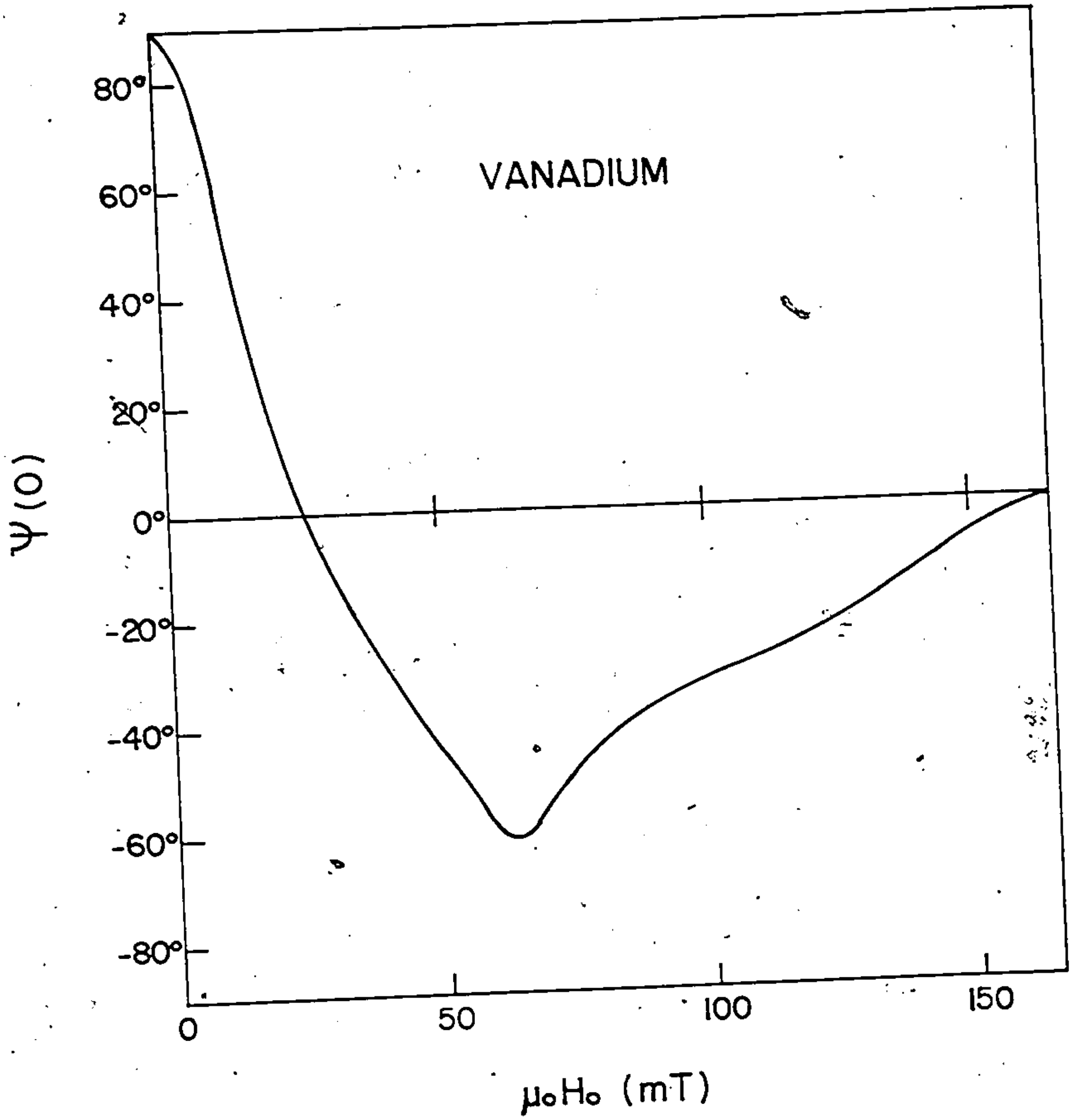


Figure 5-11 $\psi(0)$ vs $H_o$ for the vanadium sample.

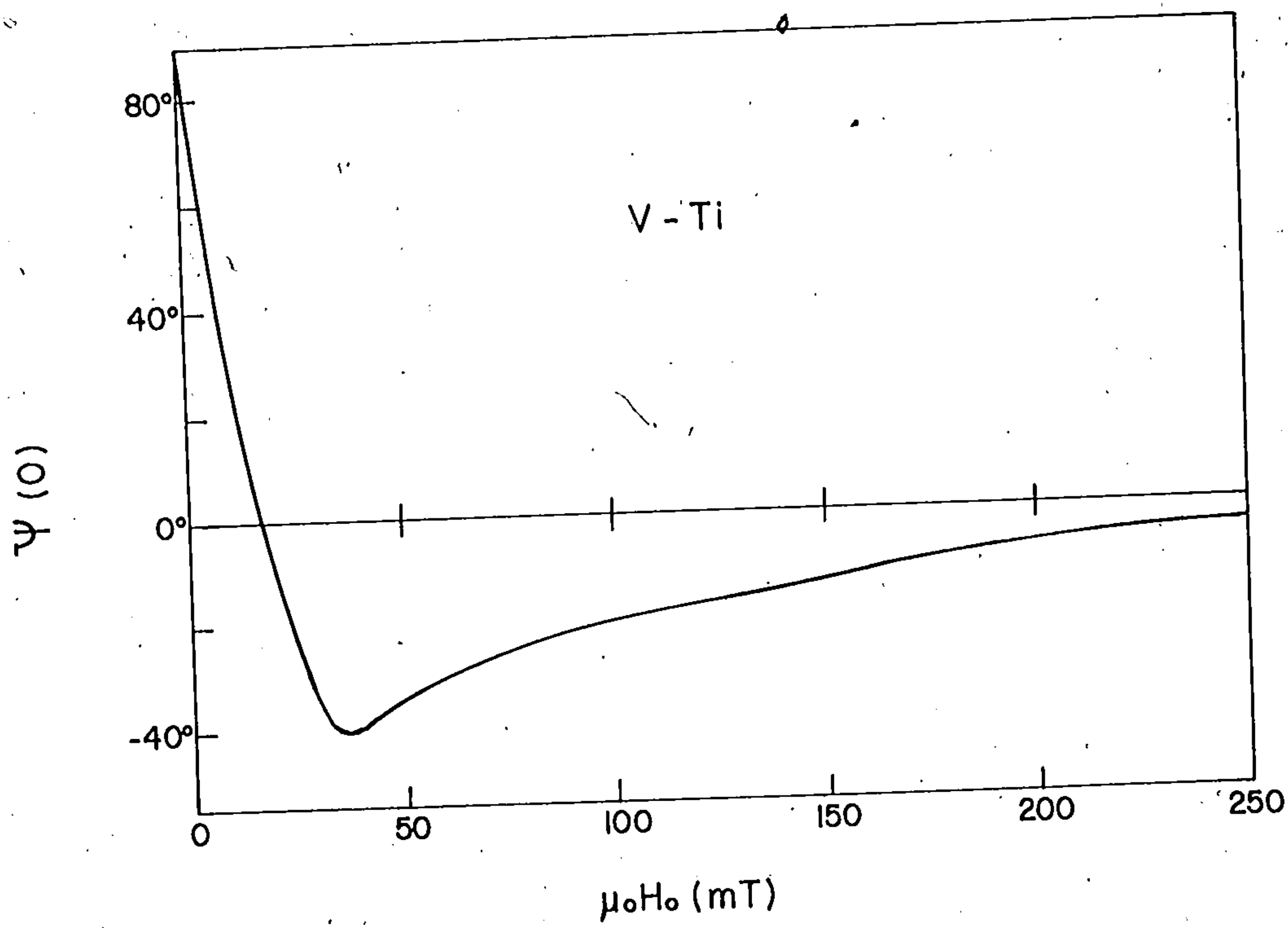


Figure 5-12 $\psi(0)$ vs $H_o$ for the VTi sample.

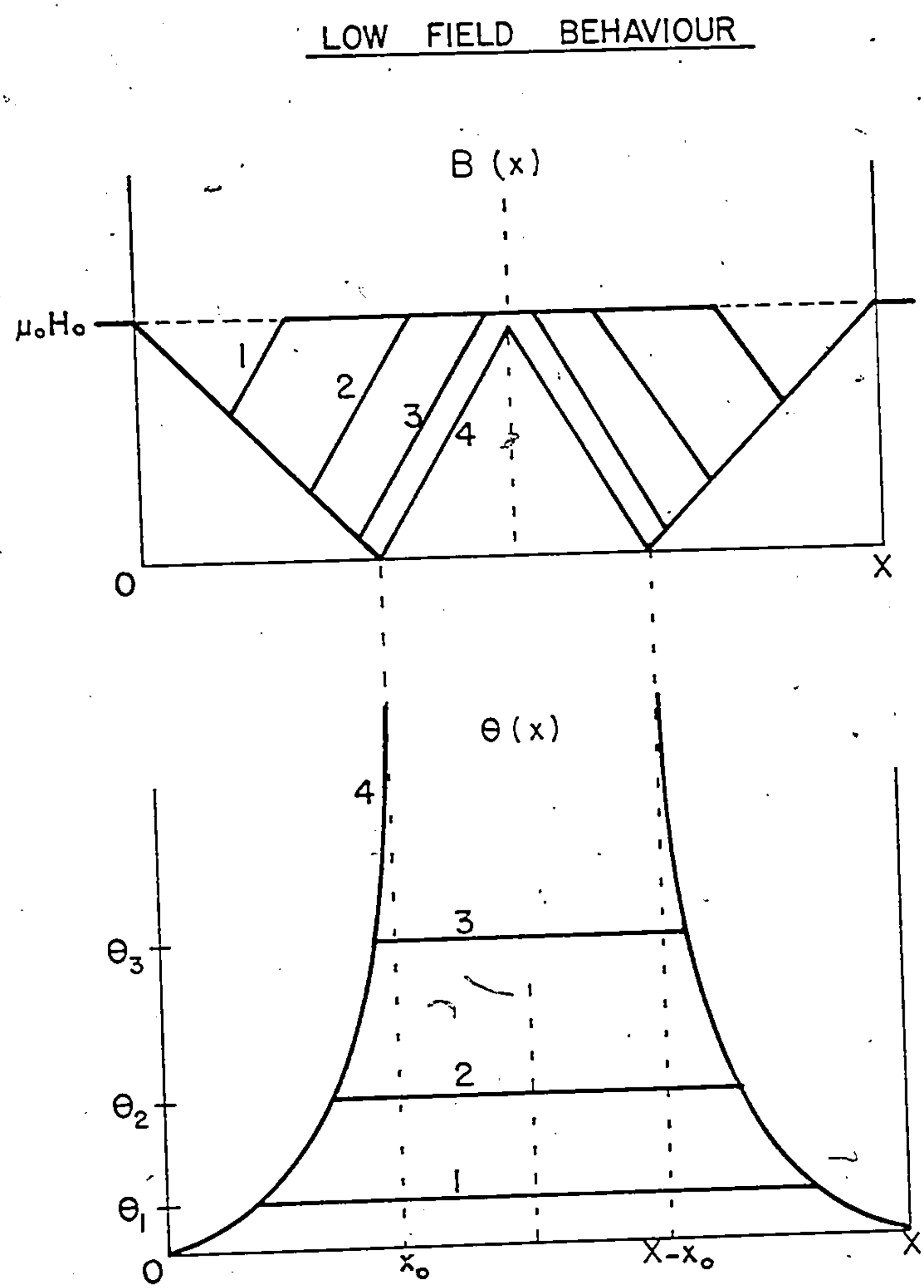


Figure 5-13 Idealised field and angle profiles inside the disk for successive increasing angles of rotation labelled from 1 to 4 ($\theta_4 = \infty$). The applied $H_o$ field is lower than H** and the disk was initially cooled in $H_o$.

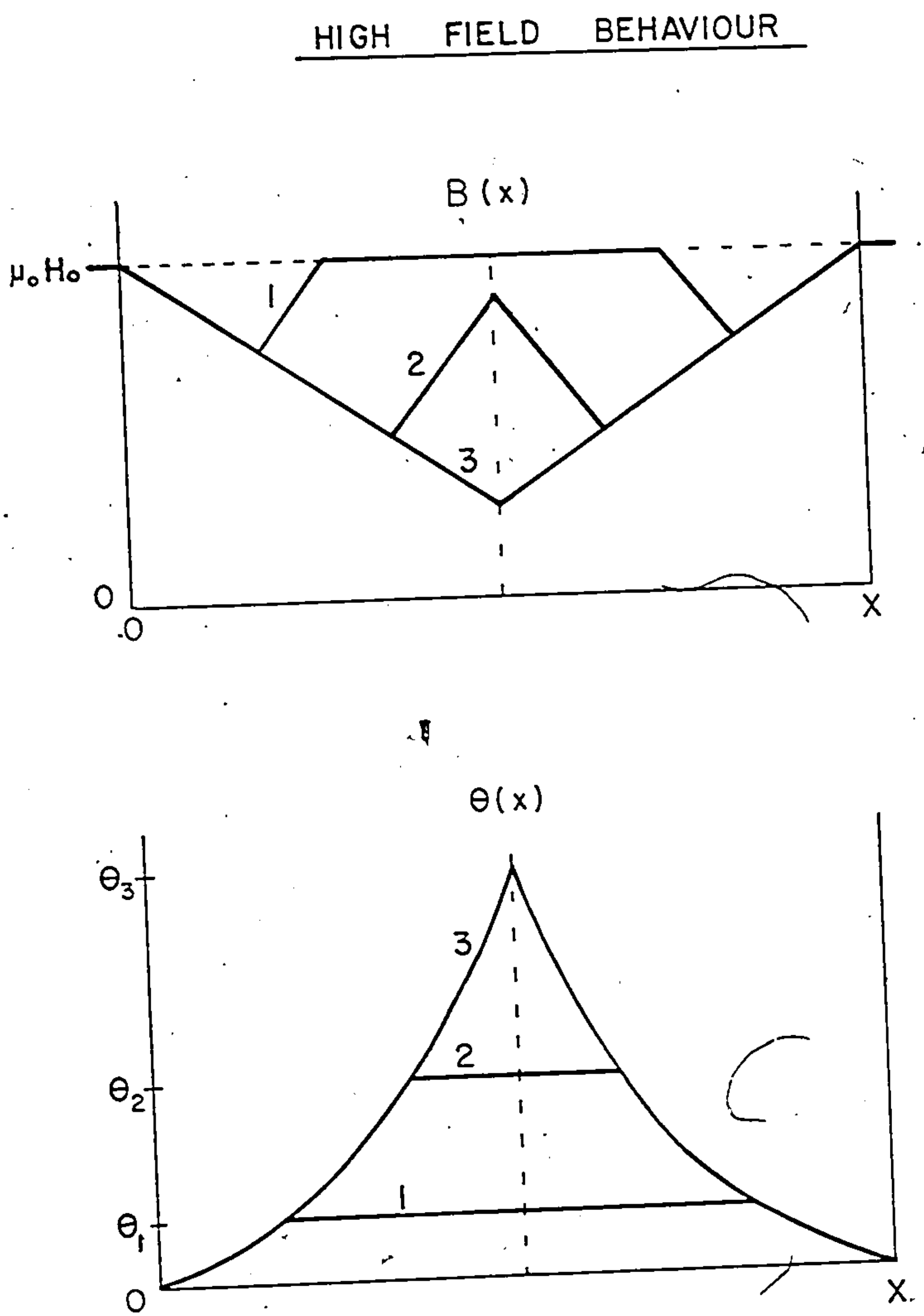


Figure 5-14 Same as in Figure 5-13 except that $H_o > H^{**}$

## Summary and Conclusion

### Part I

The magnetic behaviour of disks of V and VTi rotating slowly or incrementally in a static magnetic field $H_o$ directed perpendicularly to the axis of rotation and along the flat faces of the disks has been investigated. The components of the average magnetic induction $\langle B_z \rangle$ and $\langle B_y \rangle$, parallel and perpendicular to $H_o$, are monitored continuously with two orthogonal pick-up coils embracing the disk. The evolution of the magnetic moment tothe quasi-steady state and thereafter is followed as a function of the angle of rotation $\theta$ of the disk. The results are independent of the rate of rotation and effects due to viscous drag of the vortices can be ignored.

The magnetic response of the disks at rest has also been measured as $H_o$ is slowly increased from 0 to $H_{c2}$ and subsequently cycled between $+H_{c2}$ and $-H_{c2}$. The expulsion of flux as the disks cool from $T_c$ to 4.2 K in various static $H_o$ has also been determined. From these data information is extracted on the variation with B of $j_c'(B) = (dB/dx)_c$, the magnitude of the gradient of the critical B profile and on the dependence on $H_o$ of the surface step $I_R$ and $I_R'$ operating as flux leaves or enters the samples. This information is of intrinsic interest and is necessary for a quantitative analysis of the behaviour of the disks under rotation.

A simple but crucial picture is proposed for the sequence of configurations and the final quasi-steady state configuration of the B profiles as the disk is subjected to rotation. With this picture it is then possible to predict the residual amount of flux $\theta_t'$ remaining in the vicinity of the mid plane of the disk and rotating in step with it as a function of $H_o$ and starting with different basic initial magnetic configurations. This model is pursued quantitatively using (i) simple analytical approximations for $j'_c$ and the surface steps and (ii) the detailed data for $j'_c(B)$ and the surface steps obtained from earlier analysis of the standard magnetization curves and the flux expulsion data. The picture proposed is novel and of basic significance. It is visualized that trapped flux is expelled against the field gradient as the disk undergoes rotation to the quasi-steady state. This flux expulsion phenomenon is independent of the rate of rotation but is determined by the specific sequence of critical state B profiles proposed.

It is also examined whether the gradients of the B profile in the region where the orientation of the magnetic induction $\vec{B}(x)$ varies with distance into the disk differs from the gradients encountered in the critical state of unidirectional (non-rotational) configurations of $\vec{B}(x)$. Such a proposal was originally put forward by Bean. Following this author the region where $\vec{B}(x)$ changes direction with depth is referred to as the active region or shoulders of the B profile. This feature is measured by a parameter $\beta$. Bean found $\beta = 1/\sqrt{3}$ from a theoretical analysis using the crude approximation that $j'_c$ is a constant independent of B, taking the permeability $\mu = \mu_o$ and ignoring any surface step. The analysis of the experimental observations indicates that the gradient of B is essentially unchanged in the rotational configuration and $\beta \cong 1$.

The simple empirical rule $d\theta/dx = \pm \mu_o \gamma j'_c$, where $\gamma$ is an adjustable parameter of the material is proposed to describe the rotation of the magnetic induction with depth in the active region. Pursuing this prescription quantitatively and using the data for $j'_c$ (B), $<B_z>$ and $<B_y>$

are computed in the shoulders of the B profile, in the quasi-steady state as a function of $H_o$, and then these results are compared with the observations. The agreement is most satisfactory. This indicates that the proposed model can account quite well for the dissipation of energy in a slowly rotating disk. In order to develop this aspect it is derived, from first principles, general expressions for the energy dissipation applicable to the case of a slowly rotating disk.

It is noticed, however, that the configurations which ensue from this model do not satisfy the condition, $\vec{E} \times \vec{J} = 0$, that the electric field $\vec{E}$ generated when the disk rotates lie along the current density $\vec{J}$. To explore this aspect, general expressions for $\psi = \sin^{-1}(|\vec{E} \times \vec{J}|)/EJ)$ are derived from first principles. These expressions can serve as useful tools in improving on the initial simple choice for $d\theta/dx$.

Finally the model is applied to computations of the evolution of the components of the magnetic moment with $\theta$ (or time) starting from different initial states and in various $H_o$. These curves reproduce the experimental observations quite adequately.

# PART II

# LONGITUDINAL VELOCITY OF FLUX JUMPS IN AXIALLY MAGNETIZED TYPE II SUPERCONDUCTING WIRES CARRYING CURRENT

# CHAPTER 6

## Introduction

It is frequently observed that the magnetic moment of irreversible type II superconductors is unstable. A thermal or electromagnetic perturbation can then cause the pattern of persistent electric currents to decay and the associated configuration of magnetic induction to collapse. Such abrupt changes in the magnetic moment are referred to as flux jumps or flux avalanches. Depending on many physical quantities, the collapse can be partial or complete. The latter extreme case is called a full or catastrophic flux jump. If the collapse is total, the entire sample is driven into the normal state.

The criteria which determine whether a flux avalanche will occur and whether the avalanche will be partial or total have been examined by several workers (Wipf 67, Swartz 68). Several physical quantities enter into the picture: in particular the stored magnetic energy and hence the critical current density, the normal and flux flow resistivities, the heat capacity and the thermal conductivity (which limits heat flow inside the specimen and to the surrounding). The situation is extremely complicated since in a type II superconductor, the critical current density, the flux flow resistivity, the heat capacity and the thermal conductivity all depend on the local magnetic induction $B/H_{c2}$ and on the temperature $T/T_c$. Clearly, the problem is considerably simplified if the phenomenon can be considered as adiabatic, so that the energy dissipated locally does not diffuse to neighbouring regions while the event is taking place. The spatial and temporal evolution of the flux avalanche has been investigated theoretically for mathematically tractable geometries, namely, the case where the flux avalanche progresses simultaneously and symmetrically (i) over the circumference and along the length of a long cylinder magnetized along its axis, and (ii) over the surface of an infinite slab magnetized parallel to its surfaces. The main features of the phenomenon appear to be well understood under these circumstances and are quantitatively well reproduced by the calculations (Bussière 73, 75, Darby 73, Morton 73). This problem is immensely more difficult than that of the radial or transverse propagation of the normal phase in a type I superconductor investigated earlier for the same geometric arrangements (Pippard 50, Faber 53). The latter situation is not, however, a flux avalanche problem. The velocity of propagation of the normal front along a wire of a type II superconductor carrying a steady transport current I has also been investigated experimentally and theoretically (Whetstone 65, Overton 71). These studies have focused on the special case where the wire is immersed in a static longitudinal magnetic field but is <u>not</u> magnetized. As a consequence, the phenomenon of flux avalanching is not involved in these investigations. When I is near $I_c$, the azimuthal configuration of the magnetic induction (the $B_\theta$ profile associated with the conduction current) can become unstable and flux jumps can occur. Also it has been observed that under these circumstances, the conduction current adopts a helical configuration and an appreciable axial magnetic moment arises, although the wire is not initially axially magnetized. Whetstone and Ross and Overton have not examined the behaviour in this range of high currents. Further note that in their analysis, the normal-superconducting interface is visualized as a transverse plane and the resistivity is taken to be $\rho_n$ on the normal side and zero on the superconducting side. The latter stipulation is applicable since the wire is heated into the normal state at one end in order to initiate the advance of a normal region. The problem investigated by Whetstone and Roos is then essentially similar to that studied earlier by several workers, in which the specimen was a wire or a ribbon of a type I superconductor carrying a steady transport current (Cherry 60, Broom 60).

The velocity of propagation of a flux jump along a wire of a type II superconductor initially axially magnetized and immersed in a longitudinal applied magnetic field was first investigated by Walker and Hulm (Walker 66, 72). No conduction current was fed along the wire in their work. They noted that the stored magnetic energy associated with the axial magnetic moment played an important role in determining the velocity but they did not pursue this aspect in quantitative detail. Bussiere (Bussiere 72a, 72b) extended this work and studied the velocity of propagation of flux jumps along axially magnetized wires of various materials (NbTi, NbZr and Nb) with and without a transport current flowing along the specimen. He noted that, in special circumstances, the flux jump advanced helically rather than longitudinally. This work has been extended and the dependence of the velocity of propagation of the flux jump on various important quantities, namely, $I/I_c$, $H/H_{c2}$ and the initial state of axial magnetization of the wire (its magnitude and "polarity"), has been examined in some detail. Further, the occurrence of the helical mode of propagation has been monitored throughout and the dependence of the pitch of the helix on the quantities just enumerated has been measured. In this part of the thesis a report is given of these extensive measurements. The role played by the magnetic energy associated with the azimuthal and axial configuration of the magnetic induction in determining the velocity is also evaluated. This introduction is concluded by a mention of the fact that the velocity of propagation of flux jumps has also been investigated in transversely magnetized wires of type II superconductors immersed in a transverse magnetic field and carrying a steady conduction current (Iwasa 68, Walker 65, LeBlanc 64). In this situation, it is observed that under certain circumstances the final magnetic state of the wire in the wake of the flux jump, consists of a periodic structure of elongated macroscopic vortices. The macrovortices occupy the diameter of the wire laterally and are of larger dimension along the length of the wire (Iwasa 68). The appearance of these macroscopic entities is indeed a fascinating phenomenon.

Finally the visual observations of the dynamics of flux jumps pursued by De Sorbo (De Sorbo 64), Wertheimer and Gilchrist (Wertheimer 67) and by the group at the Royal Military College in Kingston (Harrison 73) on disks of type I and type II superconductors in transverse magnetic fields should be mentioned.

# CHAPTER 7

## Experimental Arrangement And Magnetization Curves

### 7.1 Introduction

The velocity of propagation of flux jumps along wires of Niobium and Vanadium axially magnetized in a longitudinal magnetic field has been investigated. The flux jump is triggered by applying a heat pulse at one end of the wire. The velocity of propagation of the flux jump is measured in several longitudinal magnetic fields $H_o$ for a variety of initial magnetic moments of "negative" and "positive" polarity and as a function of a steady transport current I varying from 0 to $I_c$, the critical or limiting value. The occurrence of a helical mode of propagation of the flux avalanches has also been monitored with a saddle coil embracing the wire. The angle $\phi$ of advance of the flux disturbance with respect to the axis of the wire is determined. The standard magnetization curves of the wires are also reported and a pinning function $F_p(B)$ is extracted from these data.

### 7.2 Experimental Arrangement and Procedures

The samples consist of "as received" wires of high purity Niobium and Vanadium, unannealed after the final stages of cold rolling. Table 7-1 presents pertinent data on the samples. $H_{c2}$ at 4.2 K is estimated from the standard magnetization curves (Figures 7-3 and 7-6). No reliable estimate of $H_{c1}$ can be extracted from these magnetization curves. Consequently no attempt has been made to evaluate the Ginzburg-Landau parameter $\kappa$ for these samples.

A non-inductive (bifilar) single layer heater of number 38 manganin wire is wound directly over the central section (approximately 11 cm in length) of each wire.

Two ten-turn pick-up coils made from #38 copper wire are wound around the sample wire and connected in series. These two pick-up coils are placed at a carefully measured distance from each other along the middle section of the wire sample. These are referred to as the axial coils. A saddle-shaped pick-up coil of three turns embraces the diameter of the sample wire over the length between the two pick-up coils just mentioned, and is series-connected with the latter. (See Figure 7-1 (a) ). Actually the two pick-up coils (the axial coils) and the saddle-shaped coil constitute a single unit and are wound continuously from one length of copper wire.

The role of the axial and saddle coils is the following: the two axial pick-up coils measure $V_z$, the longitudinal velocity of propagation of the flux avalanche. When the axial flux collapse reaches the first axial coil at time $t_1$, a voltage pulse is observed on the oscilloscope screen. Later at time $t_2$, when the disturbance has progressed to the second axial coil, another pulse, displaced from the first, appears on the oscilloscope screen. The time sweep $t = t_2 - t_1$ of the oscilloscope and the carefully measured distance d between the midplane of the two axial coils measures $V_z = d/t$. In auxiliary measurements with 3 and 4 axial coils Bussiere and the present author have verified that the disturbances advance without acceleration or deceleration along the wire, except in special cases which will be examined in Chapter 9.

The saddle-shaped coil can detect special types of asymmetry in the propagating flux avalanche. In particular, a periodic signal from the

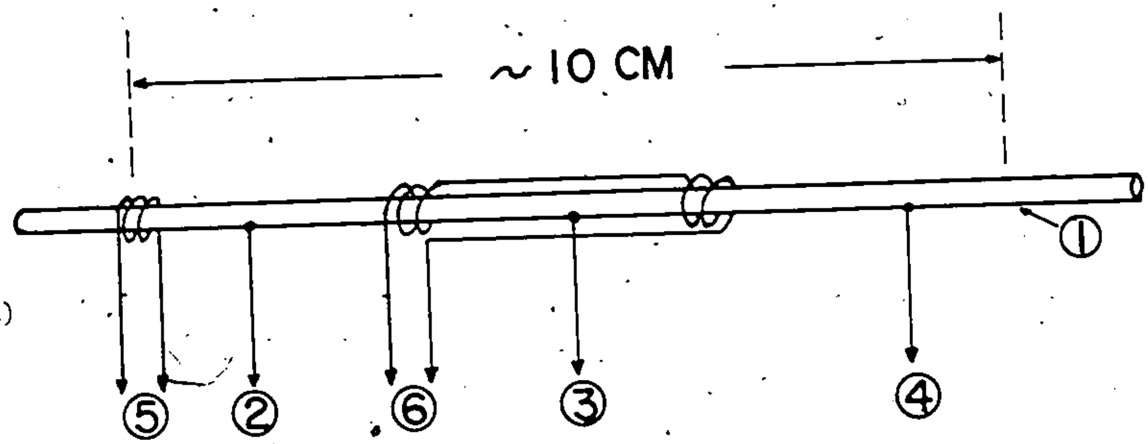


a)

1- superconducting wire
2, 3, 4- voltage probes
5- small heater to trigger the flux jumps
6- axial and saddle coils

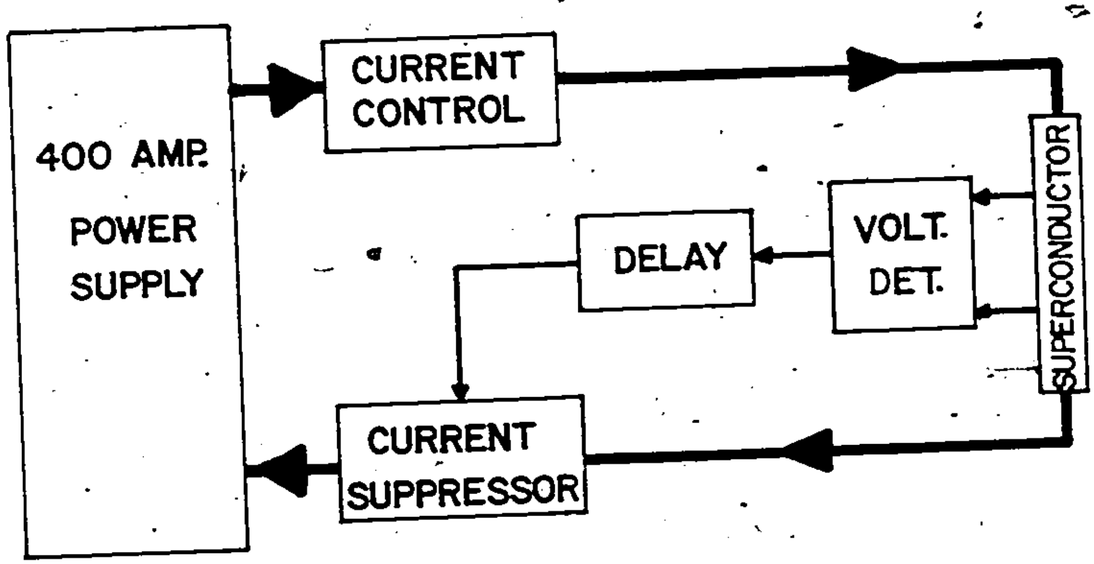


b)

Figure 7-1 a) Sample assembly, b) Current-controlling network saddle coil as the event progresses between the two axial coils provides unambiguous evidence that the flux collapse is not only cylindrically asymmetric but that this asymmetry is rotating as the disturbance advances. (See Fig. 10-1.) The number N of these periodic signals as the disturbance progresses from one axial pick-up coil to the other can readily be counted. This yields a direct measure of $V_\theta$, the azimuthal velocity of the advancing disturbance at the surface of the wire, since $V_\theta = 2\pi RN/t = 2\pi Rf$ where R is the radius of the wire. The signal from the saddle coil will be examined in more detail in chapter 10 where the data on the variation of $\phi = \tan^{-1} V_\theta/V_z$ with $H_o$, $I/I_c$ and initial magnetic moment will be presented.

Several voltage probes are spot-welded to the sample wire along its length (see Figure 7-1 (a)). The distance between these contact points is carefully measured. The signal from these voltage (resistance) probes can be used to monitor the velocity of propagation of the flux jumps when a steady current is flowing in the sample. They are needed for this purpose when the sample is not axially magnetized.

The sample assembly (wire specimen, heater, pick-up coils and voltage leads) is placed inside a glass tube and the empty space filled with epoxy. This ensures that the wire is rigidly held in place and the thermal insulation provided by the epoxy and the glass tube reduces the heat required to control the temperature of the wire specimen and to raise it above $T_c$.

The conduction current is fed into the superconducting wire via massive copper blocks tightly clamped around its ends (see Fig. 7-2). The contact resistance between the superconducting wire and the copper blocks is less than or of order 1 micro-ohm. To achieve this low contact

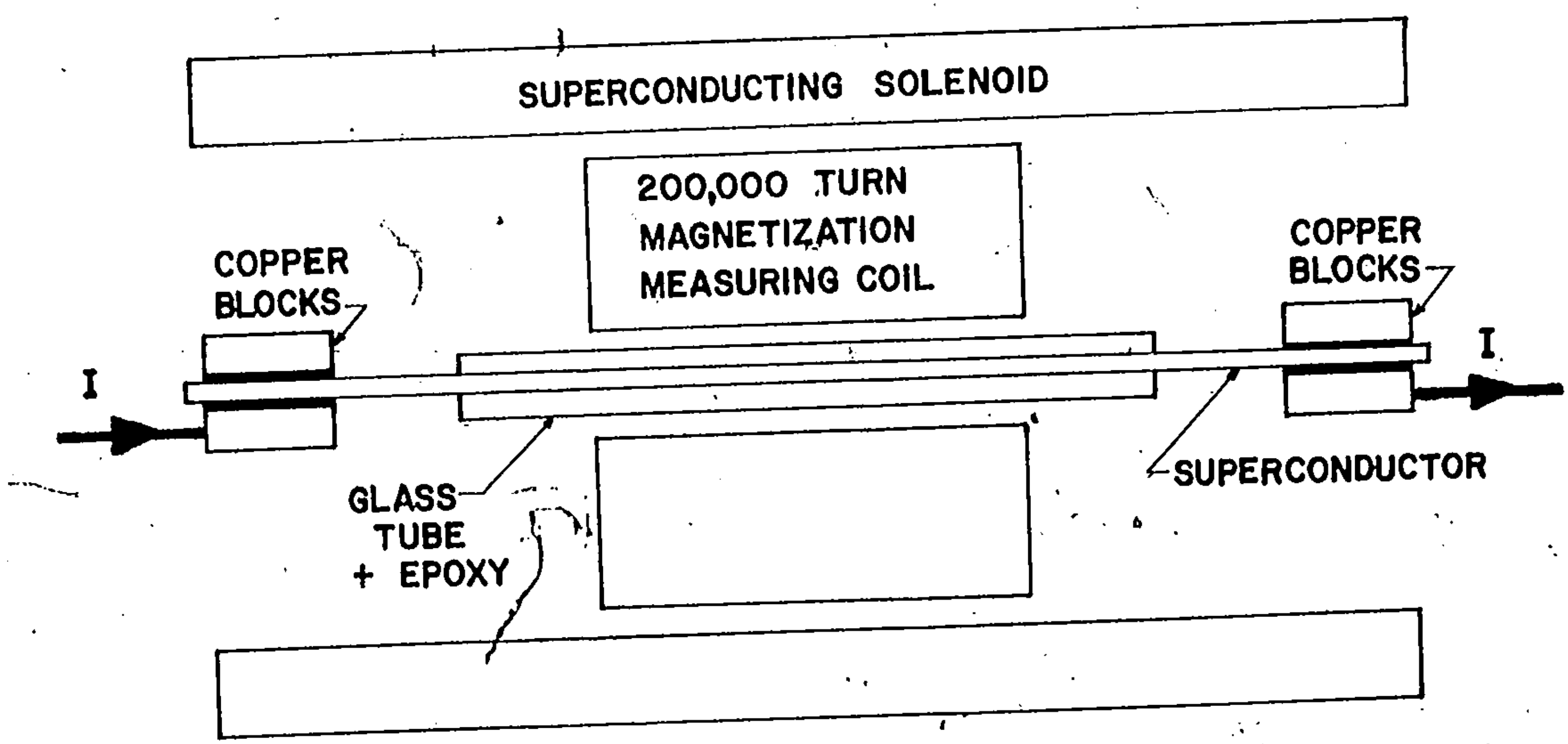


Figure 7-2 Schematic diagram of the experimental arrangement, showing the superconducting solenoid enclosing the sample and the magnetization pick-up coil.

resistance indium foil is wrapped around the freshly cleaned ends of the sample before clamping them between the copper blocks.

A transistorized power supply fed by several large 6-volt batteries in parallel delivers a steady and ripple-free current I which can be varied continuously and smoothly from 0 to about 400 A. Two voltage probes straddling the sample between the copper blocks feed an electronic amplifier-relay unit which shuts off the current flow through the sample within 100 microseconds whenever a voltage exceeding 3 millivolts is detected. A delay circuit is also coupled to this unit to delay the current cut-off suitably. This provision is used to allow slow-moving flux jumps to traverse the distance between the axial coils before interrupting the current flow. A schematic diagram of the current-controlling network is presented in Fig. 7-1 (b).

The flux jumps are observed with a dual beam oscilloscope. One beam displays the signal from the pick-up coil unit (axial coils and saddle coil in series) as a function of time. The second beam monitors the transport current I flowing in the sample as the flux jump progresses along the superconducting wire. A signal propostional to I is obtained from a shunt in the current circuit. Since the power supply is not a constant current source, I decreases by 10 to 20% as the resistive region which the flux jump leaves in its wake propagates along the wire. A camera attachment using Polaroid films is used to record the oscilloscope traces. Typical photographs are reproduced in Figures 10-7 through 10-10 of Chapter 10.

The flux jump is triggered by applying a heat pulse to one of the two small heaters embracing the wire sample near the edges of its glass enclosure. The magnitude of the heat pulse and its duration (a few microseconds) are adjusted to ensure that triggering of the avalanche occurs but the required threshold perturbation is not appreciably exceeded.

The magnetization of the portion of the sample wire inside the glass enclosure (and thus inside the long heater) is measured with a large 200,000 turn pick-up coil which embraces it. The dimensions of this main pick-up coil are: 6.0 cm length, 2.0 cm outer diameter and 0.5 cm. inner diameter. This pick-up coil is "self-balanced" in the following manner. The direction of the windings is reversed at an intermediate and pre-determined diameter. The number of turns in the outer section of this continuous pick-up coil has been incrementally adjusted until the net signal produced by the total coil is negligible as $H_o$ is varied with the sample in the normal state or absent. Thus with the sample in place and in the superconducting state, a signal proportional to its magnetization $\langle M \rangle = \langle B \rangle/\mu_o - H_o$ is recorded on the Y axis of an X-Y recorder as $H_o$ is varied. The signal from the pick-up coil is fed into an electronic amplifier-integrator which drives the Y axis of the recorder. A signal proportional to $H_o$ drives the X-axis. After the flux jump has taken place a determination of whether any magnetization still survives in the sample is made by raising its temperature to $T_c$. The expulsion of flux from the sample is also monitored as it cools from $T_c$ to 4.2 K (or entry of flux as it is heated from 4.2 K to $T_c$). As is standard procedure, the calibration is made on the basis that $\langle B \rangle = 0$ when a small field $H_o$ is applied to a virgin sample.

A superconducting solenoid wound with NbTi wire and capable of producing a magnetic field of 3.5 tesla provides the externally-applied longitudinal magnetic field $H_o$. This solenoid is 17 cm long with inner and outer diameters of 3.8 cm and 7.5 cm. The longitudinal field $H_o$ is uniform within about ± 2% over the central 8 cm length of the sample.

Table 7-1

| Sample | Diameter (mm) | $\mu_o H_{c2}$ (tesla) | $\alpha_o$ (amp/m$^2$) | $\sigma$ | $b_e$ | Source |
|---|---|---|---|---|---|---|
| Vanadium | 0.75 | 0.17 | $1.0 \times 10^9$ | 12 | 0.66 | M.R.C.[1] |
| Niobium | 0.50 | 0.53 | $7.7 \times 10^9$ | 7.8 | 0.47 | F.M.C.[2] |

[1] Materials Research Corporation,

[2] Fansteel Metallurgical Corporation.

## 7.3 Standard Magnetization Curves and Critical Current

The standard magnetization curves (branches 1, 2 and 3) of the Nb and V wires are presented in Figures 7-3 and 7-6. Flux jumps made it impossible to trace the locus of the critical magnetic moment continuously as $H_o$ is raised again after an excursion to $H_{c2}$ of opposite polarity (branch 4 or the hybrid magnetization region) for both samples.

The expulsion of flux from the Nb wire as it cools from $T_c$ to 4.2 K in various static longitudinal magnetic fields is displayed in Figure 7-4. Note that the vertical scale is greatly expanded in Figure 7-4 compared to that in Figure 7-3, and that the partial Meissner (or Abrikosov) effect in this very hysteretic sample is negligible.

The dependence of the critical current $I_c$ for the Nb wire on the longitudinal applied field is presented in Figure 7-5. $I_c$ is plotted against $H_o^2$ to illustrate the parabolic dependence of $I_c$ on $H_o$:

Thus $I_c$ is well approximated by the relation

$$I_c = I_{co} \{ 1 - ( \frac{H_o}{H_{c2}} )^2 \} \qquad (7\text{-}1)$$

where $I_{co}$ = 420 A at 4.2 K. Near and beyond $H_{c2}$ the critical current does not fall to zero because of the existence of the Saint-James-De Gennes (Saint-James 63) surface sheath which persists to an upper critical field $H_{c3}$. In the present measurements, the onset of resistance is sharp and abrupt at $I_c$, the voltage of the sample jumping from less than 1 microvolt to beyond 3 millivolts when $I_c$ is attained. Note that the $I_c$ vs $H_o$ curve of this Nb wire sample is very different from the behaviour exhibited by other type II superconducting samples reported in the literature. The latter show a hump or peak in longitudinal fields.

In view of the high degree of irreversibility exhibited by these samples, it is believed that an analysis in the frame-work developed in chapter 3 is not warranted here. Bulk pinning evidently dominates all other contributions. This feature emerges from inspection of the magnetization curves and the flux expulsion measurements of our samples.

The critical state equation for an infinite cylinder in a longitudinal field $H_o$ then reduces to

$$B_z \frac{dB_z}{dr} = \pm \mu_o F_p' (B) \approx \mu_o F_p(B) \qquad (7\text{-}2)$$

where it is assumed that $\mu = B(r)/H(r) = \mu_o$ and the surface barrier $I_B = I_B' = 0$.

It has been found that the magnetization curves of these two samples as well as those of other very irreversible materials studied in this laboratory, can be well-reproduced using the following analytical expression for the critical current density:

$$J_c = \frac{F_p}{B} = \alpha_o \left\{ \frac{1}{e^{\sigma(b - b_e)} + 1} - C \right\} \qquad (7\text{-}3)$$

where the parameters $\alpha_o$, $\sigma$ and $b_e$ are characteristic of each sample. Their values are given in Table 7-1 for the two samples used in the present study. The constant C is obtained from the requirement that $J_c$ fall to zero when b, the normalized magnetic induction ($b = B/\mu_o H_{c2}$) reaches unity (i.e. surface sheath contributions are subtracted).

No special physical significance is ascribed to this expression: it is noted simply that it generates the experimental behaviour quite accurately. The dashed curves in Figures 7-5 and 7-6 show the magnetization curves obtained using this form for $J_c$ (B) and the critical state equation 7-2.

The curves for $J_c/\alpha_o$ against $B/\mu_o H_{c2}$ obtained in this manner are displayed in Figure 7-7 and the corresponding curves of $F_p/\alpha_o H_{c2}$ against $B/\mu_o H_{c2}$ in Figure 7-8. Note that at low-fields, the critical current density $J_c$ is nearly constant (Vanadium wire) or decreases slowly with B (Niobium wire). In this range then, $J_c$ exhibits behaviour associated with the Bean pinning function. At higher fields, the variation of $J_c$ is more complicated, and is mainly governed by the parameter $\sigma$ in equation 7-3. This complicated expression will not play a significant role in the quantitative analysis of the velocity of propatation of flux jumps.

The pertinent measurements on the dependence of $V_z$ and $\phi$ on $I/I_c$, $H_o/H_{c2}$ and the initial magnetic state are presented in Chapter 8 and 10.

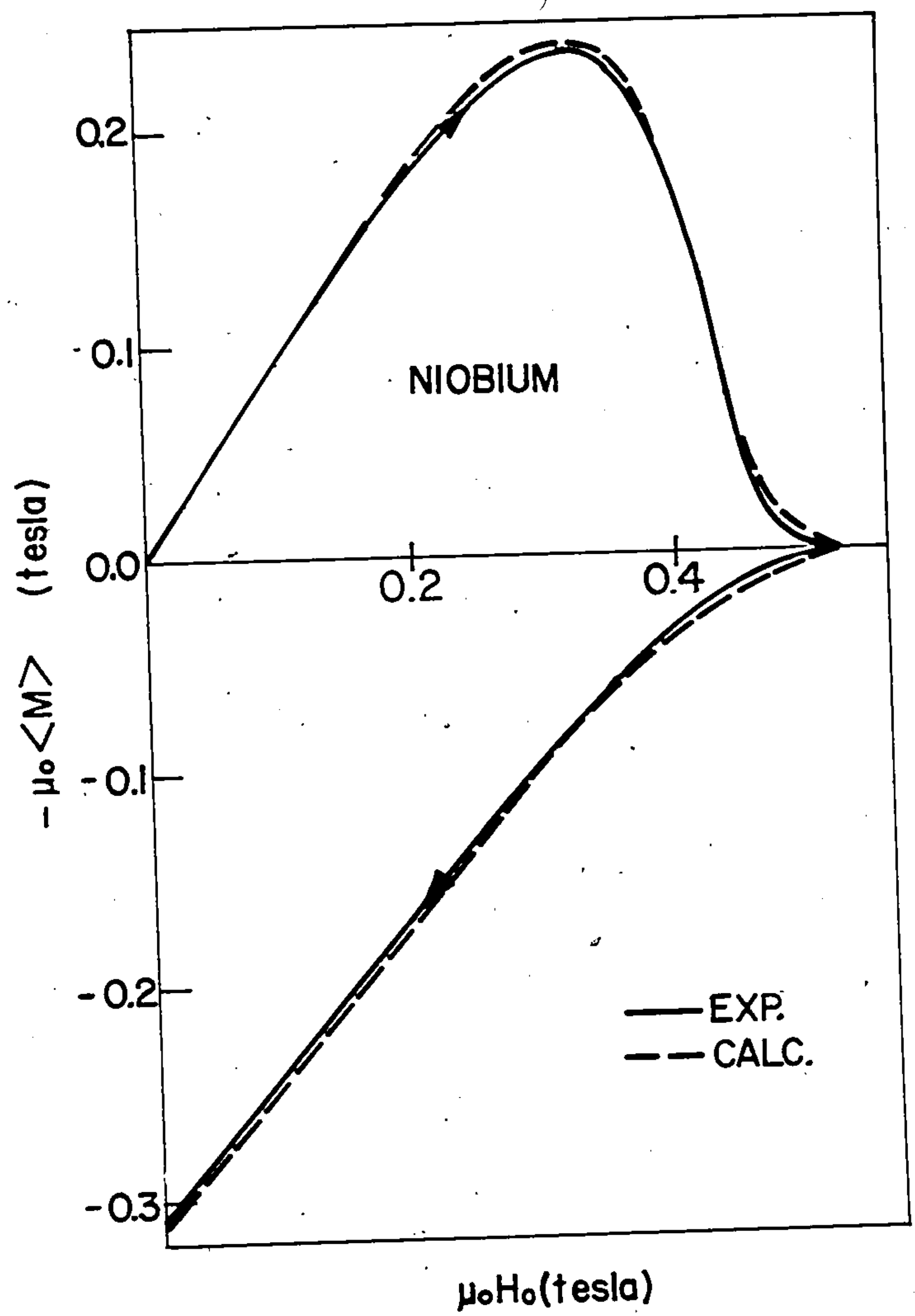


Figure 7-3 Experimental and calculated magnetization curves for the niobium wire.

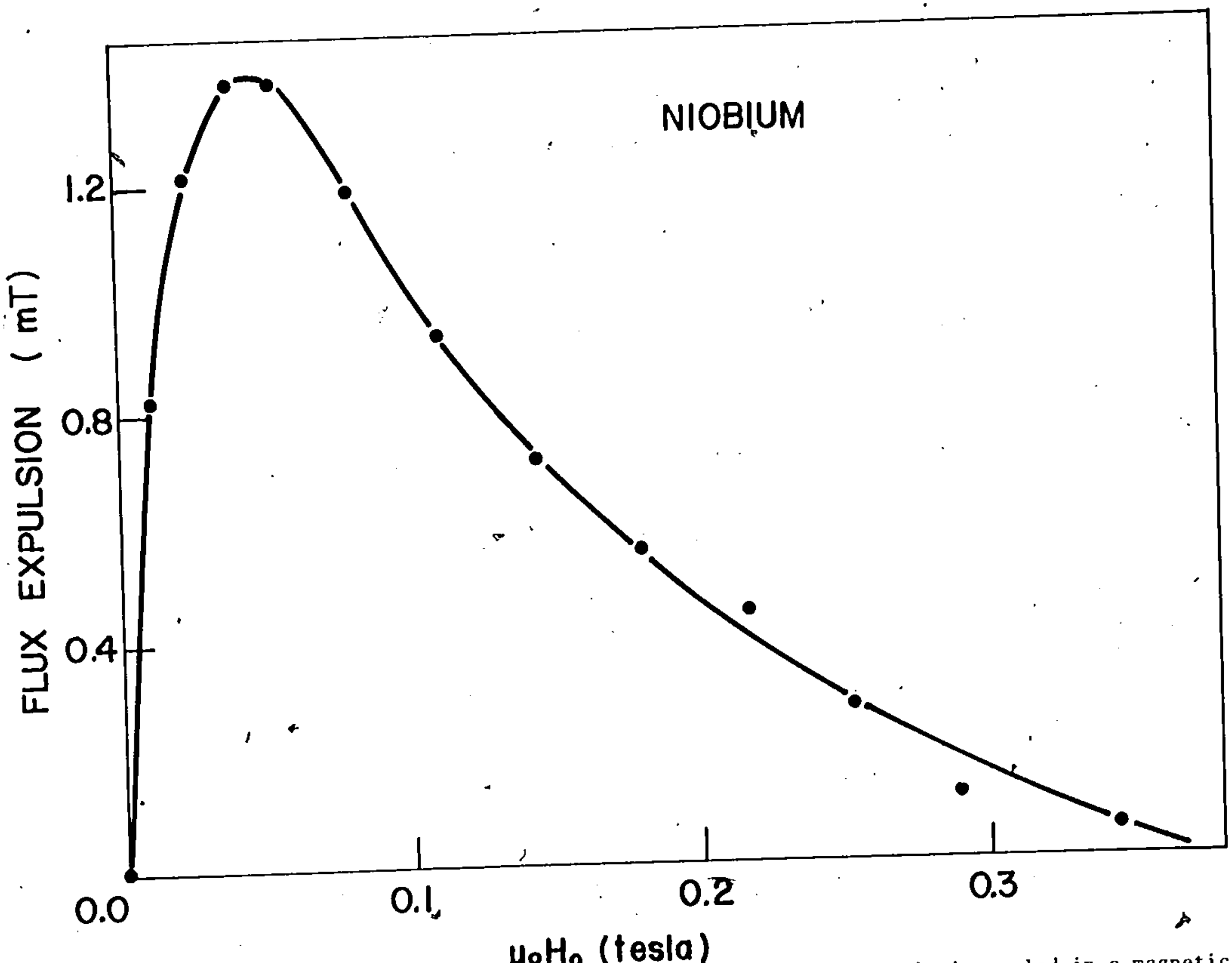


Figure 7-4 Flux expulsion observed with the niobium sample as it is cooled in a magnetic field $H_o$.

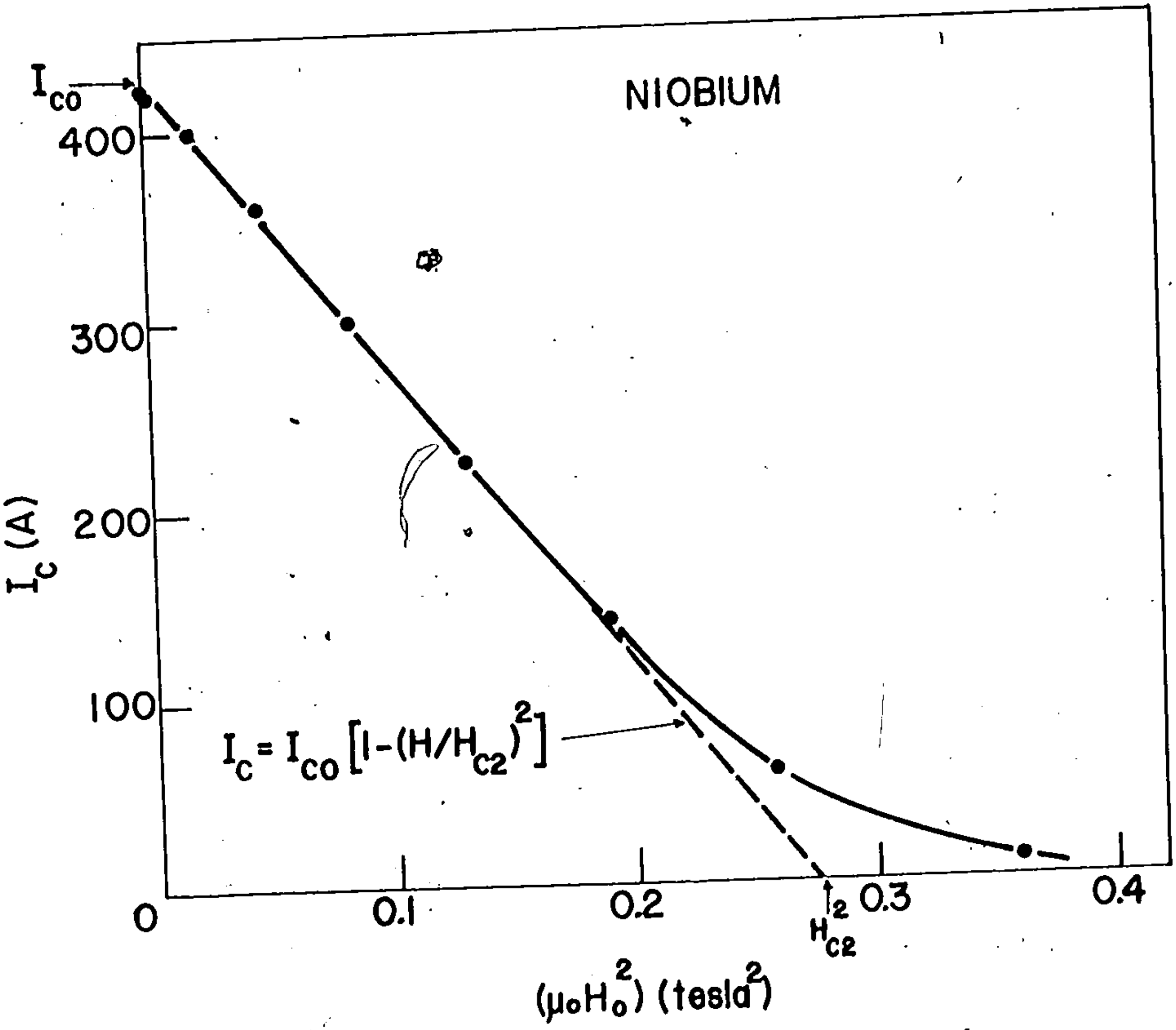


Figure 7.5 Critical transport current for the niobium sample

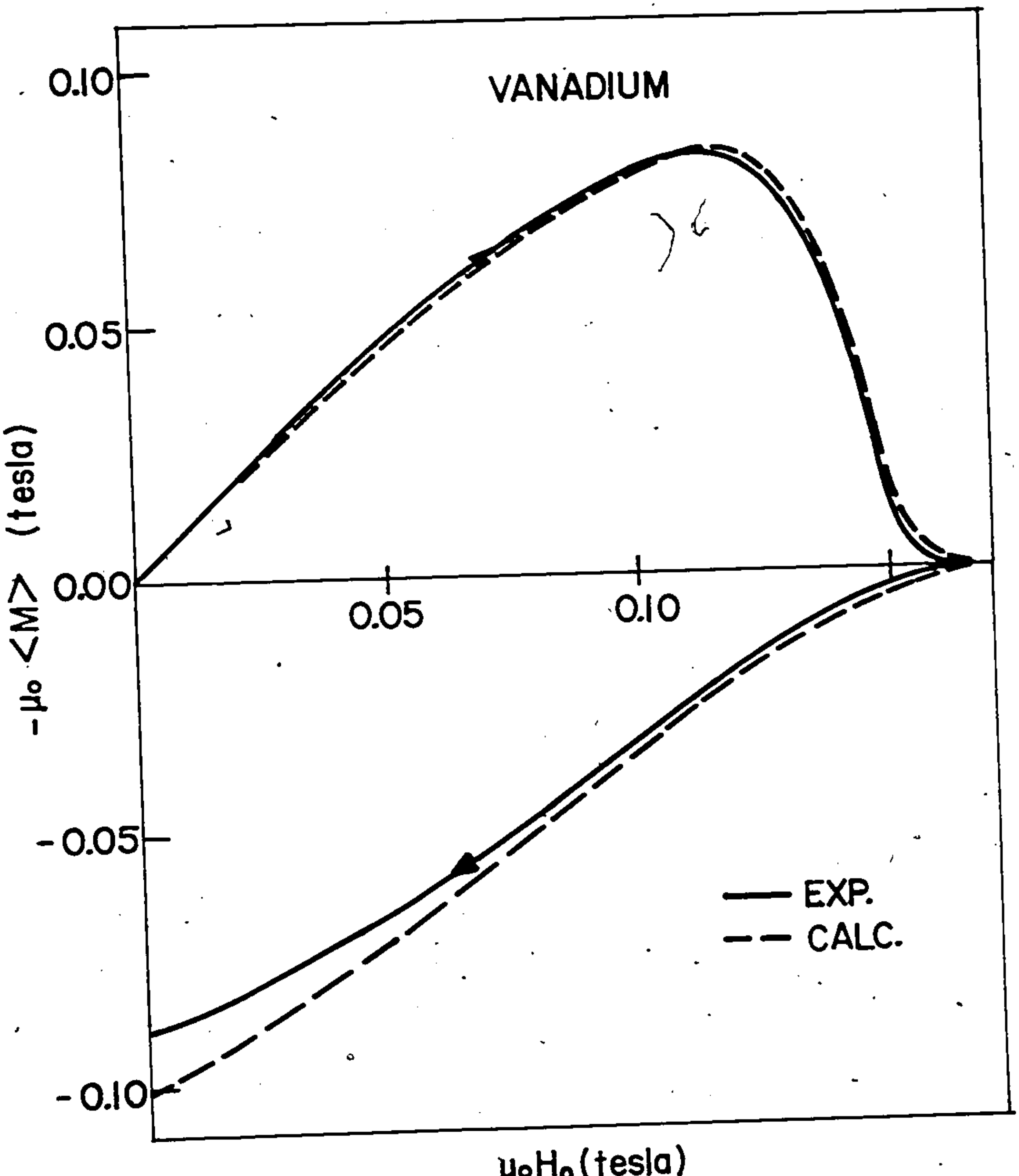


Figure 7-6 Experimental and calculated magnetization curves for the Vanadium wire

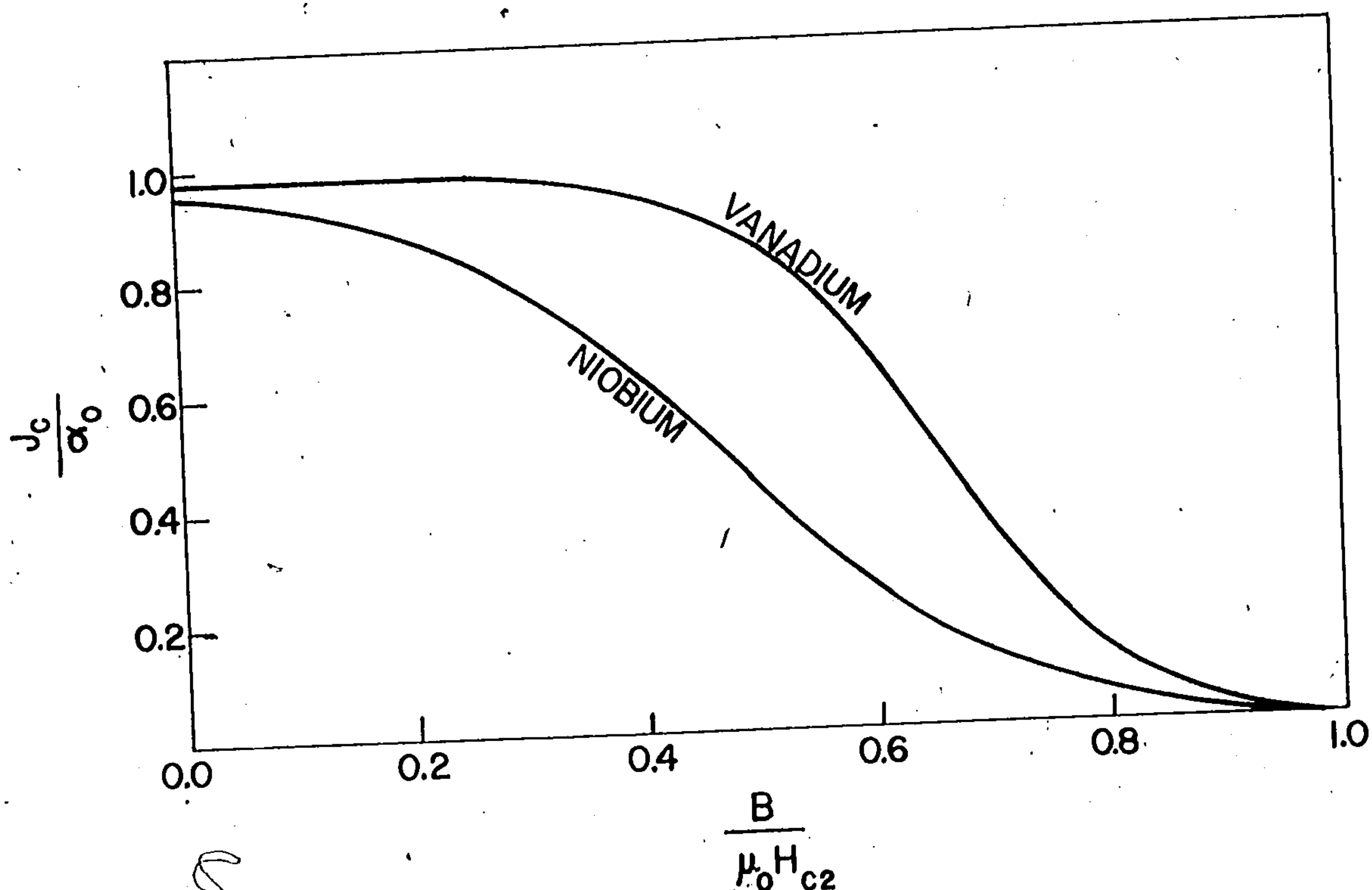


Figure 7-7  Normalized critical current density for the vanadium and niobium samples as a function of the magnetic flux density.

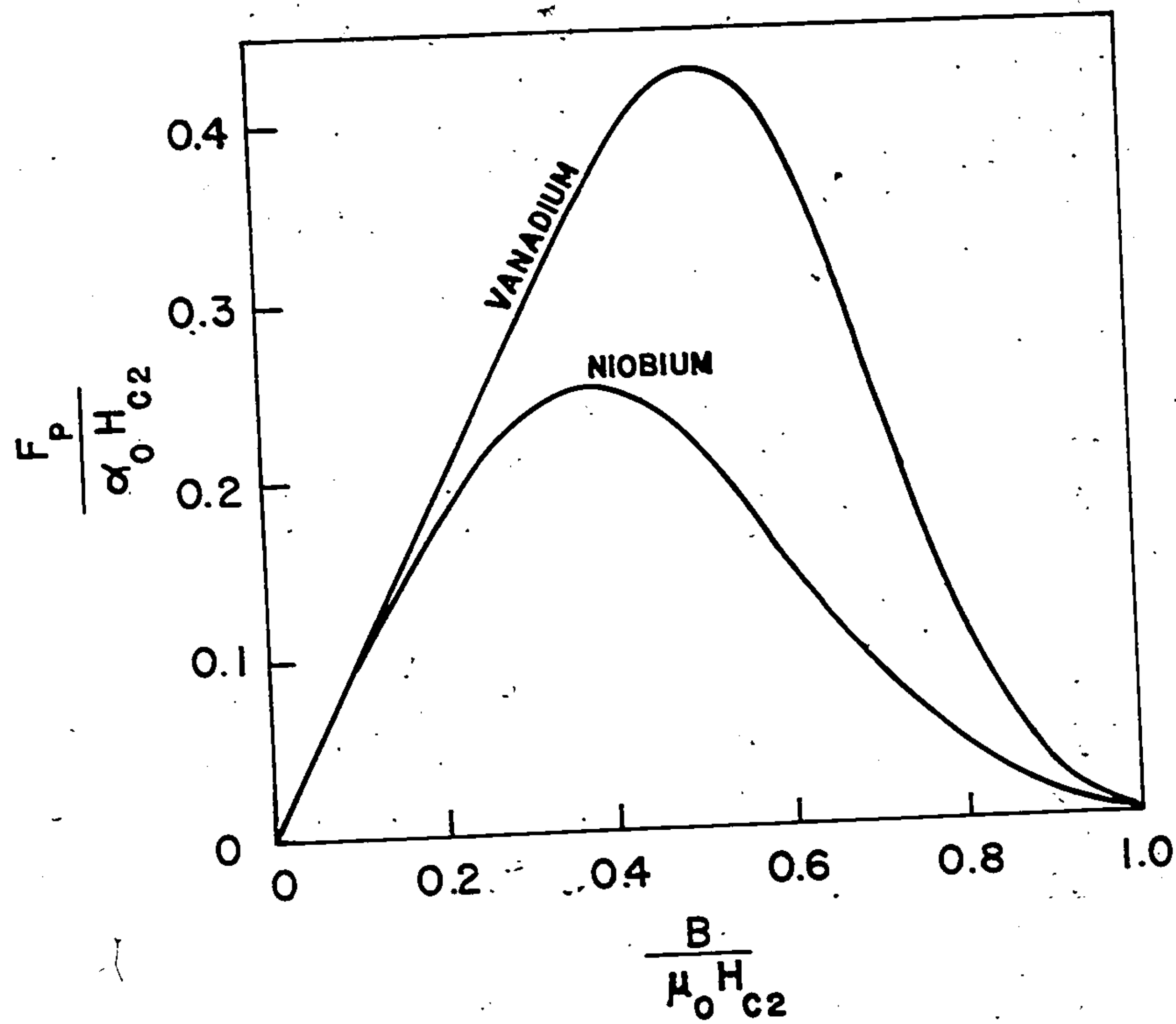


Figure 7-8 Normalized pinning function for the vanadium and the niobium samples as a function of the magnetic flux density

# CHAPTER S

## Propagation of Flux Jumps along an Axially Magnetized Wire Carrying a Transport Current

### S.1 Introduction

A heat pulse applied at one end of a superconducting wire carrying a transport current I can generate a normal region in the vicinity of the pulse. The temperature of this normal region can rise and remain above $T_c(I)$ due to joule heating ($\rho_N J^2$). Heat flowing into the adjacent superconducting regions eventually raises the temperature of the latter above $T_c(I)$. This mechanism can cause the normal phase to propagate at a constant velocity along the entire specimen. This is referred to as the thermal mode of propagation, since it is governed by a heat diffusion equation.

This phenomenon was investigated in type I superconductors (Cherry 60, Broom 60) and in type II superconductors (Whetstone 65 , Overton 71). Generally, heat flow to the outside surroundings in the vicinity of the normal front is considered negligible. Consequently the advancing normal front is visualized as a flat (planar) cross-section where $\rho = 0$ on the superconducting side and $\rho = \rho_N$ on the normal side. The radial distribution of the transport current on the superconducting side then plays no role in the analysis. The velocity of propagation is small and depends on $I/I_c$, the thermal capacity, the heat conductivity and the critical temperature $T_c(I, H)$. It should be noted that earlier, Pippard (Pippard 50) and others (Faber 53, Ittner 58) studied the similar problem of the propagation of the normal phase in type I superconductors when the applied field $H_o$ is raised above $H_c$.

Recently, many workers have turned their attention to the phenomenon of flux avalanches and, in particular, to the criterion for its occurrence and to the spatial and temporal evolution of such events. Basic geometric configurations such as a long cylinder in a longitudinal magnetic field, an infinite slab in a field parallel to the surfaces and even a disk in a field perpendicular to its flat faces, where the phenomenon can be viewed and treated as one-dimensional, have been studied experimentally and theoretically in some detail (Wipf 67, Wertheimer 68, Swartz 68, Hartison 73, Morton 73, Darby 73, Bussière 75, Mints 75). In these situations the progress of the flux avalanche can be adequately described by a set of coupled thermal and magnetic diffusion equations (Darby 73, Morton 73, Bussière 75) exploiting the concepts of the critical state and flux flow resistivity (Kim 65).

The propagation of a flux jump along the length of a wire, axially magnetized in a longitudinal field but carrying no transport current was first investigated by Walker and Hulm (Walker 66, 72) and subsequently by Bussière (Bussière 72 a). Although, the mathematically tractable one-dimensional problem of a pure radial collapse in an axially magnetized wire in a longitudinal field appears to be well understood, little progress has been achieved in explaining the longitudinal velocity of propagation of a flux avalanche under these circumstances: any understanding of the latter phenomenon remains qualitative. The flux avalanche advances longitudinally by sufficiently perturbing the critical configuration of magnetic induction in the adjacent region to trigger a flux avalanche there. The velocity of propagation which results from this process is much larger than encountered for thermal propagation and indicates unambiguously in most cases that a different mechanism operates. It is clear that the collapse of flux in one segment will generate changes in the configuration of magnetic induction and of the circulating critical currents in the adjacent region by electromagnetic induction. This mode of propagation is here referred to as the electromagnetic mode since it arises from electromagnetic coupling. In order that the disturbance continue to propagate by this mechanism, it is crucial that the flux configuration along the wire be on the verge of collapse; otherwise, the disturbance is "absorbed" in the adjacent regions and its progress along the wire ceases. Consequently, there is a "threshold state" required for the electromagnetic mode of propagation to manifest itself. Below this threshold, no propagation occurs and the externally triggered collapse is localized unless circumstances are created where thermal propagation can occur. The presence of a small steady transport current provides such a situation.

The investigations of Bussière (Bussière 72b) on the longitudinal velocity of propagation of flux avalanches in axially magnetized wires carrying a steady transport current have been extended here. The mechanism responsible for the propagation can be either thermal or electromagnetic, depending on the magnitude of the axial magnetic moment and the transport current. In this chapter the results of measurements on the dependence of $V_z$, the longitudinal velocity of propagation, on I, $H_o$ and the axial magnetization $\langle M_z \rangle$ are presented. These results are examined in the context of the two modes of propagation identified above. The effect of the helical mode of propagation of the avalanche on the observations is also considered qualitatively. In chapter 9 attention is focussed on the role of the energy stored in the magnetic configuration due to I and to $\langle M_z \rangle$ in determining $V_z$. In chapter 10 the phenomenon of helical propagation is examined in detail.

## 8.2 Dependence of $V_z$ on I, $\langle M_z \rangle$ and $H_o$

The present data on the longitudinal velocity $V_z$ of propagation of the flux jumps in the Nb and V wires are presented in Figures 8-1 through 8-6. The wire is axially magnetized by cooling through $T_c$ to 4.2 K in a chosen initial longitudinal magnetic field $H_i$ which is subsequently brought to the final value $H_o$ indicated at the top of each Figure. The inserts in the Figures should aid the reader in identifying the procedure followed in generating the axial moment. Evidently, for a given $H_o$, different initial values $H_i$ must be selected in order to produce magnetic moments of different magnitudes. The Figures are not cluttered by indicating these values of $H_i$ but they are recorded during the experiment and used in the quantitative analysis. For a chosen $H_o$, where $H_o \neq 0$, the axial moment may point in the direction of $H_o$ or opposite to it. The former is called a paramagnetic moment since $\langle B_z \rangle > H_o$. For the latter, two different configurations can occur.

i) $B_z(r)$ has the polarity of $H_o$. This is always the case when $H_i$ has the polarity of $H_o$ or is zero. Such moments are denoted as diamagnetic since $B_z(r) < H_o$.

ii) $B_z(r)$ has the polarity of $H_o$ in a cylindrical sheath surrounding a core where $B_z(r)$ opposes $H_o$. This situation is produced when $H_i$ points in the direction opposite to $H_o$. Such configurations are called hybrid. All of the magnetic moments in Figures 8-2 and 8-4 are hybrid. This is evident in all cases but one, since $|\langle M_z \rangle| > H_o$. In the case where $|\langle M_z \rangle| \lesssim H_o$, the locus of the moment on the standard magnetization curve (Figure 7-3) identifies it as hybrid. The reader may well ask why measurements in which $\langle M_z \rangle$ is diamagnetic are not presented. The reason is that this state is very stable in the present samples and flux jumps (in contrast to

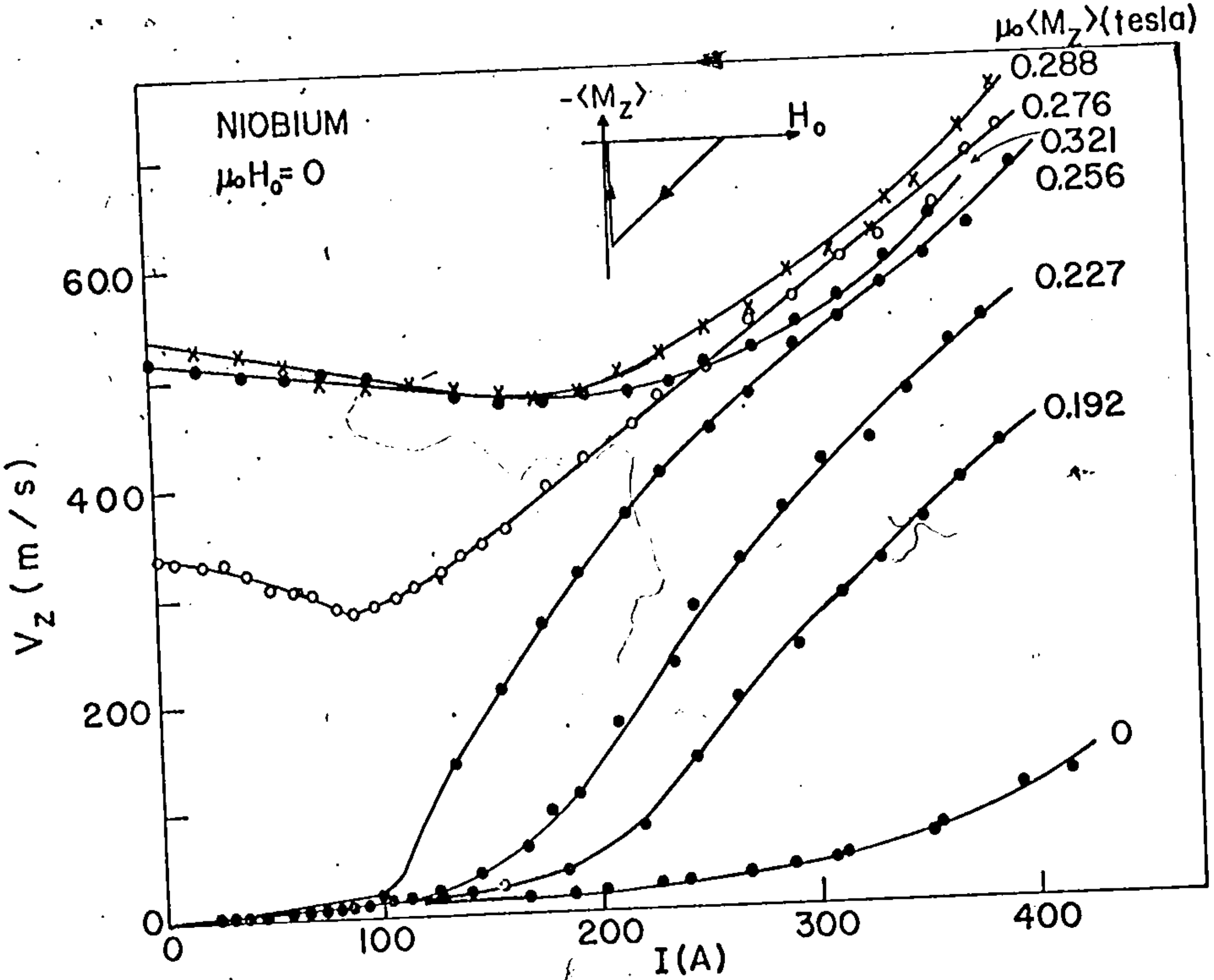


Figure 8-1 Longitudinal velocity of propagation of flux jumps versus transport current for different paramagnetic moments in zero applied field (Niobium sample)

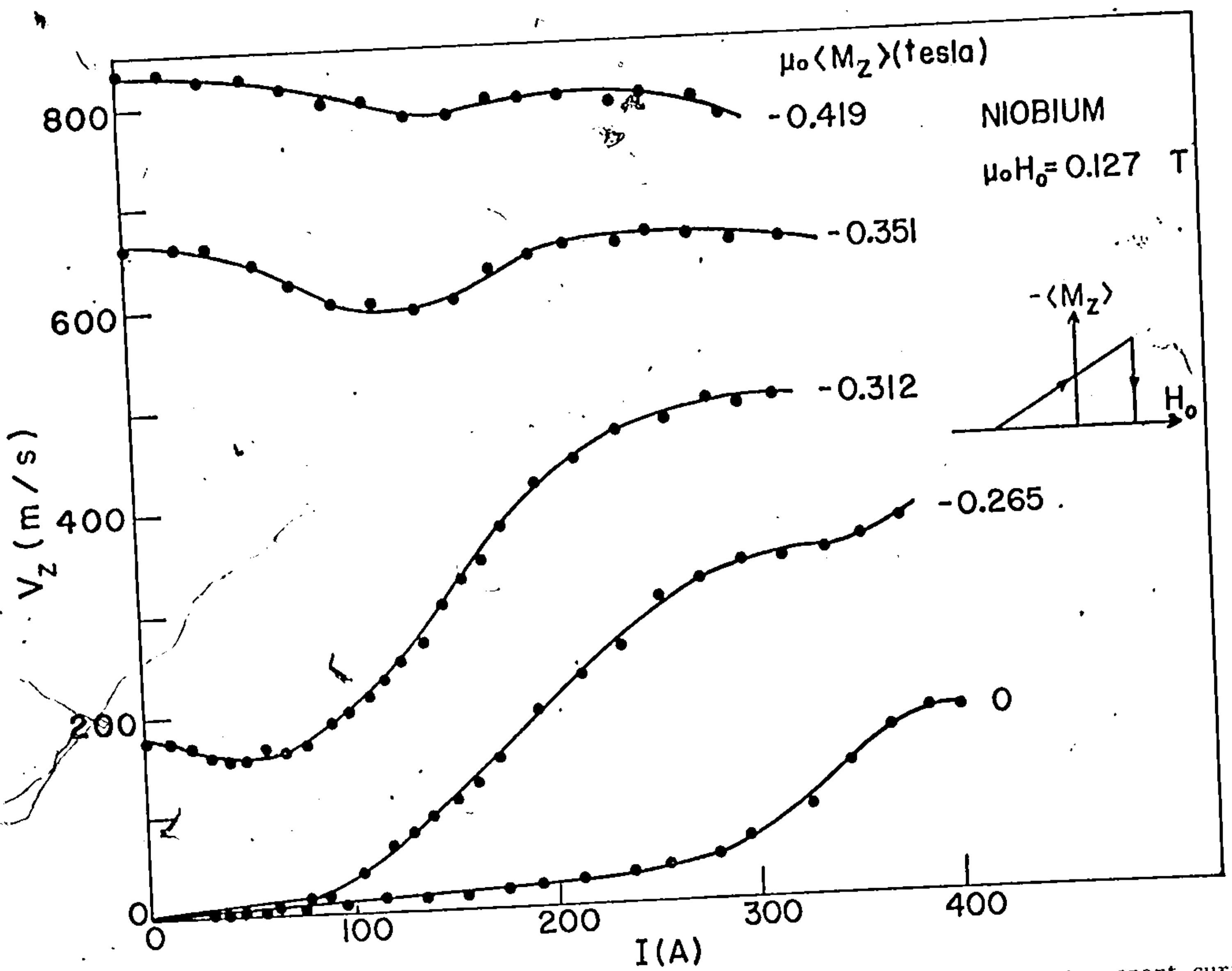


Figure 8-2 Longitudinal velocity of propagation of flux jumps versus transport current for different hybrid moments, $\mu_o H_o = 0.127$ tesla. (Niobium sample)

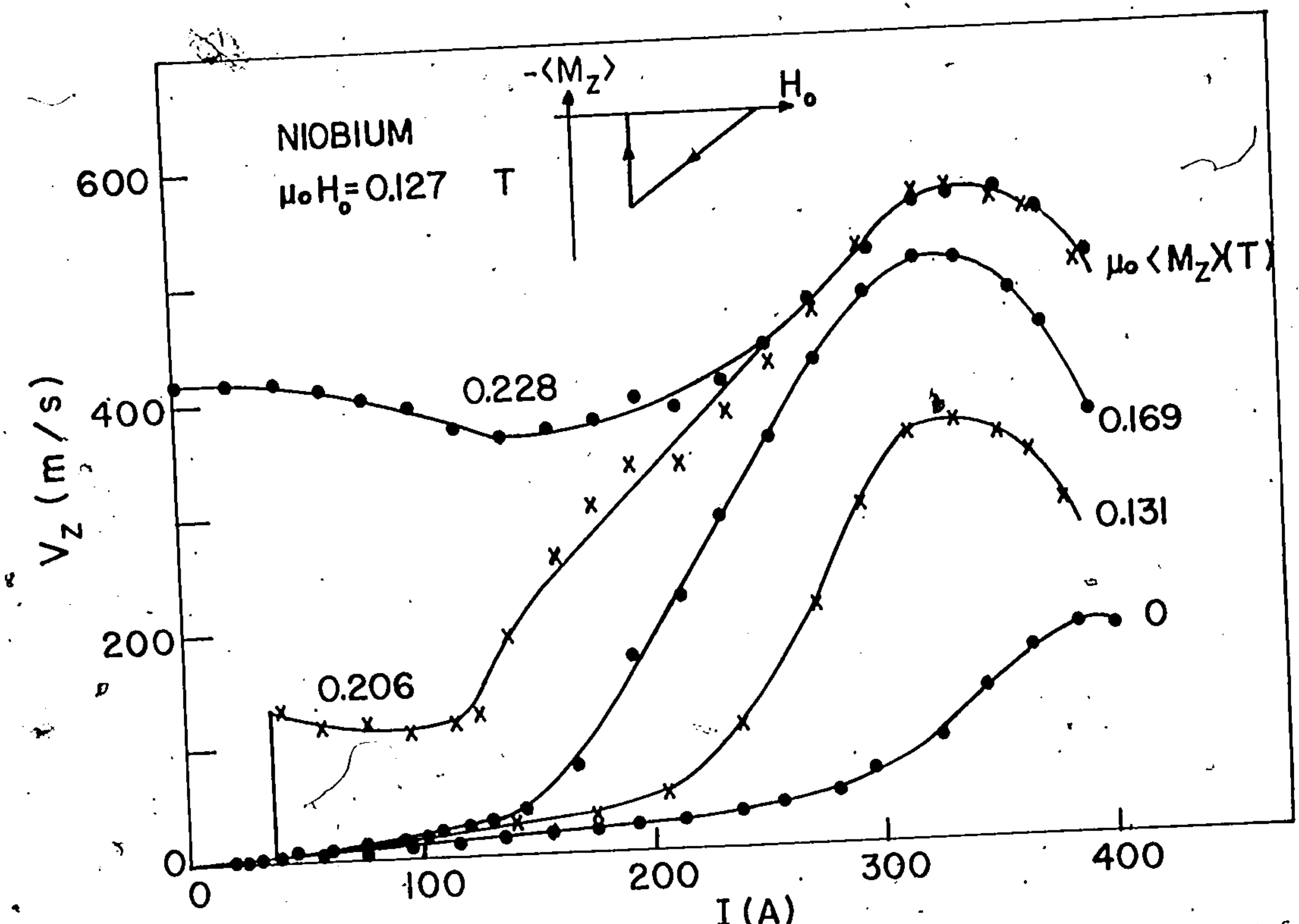


Figure 8-3 Longitudinal velocity of propagation of flux jumps versus transport current for different paramagnetic moments, $\mu_o H_o$ = 0.127 tesla (Niobium sample)

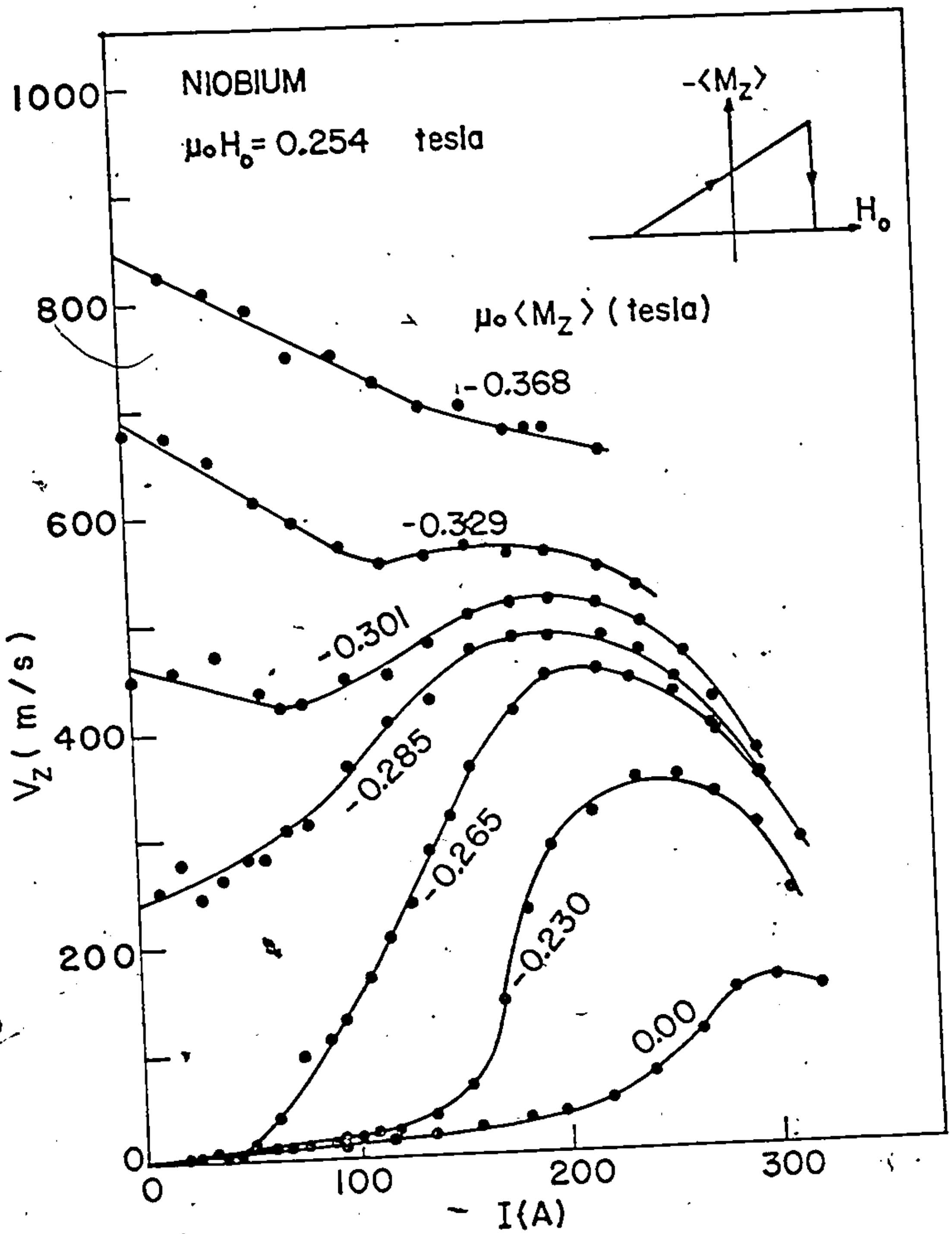


Figure 8-4 Longitudinal velocity of propagation of flux jumps versus transport current for different hybrid moments, $\mu_o H_o$ = 0.254 tesla. (Niobium sample)

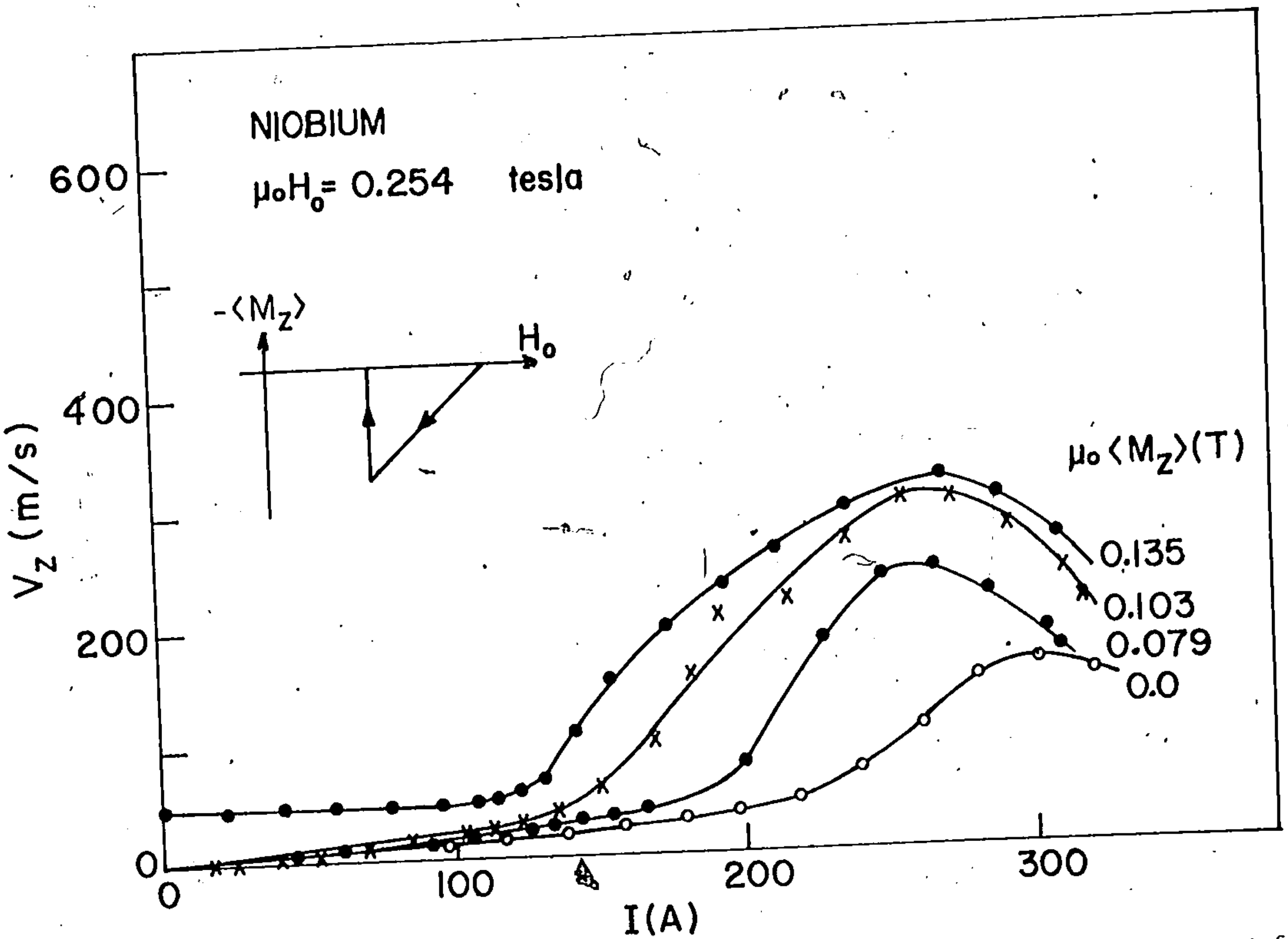


Figure 8-5 Longitudinal velocity of propagation of flux jumps versus transport current for different paramagnetic moments, $\mu_o H_o = 0.254$ tesla. (Niobium sample)

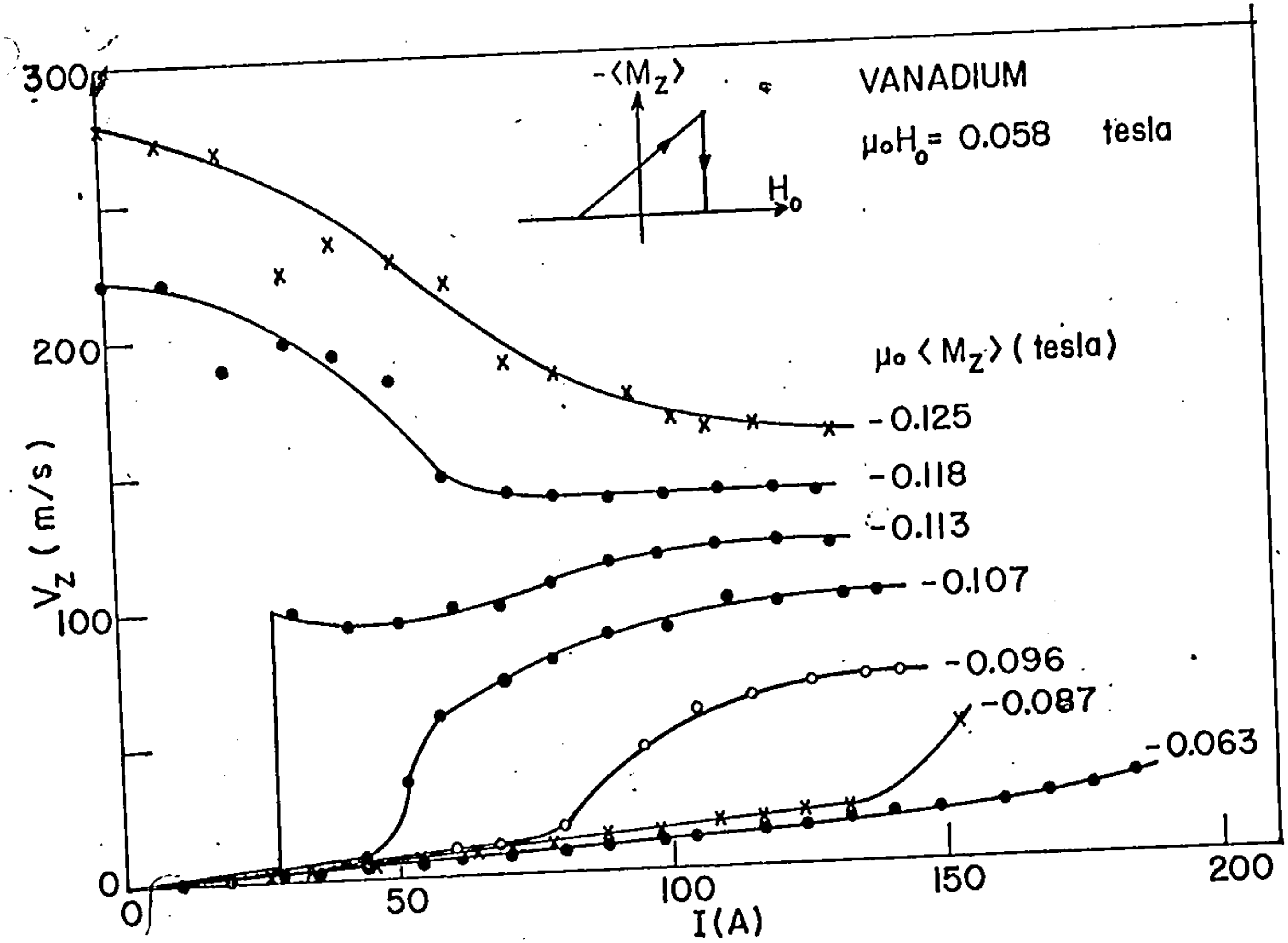


Figure 8-6 Longitudinal velocity of propagation of flux jumps versus transport current for different paramagnetic moments in zero field. (Vanadium sample)

thermal propagation) can only be triggered in a narrow range of I near $I_c$.

The measurements for a given $H_o$ (including $H_o = 0$) are grouped together. For a given $H_o$ (other than $H_o = 0$), separate Figures are used to present the data for the paramagnetic and for the hybrid moments. This manner of displaying the results illustrates not only the effect of I but also the role of the magnitude and the sign of $\langle M_z \rangle$. The initial magnetic moment $\langle M_z \rangle$ is indicated along each curve in Figures 8-1 through 8-6. Note that the largest magnetic moment indicated on each Figure corresponds to the maximum moment of that polarity which could be generated in the chosen applied field $H_o$ (including $H_o = 0$). It should be stressed that:

i) The magnetic moment when the flux jump is triggered may be substantially different from the initial magnetic moment indicated in the Figures. This is especially important to bear in mind in viewing Figures 8-4 and 8-5. The magnetic moment $|\langle M_z \rangle|$ varies (and generally decreases) as I is impressed and approaches $I_c$. It will be convenient to return to this significant feature later in this chapter.

ii) The transport current I indicated on the horizontal axis is the average current flowing in the wire during the time interval where $V_z$ is detected. As mentioned earlier, I is monitored during the flux jump and decreases fractionally as the jump progresses along the wire, thereby causing the resistance to grow.

The data presented in Figures 8-1 through 8-5 are plotted again in a different perspective in Figures 8-7, 8-8 and 8-9. Here are shown graphs of $V_z$ vs $\langle M_z \rangle$ for constant I. This alternative manner of presenting the data is more effective in illustrating the role of the magnitude and of the sign of $\langle M_z \rangle$ in controlling $V_z$. In Figures 8-7, 8-8 and 8-9 curves are presented for fixed increments of I (i.e. I = 0, 75, 150, 225, 300 and

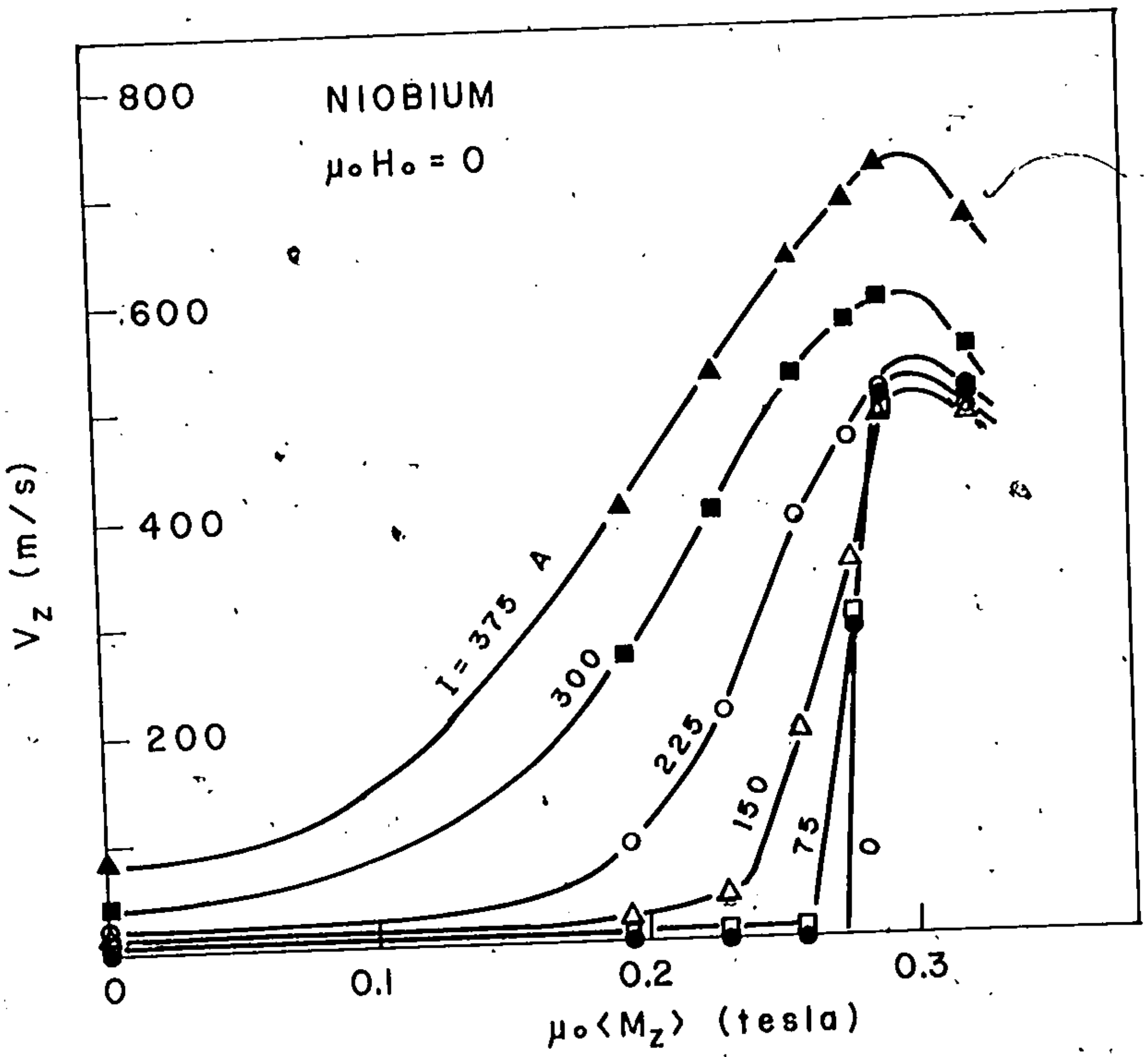


Figure 8-7 Longitudinal velocity of propagation of flux jumps versus axial magnetic moment for different values of the transport current. ($\mu_o H_o = 0$)

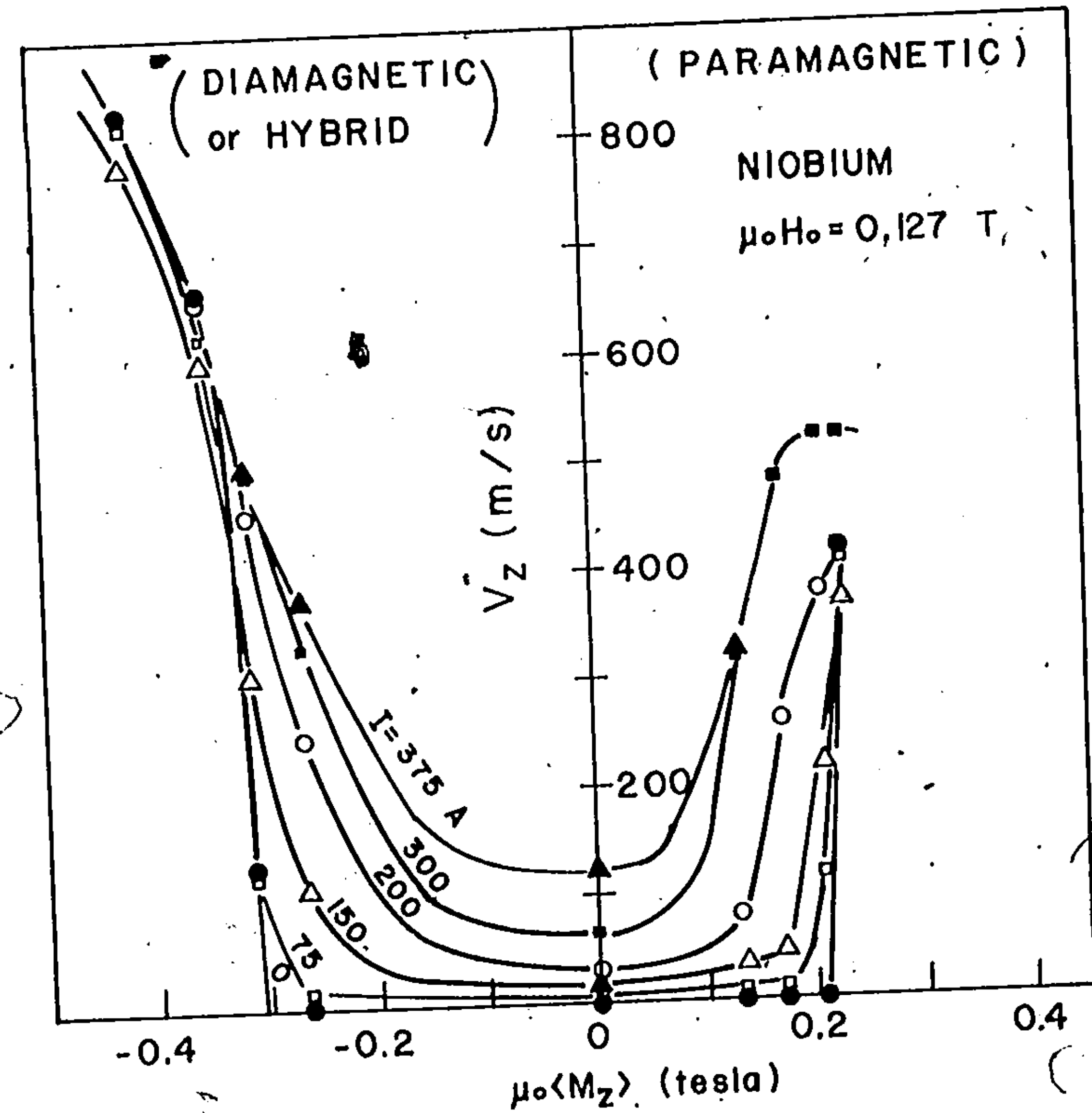


Figure 8-8 Longitudinal velocity of propagation of flux jumps versus axial magnetic moment for different values of the transport current ($\mu_o H_o$ = 0.127 tesla)

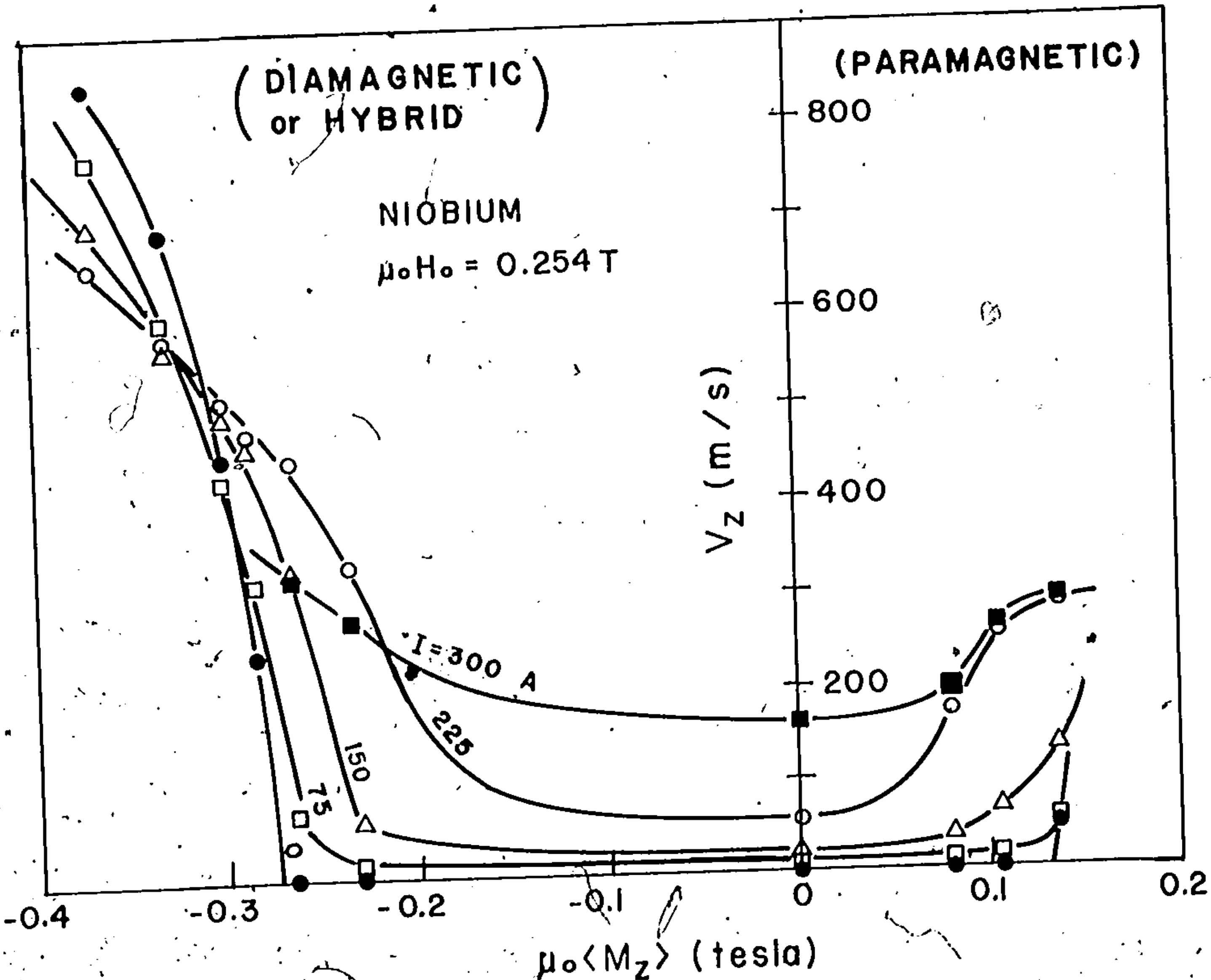


Figure 8-9 Longitudinal velocity of propagation of flux jumps versus axial mangetic moment for different values of the transport current ($\mu_o H_o = 0.254$ tesla)

375 A). Thus not all of the numerous data points from Figures 8-1 through 8-5 appear in this method of presentation.

## 8.3 Qualitative Interpretation of Flux Jump Velocity Curves

Inspection of all of these Figures leads to the following general observations.

i) Rapid and sometimes discontinuous increases in $V_z$ with I are noted.

ii) Rapid and sometimes discontinuous increases in $V_z$ with $<M_z>$ are noted.

These features, in particular, the discontinuities or abrupt variations, are indications that a threshold has been exceeded and a change in the mode of propagation from thermal to electromagnetic has occurred.

Further certain trends and salient features are noted. The reader is referred to the sketch below which "summarizes" these observations.

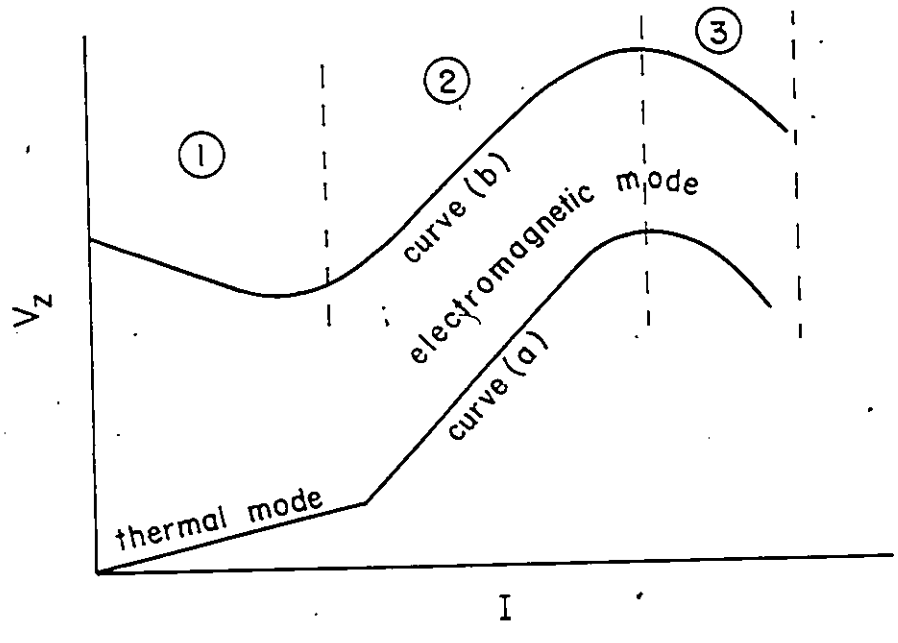


Curve (a). For small $|<M_z>|$ (i.e. $|<M_z>|$ where $V_z = 0$ when $I = 0$) a linear or nearly linear region of $V_z$ vs I is observed in the range of small I. The thermal mode of propagation operates in this linear region and the behaviour here is described by the equations of Whetstone and Roos

(Whetstone 65). The linear region is followed by a region in which $V_z$ is rising rapidly; this may reach a plateau or leveling off and sometimes forms a peak or hump. This can be interpreted as the electromagnetic mode of propagation taking over when the rapid rise begins and this mode of propagation governs the behaviour of $V_z$ for the remainder of the curve. An explanation will be proposed for the changes in slope of $V_z$ vs I in the region of large I and will be pursued in some detail later in this thesis.

Curve (b). For large $|\langle M_z \rangle|$ (i.e. $|\langle M_z \rangle|$ where tbe propagation occurs even when I = 0) the locus of $V_z$ vs I traces a minimum followed by a maximum. The sides of the minimum are asymmetric, as are the flanks of the maximum. Indeed, in some cases, the hump may be "incomplete" and only the rising flank and part or nothing of the summit are seen. The depth of the valley, and the height of the peak exhibit considerable variations from one curve to another. The electromagnetic mode of propagation determines the behaviour throughout this curve since the magnetic configuration, even when I = 0, is sufficiently unstable that a flux avalanche can be triggered and propagate.

Clearly curves (a) and (b) arise from the interplay of aiding and competing contributions which depend on I. Three basic and important elements of the situation can be identified. Each of these three contributing factors are now outlined and it is shown qualitatively that the combination of these ingredients can generate the variety of behaviour just noted and presented schematically in ~~the sketch or~~ graphical summary of the previous page.

a) $\langle M_z \rangle$ vs I.

It is observed that the axial moment decreases as I increases. This decline is especially dramatic as I approaches $I_c$ and when the longitudinal applied field $H_o$ is large. This decrease of $|\langle M_z \rangle|$ with increasing I indicates a corresponding diminution of the stored magnetic energy $U_z$, which is released (dissipated) when the $B_z$ profile collapses during the flux avalanche. (See diagram (a) ). Walker and Hulm (Walker 72) and Bussière (Bussière 72b) have, independently, proposed that the magnetic energy $U_z$ associated with $\langle M_z \rangle$ plays an important role in regulating $V_z$. They only considered the situation where I = 0. Their viewpoint is adopted here and its consequences are explored quantitatively in this thesis, in situations where a transport current is present. For the immediate purpose it is sufficient to note that, according to this idea, $V_z$ should decrease when $|\langle M_z \rangle|$, hence $U_z$ decreases, as I increases. This behaviour is shown schematically in diagram (d).

b) $U_\theta$ vs. I.

The stored magnetic energy $U_\theta$, which is released (dissipated) when the azimuthal magnetic induction (the $B_\theta$ profile) collapses during the flux avalanche depends on I as illustrated schematically in diagram (e). Since the transport current I is maintained constant (or nearly constant) as the flux avalanche progresses, the $B_\theta$ profile of the superconducting state evolves until the linear $B_\theta$ profile of the normal state is reached, as shown in diagram (b). The dependence of the $B_\theta$ profiles and of $U_\theta$ on $I/I_c$ will be examined in detail in the next chapter. Only the salient features of the results of this analysis are presented at this stage. Pursuing the idea that the velocity of propagation in the electromagnetic mode varies according to $U_\theta$, a corresponding dependence of V on I is anticipated.

In the thermal mode, the velocity of advance of a normal front depends

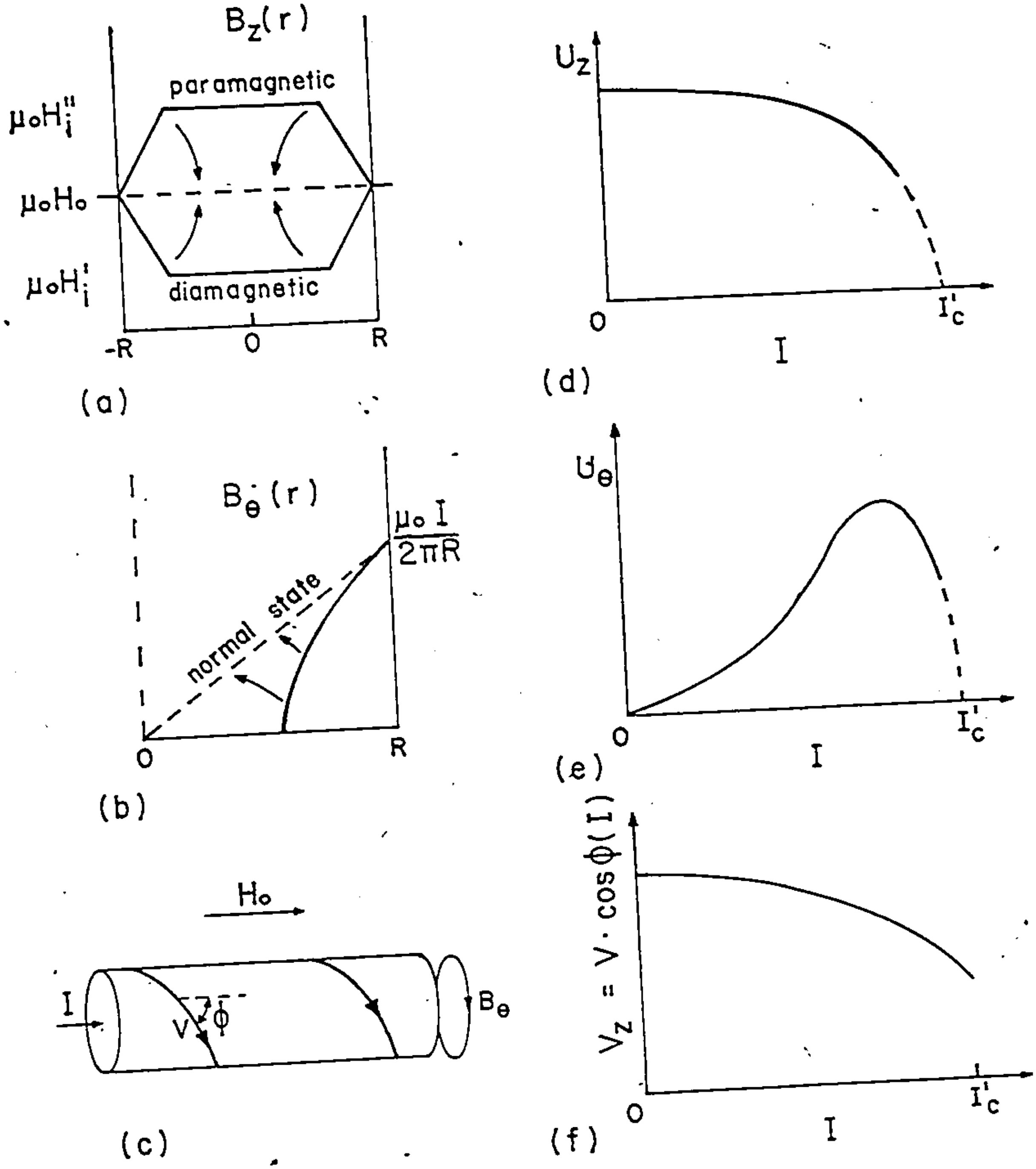


Diagrams: a) axial field profiles, before and after a flux jump; b) azimuthal field profiles, before and after a flux jump; c) helical propagation of a flux jump; d) and e) magnetic energy dissipated during a flux jump and due to the collapse of the axial and azimuthal field profiles respectively; f) decrease of the net axial velocity $V_z$ due to the increase of the helicity of the path followed by the flux jump.

on $I^2R$ heating (where R is the normal state resistance per unit length), and leads to a nearly linear variation of V with I, as demonstrated experimentally and theoretically by Whetstone and Roos (Whetstone 65). Evidently, in the wake of the flux avalanche propagating by electromagnetic coupling, $I^2R$ heating will take place. This $I^2R$ heating then plays no role in the actual propagation since, in any segment of the wire, it takes place after the advancing disturbance has gone on further along the wire. If the stored magnetic energy, $U = U_\theta + U_z$, is insufficient to sustain the propagation of a magnetic instability (that is, it lies below the required threshold) then V electromagnetic is zero. Pulses will nevertheless be observed with the axial pick-up coils when $I \neq 0$ and $\langle M_z \rangle \neq 0$. These pulses arise because the thermal propagation of the normal front causes the axial moment in the segments of the wire embraced by the axial coils to collapse when it reaches these segments at time $t_1$ and $t_2$. Under these circumstances, the stored energy $U_z$ (and $U_\theta$), although inadequate to ensure electromagnetic propagation, will also be released (dissipated) upon arrival of the normal front. The heat generated by the liberation of this stored energy will add to the $I^2R$ heat flowing through the normal front into the adjacent superconducting region. As a consequence it is expected (and observed) that $V_z$ is fractionally enhanced by the presence of an axial moment. Whetstone and Roos did not include any contributions arising from $U_z$ and $U_\theta$ in their analysis of thermal propagation. An examination of the present data shows that $\langle M_z \rangle$ has some small effect in increasing the slope of the locus of $V_z$ vs I over the linear (thermal propagation) portions of the curves. The minuscule influence of $\langle M_z \rangle$ on $V_z$ in the linear region again emphasizes that a different mode of propagation takes over when $|\langle M_z \rangle|$ exceeds a (current-dependent) threshold. This feature emerges more clearly when the data is presented as a function of $\langle M_z \rangle$, as in Figures 8-7 through 8-9.

For small $|\langle M_z \rangle|$ when the slope of $V_z$ vs I increases only gradually, it is of course difficult to determine unambiguously the point of onset of electromagnetic propagation, and indeed even whether the latter does intervene. The transition from the thermal to the electromagnetic mode of propagation is fairly clear-cut, however, when $V_z$ vs I exhibits a rapid or abrupt rise. In these cases, the point of intersection of the linear and the steeply rising portions of the $V_z$ vs I curve (at constant $|\langle M_z \rangle|$) yields a threshold current for the onset of the electromagnetic mode. Note that this threshold current $I_t$, for a chosen $H_o$, decreases as $|\langle M \rangle|$ increases. This is not surprising, since the total magnetic energy which can be dissipated during the flux avalanche can be written as

$$U = U_z(\langle M_z \rangle) + U_\theta(I) \tag{8-1}$$

for the situation considered here, in which the magnetic configuration is the vector sum of the $B_z$ and $B_\theta$ profiles. Consequently, the threshold or critical energy $U_c$, for a flux avalanche (and hence for electromagnetic propagation) will depend both on I and on $\langle M_z \rangle$. If the contribution of $U_z(\langle M_z \rangle)$ to $U_c$ is increased, then clearly the contribution required from $U_\theta$ (and hence I) is diminished correspondingly.

The relationship between the threshold or critical magnetic moment $\langle M_z \rangle_c$ and the threshold current $I_t$ for electromagnetic propagation is shown schematically in the accompanying sketch. Outside

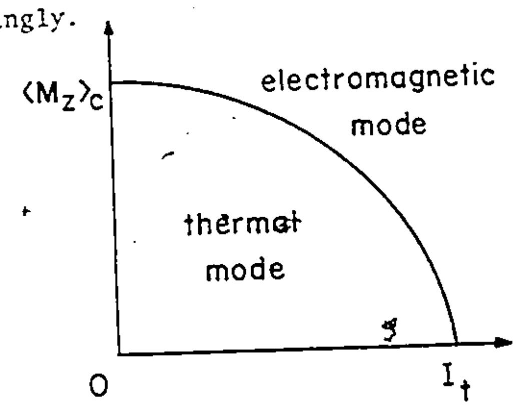

of the boundary curve, the magnetic energy stored in the magnetic induction profiles is large enough to sustain the propagation of a flux avalanche. The present data indicate that the boundary curve varies with $H_o$ and depends on the sign of $\langle M_z \rangle$.

c) Helical Propagation.

As indicated earlier, under certain conditions, the flux avalanche does not travel straight down the wire. The flux jump is azimuthally asymmetric and rotates as it advances by electromagnetic coupling. This behaviour is shown schematically in diagram (c). In chapter 10 extensive observations of this phenomenon will be presented and discussed, as will the data on the angle $\phi$ subtended by the velocity $\vec{V}$ of the avalanche and the longitudinal magnetic field $H_o$. It will be seen that for a given $H_o$ and $\langle M_z \rangle$, the angle $\phi$ generally increases as I (hence as $B_\theta(R)$ ) increases. For now, it will suffice to state that the variation of $\phi$ with I is complicated and is not determined by the helical configuration of the magnetic induction $\vec{B}(R) = \hat{\theta}\, B_\theta(R) + \hat{z}\, H_o$ at the surface of the wire. For immediate purposes, it is sufficient to note that for a given V, the longitudinal velocity of propagation will vary according to the relation $V_z = V \cos\phi\,(I)$, where $\phi$ increases with I. The resulting behaviour is shown schematically in diagram (f).

## 8.4 Synthesis of 8.3 a), b) and c)

The three basic elements of the total picture just outlined appear to determine the longitudinal velocity of propagation which is encountered when a flux avalanche advances under electromagnetic coupling. It is not surprising then that a large variety of curves are observed, depending on which contribution dominates over the various portions of the different curves. Attention is now focussed on curve (b) sketched in section 8.3 in order to illustrate the consequences of a particular mix of these three factors. To do this, it is useful to identify three regions in curve (b). In region (1), $\dot{V}_z$ declines mainly because the helicity ($\phi$) is increasing with I. In region (2), the rapid rise in $U_\theta$ offsets and dominates the former. In region (3), the increase in helicity, the decrease in $U_\theta$ with I and the decrease in $|<M_z>|$ with I in the range of large I, all combine to cause $\dot{V}_z$ to diminish.

Two other possibilities are now considered which are consistent with other observations to be presented later.

If the increase in $\phi$ is modest, the change of $<M_z>$ with I is small and the curve of $U_\theta$ vs I does not progress beyond its peak, then region (3) will not appear in the resultant curve. In the next chapter evidence will be presented which indicates that $I_c$ can occur before or when the summit of $U_\theta$ vs I is attained.

If $<M_z>$ is diminishing significantly throughout, $\phi$ is increasing rapidly and the climb of $U_\theta$ with I is interrupted by the onset of $I_c$, then only region (1) will be mapped out.

The three types of behaviour just described are evident in Figures 8-1 through 8-5.

In the remainder of this thesis, items (a), (b) and (c) are developed in some detail and pertinent observations are presented.

## 8.5 Variation of $<M_z>$ with I

The axial magnetic moment does not remain constant as I is introduced and raised to $I_c$. If this were the case, the task would be considerably simplified. Instead it is found that $|<M_z>|$ diminishes monotonically and reaches a minimum when $I_c$ is attained. The observations are presented in Figures 8-10 through 8-13 where the variation of $<M_z>$ with I starting with different initial magnetic moments and for various longitudinal applied fields $H_o$ are shown. Note that the decrease of $|<M_z>|$ with I becomes particularly dramatic as $H_o$ increases. Also, when $<M_z> = 0$ initially, a small paramagnetic moment develops which attains a weak maximum at $I_c$.

The behaviour displayed in Figures 8-10 through 8-13 has been observed previously by several workers (LeBlanc 65, Belanger 68, Walmsley 72, Gauthier 76). Gauthier (1976) has successfully accounted for the evolution of $<M_z>$ with I in wires of several materials (NbTi, NbZr, NbTa, VTi). The sequences of configurations of $\vec{B}(r)$ vs I which follow from his model are quite complicated, especially when the wire is initially paramagnetically axially magnetized. Further the analysis requires elaborate computations. This approach has not been exploited for these and other reasons.

i) In the exploration of the complicated behaviour of $V_z$, the simplest, physically reasonable $B_z$ and $B_\theta$ profiles are introduced. It is felt that with this approach it is easier to assess the relative importance of the various elements which need to be introduced. Thus, a framework is constructed which is perhaps crude, but which allows one to visualize the physical processes which occur. Improvements and refinements can readily follow from this basis.

ii) The behaviour of the Nb sample differs significantly from that of the materials examined by Gauthier.

a) It has already been noted in Chapter 7 that the $I_c$ vs $H_o$ curve for the Nb specimen is parabolic. The wires studied by Gauthier

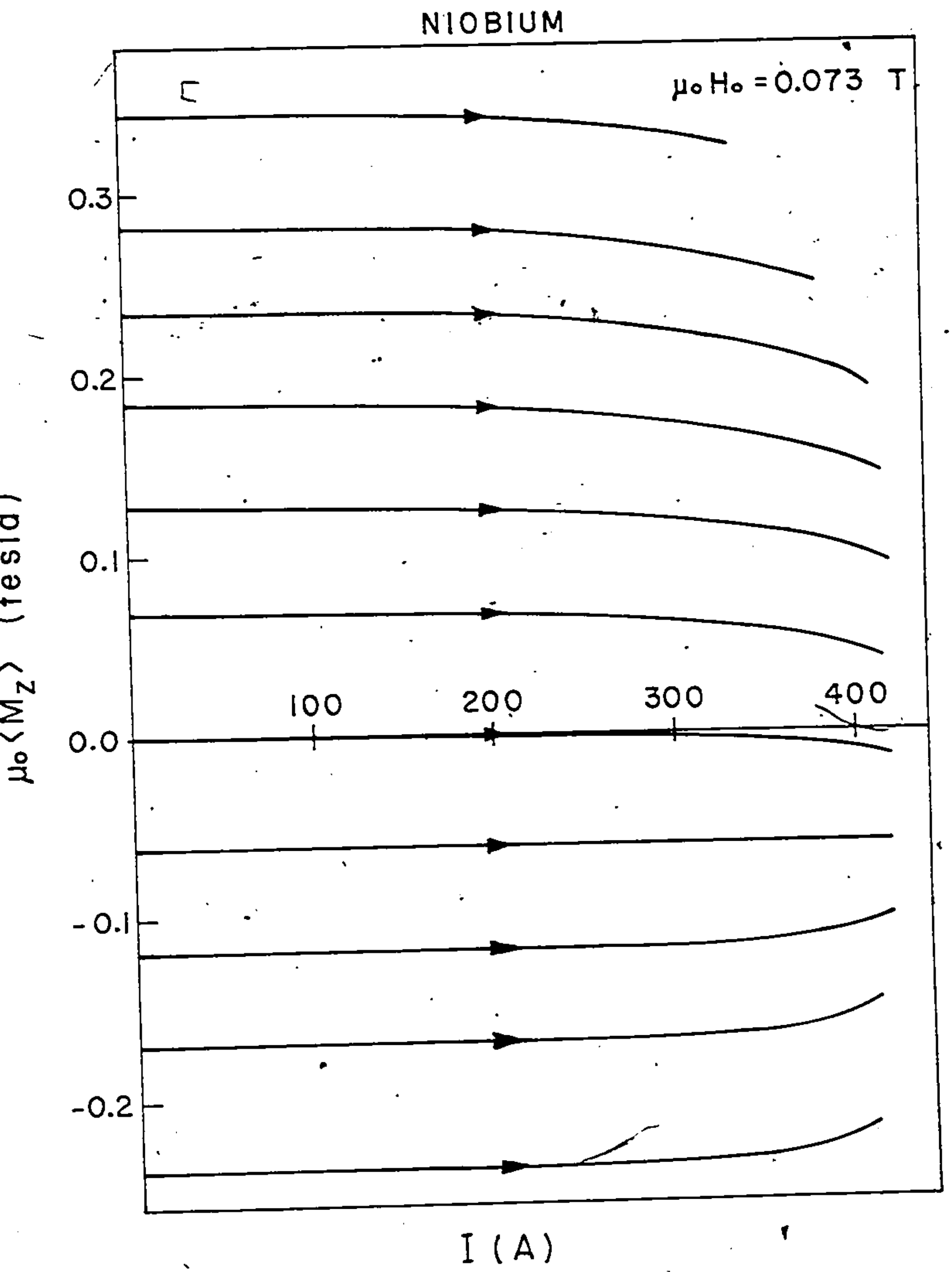


Figure 8-10 Variation of the axial magnetic moment $\langle M_z \rangle$ as the transport current I increases. Family of curves for $\mu_o H_o$ = 0.073 tesla.

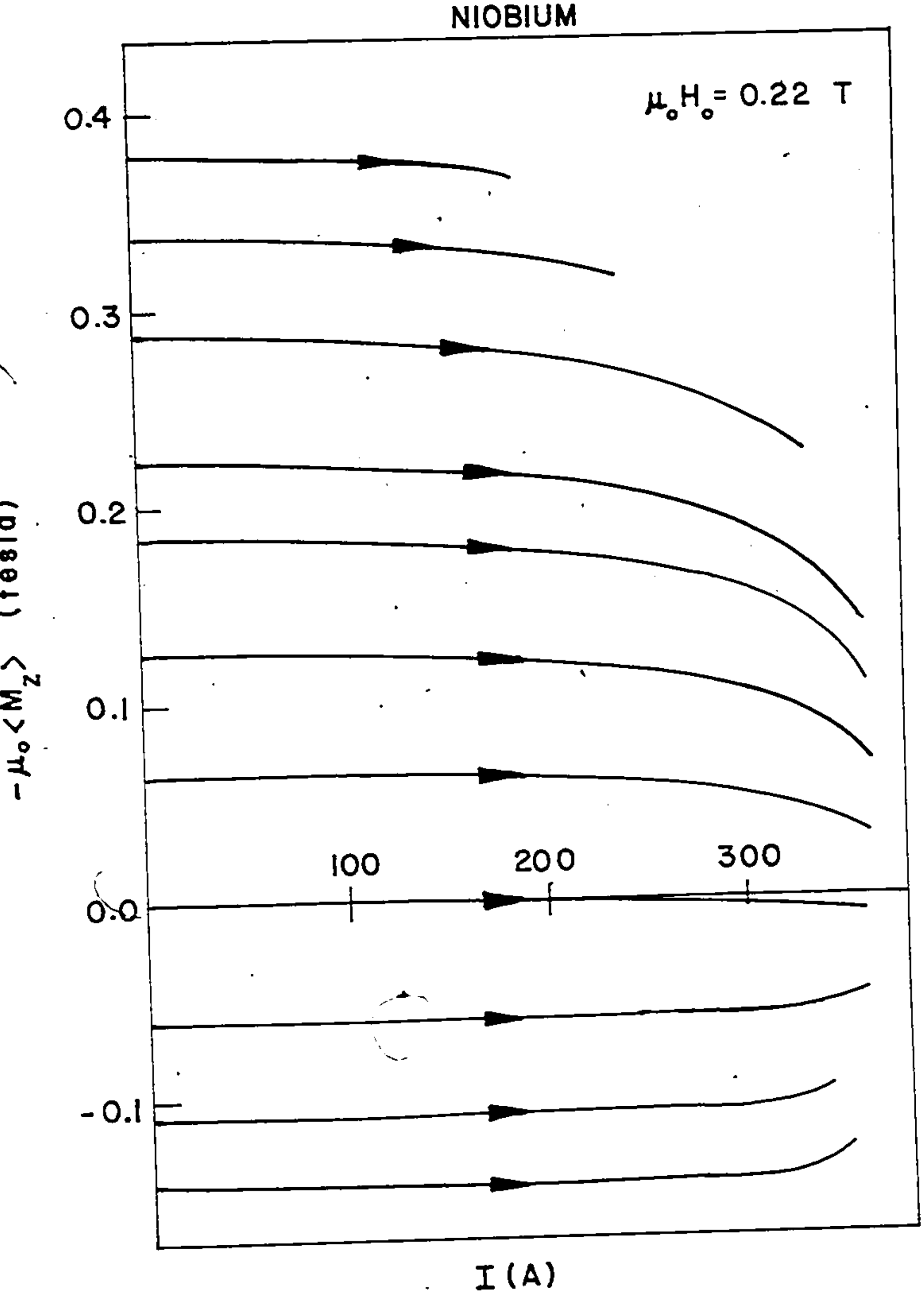


Figure 8-11 Variation of the axial magnetic moment $\langle M_z \rangle$ as the transport current I increases. Family of curves for $\mu_o H_o$ = 0.22 tesla.

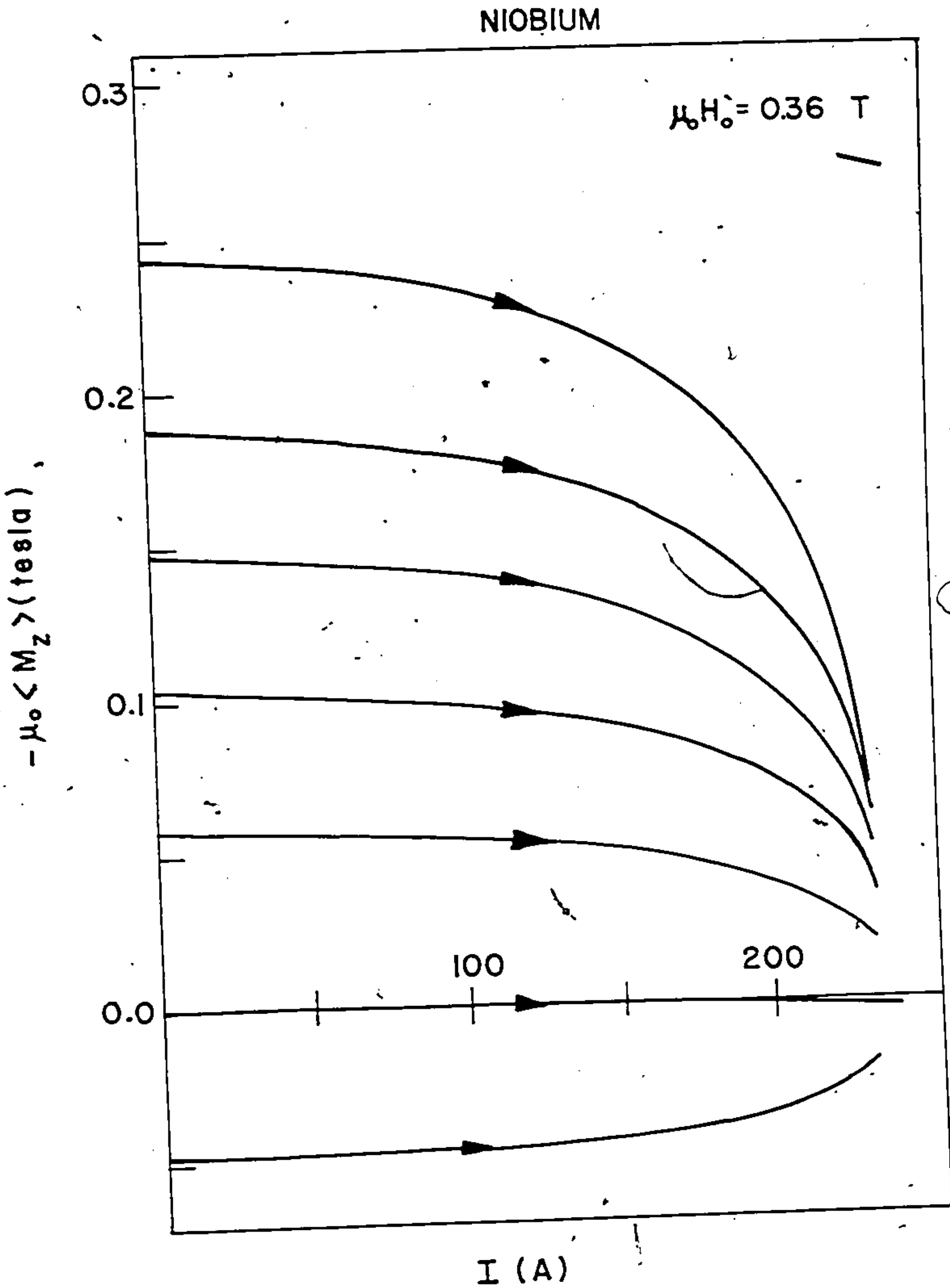


Figure 8-12 Variation of the axial magnetic moment $\langle M_z \rangle$ as the transport current I increases. Family of curves for $\mu_o H_o$ = 0.36 tesla.

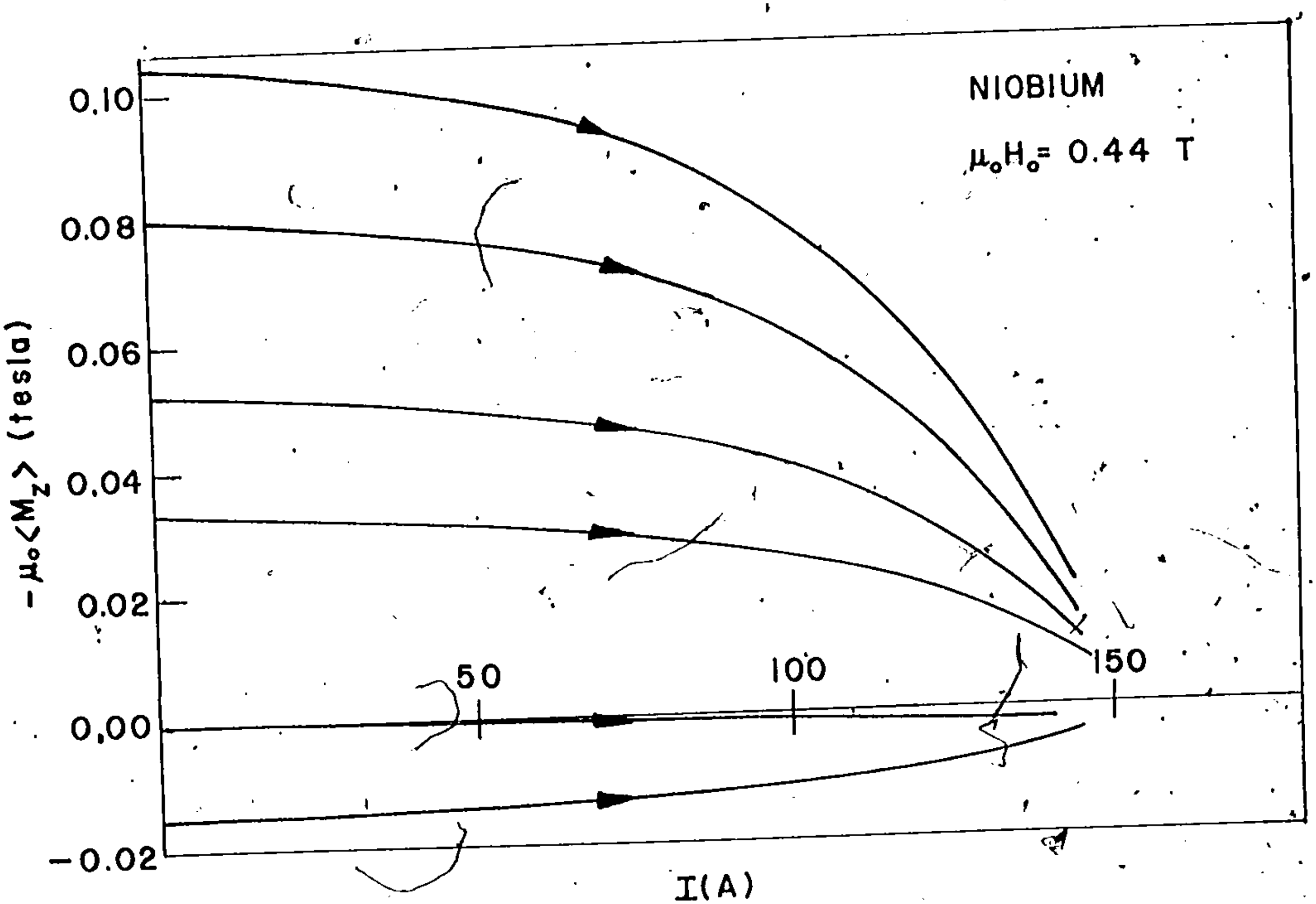


Figure 8-13 Variation of the axial magnetic moment $\langle M_z\rangle$ as the transport current I increases. Family of curves for $\mu_o H_o = 0.44$ tesla.

exhibit humped $I_c$ vs $H_o$ curves.

b) The $<M_z>$ vs I curves in Gauthier's samples terminate at or extrapolate to the same paramagnetic moment at $I_c$ in a given $H_o$, regardless of the initial axial magnetization. Also, the paramagnetic moments he observes at $I_c$ are quite appreciable.

In Gauthier's model, the hump in the $I_c$ curve and the locus of $<M_z>$ vs I are interrelated. Clearly (a) and (b) are at variance with the behaviour of the present Nb sample. It appears then that Gauthier's model is inapplicable in this case and a radically different solution must be envisaged.

It is not proposed in this thesis, to solve this formidable problem. However, a simple scheme is needed whereby the contribution of $|<M_z>|$ to the stored magnetic energy $U_z$ can be estimated as a function of I in various $H_o$. An empirical method for achieving this objective is now described and the results which it yields are presented.

i) It is assumed, for simplicity, that the $B_z$ profiles have constant slopes initially and at all later stages of their evolution as I is impressed and reaches $I_c$.

ii) The changes in $|<M_z>|$ with I in different $H_o$ are allowed for by letting the slope of the $B_z$ profiles become shallower as I increases.

Thus a mathematically and physically simple configuration for the $B_z$ profiles is used. These configurations, in which the critical current density $J_c$ is taken as spatially constant, are known as the Bean-London approximation (Bean 62, 64; London 63). Since the magnetic moments vary with I it is necessary to amend this simple picture. $J_c$ is still taken to be spatially constant but its magnitude is allowed to decrease monotonically as I increases. The reader is referred to the accompanying sketch.

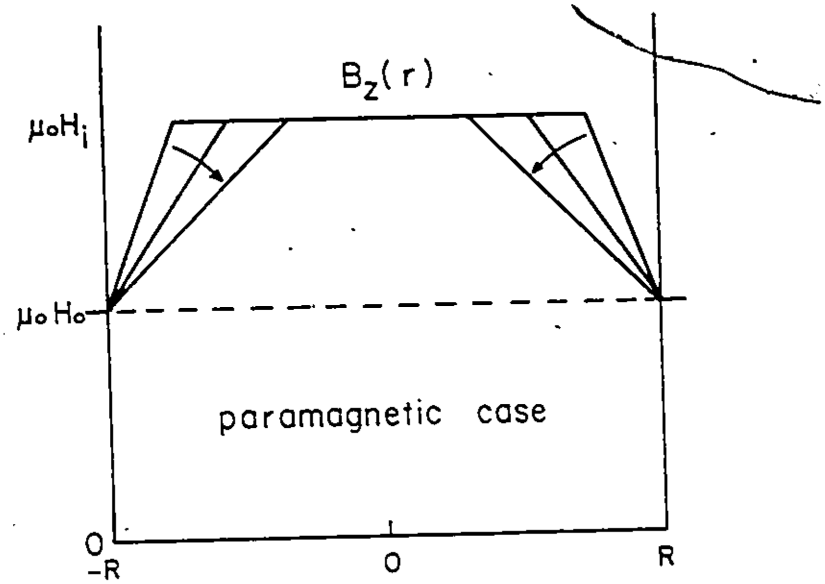


The empirical prescription taken to govern the variation of the spatially uniform, azimuthally circulating $J_c$ as the transport current I is impressed is the following,

$$J_c = \alpha f(\langle B\rangle) \{ 1 - (\frac{I}{I'_c})^2 \}^{\frac{1}{2}} \qquad (8\text{-}2)$$

where

$$f(\langle B\rangle) = \frac{1}{1 + e^{\sigma}(\frac{\langle B\rangle}{\mu_o H_{c2}} - b_e)} - C \qquad (8\text{-}3)$$

is an expression found useful in chapter 7 for describing the standard magnetization curves of the Nb and V specimens. $\langle B\rangle$ is the average magnetic induction defined as follows

$$\langle B\rangle = \frac{B_s + B_i}{2} \qquad (8\text{-}4)$$

where $B_s/\mu_o = \{ H_o^2 + (I/2\pi R)^2\}^{\frac{1}{2}}$ and $B_i$ is the magnetic induction threading the sample when it becomes superconducting.

It should be emphasized that no physical meaning whatsoever is ascribed to equation 8-2. It is only a computational tool for generating

$\langle M_z \rangle$ vs I curves which correspond with observations. In this respect, it is quite possible that other, much simpler, analytical formulae could be found which achieve the same end. It was convenient to use this particular expression since a program had already been written to compute $f(\langle B \rangle)$. Also, $f(\langle B \rangle)$ already contains the correct dependence on $\langle B \rangle$. An entirely equivalent, but more tedious approach in practice, would be to establish the particular Bean-London profile numerically from each experimental value of $\langle M_z(I) \rangle$ vs I.

The physics of the situation is completely contained in the $B_z$ profiles. Thus, any errors which are introduced do not arise from the numerical method used to establish the profiles, but from the assumption that the profiles are adequately described using the Bean-London approximation. Another advantage of the Bean-London approximation, apart from its obvious simplicity, is that the changes in the stored magnetic energy which would follow from replacing it by more sophisticated and realistic profiles can readily be estimated. This aspect will be pursued further later.

It is useful to indicate how $J_c$ is obtained in the Bean-London approximation. This same procedure could be used to evaluate $J_c$ from the experimental moments as a function of the transport current I (i.e., a point by point numerical method). It was found to be more convenient to use the procedure now described to obtain $J_c$ at I = 0 only, and then to exploit equation 8-2 to determine $J_c$ vs I (i.e. a continuous computational method). The reader is referred to the accompanying sketch where a paramagnetic $B_z$ profile is shown. (The algebra is not altered if $B_z$ is

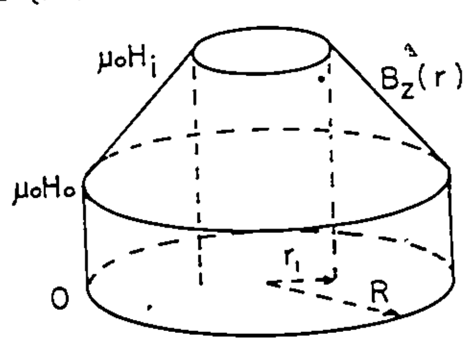

diamagnetic or hybrid.) The magnetic moment is obtained from evaluating the volume inside the truncated cone between the $H_o$ and $H_i$ planes. $H_i$ is a known quantity, since it is the axial magnetic field in which the wire became superconducting. The $B_z$ profile is described by

$$H(r) = H_i - J_c(r - r_1), \quad r_1 \leq r \leq R \tag{8-5a}$$

$$H(r) = H_i \quad , \quad 0 \leq r \leq r_1 \tag{8-5b}$$

From 8.5a it follows that

$$J_c = \frac{H_i - H_o}{R - r_1} \quad , \tag{8-6}$$

since $H(R) = H_o$. Introducing equation 8-5 in the definition for the magnetization gives:

$$\langle M_z \rangle = \frac{2}{R^2} \int_o^R \{ H(r) - H_o \} \, r \, dr,$$

and integrating leads, after some rearrangement, to:

$$\langle M_z \rangle = \frac{J_c \, (R^3 - r_1^3)}{3R^2} \tag{8-7}$$

Combining this with equation 8-6 gives

$$\langle M_z \rangle = \frac{(H_i - H_o)}{3R^2} \quad \{ R^2 + r_1 R + r_1^2 \} \tag{8-8}$$

which can readily be solved to yield $r_1$. $J_c$ is then found using equation 8-6. The sign of $J_c$ must be changed for diamagnetic and hybrid magnetic moments.

The computation is limited to establishing $J_c$ and $r_1$ at $I = 0$ in the manner just outlined, for a particular $\langle M_z \rangle$ vs I curve. Introducing this value for $J_c$ at $I = 0$ into equation 8-2, the appropriate $\alpha$ is determined. $J_c$ is then allowed to evolve using equation 8-2 and the concomitant migration of $r_1$ is determined from equation 8-6. A typical family of curves of $\langle M_z \rangle$ vs I which are generated by this procedure (equations 8-2 and 8-6) is displayed in Figure 8-14. In the calculations $\langle M_z \rangle$ has been allowed to decrease to zero by letting I grow to $I'_c$. It is of course, the $B_z$ profiles and hence $r_1$ (and $J_c$ when r = 0) which are of interest for subsequent calculations of the stored magnetic energy $U_z(I)$. This information, obtained in the process of mapping families of curves as shown in Figure 8-14, is retained in the computer program and used when needed.

It is important to indicate that in the exercise just described for calculating $J_c$ and $r_1$, the quantity $I'_c$ appearing in equation 8-2 is essentially another adjustable parameter at this stage of the analysis. This adjustable parameter varies with $H_o$. It is found that the observed series of families of curves of $\langle M_z \rangle$ vs I is reproduced by taking

$$I'_c = I'_{co} \{ 1 - ( \frac{H_o}{H_{c2}} )^2 \} \qquad (8\text{-}9)$$

where $I'_{co}$ = 500 A. Note that $I'_c$ exhibits a parabolic dependence on $H_o/H_{c2}$ and recall that the experimentally measured critical current $I_c$ also showed parabolic behaviour. Since the experimental $\langle M_z \rangle$ vs I curves terminate at $I_c$, with $|\langle M_z \rangle| > 0$, it is clear that the parameter $I'_c$ $(H_o)$ must be larger than $I_c(H_o)$. In the next chapter the quantity $I'_c$ will again be introduced in the description of the evolution of the $B_\theta$ profiles with I. In that context, physical significance will be ascribed to $I'_c$. It is important then to point out that $I'_c$ in the procedure just completed is the current obtained by extrapolating a family of observed $\langle M_z \rangle$ vs I curves until they intersect. In other materials studied by Gauthier this junction of the $\langle M_z \rangle$ curves occurs at $I'_c = I_c$, where $I_c$ is the maximum lossless current. In the present specimen $I_c$ and $I'_c$ are physically

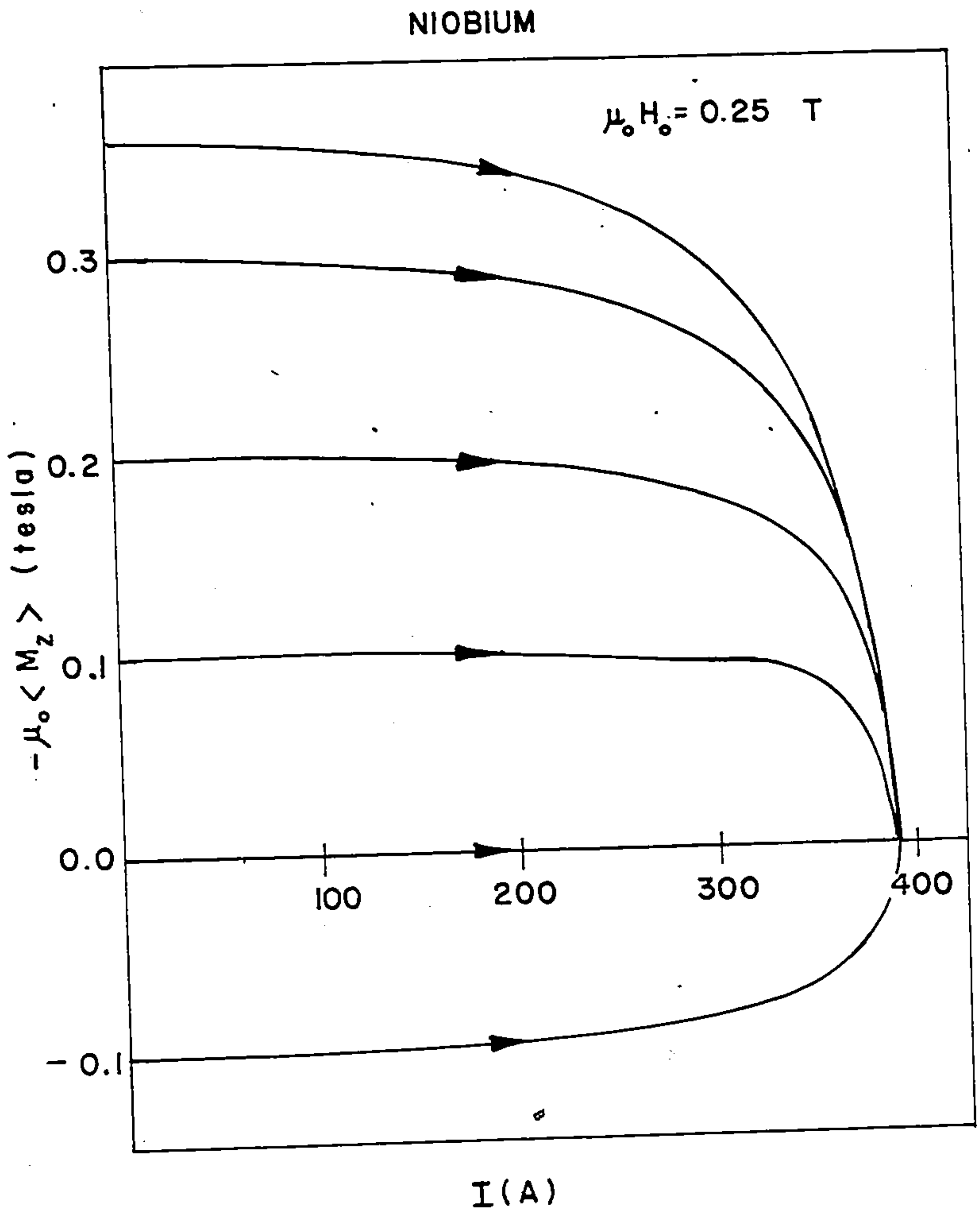


Figure 8-14 Variation of the axial magnetic moment $\langle M_z \rangle$ as the transport current I increases, as calculated from the model described in section 8.5. Family of curves for $\mu_o H_o = 0.25$ tesla.

related quantities, although they do not coincide. It is not surprising then that they display the same parabolic behaviour.

# Chapter 9

## Energy Dissipated During Flux Jumps

### 9.1 Introduction

The general expressions for the energy dissipated during a flux avalanche occurring in a long axially magnetized wire carrying a steady transport current I are developed. These formulae are exploited in order to calculate the energy dissipated, in the framework of Bean-London configurations for the initial $B_\theta$ and $B_z$ profiles. The families of curves of $U_{fj}$, the total energy released, as a function of the transport current I are then compared with the $V_z$ vs I curves presented in chapter 8. Since the similarities are quite noteworthy, a relationship between $V_z$ and $U_{fj}$ is assumed.

### 9.2 General Expressions for the Energy Dissipated

Consider a long (infinite) cylinder carrying a steady transport current I in a stationary longitudinal magnetic field $H_z$ with the attention focussed on a unit length of the cylinder. When the flux avalanche takes place, the rate of energy dissipation, according to the Poynting formulation can be written as:

$$\int_V \vec{E} \cdot \vec{J} \, dv = -\int_V \vec{H} \cdot \frac{\partial \vec{B}}{\partial t} \, dv - \int_S (\vec{E} \times \vec{H}) \cdot d\vec{s} \qquad (9\text{-}1)$$

This equation states that the rate of energy dissipation is governed by the rate of decrease of magnetic energy and the rate of flow of energy across the surface S surrounding the volume V.

The energy $U_{fj}$ dissipated in the superconductor during the flux avalanche is given by

$$U_{fj} = \iint_V (\vec{E}\,.\,\vec{J})\, dv\, dt = - \iint_V \vec{H}\,.\,\frac{\partial \vec{B}}{\partial t}\, dv\, dt - \iint_S (\vec{E} \times \vec{H}).d\vec{s}\, dt \qquad (9.2)$$

where the time integral is performed from the beginning to the end of the flux jump.

It is now assumed for simplicity that $\vec{B}(r) = \mu_o \vec{H}(r)$, and hence the permeability is taken to be $\mu = \mu_o$; the intrinsic Abrikosov diamagnetism is ignored. The first term on the right-hand-side of equation 9-2 then becomes:

$$\frac{1}{\mu_o} \iint_V \vec{B}.\,\frac{\partial \vec{B}}{\partial t}\, dv\, dt = \frac{\pi}{\mu_o} \int_o^R (B_{zf}^2 - B_{zi}^2) r\, dr + \frac{\pi}{\mu_o} \int_o^R (B_{\theta f}^2 - B_{\theta i}^2) r\, dr \qquad (9.3)$$

where R is the radius of the cylindrical volume V of unit length, $B_\theta$ and $B_z$ are the azimuthal and longitudinal components of the magnetic induction $\vec{B}(r)$. The subscripts i and f indicate the initial and final states, that is, the states before and after the flux jump.

The second term on the right-hand-side of equation 9-2 can be written:

$$\iint_S (\vec{E} \times \vec{H}).d\vec{s}\, dt = 2\pi R \int (E_z H_\theta - E_\theta H_z)_S\, dt \qquad (9\text{-}4)$$

for infinite cylindrical geometry, since $\vec{E} \times \vec{H}$ then has a radial component only. Also, by symmetry, $E_z$, $E_\theta$, $H_\theta$ and $H_z$ do not vary over the surface of the cylinder.

Using Faraday's law of induction $\nabla \times \vec{E} = - \partial\vec{B}/\partial t$ gives:

$$\int E_z\, dt = \int_o^R (B_{\theta f} - B_{\theta i})\, dr \qquad (9\text{-}5\text{ a})$$

and

$$R \int E_\theta\, dt = -2\pi \int_o^R (B_{zf} - B_{zi}) r\, dr \qquad (9\text{-}5\text{ b})$$

Introducing these results into equation 9-4 yields

$$-\iint_S (\vec{E} \times \vec{H}).d\vec{s}\, dt = 2\pi R H_\theta \int_o^R (B_{\theta f} - B_{\theta i})\, dr + 2\pi\, H_z \int_o^R (B_{zf} - B_{zi}) r\, dr \qquad (9\text{-}6)$$

Substitution of these results (equations 9-3 and 9-6) into 9-2 shows that the energy dissipated during the flux jump can be written as the sum of two contributions:

$$U_{fj} = U_z + U_\theta$$

where

$$U_\theta = 2\pi R H_\theta \int_0^R (B_{\theta f} - B_{\theta i})\, dr - \frac{\pi}{\mu_o} \int_0^R (B^2_{\theta f} - B^2_{\theta i}) r\, dr \qquad (9\text{-}7)$$

arises from the collapse of the $B_\theta$ profile at constant I, and,

$$U_z = 2\pi H_z \int_0^R (B_{zf} - B_{zi}) r\, dr - \frac{\pi}{\mu_o} \int_0^R (B^2_{zf} - B^2_{zi}) r\, dr \qquad (9\text{-}8\text{ a})$$

arises from the collapse of the $B_z$ profile at constant $H_z(R) = H_o$.

Making use of the relation

$$\frac{B_z(r)}{\mu_o} = H_z + M_z(r) \qquad (9\text{-}9)$$

this last expression can be rewritten more simply as

$$U_z = -\mu_o \pi \int_0^R (M^2_{zf} - M^2_{zi}) r\, dr \qquad (9\text{-}8\text{ b})$$

In order to utilize these general expressions (equations 9-7 and 9-8), the initial and final $B_z$ and $B_\theta$ profiles must be known. The final state is taken to be the normal state. Since $U_{fj}$ is related to the velocity of propagation of the flux avalanche in the electromagnetic mode it is important to note that this final normal state is reached when the flux avalanche occurs, and not as a consequence of joule heating in the wake of the avalanche. This conclusion that the superconducting state completely collapses to the normal state at the "front" of the flux avalanche is substantiated by measurements of the area under the pulses from the axial pick-up coils as the flux jump sweeps through them.

## 9.3 $U_\theta$ vs I

A stationary transport (D.C.) current I fills the cross-section of a normal conducting wire with a uniform current density $J_n = I/\pi R^2$ and the $B_\theta$ profile inside the wire, by Ampere's law is then:

$$B_\theta(r) = B_{\theta f}(r) = \mu_o \frac{J_n r}{2} = \frac{\mu_o}{2} \left(\frac{I}{\pi R^2}\right) r \qquad (9\text{-}10)$$

It is assumed that the normal state configuration of the azimuthal magnetic induction ensues from a total flux avalanche in agreement with the measurements, as indicated before.

The accurate determination of the initial $B_{\theta i}$ profiles in the superconducting state, before the flux avalanche, requires a detailed model. As indicated earlier, in this analysis the procedure is to adopt the Bean-London approximation and to take the axial current density $J_z(r) = J_s$ where $J_s$ is spatially constant and determined by the relation

$$J_s = \frac{I'_c}{\pi R^2} \qquad (9\text{-}11)$$

where

$$I'_c = I'_{co} \left\{1 - \left(\frac{H_o}{H_{c2}}\right)^2\right\} \qquad (9\text{-}12)$$

and $I'_{co}$ = 500 A at 4.2K for the Nb wire. The difference between $I'_c$ and $I_c$ has been discussed in the previous chapter. The choice of $I'_c$ instead of $I_c$ to govern the $B_{\theta i}$ profiles will be explained shortly. Note, according to equations 9-11 and 9-12 that although $J_s$ is spatially constant it nevertheless depends on $H_o$.

The transport current I fills a cylindrical sheath of thickness $\delta_o = R - r_o$ which expands radially inwards from the surface of the wire as I increases and eventually occupies the entire cross section when I attains $I'_c$ (see Figure 9-1).

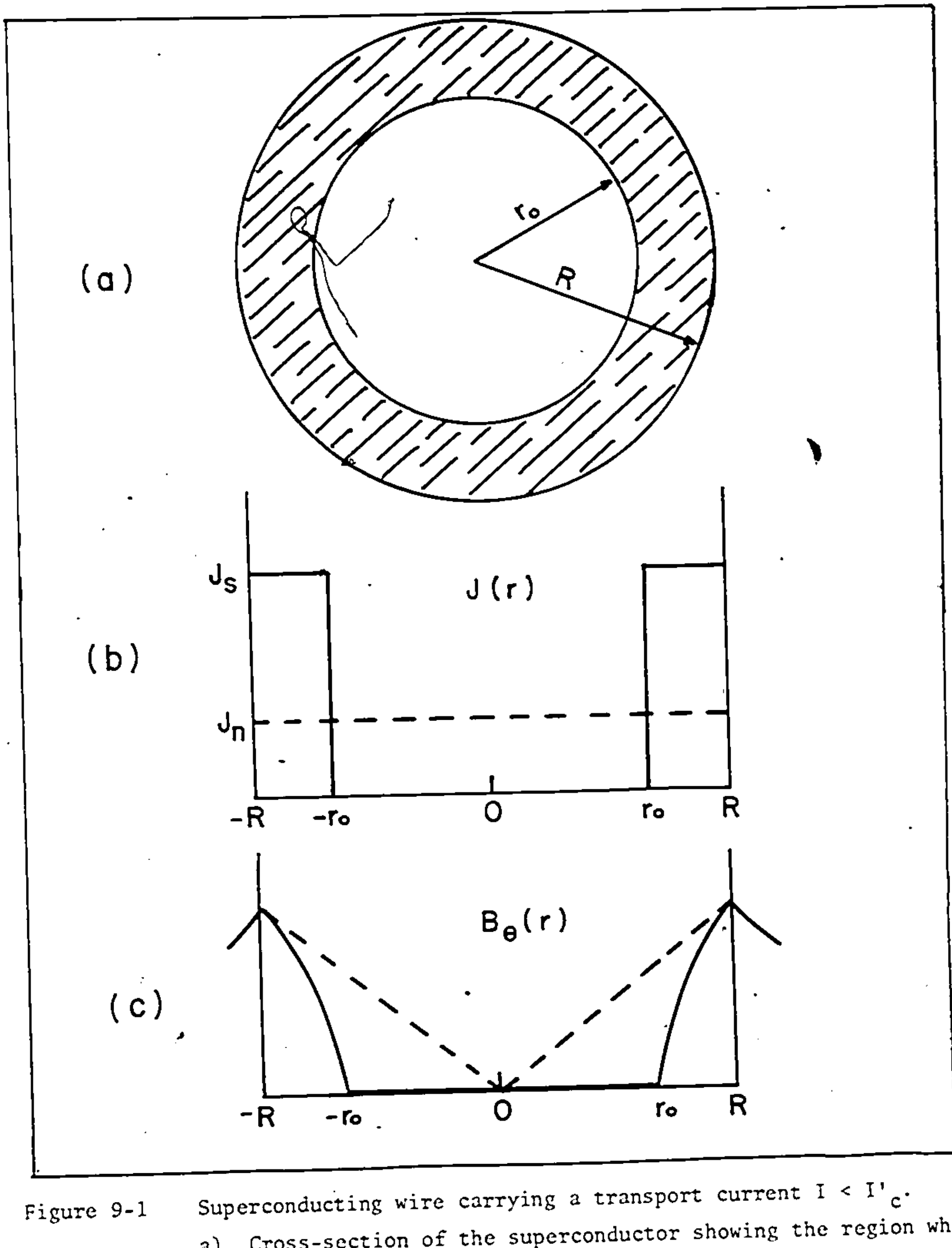


Figure 9-1 Superconducting wire carrying a transport current $I < I'_c$.
a) Cross-section of the superconductor showing the region where currents circulate, shaded region. b) and c) Current density $J(r)$ and azimuthal field $B_\theta(r)$ for a superconductor (full line) and an ordinary conductor (dashed lines) for the same transport current I.

Introducing equations 9-11 and 9-12 into Amperes law, there results:

$$B_{\theta i} = 0 \quad \text{when} \quad 0 \leq r \leq r_o \tag{9-13 a}$$

and

$$B_{\theta i}(r) = \frac{\mu_o I'_c}{2\pi R^2} \left(r - \frac{r_o^2}{r}\right) \quad \text{when} \quad r_o \leq r \leq R \tag{9-13 b}$$

where $r_o / R = (1 - I/I'_c)^{\frac{1}{2}}$. Equation (9-13 b) can be rewritten in terms of the variable $I/I'_c$ as:

$$B_{\theta i}(r) = \frac{\mu_o I'_c}{2\pi R} \left(\frac{r}{R}\right) \left\{1 - \left(\frac{R}{r}\right)^2 \left(1 - \frac{I}{I'_c}\right)\right\} \tag{9-13 c}$$

The current density distribution and the azimuthal field profile are illustrated in Figure 9-1. The growth of the thickness of the cylindrical sheath occupied by the transport current as I increases is given by:

$$\frac{\dot{\delta}_o}{R} = 1 - \left(1 - \frac{I}{I'_c}\right)^{\frac{1}{2}} \tag{9-14}$$

and is displayed in Figure 9-2.

Introducing these results for the initial and final $B_\theta$ profiles (equations 9-13 and 9-10) into the expression for the energy dissipated by the collapse of the azimuthal configuration while I is stationary (equation 9-7) and integrating gives

$$U_\theta = \frac{\mu_o I'^2_c}{8\pi} (1 - \gamma) \left[-\gamma - (\gamma + 1) \ln (1 - \gamma)\right] \tag{9-15}$$

where $\gamma = I/I'_c$. The variation of the energy $U_\theta$ with the transport current I is presented in Figure 9-3. The important features are that $U_\theta$ goes through a maximum and that $U_\theta$ and $U_z$ can be comparable in magnitude. Although the value of $I/I'_c$ at the point where the maximum occurs and the height of the maximum are model dependent, (since $B_{\theta i}(r)$ is model dependent) the occurrence of a maximum is a basic feature of the dependence of I. This can be appreciated by considering the sketches below in the

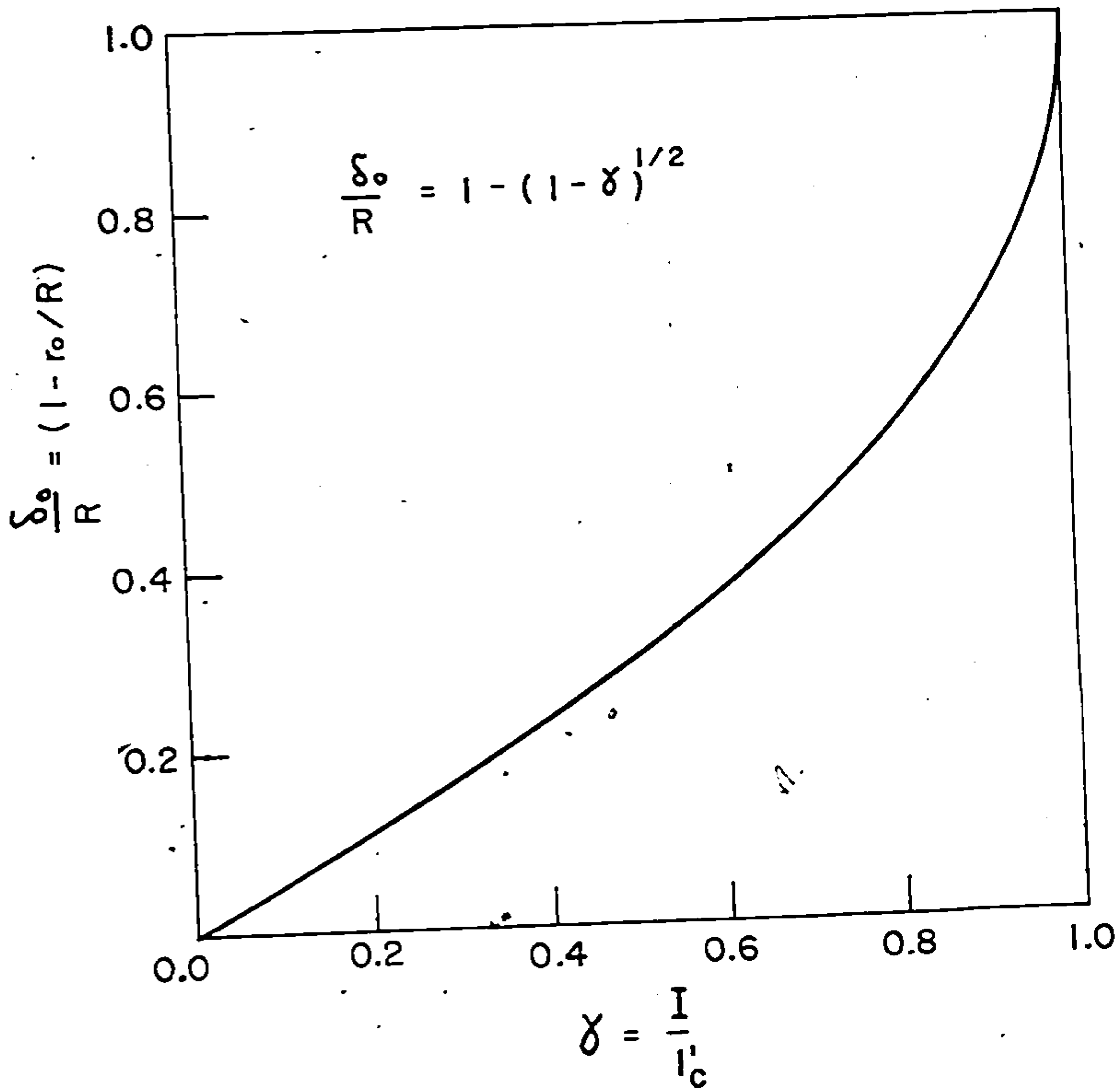


Figure 9-2 Thickness $\delta_o$ of the cylindrical sheath occupied by the transport current versus transport current (normalized quantities).

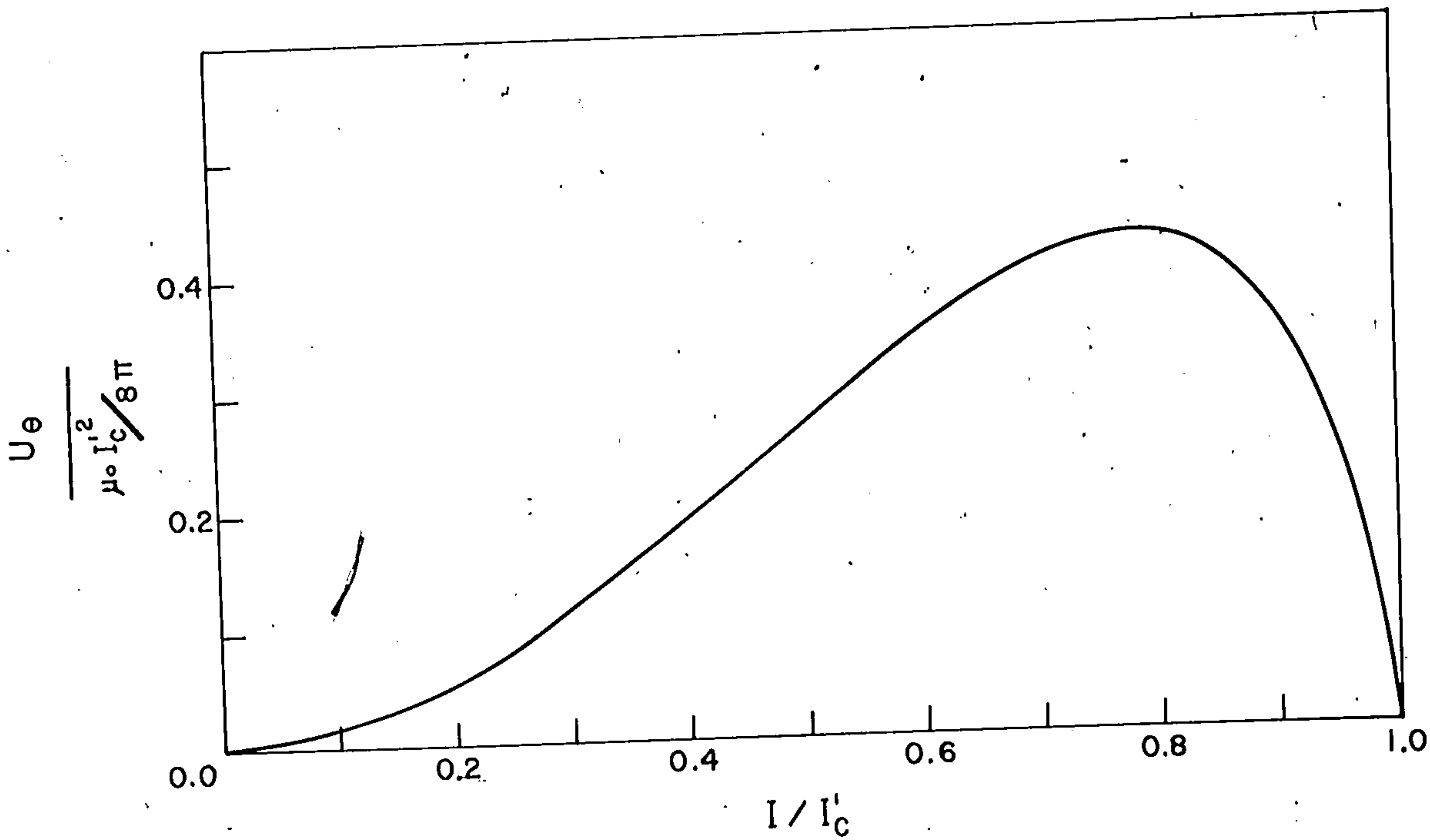


Figure 9-3 Variation of $U_\theta$ with the transport current I. (normalized quantities, see equation 9-15).

light of equation 9-7. With Bean-London approximation for the $B_{\theta i}$

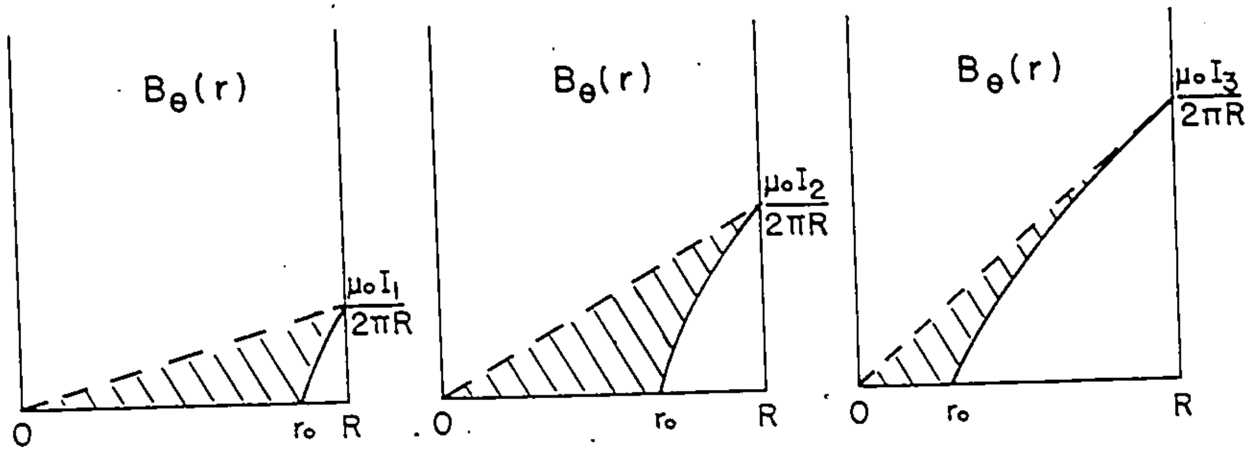


profile, the maximum in $U_\theta$ occurs at $\gamma \equiv I/I_c' \approx 0.77 = \gamma_c$. Furthermore, in this approximation the height of the maximum increases quadratically with $I_c'$.

## 9.4 $I_c'$ and $I_c$

Attention is now focussed on the concepts of $I_c$ and $I_c'$ and their physical meaning. The occurrence of a maximum in the $U_\theta$ vs I curve indicates that the configuration of the $B_\theta$ profile may be energetically unstable when $I/I_c'$ is in the vicinity of $\gamma_c$. It is conceivable then that the magnetic configuration may undergo a "spontaneous" flux avalanche under these circumstances, and there is no need to trigger a controlled flux jump by applying a heat pulse at one end of the wire as is done in these measurements when $I < I_c$. Note also that the total magnetic energy at $I/I_c' = \gamma_c$, when $H_o \neq 0$ and $\langle M_z \rangle = 0$ initially, is fractionally higher than indicated in Figure 9-3, since a small paramagnetic moment appears as I is raised to $I_c$. Thus the magnetic configuration is expected to be energetically more unstable at $I/I_c' = \gamma_c$ under the latter circumstances than when $H_o = 0$ and $\langle M_z \rangle = 0$.

The anticipated critical current, denoted by $I''_c$ can be estimated in the following manner. $J_c(B)$ is known from the analysis of the standard magnetization curve (Figures 7-7) in chapter 7. It is stipulated that the transport current flows straight down the wire. This is a reasonable assumption since the paramagnetic effect is very small for these specimens. It is then possible to compute $I''_c$ as a function of $H_o$ for the Nb wire using the definition

$$I''_c = 2\pi \int_0^R J_c(B(r))r\,dr \tag{9-16}$$

where $J_c(B)$ is given by the curve traced in Figure 7-7, and $B = (\mu_o^2 H_o^2 + B_\theta^2(r))^{1/2}$. Note that $I''_c$ is obtained on the assumption that $J_c(r)$ fills the entire cross-section of the wire and that the bulk pinning is isotropic. The $I''_c$ which is obtained in this manner corresponds approximately to $I'_c$ but deviates appreciably from $I_c$. It is observed that $I_c/I'_c \approx 0.84$, which is suggestively similar to $\gamma_c \approx 0.77$.

Finally, it is recalled that the curves of $\langle M_z \rangle$ vs I at constant $H_o$ do not meet at $I_c$ as observed by Gauthier in other materials and as expected from his model, but they do meet at $I'_c$ when extrapolated. All of these considerations lead to the following conclusion. In the present Nb wire, the measured critical current $I_c$ occurs before the cross-section of the wire is filled with axial current density. The appropriate quantity then to introduce in the Bean-London calculation of the $B_{\theta i}$ profiles is clearly $I'_c$ since $I'_c \approx I''_c$ and not $I_c$. These considerations also suggest that $I_c$ is determined by the onset of a spontaneous flux avalanche. It is possible also that, although the contact resistances are small, joule heating at the contacts contributes to depressing $I_c$ below $I'_c$ in the range of small $H_o$ (large $I_c$).

## 9.5 $U_z$ vs I

The profiles showing $B_z$ as a function of I, starting with different initial axial moments $\langle M_z\rangle$ and in various $H_o$ have been analyzed in detail in chapter 8 in the spirit of the Bean-London approximation. It is a straightforward matter now to calculate the energy $U_z$ on the assumption that $B_{zf} = \mu_o H_o$ and:

$$\frac{B_{zi}(r)}{\mu_o} = H_o \pm J_c (r - R), \text{ when } r_1 \leq r \leq R \qquad (9\text{-}17\text{ a})$$

and $$B_{zi}(r) = \mu_o H_i, \text{ when } 0 \leq r_1 \leq R \qquad (9\text{-}17\text{ b})$$

Introducing these results into the expression for $U_z$ (equation 9-8) and integrating, yields

$$U_z = \pi\mu_o J_c^2 \left( \frac{R^4}{12} - \frac{r_1^3 R}{3} + \frac{r_1^4}{4} \right) \qquad (9\text{-}18)$$

where $r_1$ and $J_c$ are computed from $\langle M_z\rangle$(I) as described in the previous chapter.

It is of interest to examine the variation of $U_z$ with $\langle M_z\rangle$ which follows from equations 9-18 and the expression for $\langle M_z\rangle$ derived in chapter 8 (equations 8-7 and 8-8). (a) If $r_1 = 0$ then equation 9-18 shows that $U_z$ increases quadratically with $J_c$ while equation 8-7 shows that $|\langle M_z\rangle|$ increases linearly with $J_c$. (b) With a fixed $J_c$, $U_z$ varies with $\langle M_z\rangle$ more rapidly than quadratically as shown in Figure 9-4, where the results of the calculation are presented in normalized form. The insert in this figure illustrates the family of $B_z$ profiles appearing in this calculation. In the Bean-London approximation this result applies regardless of whether the profiles are diamagnetic, paramagnetic or hybrid. Computations of this nature, using more realistic $B_z$ profiles, such as produced by the Kim approximation, reveal that $U_z$ exhibits a variety of

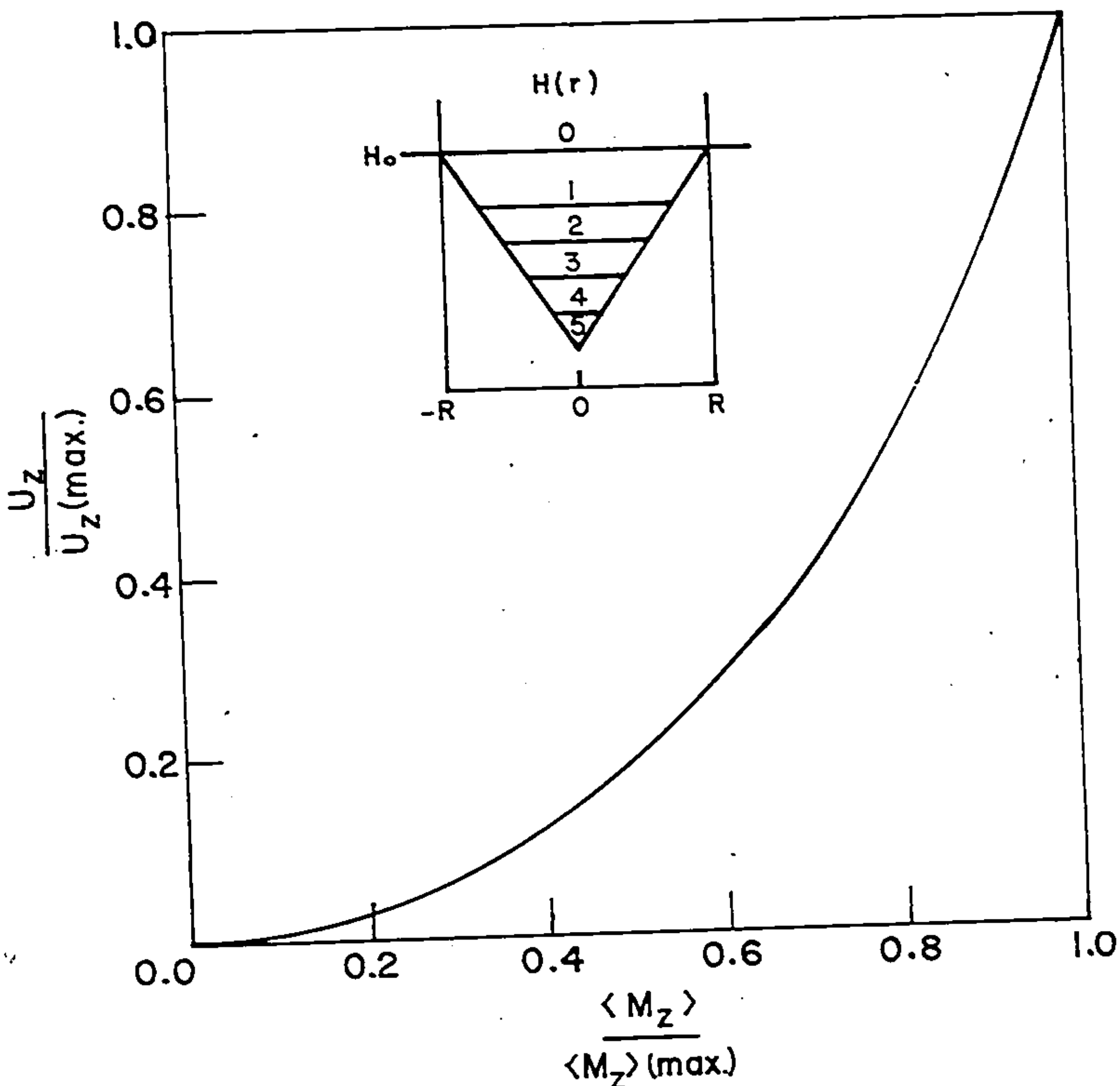


Figure 9-4 Variation of $U_z$ versus $\langle M_z \rangle$ for fixed $J_c$. Upon increasing $\langle M_z \rangle$ the axial field profiles labelled 0 to 5 are encountered.

dependences on $\langle M_z \rangle$ ranging from nearly quadratic to nearly cubic. In the Kim approximation and other analogous approximations the behaviour depends on $H_o/H_{c2}$ and the sign of $\langle M_z \rangle$ for a constant pinning strength parameter $\alpha$. This can readily be seen, since in the Kim approximation $J_c = \alpha/B$. These considerations are pertinent when the relationship between V and $U_{fj}$ is explored beyond the simple Bean-London framework exploited in this part of the thesis.

The degree of error which is introduced in the estimated $U_z$ from using the Bean-London approximation is now explored. This is done by considering a constant $\langle M_z \rangle$ and by progressively modifying the structure of the $B_z$ profiles associated with this fixed $\langle M_z \rangle$. Thus the $B_z$ profile is allowed to adopt various simple configurations as depicted in the inserts of Figure 9-5. Note that the first insert corresponds to the extreme case in which the bulk pinning parameter is zero. Thus, reversible and/or irreversible surface currents produce the abrupt change in B at the surface. The middle sketch can be regarded as an approximation to a convex-upward or convex-downward variation of $B_z(r)$ in the shoulders of the profile. The third sketch, or course, corresponds to the Bean-London limit for the chosen $\langle M_z \rangle$. A "sweep" through these various configurations is achieved in the computation by letting $\delta/R = 1 - r_1/R$ and $J_c$ vary while maintaining $\langle M_z \rangle$ constant. The locus of $U_z$ vs $\delta/R$ presented in Figure 9-5, shows that the maximum range of "error" ensuing from this variety of profiles is ± 20%. At first glance, this appears appreciable. It must be borne in mind in this assessment, however, that in practice the possible profiles will not span the wide spectrum shown here but only a portion of the curve. In particular, the left-hand region will not be encountered in the present specimen for the large moments that exist when flux avalan-

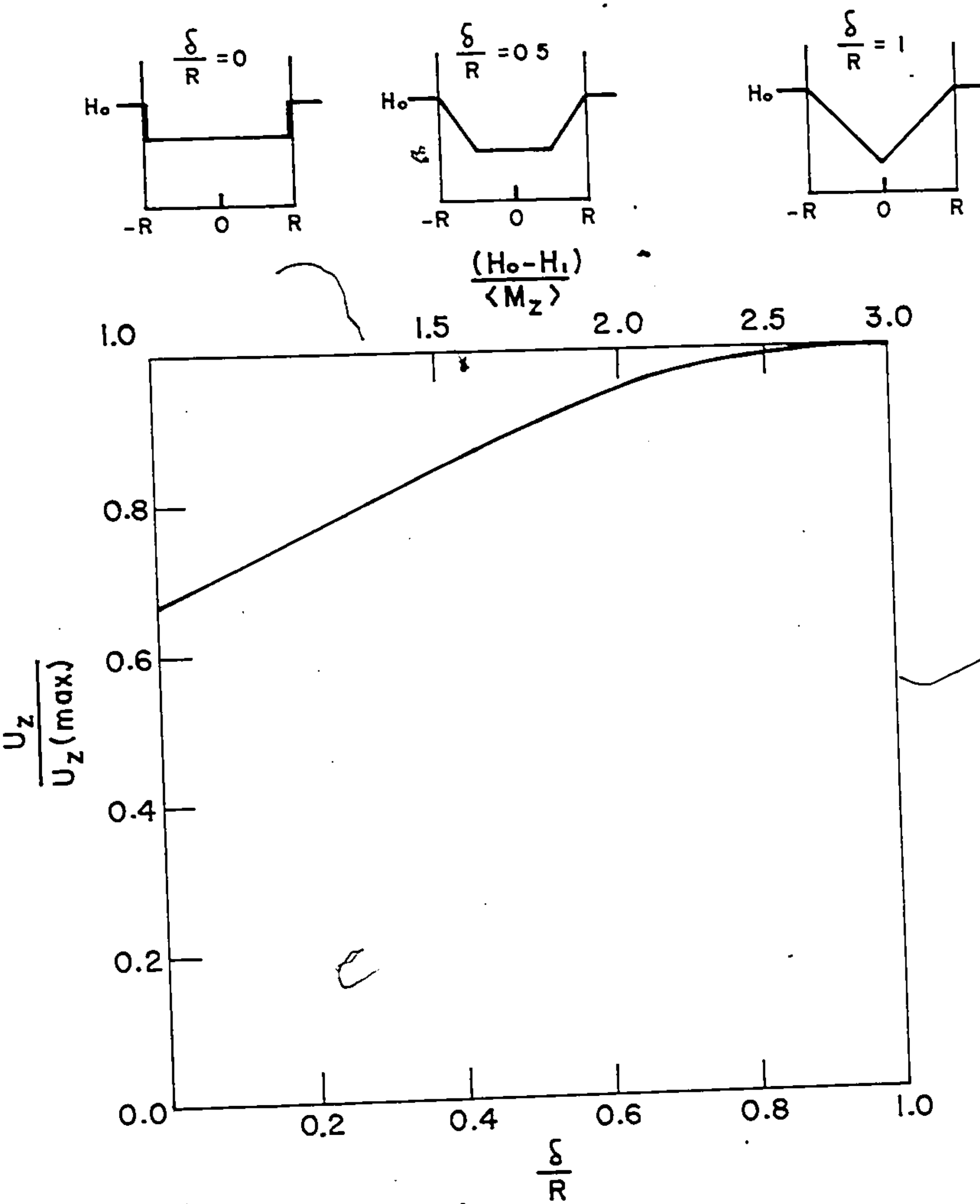


Figure 9-5 Variation of $U_z$ for different field profiles but with the same value of the magnetic moment $\langle M_z \rangle$. The parameter $\delta/R = 1 - r_1/R$ characterizes the profiles. $U_{z\ max} = \pi\mu_o J_c^2 \frac{R^4}{12} = \frac{3}{4}\pi\mu_o R^2 \langle M_z \rangle^2$.

ches occur. The uncertainty in the estimates of $U_z$ in most situations is probably less than or of order ± 10%, in the author's opinion.

## 9.6 Results of Calculations of $U_{fj}$

Proceeding in the Bean-London context that has been described in the two preceding sections, sets of families of curves of $U_{fj}$ vs I were calculated. In the calculations, families of curves are chosen such that the initial ± $\langle M_z \rangle$ correspond to the values encountered in the measurements of $V_z$ vs I reported in chapter 8. Also, in the computations the same values for $H_o/H_{c2}$ (including $H_o = 0$) that were selected for measurements are introduced. Thus the theoretical curves of $U_{fj}$ vs I span the full spectrum of the previously given extensive observations on the Nb specimen. The results of this exercise are presented in Figures 9-6 through 9-10. These figures should be examined in sequence in conjunction with the corresponding series of Figures in chapter 8 (Figures 8-1 through 8-5) which display the experimental data for $V_z$ vs I.

It is remarked that the major trends and the salient features of the experimental $V_z$ vs I curves are surprisingly well reproduced by the estimated $U_{fj}$ vs I curves. This correspondence, in the author's view is especially noteworthy since in the experimental curves (i) the helical (rotational) mode of propagation plays a significant role and distorts the curves, where electromagnetic propagation occurs, in a continuous way, since $V_z = V \cos \phi$ , (ii) the data for $V_z$ appears regardless of whether the thermal or electromagnetic mode of propagation prevails. Furthermore, in the computed $U_{fj}$ vs I curves, no account is taken of the observation that a threshold energy $U_c$ is required for a flux avalanche to propagate. The horizontal lines in Figures 9-6 through 9-10,

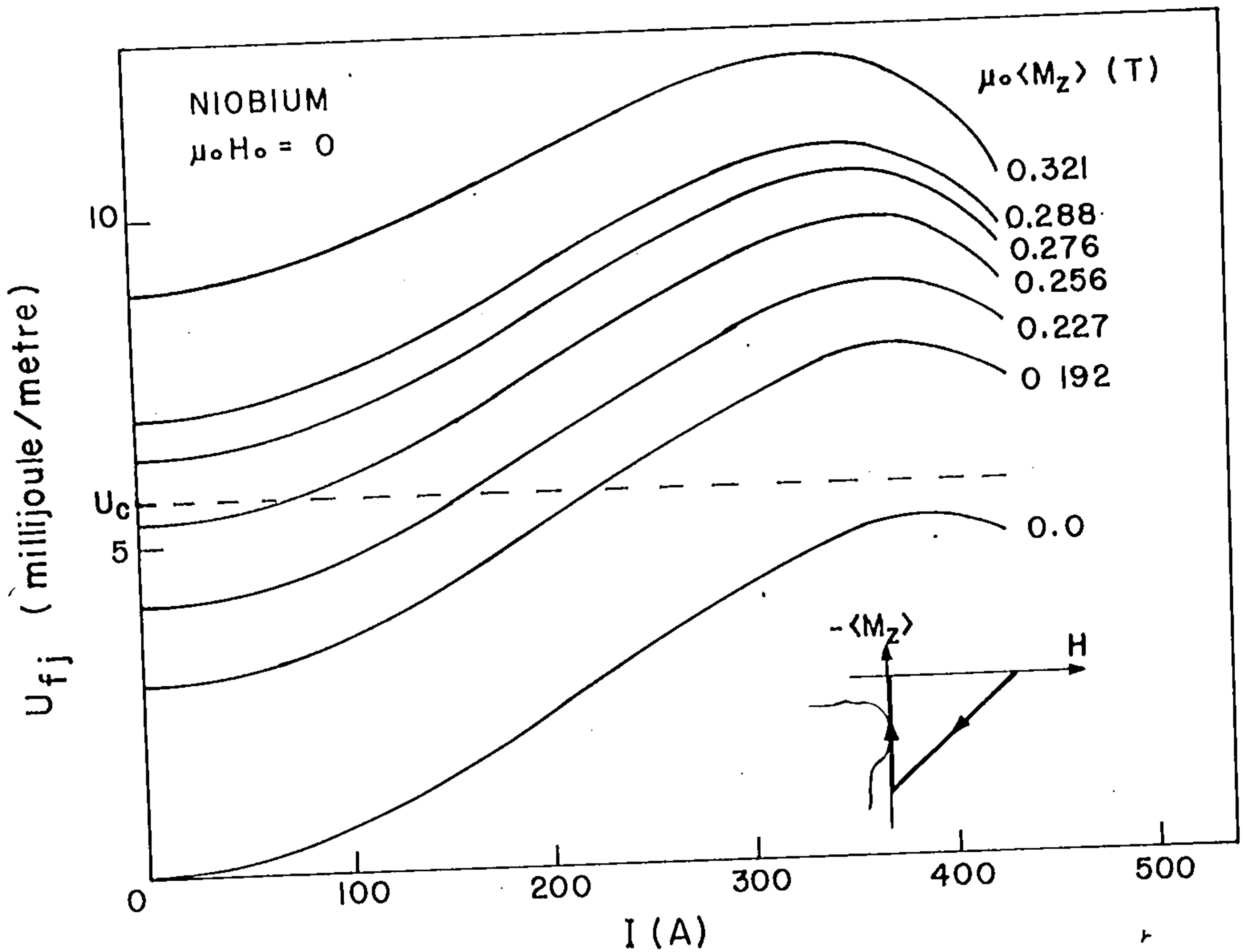


Figure 9-6 Energy $U_{fj}$ dissipated during a flux jump as a function of the transport current I and for several initial axial moments $\langle M_z \rangle$ . $(\mu_o H_o = 0)$.

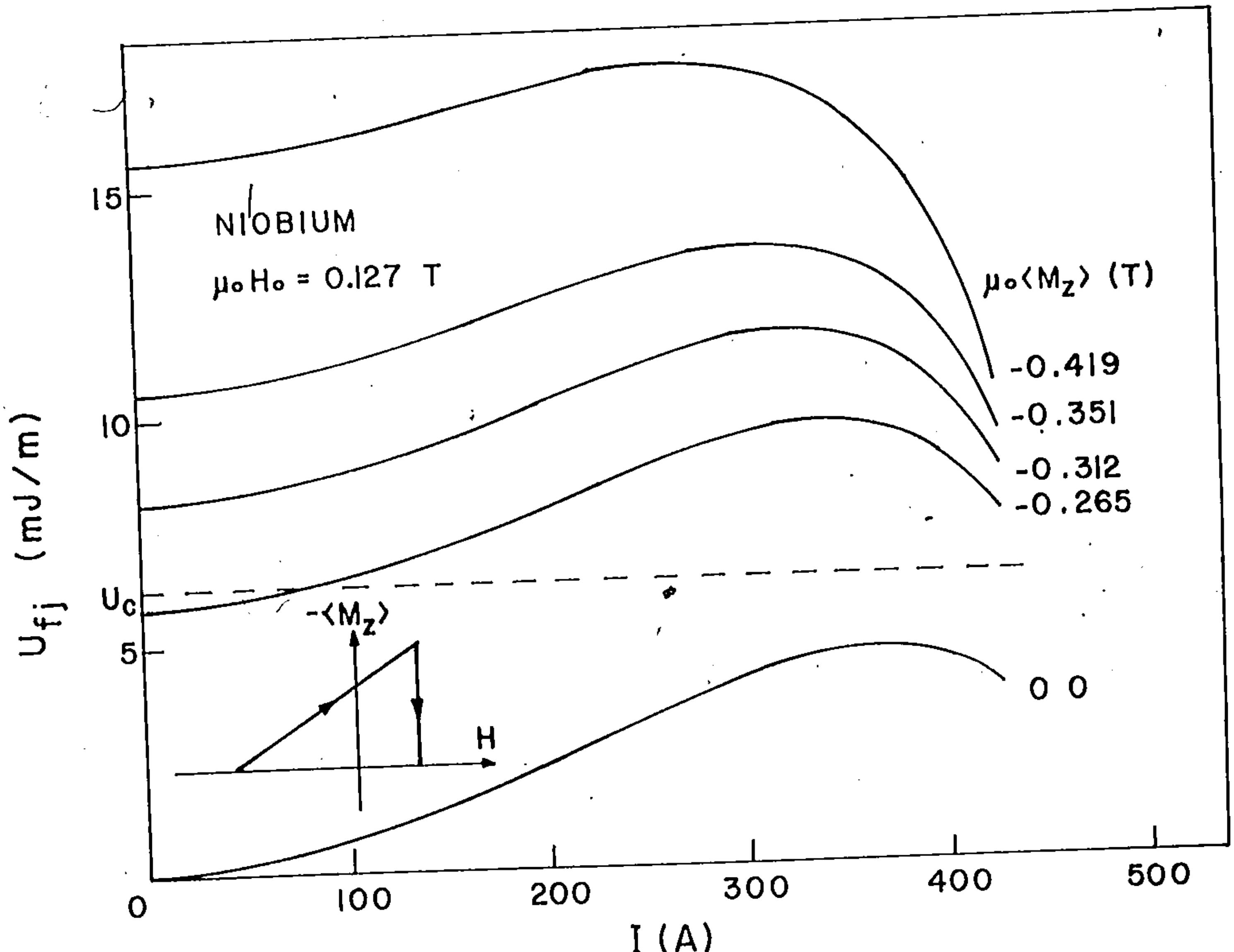


Figure 9-7 Energy $U_{fj}$ dissipated during a flux jump as a function of the transport current I and for several initial axial moments $\langle M_z \rangle$. ($\mu_o H_o$ = 0.127 tesla).

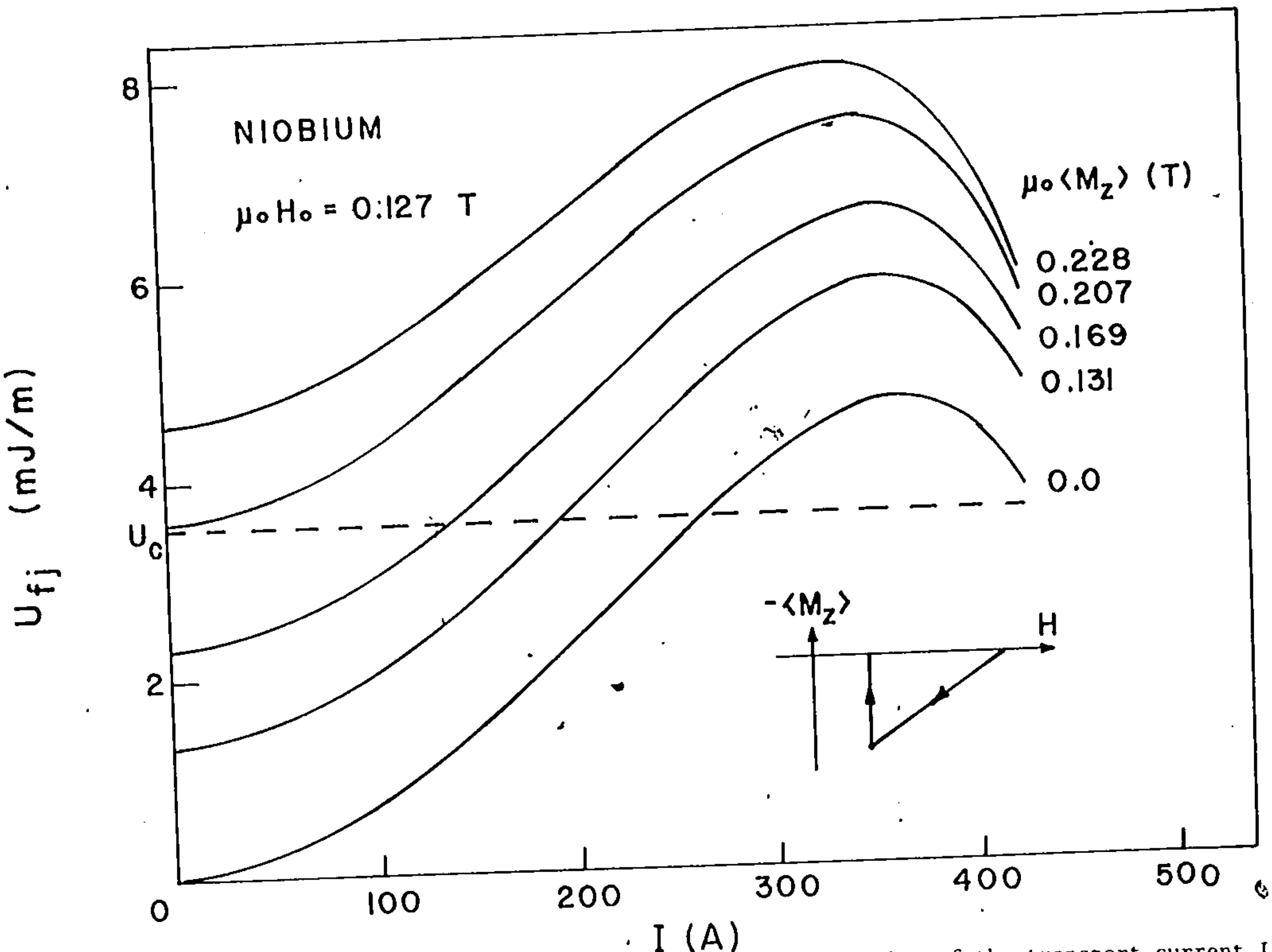


Figure 9-8 Energy $U_{fj}$ dissipated during a flux jump as a function of the transport current I and for several initial axial moments $\langle M_z \rangle$ . $(\mu_o H_o = 0.127$ tesla).

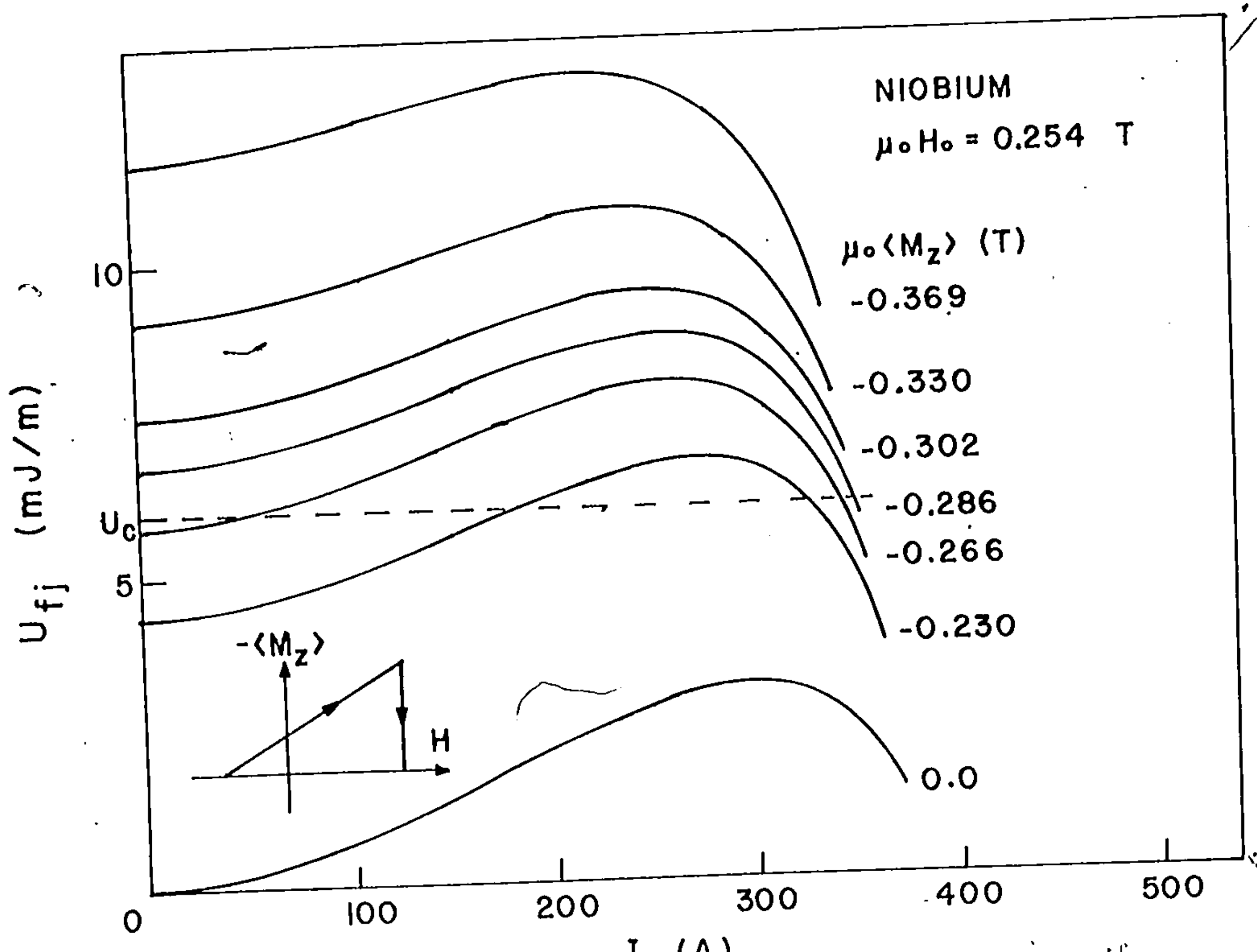


Figure 9-9 Energy $U_{fj}$ dissipated during a flux jump as a function of the transport current I and for several initial axial moments $\langle M_z \rangle$ . ($\mu_o H_o$ = 0.254 tesla).

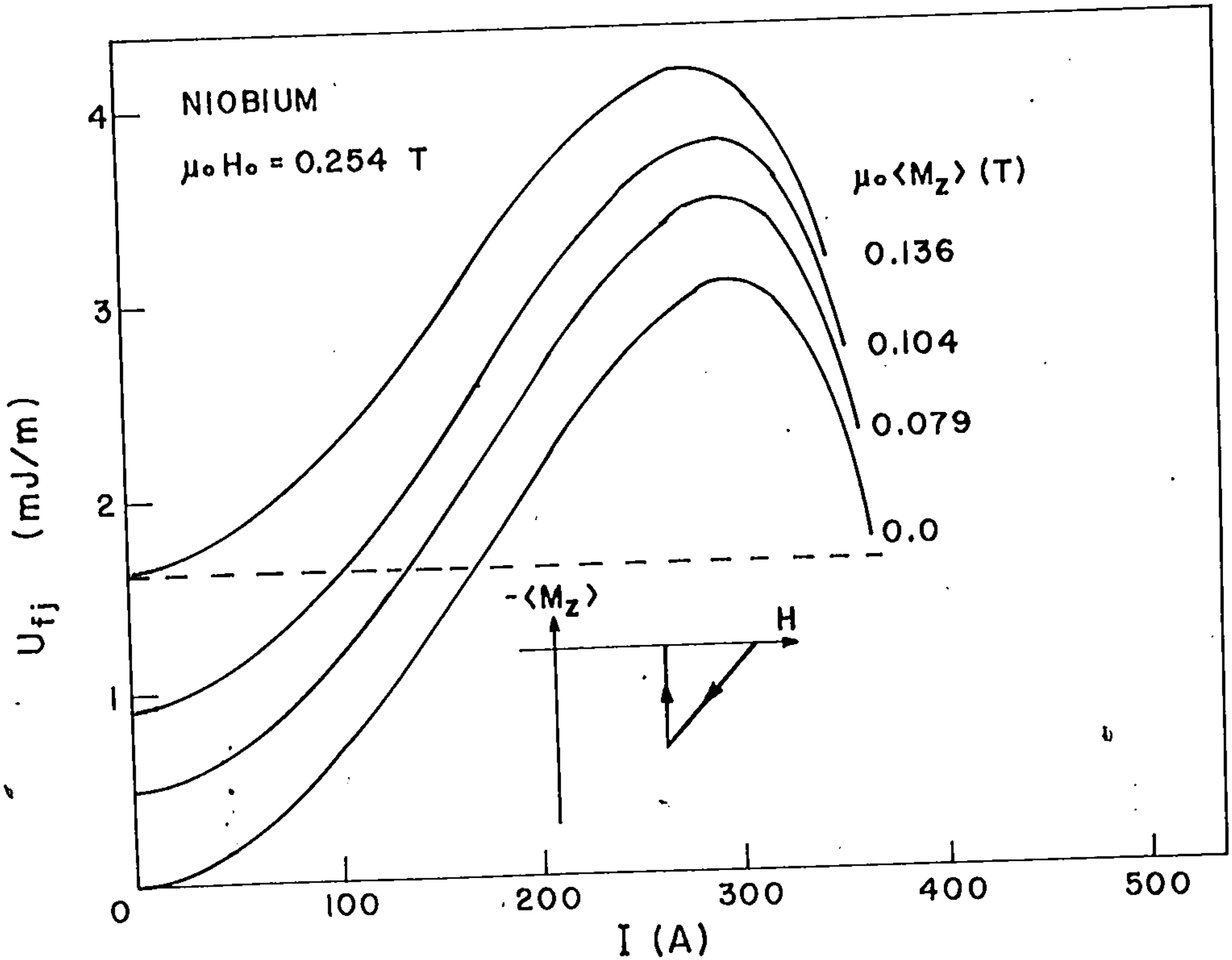


Figure 9-10 Energy $U_{fj}$ dissipated during a flux jump as a function of the transport current I and for several initial axial moments $<M_z>$ . $(\mu_o H_o = 0)$.

indicate the estimated threshold energy for each situation. These estimates are obtained from noting the magnetic moment $\langle M_z \rangle_c$ at $I = 0$ which is necessary for propagation of a flux avalanche to take place. The magnetic energy $U_z$ associated with the threshold magnetic moments $\langle M_z \rangle_c$ is calculated as described in the previous section.

Figure 9-11 illustrates the variation with I of the fractional contribution of $U_z$ and $U_\theta$ to $U_{fj}$. This particular curve is calculated for the situation where $\mu_o H_o = 0.255$ tesla and the initial magnetic moment $\mu_o \langle M_z \rangle = -0.23$ tesla. Analogous behaviour but with a different "mix" of $U_z$ and $U_\theta$ will be encountered for other situations. Note that $U_z$ is a maximum at $I = 0$ and decreases monotonically to 0 at $I_c'$. This is a direct consequence of the following; (i) the observations that $|\langle M_z \rangle|$ decreases monotonically from 0 to $I_c$, (ii) with the magnetic moment $\langle M_z \rangle(I)$ the associated $B_z$ profile varies continuously through simple Bean-London configurations as I increases and (iii) $I_c'$ is determined by extrapolating the experimental $\langle M_z \rangle$ curves to zero. $U_\theta$, after traversing a maximum, descends precipitously to zero at a limiting current $I_c'' \cong I_c'$. It is recalled that $I_c''$ is defined as the transport current which fills the cross-section of the wire. The observations and the interpretation given indicate that $I_c''$ and $I_c'$ coincide closely. The experimental data, however, terminates at $I_c < I_c' \tilde{\approx} I_c'$, presumably because the magnetic configuration undergoes a flux avalanche at this point and/or (but more improbably) joule heating is generated at the current contacts.

## 9.7 $V_z$ vs $U_{fj}$ and Threshold Energy

Lets now proceed on the basis that there exists a functional relationship between the velocity of propagation of the flux avalanches and the magnetic energy $U_{fj}$. An attempt is made to extract information about

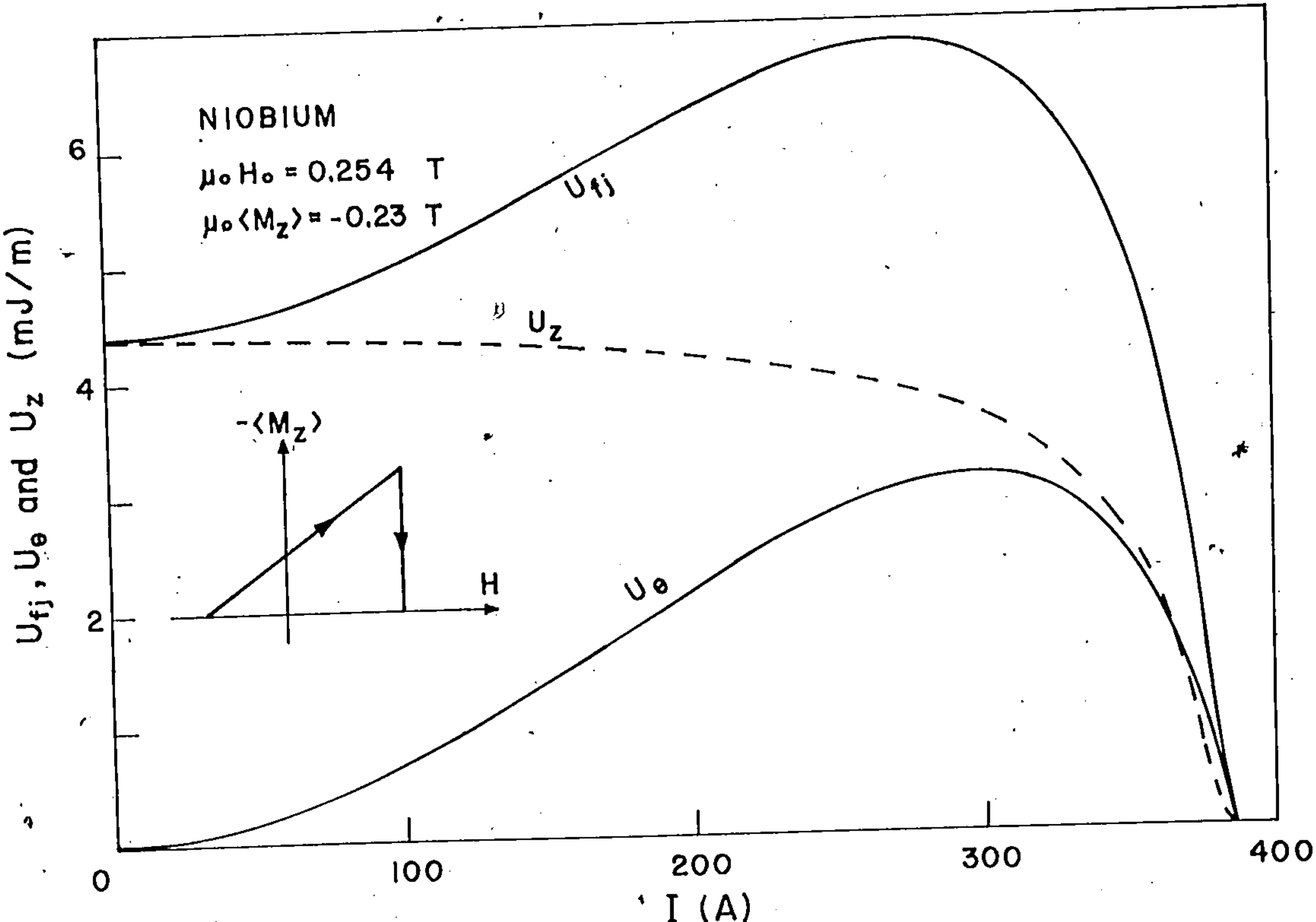


Figure 9-11 Fractional contribution $U_z$ and $U_\theta$ to $U_{fj}$ versus I . $\mu_o\langle M_z\rangle$ = -0.23 tesla and $\mu_o H_o$ = 0.254 tesla.

this relationship in the following manner. Continuous curves are drawn through the experimental data for $V_z$ vs I displayed in Figures 8-1 through 8-5. At regular intervals along these curves $U_{fj}$ is computed following the procedure described earlier i.e., from $<M_z>$ at I, $U_z$ is estimated and introducing $I/I_c'(H_o)$ into equation 9-15 permits the evaluation of $U_\theta$. Attention is then focussed on the curves or portions of the curves where electromagnetic propagation clearly determines $V_z$. In the next chapter this exercise will be repeated but using $V = V_z \cos\phi(I)$ instead of V.

The plots of $V_z$ vs $U_{fj}$ are displayed in Figures 9-12 through 9-16. These graphs corroborate the view that $V_z$ depends strongly on $U_{fj}$. The appreciable scatter in the data points, however, indicates that other features also play an important role. Nevertheless continuous lines are drawn through the data points and these curves are presented in juxtaposition in Figure 9-17. For each curve the threshold energy $U_c$ for the onset of the electromagnetic mode of propagation can be estimated. It is evident that the curves shift horizontally by an amount which depends on $H_o$ and the sign of $<M_z>$. For the three curves where $<M_z>$ is paramagnetic, the trend is clearly towards a decrease of $U_c$ with $H_o$ increasing (curves 1, 2 and 3). The curve where $H_o = 0$ belongs physically in the paramagnetic group since $<B_z> > H_o = 0$. This decrease of $U_c$ indicates that the average magnetic induction $<B_z>$ plays an important role in governing $V_z$. This suggests strongly that the flux flow resistivity $\rho(r,t) \doteq \rho_n B(r,t)/H_{c2}(T)$ which enters in the determination of the rate of energy dissipation must be taken into account, as well as the amount of energy dissipated, in calculating $V_z$. Curves 4 and 5 of Figures 9-17 (where the initial $B_z$ profile is of the hybrid type) also fit into this pattern. It must then be kept in mind that the flux flow resistivity

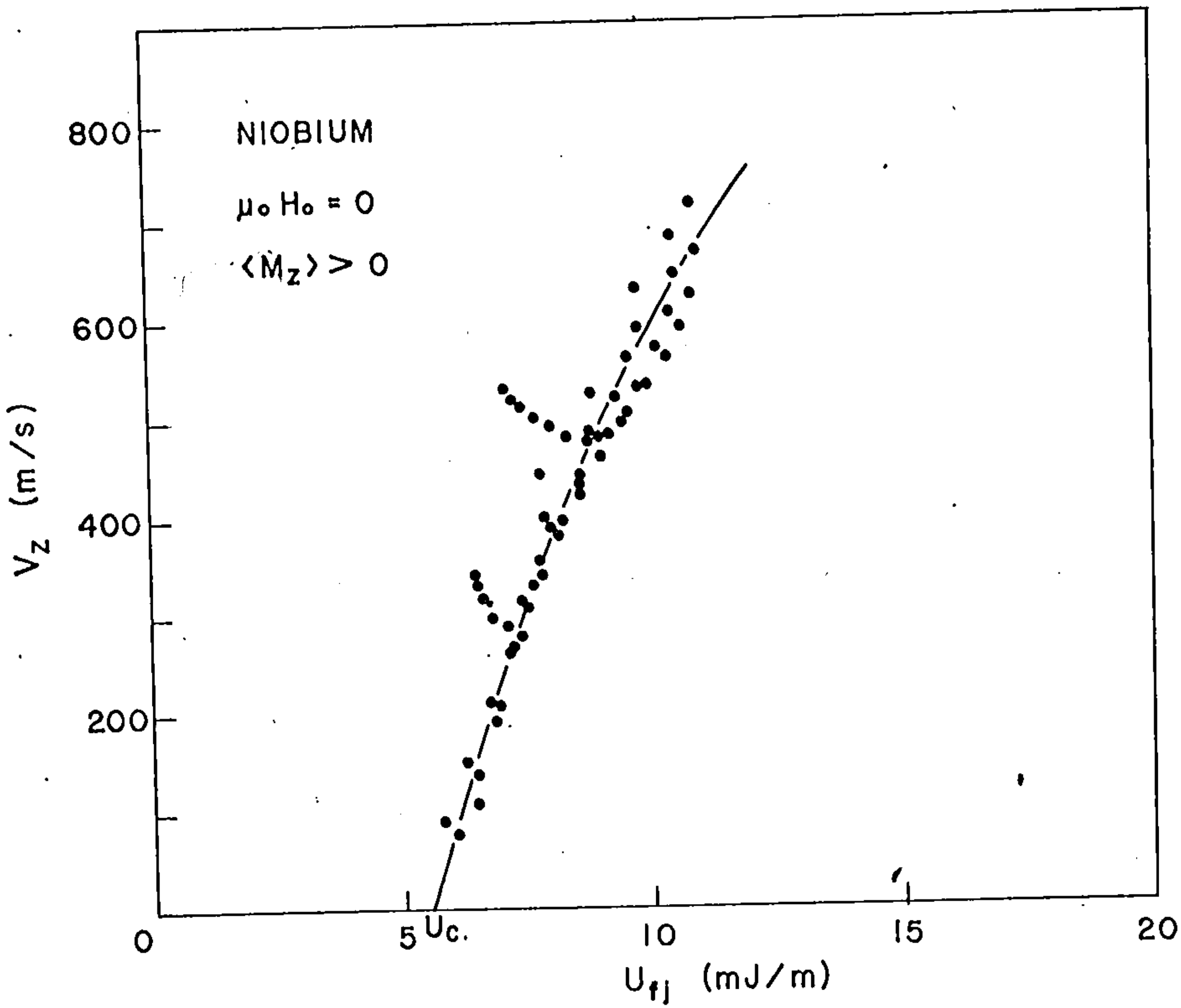


Figure 9-12 Experimental velocity $V_z$ versus calculated energy $U_{fj}$ for $H_o = 0$. The plotted data cover the complete range of transport current I and magnetic moment $\langle M_z \rangle$ where electromagnetic propagation occurs.

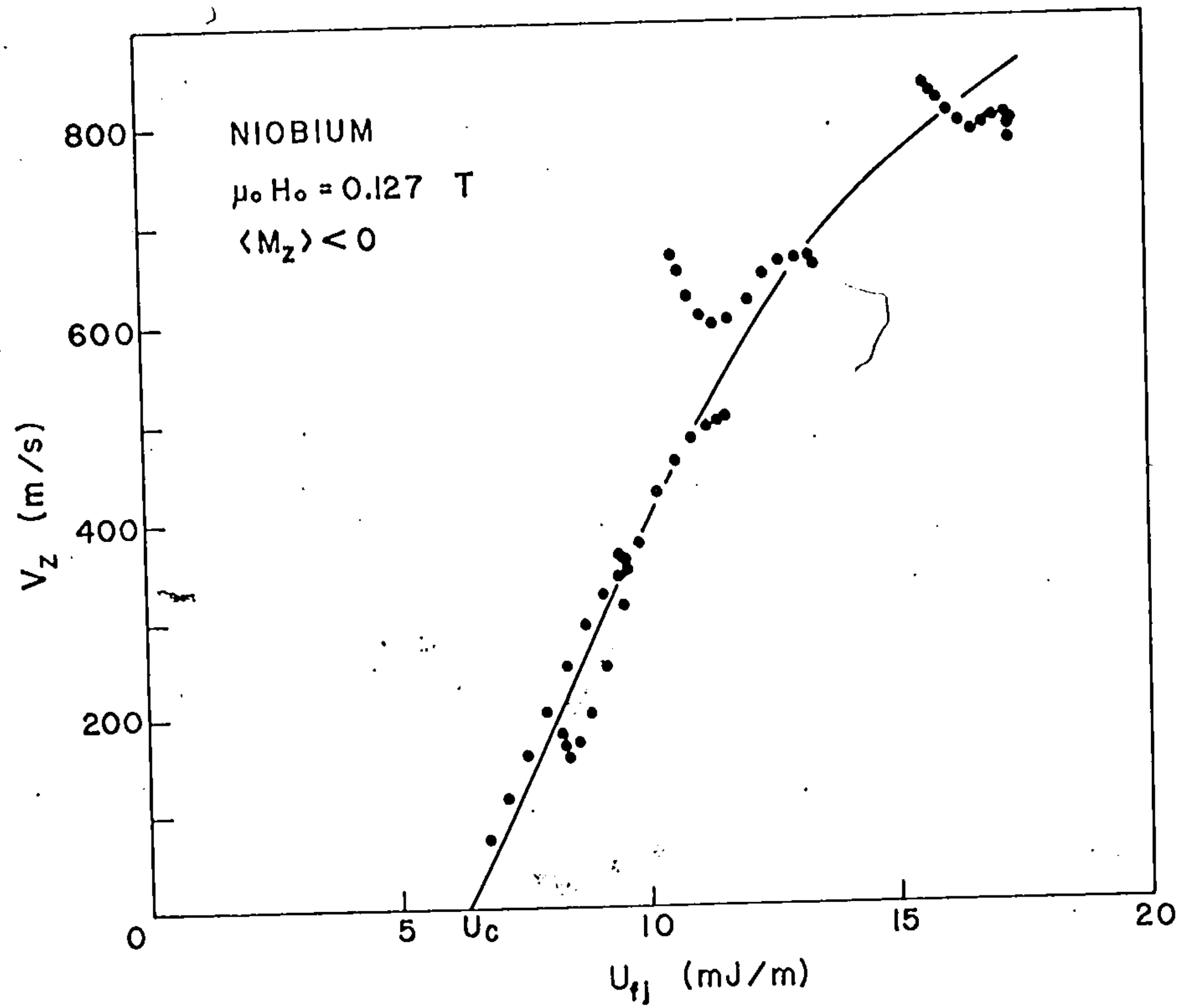


Figure 9-13 Experimental velocity $V_z$ versus calculated energy $U_{fj}$ for $\mu_o H_o = 0.127$ tesla. The plotted data cover the complete range of transport current I and hybrid magnetic moment $\langle M_z \rangle$ where electromagnetic propagation occurs.

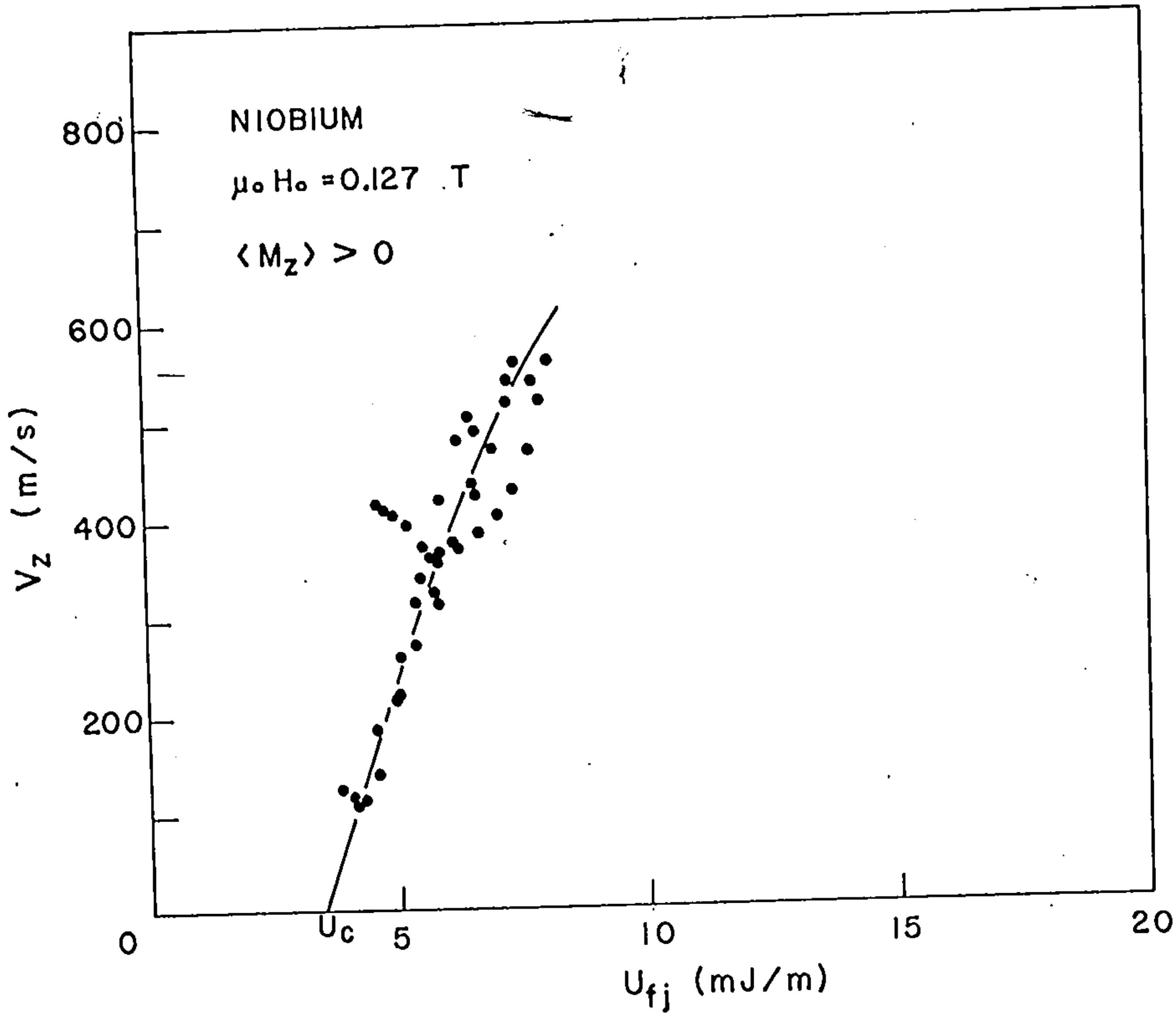


Figure 9-14 Experimental velocity $V_z$ versus calculated energy $U_{fj}$ for $\mu_o H_o$ = 0.127 tesla. The plotted data cover the complete range of transport current I and paramagnetic moment $\langle M_z \rangle$ where electromagnetic propagation occurs.

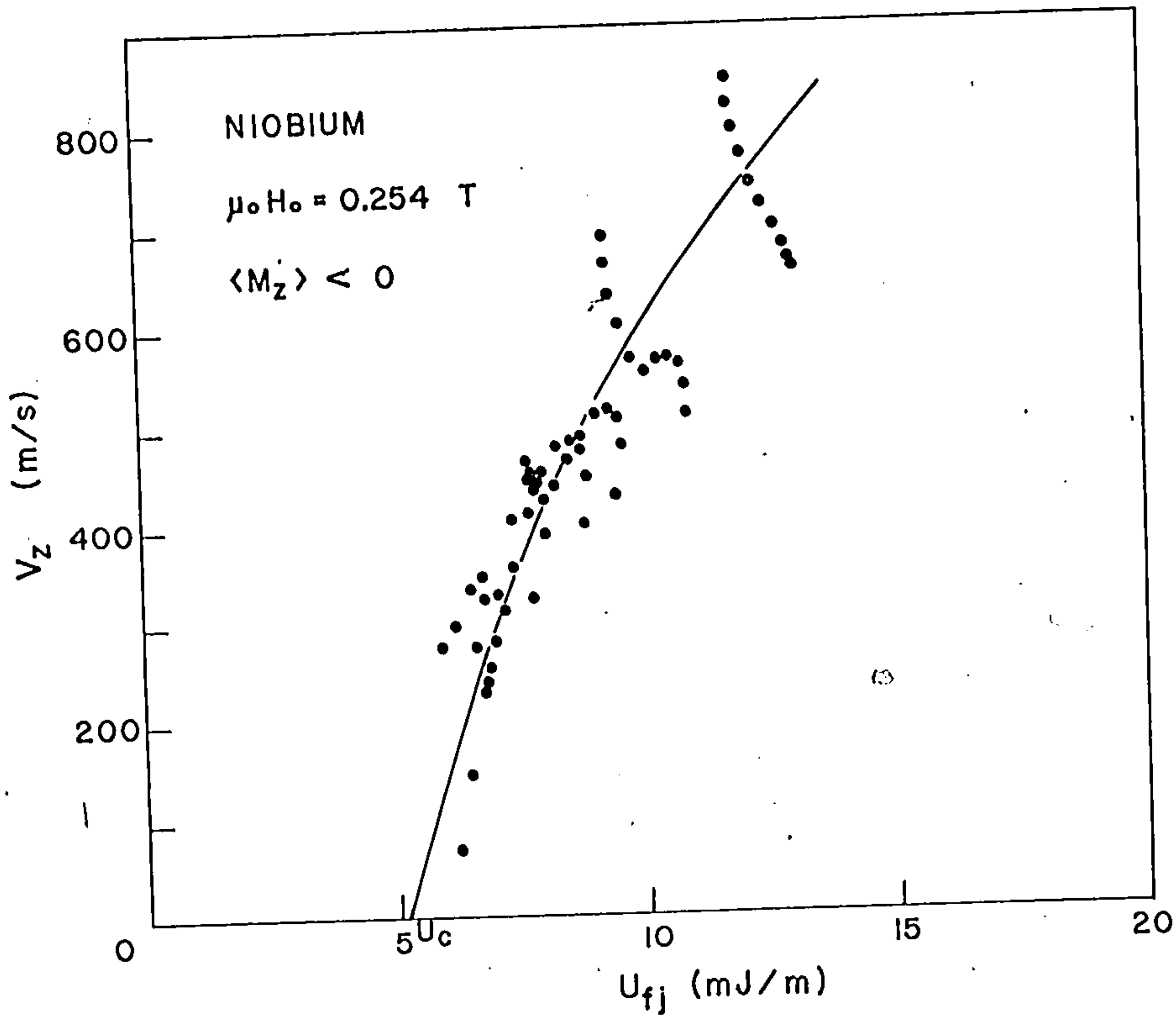


Figure 9-15 Experimental velocity $V_z$ versus calculated energy $U_{fj}$ for $\mu_o H_o$ = 0.254 tesla. The plotted data cover the complete range of transport current I and hybrid magnetic moment $\langle M_z \rangle$ where the electromagnetic propagation occurs.

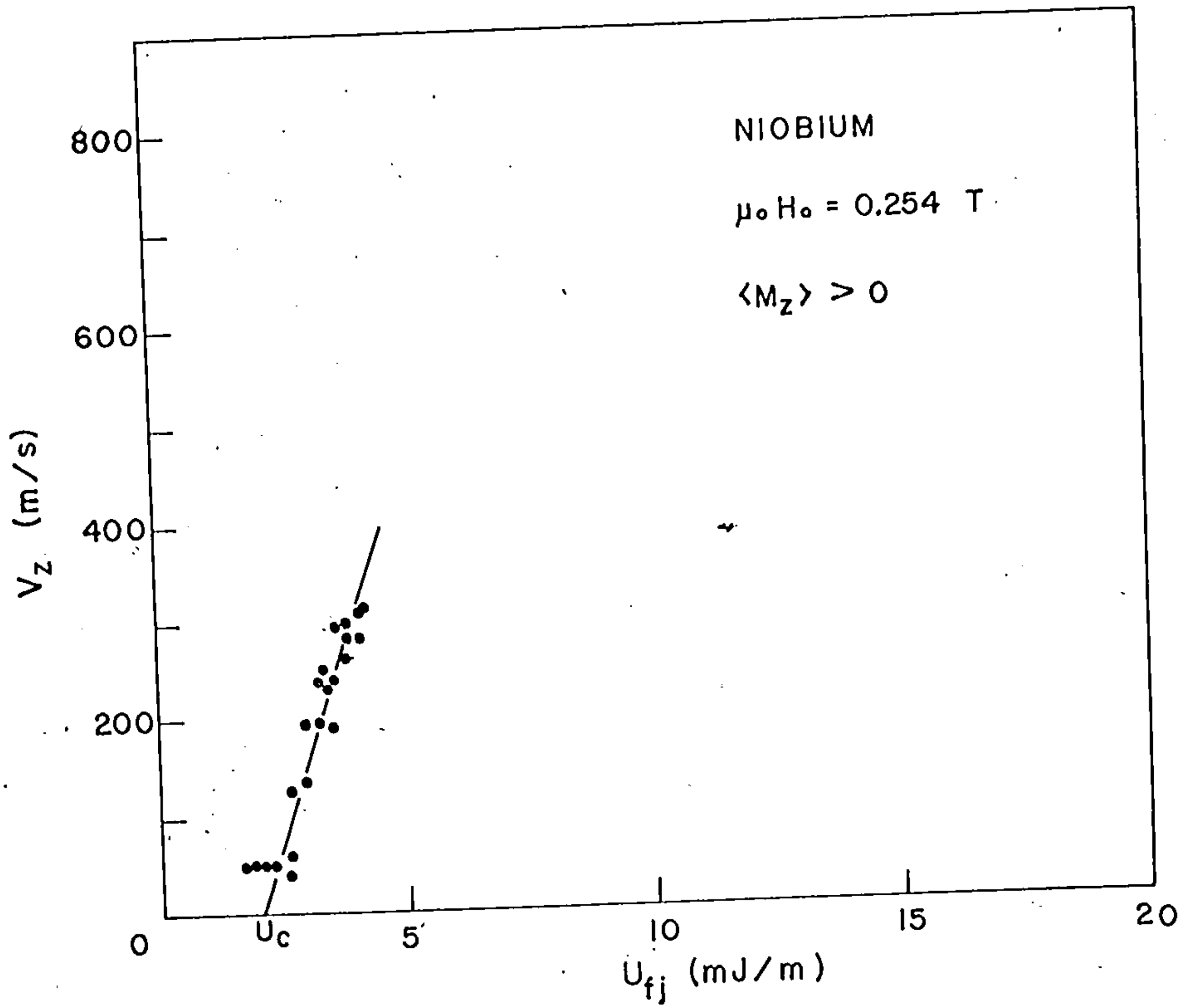


Figure 9-16 Experimental velocity $V_z$ versus calculated energy $U_{fj}$ for $\mu_o H_o$ = 0.254 tesla. The plotted data cover the complete range of transport current I and paramagnetic moment $\langle M_z \rangle$ where electromagnetic propagation occurs.

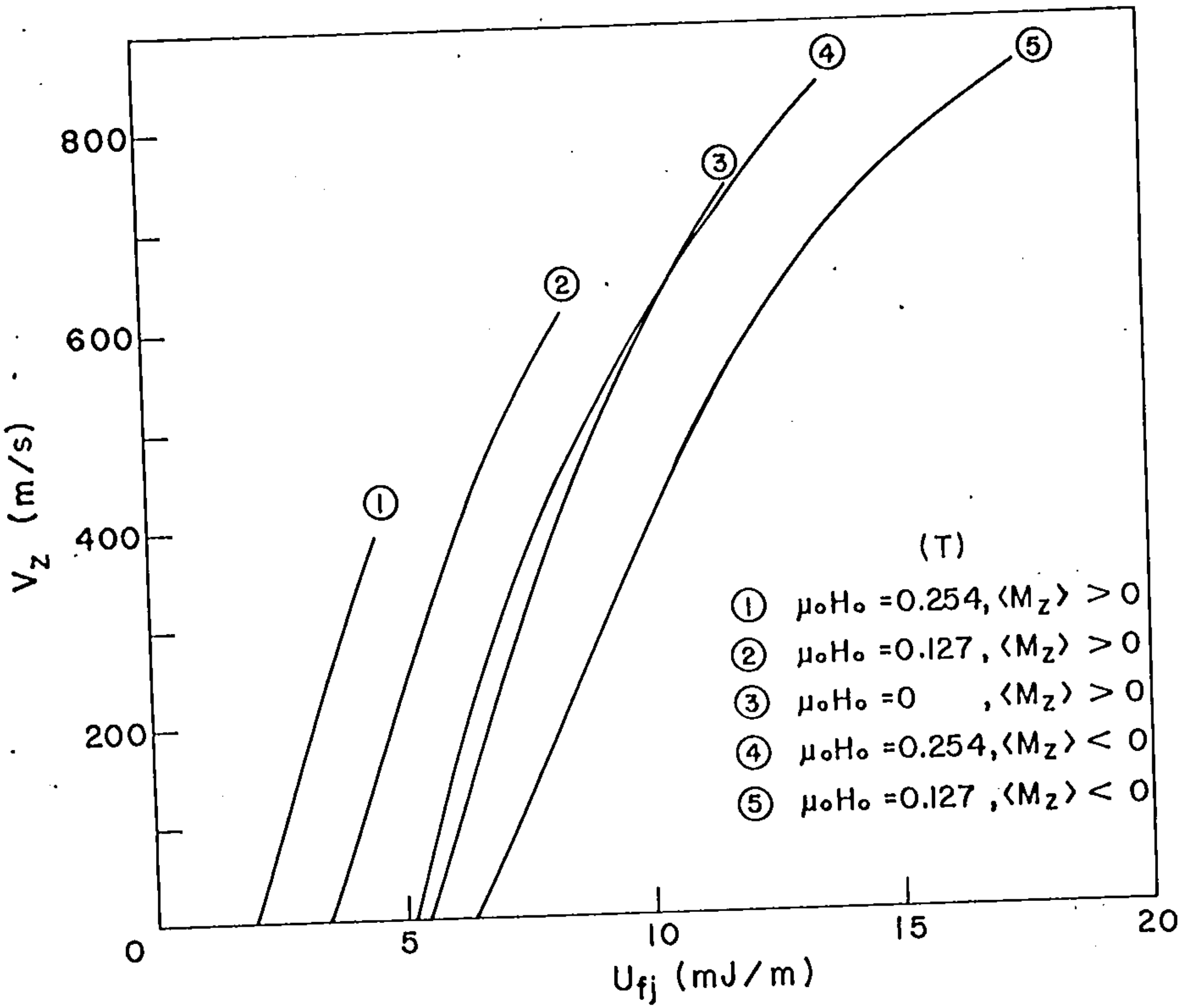


Figure 9-17 Average dependence of $V_z$ on $U_{fj}$ observed in the five previous Figures.

depends on the magnitude of the magnetic induction $\vec{B}(r)$. Simple estimates of $<|B_z|>$, the average initial value of the magnitude of $B_z$, indicate that $<|B_z|>$ for curve 5 is lower that for curve 3 and it is comparable to curve 3 for curve 4.

It is clearly a complicated matter to pursue the effect of flux-flow resistivity on $V_z$ (or V) in quantitative detail. The problem is multi-dimensional since it involves spatial variables (r and z) and the time t. Further, as will be seen in detail in the next chapter, the progress of the event is asymmetric and helical. Fortunately, for propagation by electromagnetic coupling, the process is adiabatic and the thermal conductivity can be ignored. Focussing on a segment of the wire, the evolution of the avalanche, although complicated, is mathematically tractable provided that it is azimuthally symmetric. The symmetric problem has already been examined by Bussière (Bussière 75), Morton (Morton 73) and Darby (Darby 73) in the context where the phenomenon is purely radial, and hence no z dependence enters. Furthermore, the adiabatic approximation is generally valid. Nevertheless, the solution requires considerable computation since B(r), and hence $\rho(r)$ vary with time as the avalanche evolves. The heat capacity, which depends on the induction $B/H_{c2}(T)$ in the superconducting state, must be taken into account in writing the energy balance. These aspects of the problem have not been pursued here. As indicated earlier, at this stage of the present investigations, an attempt has been made to identify only the major factors which govern $V_z$ (or V) and establish, if possible, general empirical relationships. The complicated behaviour of the curves presented in Figure 9-17, however, does not lead to any simple expressions. The results do bring out the strong correlation between $V_z$ (or V) and $(U_{fj} - U_c)$ as well as the strong dependence of $U_c$, and hence $V_z$ on $<|B_z|>$.

# Chapter 10

## Helical Propagation of Flux Jumps

### 10.1 Introduction

In examining and interpreting the standard magnetization curves of long cylinders (or ribbons) of type II superconductors subjected to a slowly varying longitudinal magnetic field it is generally assumed that cylindrical and axial symmetry prevail as entry or exit of the flux progresses. This idealized picture may not always correspond with complex reality. Surface conditions may vary along the length and around the circumference of the specimen. These imperfections will lead to some "smearing" in the initial magnetization curves and introduce uncertainty in the determination of $H_{c1}$. Within the bulk, an inhomogeneous distribution of pinning sites on a macroscopic scale may occur. These departures from the ideal, unless grossly exaggerated, will not invalidate the analysis of the data since these features usually average out on the scale of the sample. In Figure 10-1 (a) and (b) the effect of an extensive weak pinning region on the B profile is illustrated.

In observations of flux avalanches, however, these coarse imperfections, generally referred to as weak points, can play a dominant role. This is a consequence of the very nature of the flux avalanche phenomenon which is a non linear amplification or magnification process originating in a perturbation (or weak spot), but growing disproportionately to its immediate cause. It is very unlikely that a flux jump will be initiated simultaneously along the length and around the circumference of the superconductor. Usually, a perturbing flux change occurs in a small region at or in the vicinity of the surface. The rapid local flux movement increases

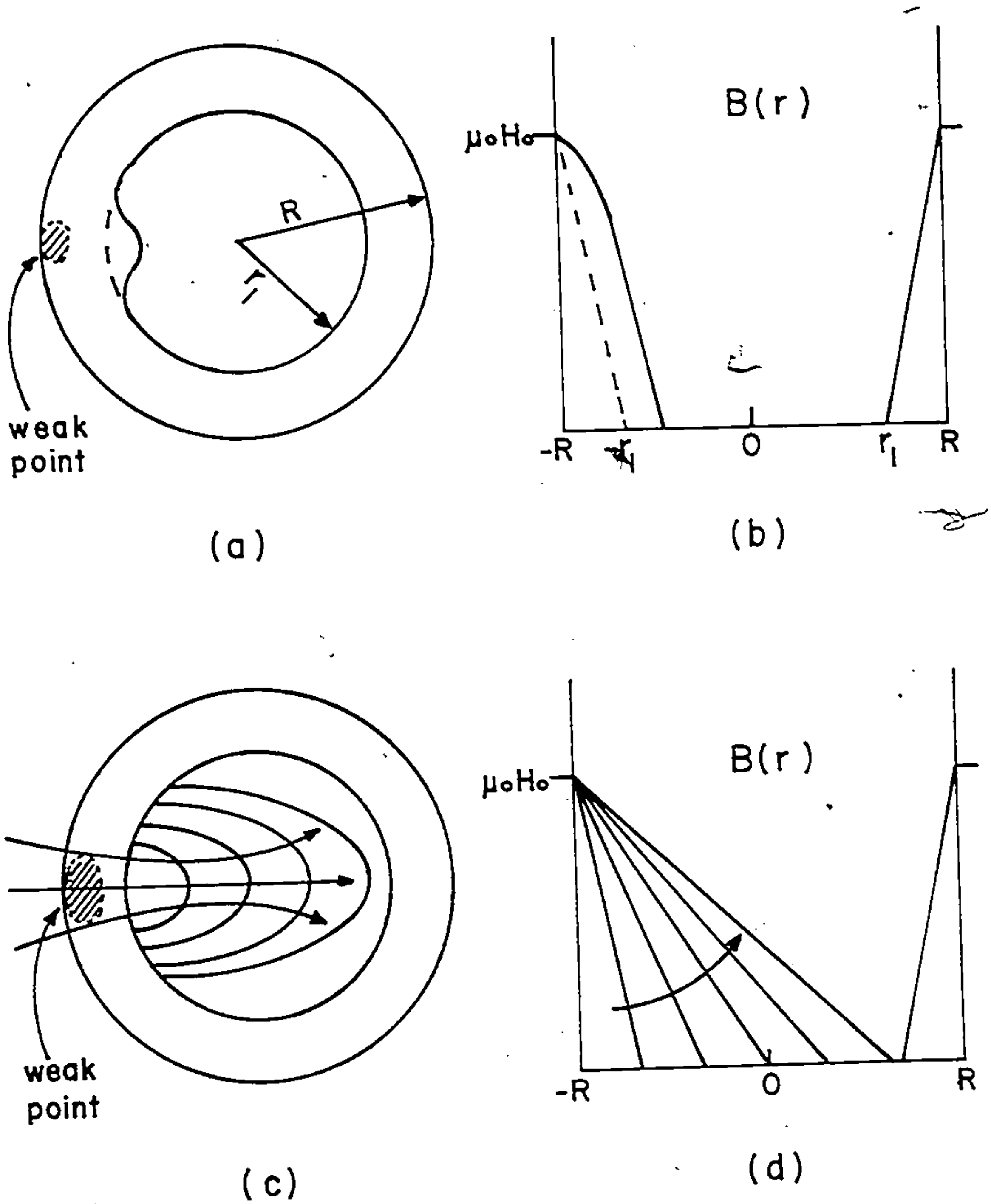


Figure 10-1 Penetration depth and field profile inside a superconducting wire. a) and b) effect of a weak point during quasi-static magnetization. c) and d) flux jump initiated at a weak point.

the temperature within the volume of the superconductor where the perturbing flux entry (or exit) takes place. Consequently the pinning strength decreases, allowing for further flux movement and an avalanche can ensue, as illustrated in Figure 10-1 (c) and (d).

The large-scale asymmetric entry and exit of flux in type I superconductors was first observed by DeSorbo and Healy (DeSorbo 64). These workers studied the movement of flux in the intermediate state of disk samples using the optical Faraday rotation technique. The applied field is transverse to the plane of the disk. Later, Wertheimer and Gilchrist (Wertheimer 67) and Harrison et al (Harrison 73) used a high-speed cine-camera and improved resolution to monitor the rapid evolution of flux jumps in type II materials. The collapse of the flux configuration during these events displays considerable sequential asymmetry around the periphery and in the body of the disk.

Irie et al (Irie 75) and Ezaki et al (Ezaki 76a, 76b) have reported on measurements of flux flow voltages around the circumference as well as along the length of wires of type II superconductors carrying a stationary transport current in a static longitudinal magnetic field. They observe an appreciable azimuthal flux-flow voltage, and the pattern of this azimuthal electric field $E_\theta(\theta, z)$ rotates along the length of the wire. These observations indicate that the movement of the flux configuration is azimuthally asymmetric and that the asymmetry varies helically along the the length of the wire, as shown schematically on the following page. Their results are consistent with a picture of two helical patterns of oppositely moving streams of flux.

In the flux flow state in hollow wires of $In_{0.90}Pb_{0.10}$, carrying a steady transport current, Makiej et al (Makiej 75), have observed a

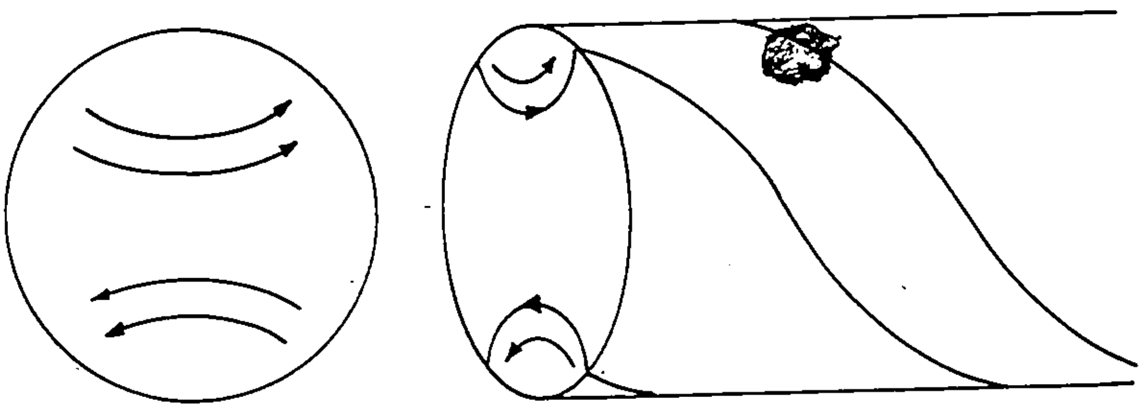

potential difference between the inner and outer surfaces. These observations of a radial electric field component also indicate that azimuthal rotation of helical flux lines is taking place.

From all of these observations it is clear that the configuration of magnetic induction in cylindrical geometry may lose its rotational invariance in situations where catastrophic flux movements (flux jumps) or steady flux movement (flux flow regime) occur. In this chapter, detailed observations of the helical propagation of flux avalanches along Nb wires carrying a steady transport current and axially magnetized in a longitudinal magnetic field are reported.

## 10.2 . Evidence of Helical Propagation of Asymmetric Flux Collapse.

Let us examine in detail the arrangement and observations which lead to the conclusion that the flux avalanches, in certain circumstances, are azimuthally asymmetric and advance helically. As indicated in Chapter 7, the pick-up coil system for detecting the propagation of the flux avalanches, although constructed as one continuous unit, consists of three distinct sections as shown schematically in Figure 10-2: two axial pick-

(a)

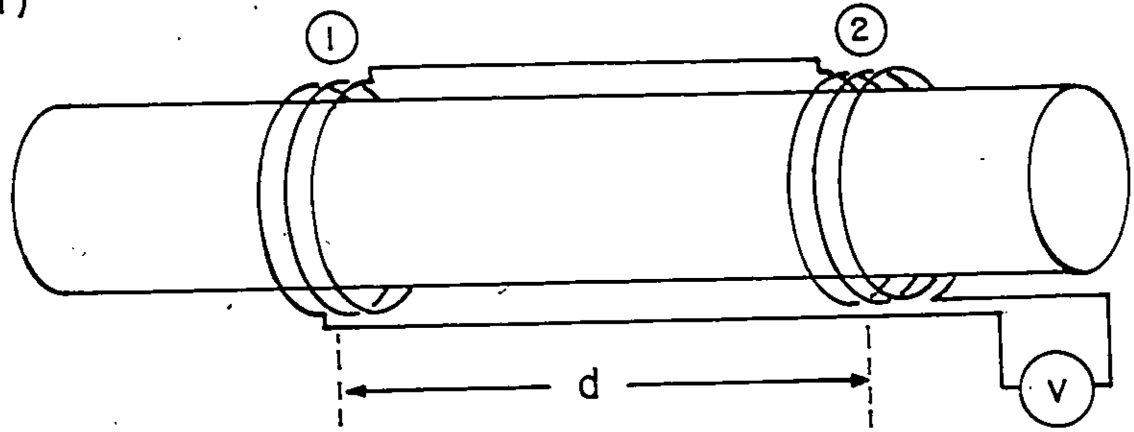


(b)

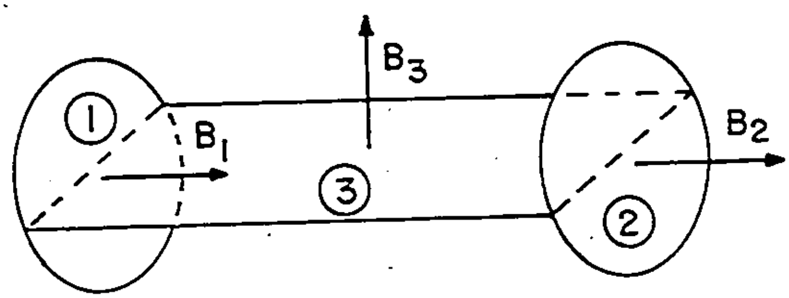


Figure 10-2 a) Pick-up coil used for measuring the longitudinal velocity of propagation of flux jumps. b) Schematic diagram of the three sections of the pick-up coil with the respective directions of the field causing a signal.

up coils (labelled 1 and 2 in the Figure) and a saddle-shaped or rectangular coil (labelled 3). The edges of the saddle or rectangular coil are positioned on opposite sides and along the length of the superconducting wire. The rectangular coil then embraces an area $A_3 = 2Rd$ located between the two axial coils. The rectangular coil consists of three turns and the axial coils of ten turns each. The arrows in Figure 10-2 indicate the component of the magnetic induction which causes a signal to be induced in each section. Obviously, the axial coils detect changes in the axial magnetization. The rectangular coil generates a signal when the flux entry or exit is asymmetric and this aspect is now developed for different modes of flux entry (exit).

a) Flux jump with radial symmetry propagating along the wire.

This situation is straightforward. Typical initial and final $B_z$ profiles are sketched in Figure 10-3 (a). As the flux avalanche reaches axial coil 1 at time $t_1$, a voltage pulse is observed. The flux jump continues to move along the wire and eventually reaches the second axial coil at a time $t_2$, producing a second pulse. No signal is generated by the rectangular coil.

The axial velocity of the flux jump is simply $V_z = d/(t_2 - t_1)$ where d is the distance separating the mid-plane of the two axial coils. When the flux jump propagates in the thermal mode this kind of signal is always observed (see Figure 10-7 (a) ).

b) Asymmetric flux jump propagating longitudinally (without rotation).

Consider a situation in which the radial flux movement takes place asymmetrically, as shown in Figure 10-1 (c) and (d). It is also assumed that the flux entry (or expulsion) always takes place from the same side

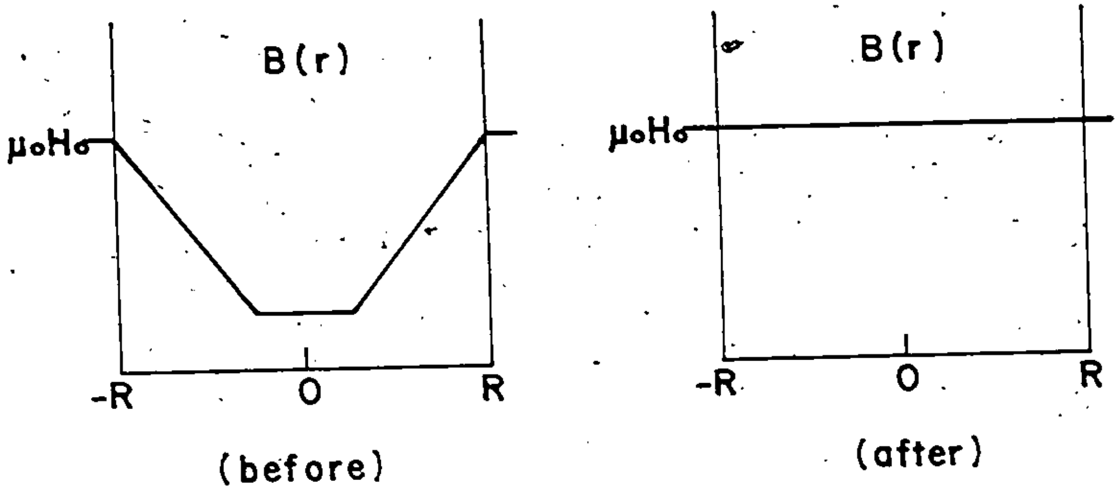


(a)

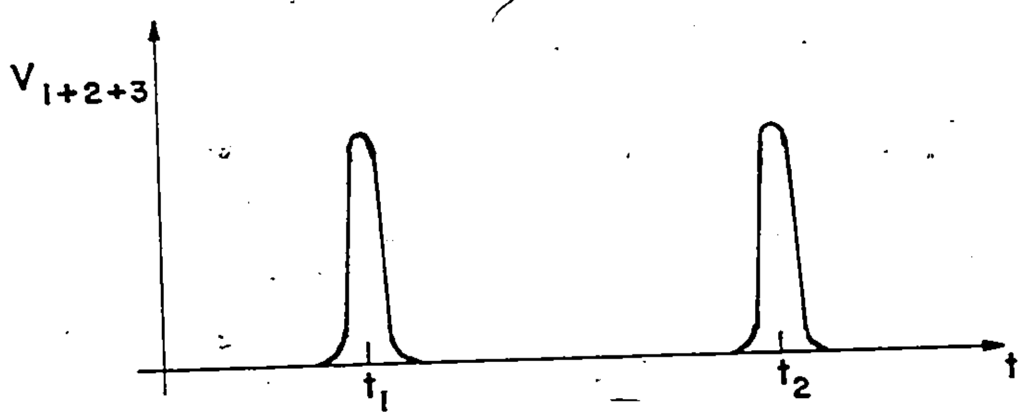


(b)

Figure 10-3 a) Axial field profiles before and after an axially symmetric flux jump. b) Pick-up coil signal produced when the flux jump propagates along the superconducting wire.

of the wire. In Figure 10-4 a cross sectional view of the flux configuration in the z-r plane is presented. The lines represent the magnetic flux density. The azimuthal component of the magnetic induction due to the transport current is perpendicular to the plane of the paper and can be ignored.

The dashed line bisecting the superconductor in the middle of the Figure indicates the front of the flux avalanche. This front advances from left to right as the avalanche progresses. The flux entry takes place from the top of the wire. Note that in the region where the flux jump is taking place, the magnetic induction has an upward component. Thus a pulse will be generated when the flux jump reaches the front of the rectangular loop and another pulse of opposite sign will be produced when the avalanche passes beyond the end of the loop. The signals produced by the system of pick-up coils and the individual sections are depicted in Figure 10-5.

c) Helical propagation of an asymmetric flux jump.

Let us consider, as a third case, the situation shown schematically in Figure 10-6 (a). Region A, where the flux entry (exit) is taking place, moves helically along the surface of the superconducting wire. In such a case, the signal due to the rectangular coil (section 3) will consist of a continuous series of oscillations, each cycle corresponding to a full revolution of the region A around the circumference of the superconducting wire (see Figure 10-6(b) ). The total signal observed across the pick-up coil system is shown in Figure 10-6 (c).

This corresponds to the type of signals generally observed when the flux jump is propagating by electromagnetic coupling. A representative photograph of such an event displayed on the oscilloscope screen is

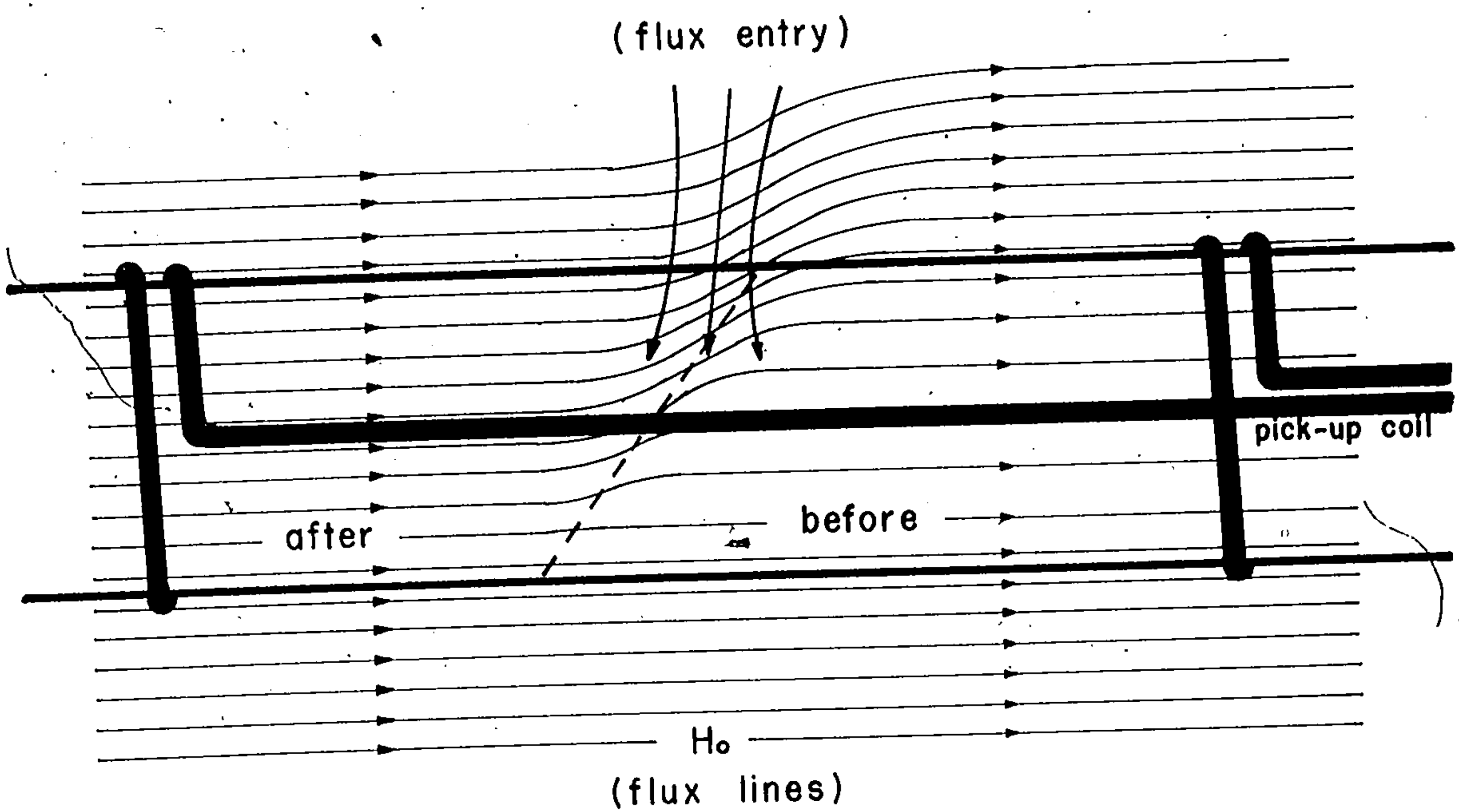


Figure 10-4 Longitudinal cross section of the axial field lines during an asymmetric flux entry. The field lines approximatively represents the field intensity.

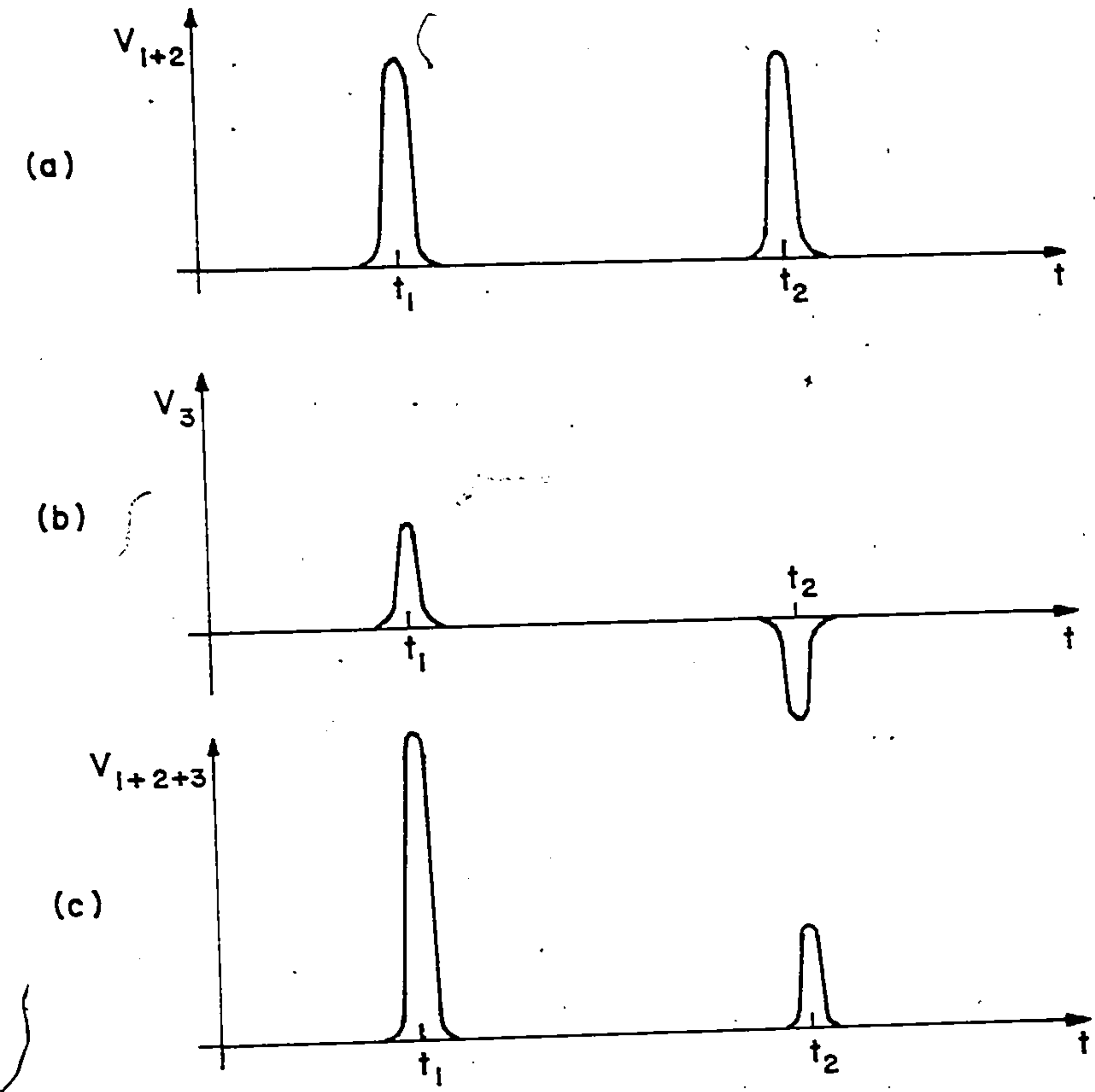


Figure 10-5 Flux jump with asymmetric flux entry (without rotation) propagating along the wire. a) Signal due to the two series windings; b) Signal due to the rectangular longitudinal coil (asymmetric flux penetration); c) Total signal generated by the pick-up coil.

(a)

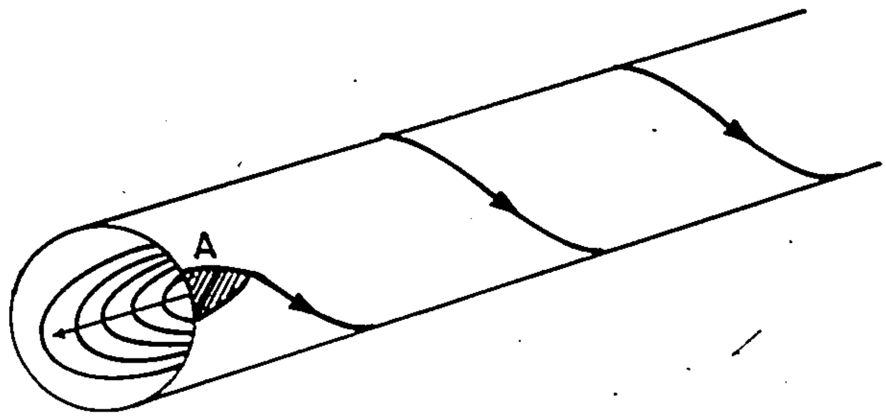


(b)

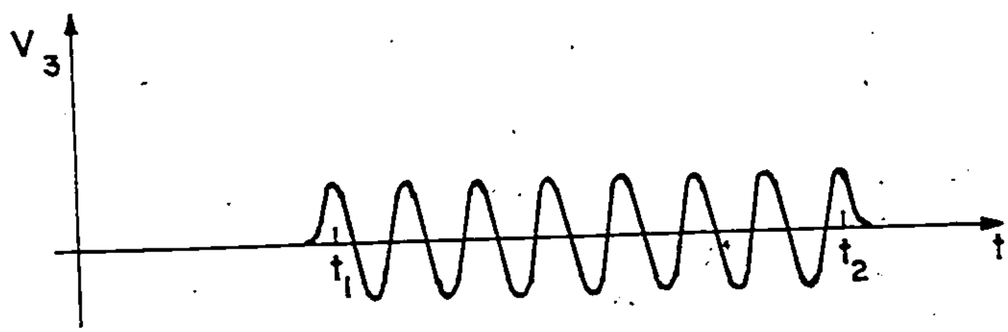


(c)

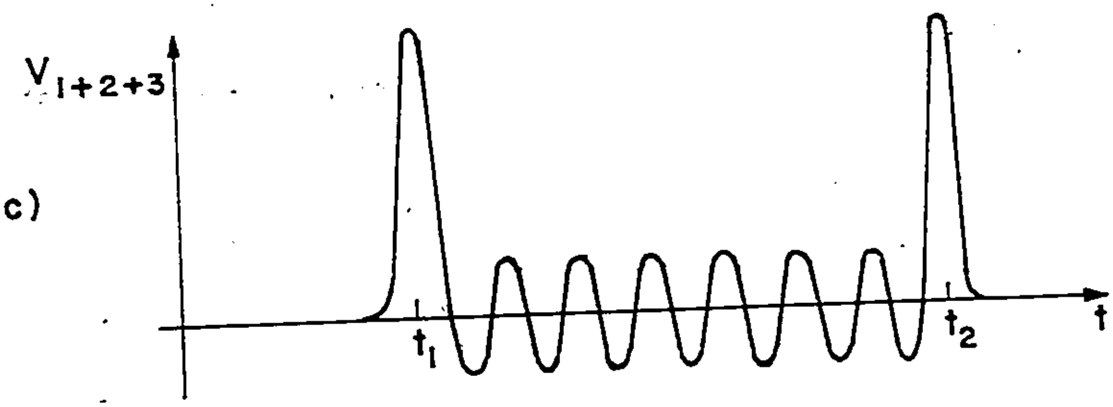


Figure 10-6 a) Helical propagation of the asymmetric flux entry. b) Signal generated in the longitudinal rectangular coil. c) Total signal observed.

reproduced in Figure 10-7 (b). The two leads emerging from the second axial coil of the pick-up coil system are taken out along the superconducting wire on opposite sides and thus form a single turn rectangular loop embracing the rest of the sample. Consequently, oscillations of reduced (1/3) amplitude are detected as the flux avalanche advances beyond the second axial coil along this length of the wire.

## 10.3 Experimental Survey of Helical Flux Avalanches

In the preceding section an analysis has been made of the kind of signals expected to be observed with the pick-up coil system when an asymmetric flux jump propagates along a helical trajectory at the surface of the superconducting wire. The signal expected is indeed observed in most situations where the electromagnetic mode of propagation prevails and typical examples are displayed in Figures 10-7(b) and 10-8(a). In these examples, the helix is very regular and the asymmetric flux collapse is well behaved as in the idealized picture of Figure 10-1(c) and (d).

The ideal behaviour shown in Figures 10-7(b) and 10-8(a), does not, however, always occur and in certain circumstances, the signals observed are more complicated and less regular. In Figures 10-7 through 10-10, examples of the variety of types of signals that are encountered in this work are reproduced. It has been previously remarked that in the thermal mode of propagation, no oscillations are detected although $\langle M_z \rangle \neq 0$ as seen in Figure 10-7 (a).

The periodicity and the structure of the oscillations displayed in Figures 10-8(b), 10-9(a) and (b) evidently depart from the idealized picture. In these cases it is obviously more difficult to define

(a)

Vanadium $H_o = 0$

$\mu_o \langle M_z \rangle = 0.068$ tesla

$\langle I \rangle = 94$ amp.

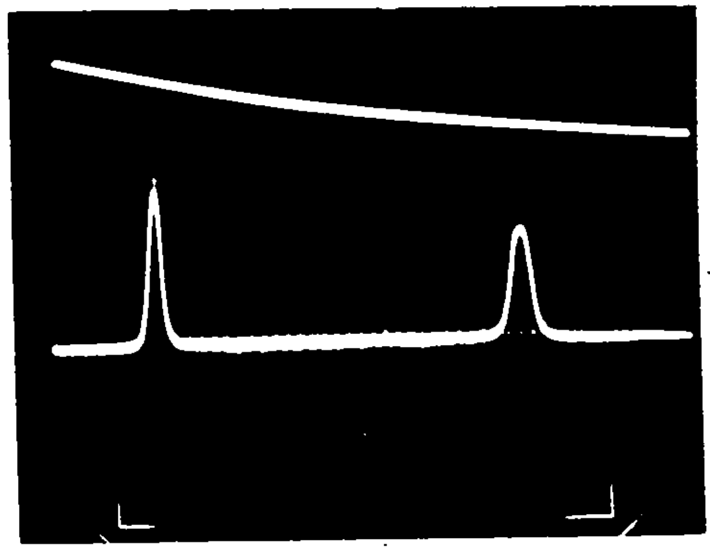

(b)

Vanadium

$\mu_o H_o = 0.058$ tesla

$\mu_o \langle M_z \rangle = -0.096$ tesla

$\langle I \rangle = 126$ amp.

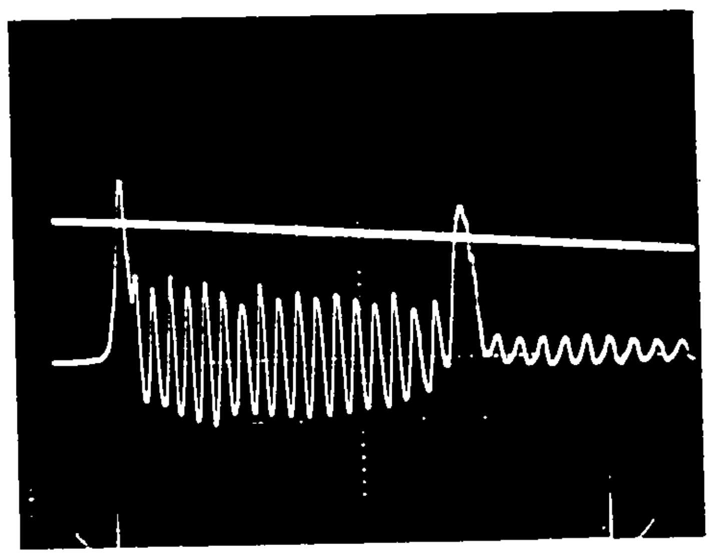

Figure 10-7 Signal observed across the pick-up coil during the propagation of a flux jump a) thermal mode of propagation
b) electromagnetic mode of propagation.
(The upper trace monitors the magnitude of the transport current.)

(a)

Niobium

$\mu_o H_o$ = 0.127 tesla

$\mu_o \langle M_z \rangle$ = -0.266 tesla

<I> = 140 amp.

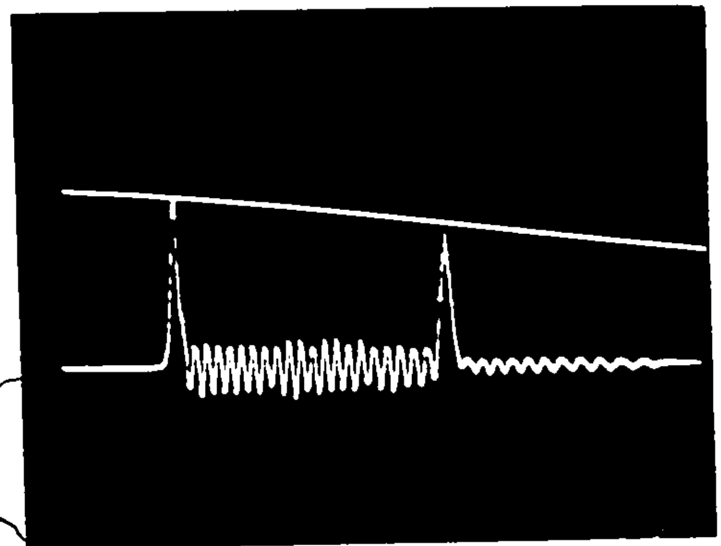

(b)

Niobium

$\mu_o H_o$ = 0.127 tesla

$\mu_o \langle M_z \rangle$ = -0.313 tesla

<I> = 58 amp.

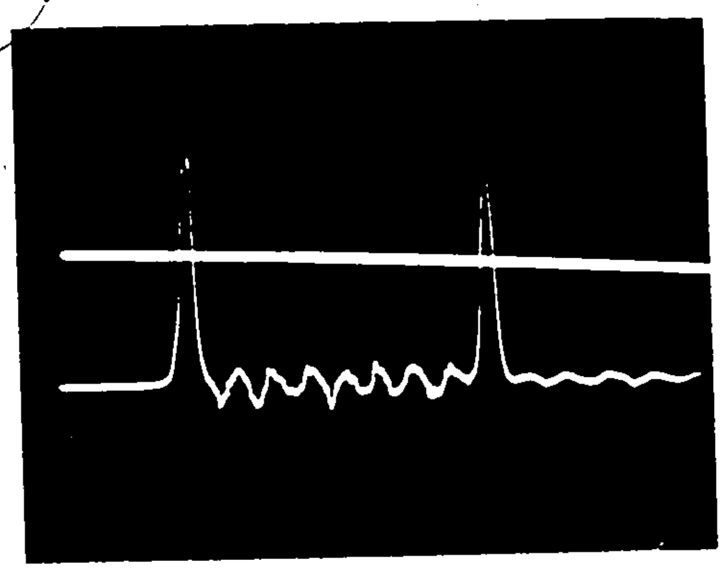

Figure 10-8 Signal observed across the pick-up coil during the electromagnetic propagation of a flux jump. The upper trace represents the transport current.

(a)

Niobium

$\mu_o H_o$ = 0.127 tesla

$\mu_o \langle M_z \rangle$ = -0.351 tesla

$\langle I \rangle$ = 256 amp

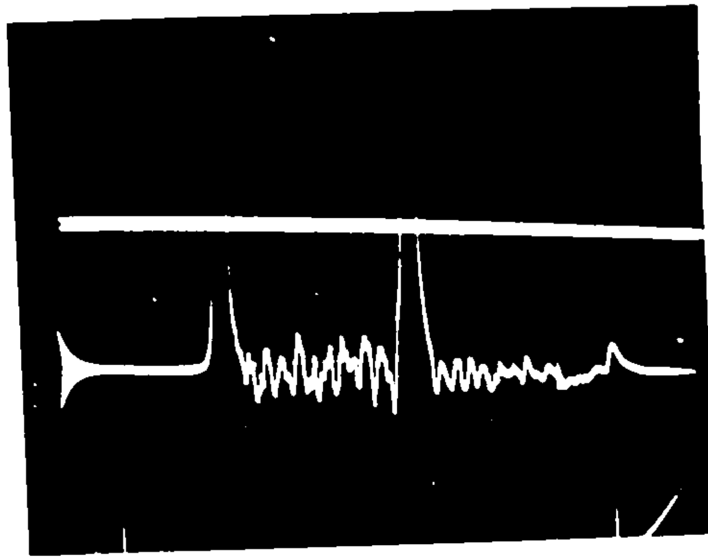

(b)

Niobium

$\mu_o H_o$ = 0.127 tesla

$\mu_o \langle M_z \rangle$ = -0.351 tesla

$\langle I \rangle$ = 240 amp.

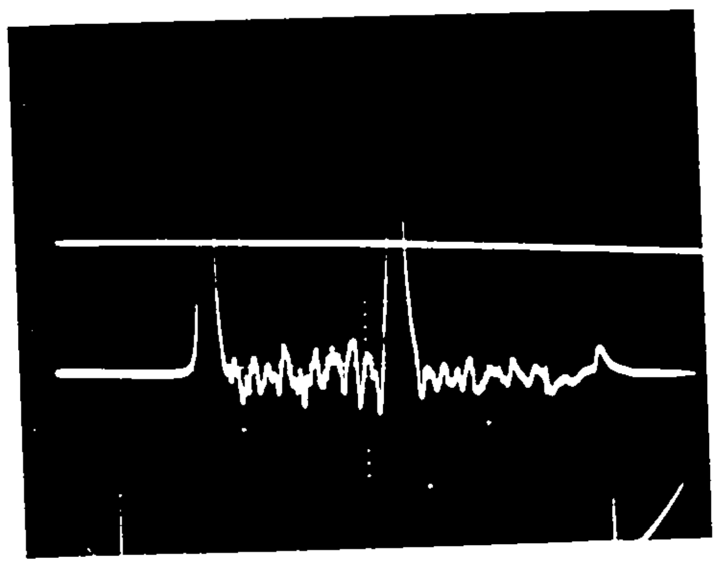

Figure 10-9 Signal observed across the pick-up coil during the electromagnetic propagation of a flux jump. The upper trace represents the transport current.

(a)

Vanadium

$\mu_o H_o = 0$

$\mu_o \langle M_z \rangle = 0.070$ tesla

$\langle I \rangle = 135$ amp

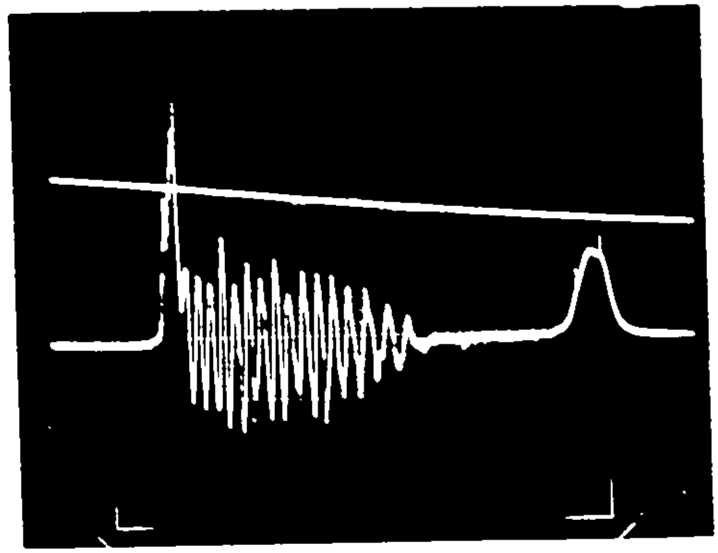

(b)

Niobium

$\mu_o H_o = 0.127$ tesla

$\mu_o \langle M_z \rangle = -0.266$ tesla

$\langle I \rangle = 104$ amp.

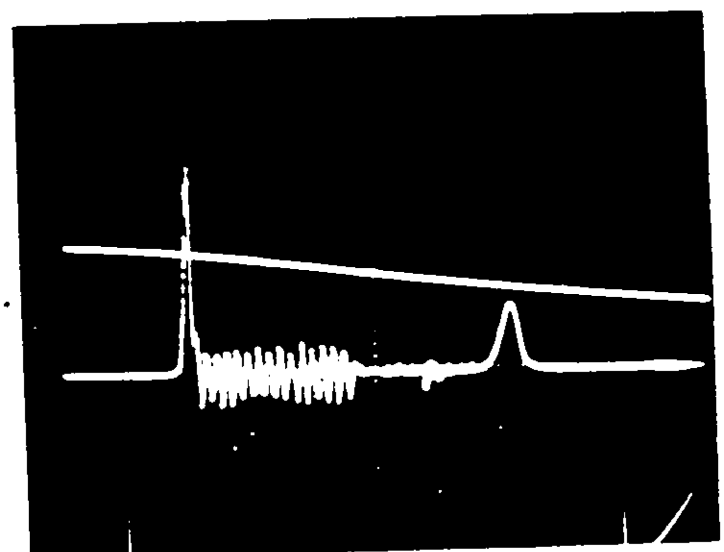

Figure 10-10 Signal produced across the pick-up coil when the flux jump changes from the electromagnetic mode (on the left) to the thermal mode (on the right) of propagation.

accurately the helix followed by the flux jump although the overall behaviour is still consistent with the picture of an asymmetric flux jump advancing helically. Several possible explanations can be visualized for the less than ideal behaviour. For instance, (i) the asymmetric flux avalanche does not evolve identically in the various segments of its trajectory (ii) the rate of progress along the wire is irregular and (iii) satellite flux jumps in the vicinity of the main avalanche suddenly appear, move along and disappear.

It has been noticed that the oscillations tend to be nicely periodic and very regular when the velocity of propagation is less rapid, hence when $U_{fj}$, the energy dissipated does not appreciably exceed $U_c$, the threshold value for propagation. Under these circumstances, the configuration of magnetic induction is relatively less unstable and a stronger perturbation is needed to trigger the progress of the flux jump. The flux avalanche then evolves more smoothly and is itself the only adequate source present for triggering the collapse of the critical field profiles in the adjacent region where it propagates.

On the other hand, the rapidly travelling flux jumps correspond to situations where large quantities of energy are dissipated, well in excess of the threshold required for propagation to occur. The configurations of magnetic induction are highly unstable. Thus, small perturbations are more likely to induce collapse and weak spots become more important. Consequently we expect and observe that the oscillations are less regular and noisy under these circumstances.

The upper trace in Figures 10-7 to 10-10 measures the transport current flowing through the wire. The zero level is the horizontal grid line, 2 cm above the bottom of the photographs. The growth of the electrical resistance along the wire as the flux jump progresses, causes the transport current to decrease fractionally. This feature leads to interesting and important consequences.

We note that the energy $U_\theta$ associated with the azimuthal magnetic induction of the transport current and available for propagation of the flux avalanche will also decrease as the transport current decreases. In certain cases, when $U_{fj}$ initially is not appreciably greater than $U_c$, the total energy $U_z + U_\theta$ may consequently fall below the threshold value $U_c$ for electromagnetic propagation. In such a situation, the mode of propagation should then switch from electromagnetic to thermal. In the latter mode, a normal front, extending over the cross section of the wire, advances by thermal diffusion of joule ($I^2R$) heating. The collapse of the flux in the superconducting region is then radially symmetric and consequently no oscillations should be observed. Figure 10-10 shows two examples of this transition from electromagnetic to thermal coupling. In one case the transition is gradual and in the other it is evidently abrupt. On the left of the pictures, the propagation is helical (hence, unambiguously electromagnetic). Later in the pictures, the transport current has sufficiently diminished that $U_{fj} < U_c$ and the thermal mode of propagation then takes over and the oscillations disappear.

## 10.4 Flux Jumps with Helical Trajectories: Results and Analysis

Measurements are now presented on the variation of the helical trajectories followed by the flux avalanches with I, $H_o$ and $\langle M_z \rangle$. Let $\phi_{obs}$ denote the angle at the surface of the superconducting wire between the path followed by the flux jump and the z axis as shown in the sketch on the following page. This angle $\phi$ can be measured in the following manner.

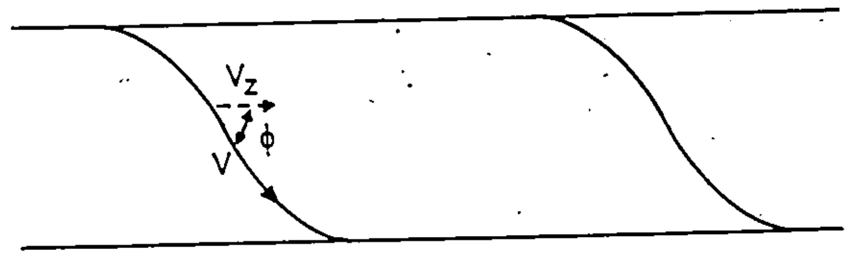


If the number N of oscillations in the time interval $t_2 - t_1$ in the photograph of the event is counted then the frequency of rotation f of the flux jump around the circumference of the wire can be obtained

$$f = \frac{N}{t_2 - t_1} \qquad (10\text{-}1)$$

The azimuthal velocity of propagation at the surface is then

$$V_\theta = 2\pi Rf \qquad (10\text{-}2)$$

where R is the radius of the wire. The total velocity of the flux jump is

$$V = \sqrt{V_\theta^2 + V_z^2} \qquad (10\text{-}3)$$

where

$$V_z = \frac{d}{t_2 - t_1} \qquad (10\text{-}4)$$

The angle $\phi$ which is measured is then given by

$$\phi_{obs} = \tan^{-1} \frac{V_\theta}{V_z} = \tan^{-1} \left( \frac{2\pi RN}{d} \right) \qquad (10\text{-}5)$$

Let us now turn to the fundamental questions:

(i) why are the flux avalanches travelling along helical trajectories in the electromagnetic mode of propagation? and

(ii) what determines the helical path that is followed?

In a wire of a type II superconductor carrying a transport current in a longitudinal magnetic field, the vortices are helical, in the cylindrical sheath occupied by the transport current, regardless of whether the specimen is axially magnetized or not. (In this discussion, reversible Abrikosov surface currents and irreversible surface currents are ignored.) It is natural then to associate the helical trajectories of the flux avalanches with the helical configuration of the flux filaments and to visualize the flux jump advancing along the flux lines. This association, however, bears careful scrutiny.

We note that the orientation of the magnetic induction $\vec{B}(r) = \hat{\theta}B_{\theta}(r) + \hat{z}B_z(r)$, varies with distance from the surface. Thus the pitch of the helix of the magnetic configuration is far from constant but varies considerably with depth. The question then remains: which of the many helices encountered in a given flux configuration is followed?

The interesting possibility that the helix existing at the surface determines the trajectory of the flux avalanche can be immediately rejected. The reason for setting this aside is that helical propagation of flux jumps is observed when the wire is axially magnetized and carrying a transport current in $H_o = 0$ (see Figure 10-11 ). Under these circumstances, $B_z(R) = 0$, $B_{\theta}(R) > 0$ and the pitch is infinite since the lines of magnetic induction at the surface are purely azimuthal.

Further, we note that inside the cylindrical sheath occupied by the transport current, $B_z(r) \neq 0$ in all of the measurements where helical propagation is encountered. The vortices in the core of the wire are straight. Nevertheless, helical propagation is occurring. Clearly this core region does not dominate the behaviour.

As a first crude approximation an intermediate helix is chosen between that existing at the surface and the purely axial direction of the vortices deep inside the wire. In the spirit of the Bean-London approximation an arithmetic average $\phi_{calc}$

$$\phi_{calc} = \tan^{-1}\left\{ \frac{H_\theta}{|H_o| + |H_i|} \right\} \qquad (10\text{-}6)$$

is taken. This corresponds to defining a helix where the azimuthal magnetic induction $\langle B_\theta \rangle = B_\theta(R)/2 = \mu_o H_\theta(R)/2$ and the longitudinal magnetic induction $\langle |B_z| \rangle / \mu_o = (|H_o| + |H_i|)/2$. Here $H_\theta$ is the azimuthal field at the surface of the wire and $\mu_o H_o$ and $\mu_o H_i$ are the longitudinal magnetic induction at the surface and deep inside the superconductor respectively, and as sketched below for a paramagnetic and a diamagnetic $B_z$ profiles.

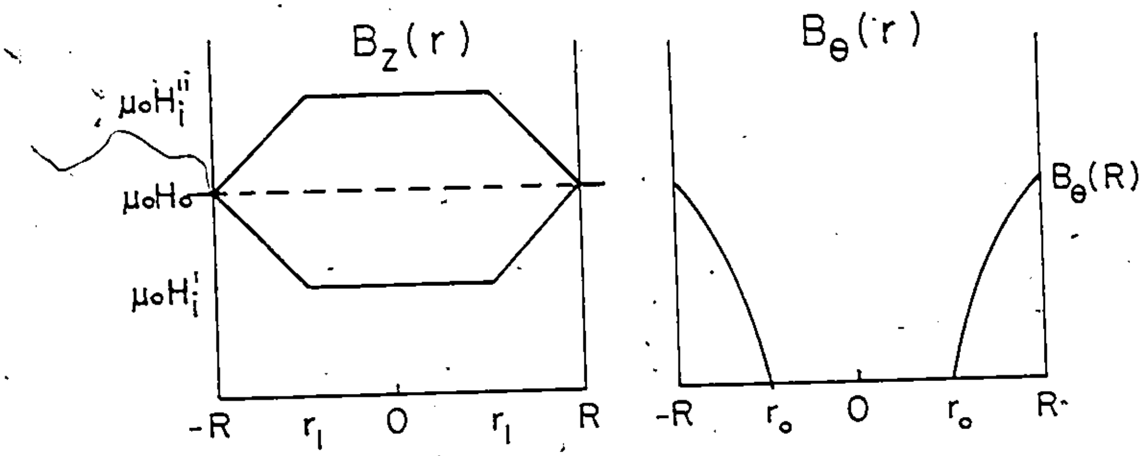


In Figures 10-11, 10-12 and 10-13 the helix generated by this crude approximation is compared to the extensive observations on the Nb wire. For a given curve in any of these Figures, the transport current I is increasing as $\phi_{calc}$ increases since the denominator in the argument of equation 10-6 is constant. Perfect agreement between the two quantities, $\phi_{calc}$ and $\phi_{obs}$ would yield the straight dashed lines. It is evident that the overall correspondence is only mildly satisfactory. This is not too surprising in view of the crude averaging procedure embodied in $\phi_{calc}$. Further, the error in many of the data points can be several percent as can be appreciated by inspecting the photographs displayed in Figures 10-7 through 10-10. Finally, the approach exploited in estimating $\phi$ is particularly questionable when the $B_z$ profile is strongly hybrid. Strangely,

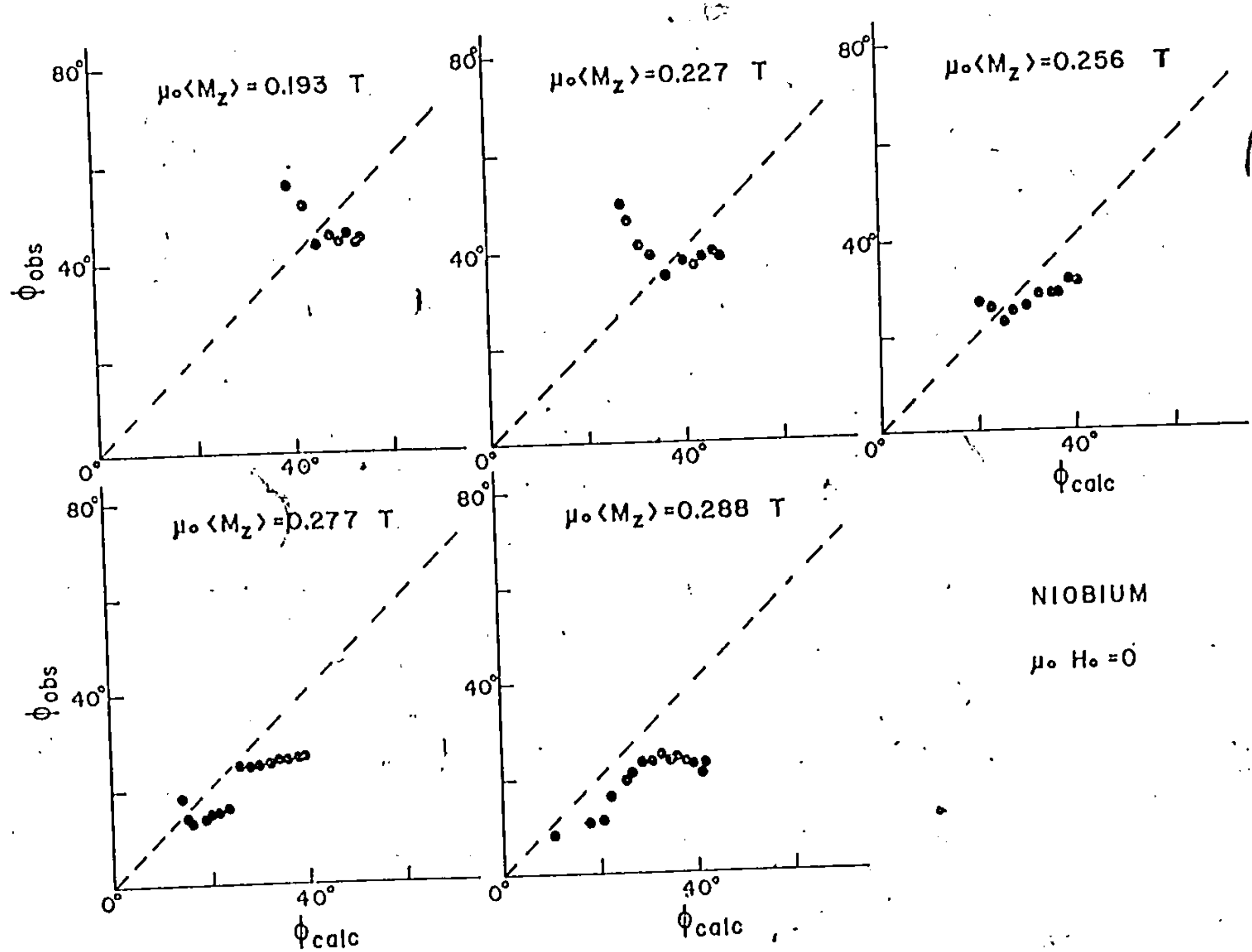


Figure 10-11 Comparison between $\phi_{obs}$ and $\phi_{calc}$ ($H_o = 0$).

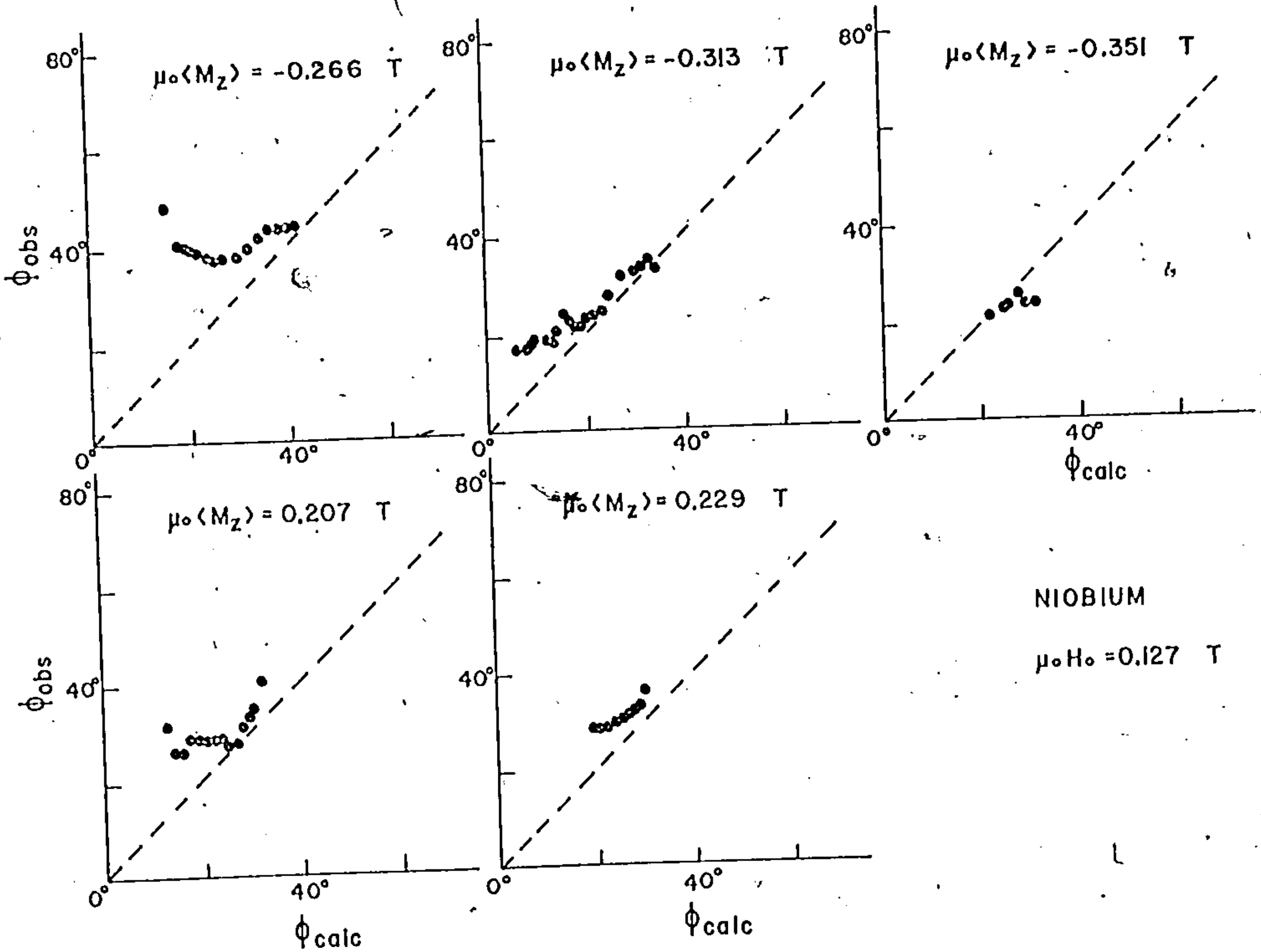


Figure 10-12 Comparison between $\phi_{obs}$ and $\phi_{calc}$. ($\mu_o H_o$ = 0.127 tesla)

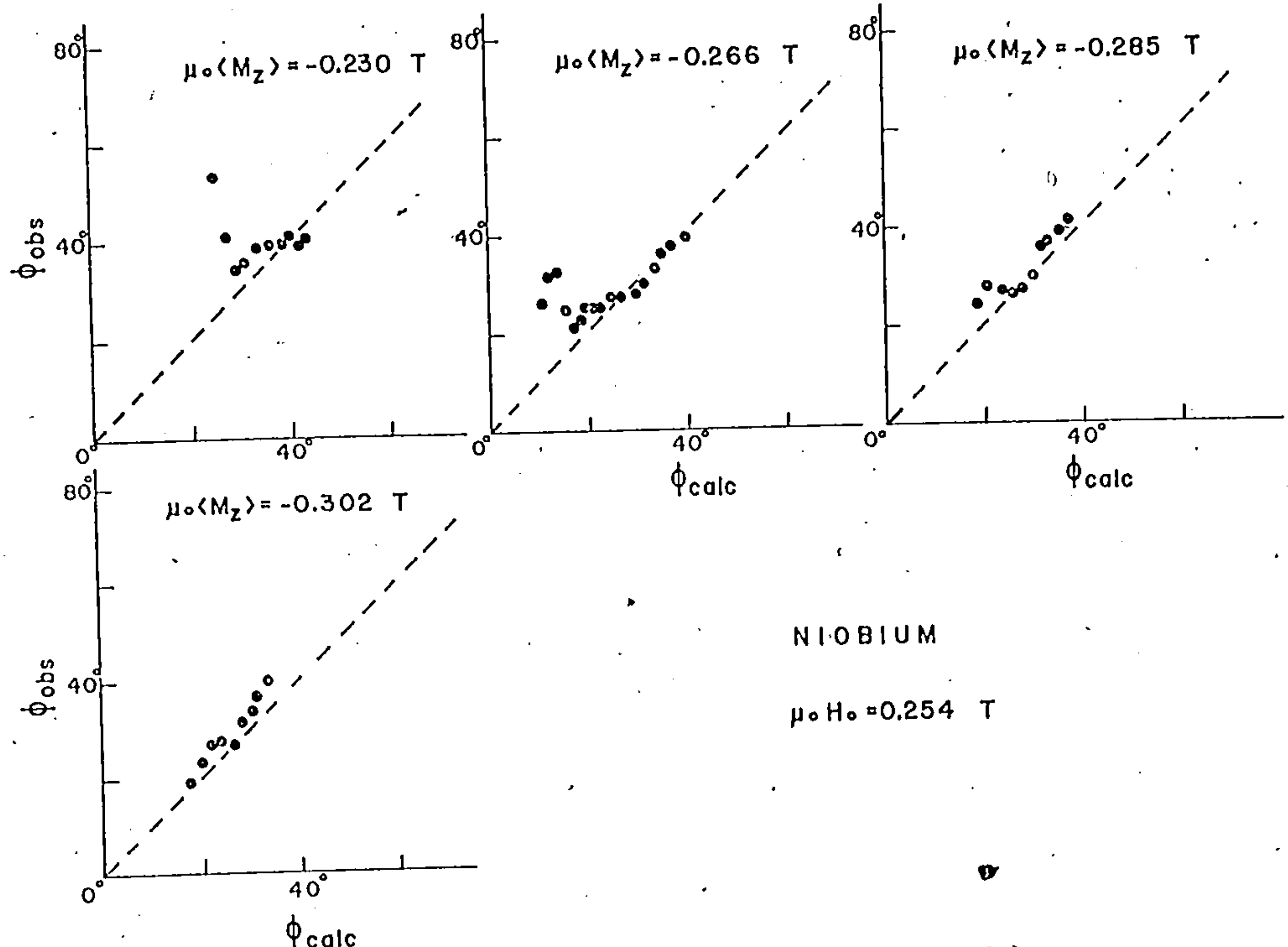


Figure 10-13 Comparison between $\phi_{obs}$ and $\phi_{calc}$ ($\mu_o H_o$ = 0.254 tesla)

however, the agreement is generally better in these circumstances. The phenomenon of helical propagation was also observed in the Vanadium wire and exhibited the various features that were discussed in the previous section. The measurements of the helical propagation in this sample, however, were not as detailed as for the Nb specimen and are not shown.

## 10.5 V vs $U_{fj}$ and Threshold Energy

In trying to establish a functional relationship between the velocity of propagation of the flux jumps and $U_{fj}$, the total energy dissipated during the avalanche, the fact that the avalanche follows helical paths must be taken into account. The total velocity of propagation of the flux jump at the surface of the wire is then

$$V = \frac{V_z}{\cos \phi} \tag{10-7 a}$$

or equivalently

$$V = (V_z^2 + V_\theta^2)^{\frac{1}{2}} \tag{10-7 b}$$

In chapter 8, the raw data were presented for $V_z$ as a function of I, $H_o$ and $<M_z>$. The actual state of affairs would be more appropriately displayed by presenting graphs of V vs the variables I, $H_o$ and $<M_z>$. To determine V, however, measurements of both $V_z$ and $V_\theta$ (or $\phi$) are required. As indicated earlier in this chapter, the oscillations from which $V_\theta$ (or $\phi$) were extracted are too irregular, in many sets of circumstances, to yield any reliable or significant information. Consequently, much less information on V than on $V_z$ was obtained experimentally.

In view of the approximate agreement between $\phi_{obs}$ and $\phi_{calc}$ and since the latter can, of course, be determined for all situations, it is chosen, for convenience, to exploit this empirical relation, although it provides only a crude description of the observations. With this empirical expression $V_z$ in Figures 8-1 through 8-5 can be converted to V by equation 10-7 and the results of this exercise compared with the $U_{fj}$ vs I curves displayed in Figures 9-6 through 9-10. This approach, however, only reconfirms that V and $U_{fj}$ are functionally related and provides little additional information. Since it is ultimately desired to delineate this functional relationship and the behaviour of the threshold energy $U_c$, it is more instructive to proceed as we have done earlier in chapter 9 and plot V vs $U_{fj}$.

Figures 10-14 through 10-18 therefore display the correlation between V and $(U_{fj} - U_c)$ where $U_c$ is the threshold energy for the onset of electromagnetic propagation. It is again evident that curves drawn through the data points shift horizontally depending on $H_o$ and the sign of $\langle M_z \rangle$. $U_c(H_o)$ obtained from these Figures is only slightly different from that extracted from Figures 9-6 through 9-10. The variation of $U_c$ with $H_o$ and the horizontal shift of the entire curves, confirm the conclusion reached earlier that the flux flow resistivity $\rho = \rho_n B/H_{c2}(T)$ plays a role comparable to $U_{fj}$ in governing the rate of energy dissipation during the flux collapse, hence, the rate of electromagnetic propagation of the flux avalanche. The remarks made in chapter 9 regarding the two Figures where the initial $\langle M_z \rangle$ is hybrid, namely; that it is $\langle |B_z| \rangle$ rather than $\langle B_z \rangle$ which must be considered in the flux flow resistivity, continue to apply. It is noticed that $\langle |B_z| \rangle$ plays a role, not only in the horizontal shift from one Figure to another, but also in the horizontal distribution of the data points within each Figure. For this and other reasons it has not been considered meaningful to extract an empirical functional form for V in terms of $(U_{fj} - U_c)$ from these Figures. This analysis however suggests the direction which could be pursued to establish such empirical relation and the accompanying model for the velocity of propagation of flux avalanches under electromagnetic coupling.

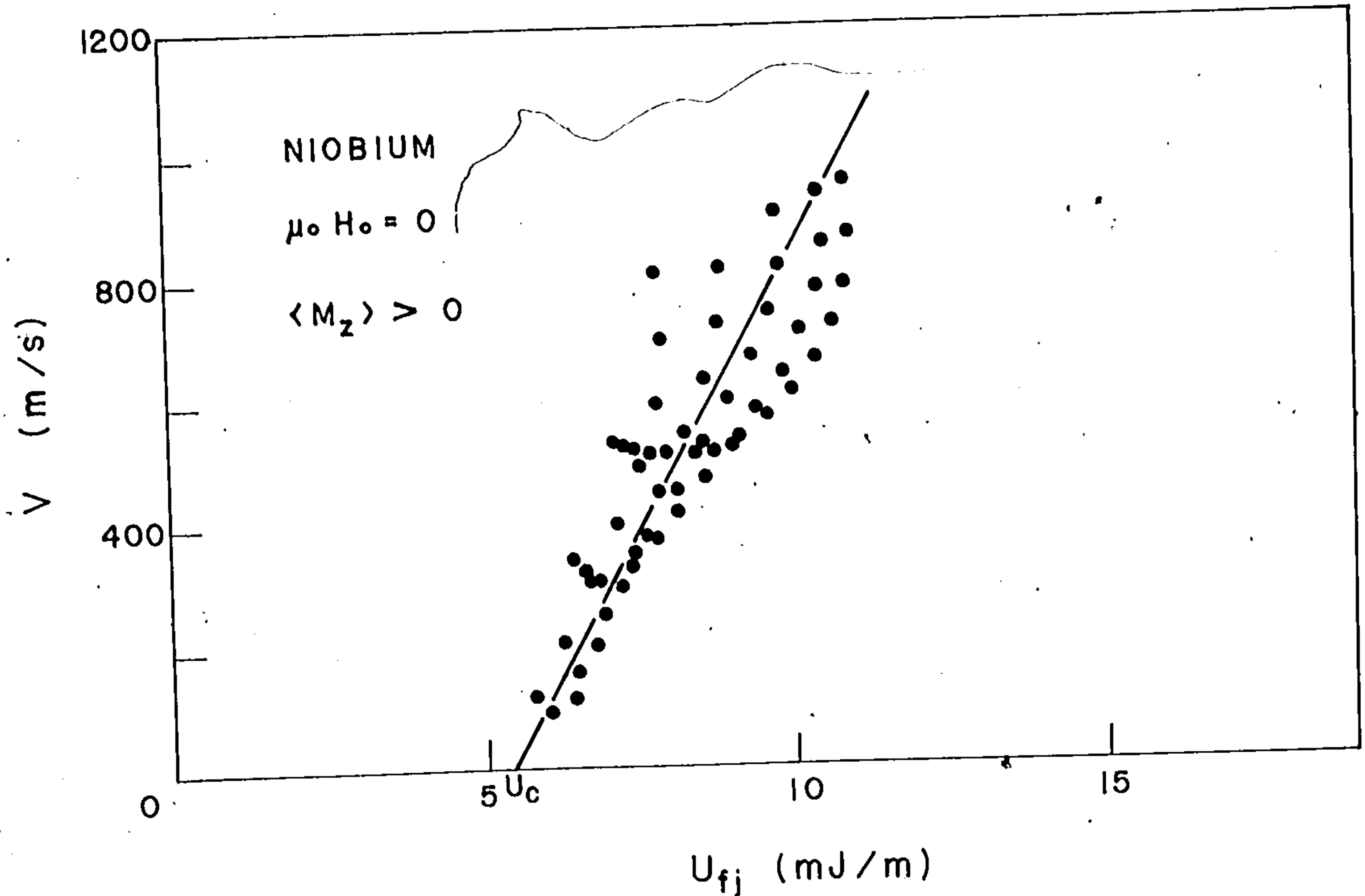


Figure 10-14 Experimental velocity V versus calculated energy $U_{fj}$ for $H_o = 0$. The plotted data cover the complete range of transport current I and magnetic moment $\langle M_z \rangle$ where electromagnetic propagation occurs.

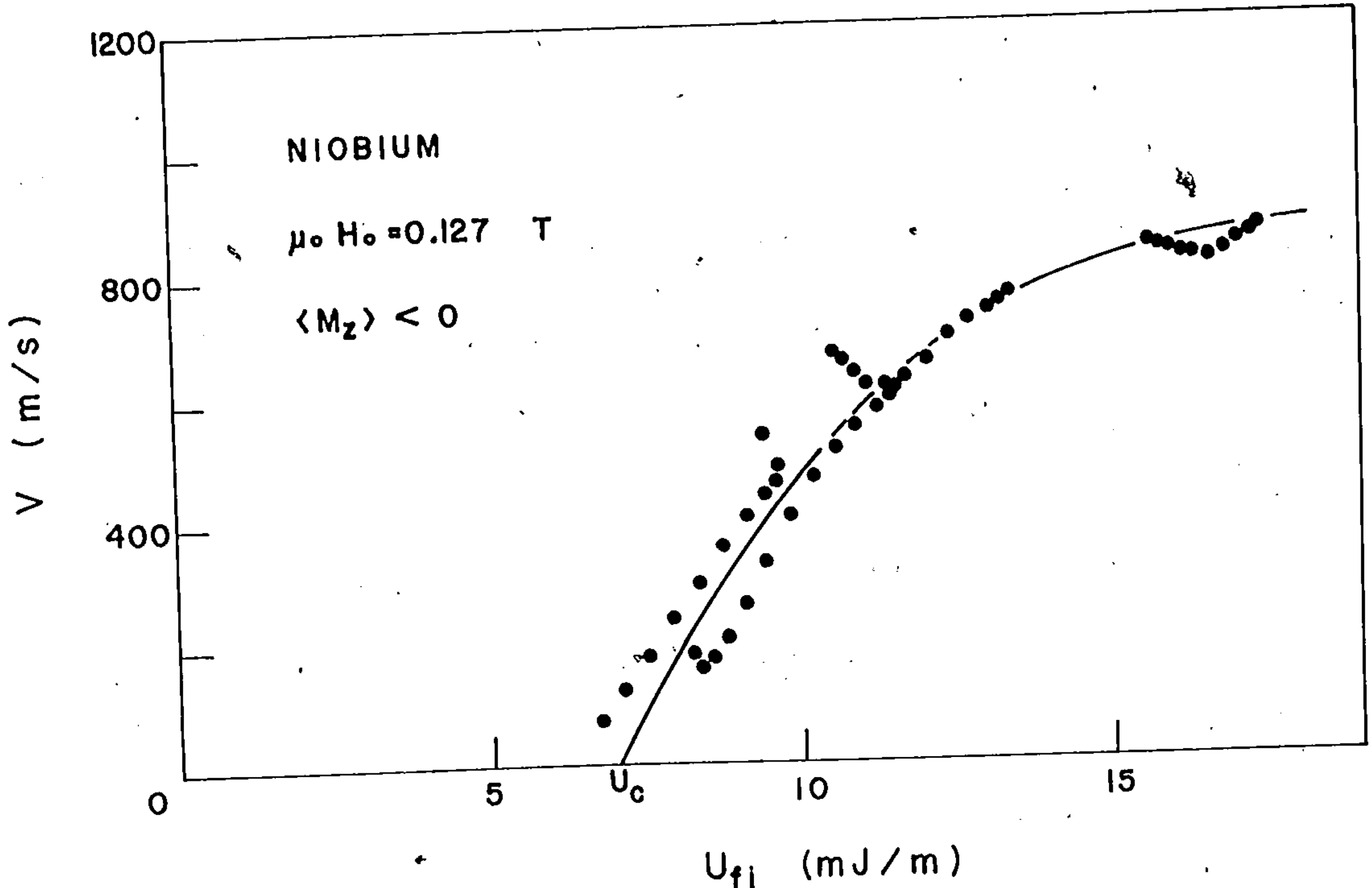


Figure 10-15 Experimental velocity V versus calculated energy $U_{fj}$ for $\mu_o H_o$ = 0.127 tesla. The plotted data cover the complete range of transport current I and hybrid magnetic moment $\langle M_z \rangle$ where electromagnetic propagation occurs.

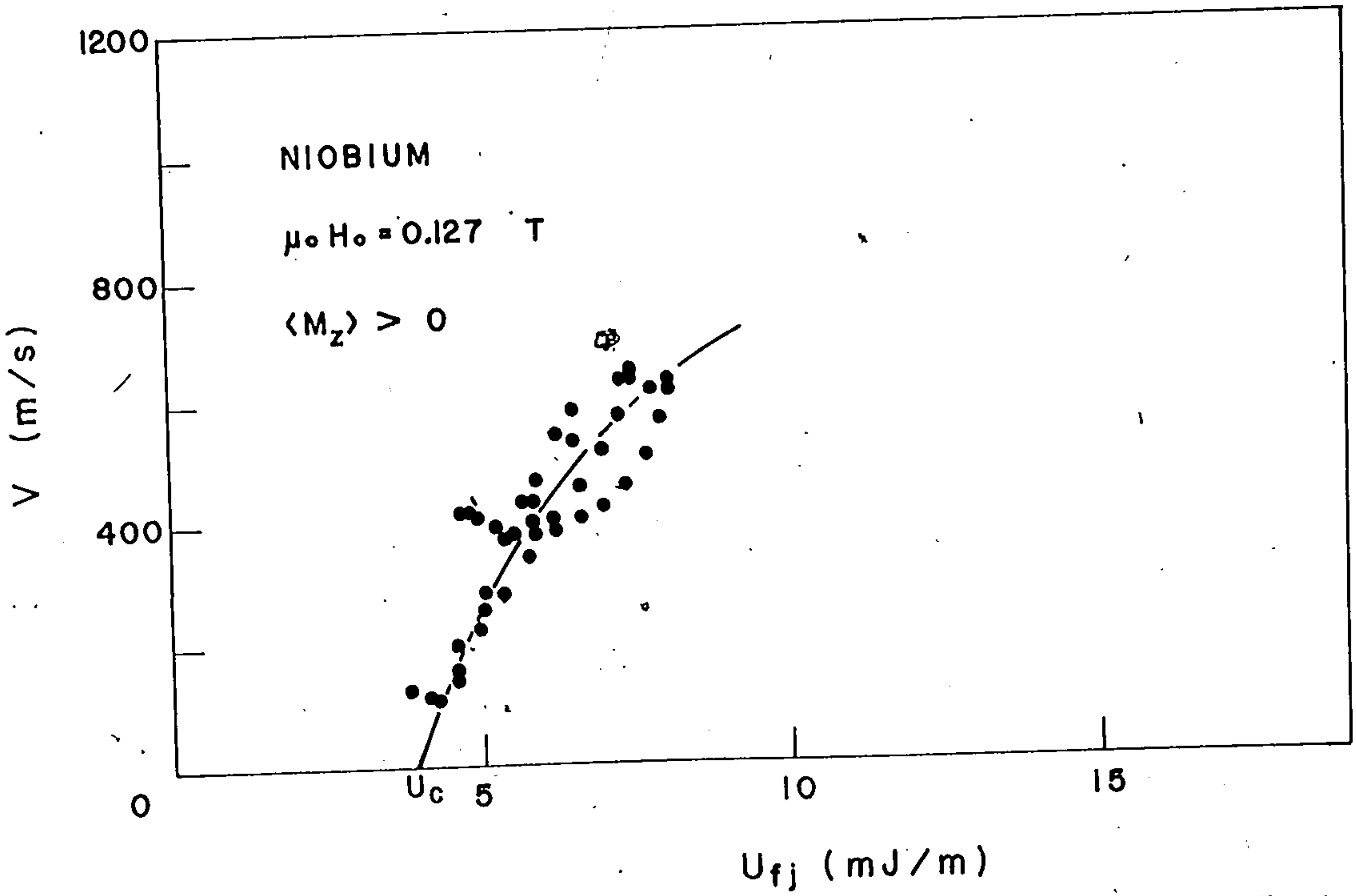


Figure 10-16 Experimental velocity V versus calculated energy $U_{fj}$ for $\mu_o H_o$ = 0.127 tesla. The plotted data cover the complete range of transport current I and paramagnetic moment $<M_z>$ where electromagnetic propagation occurs.

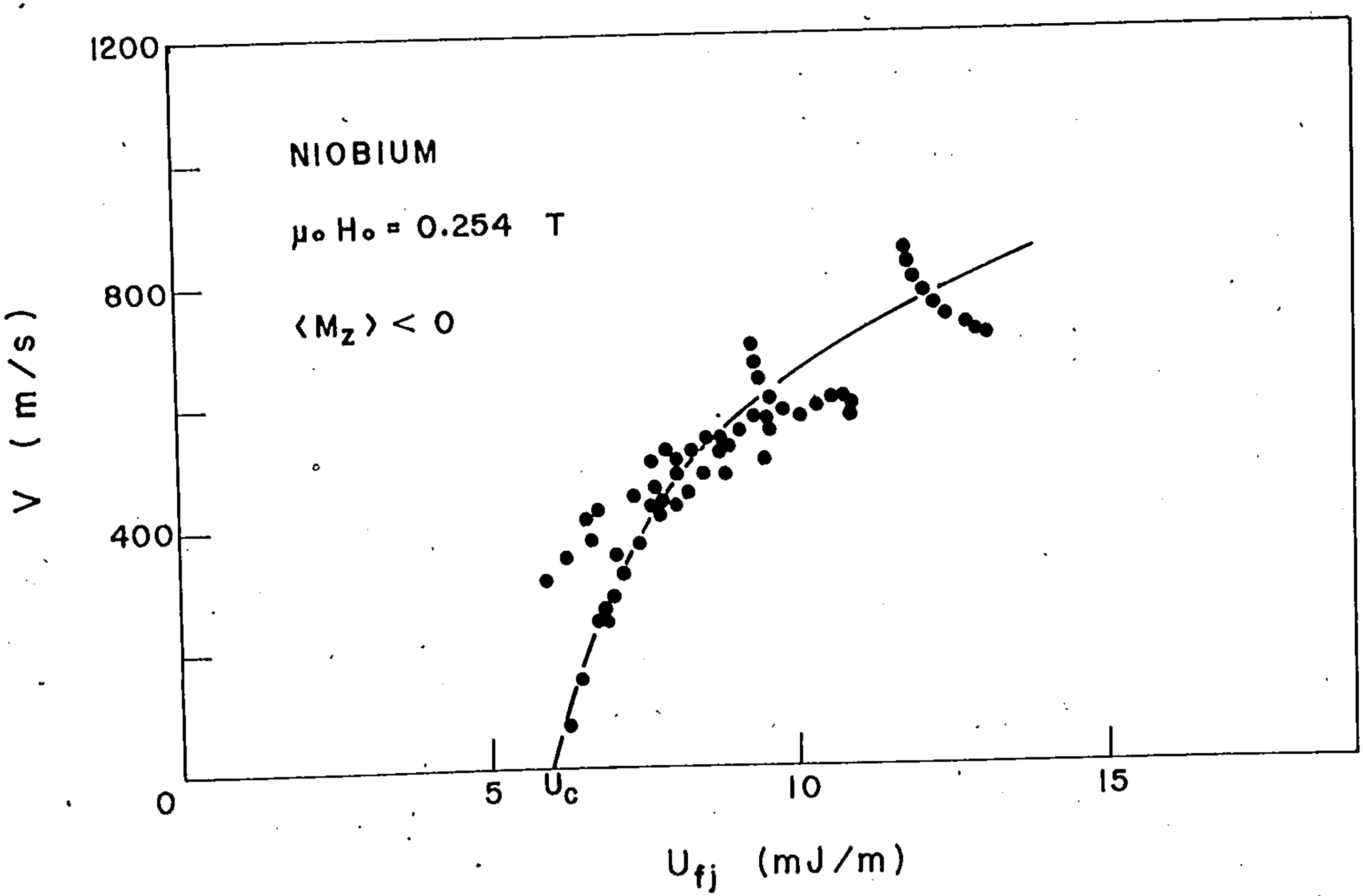


Figure 10-17 Experimental velocity V versus calculated energy $U_{fj}$ for $\mu_o H_o = 0.254$ tesla. The plotted data cover the complete range of transport current I and hybrid magnetic moment $\langle M_z \rangle$ where electromagnetic propagation occurs.

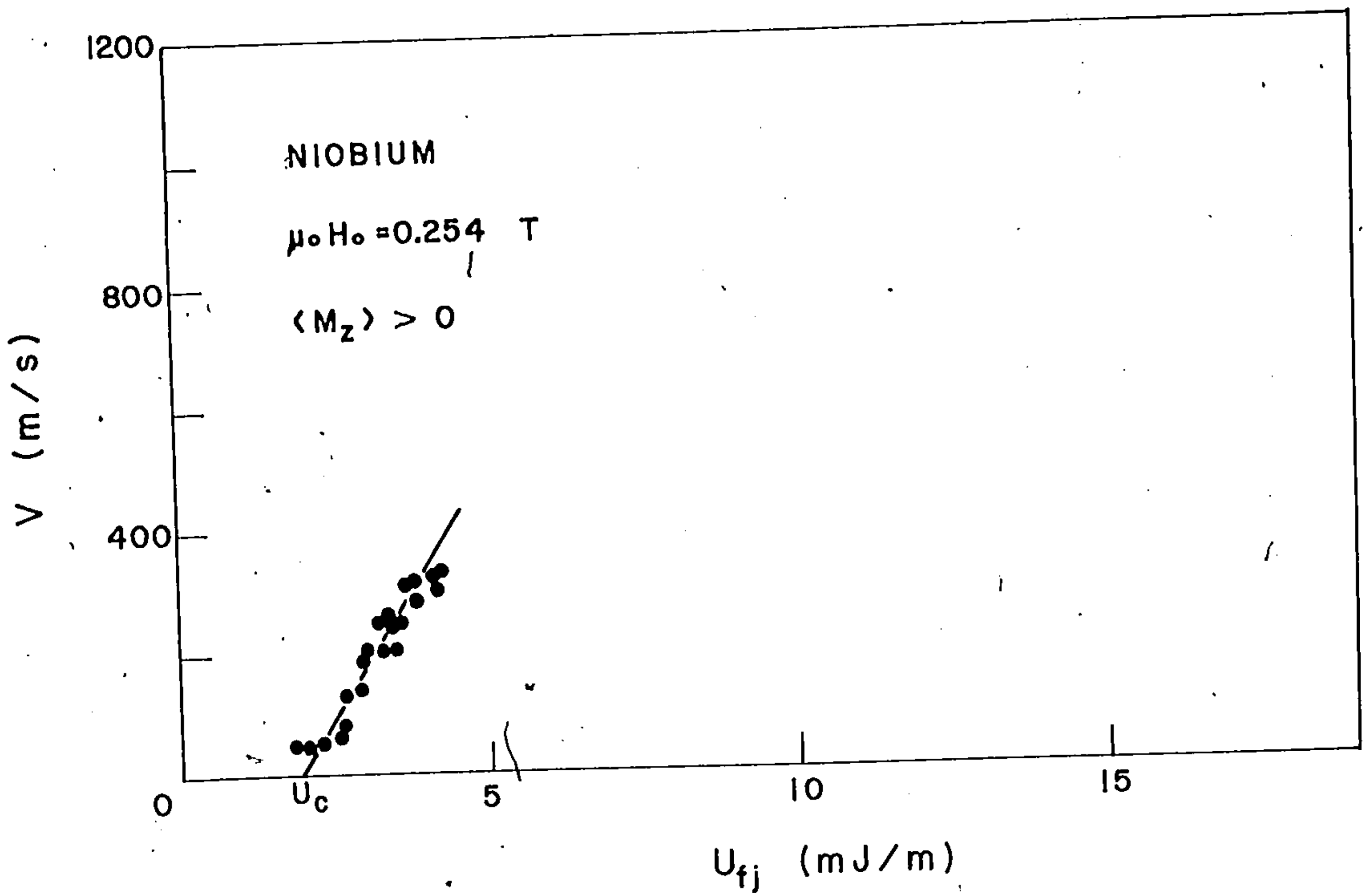


Figure 10-18 Experimental velocity V versus calculated energy $U_{fj}$ for $\mu_o H_o = 0.254$ tesla. The plotted data cover the complete range of transport current I and paramagnetic moment $\langle M_z \rangle$ where electromagnetic propagation occurs.

## Summary and Conclusion

### Part II

The velocity of propagation of flux jumps in wires of type II superconductors carrying a transport current and axially magnetized in a longitudinal magnetic field has been investigated. Two distinct mechanisms for the propagation of the collapse of the superconducting state were identified. They are referred to as thermal coupling (or mode) and electromagnetic coupling (mode).

When the wire is not axially magnetized (or at least not strongly magnetized) and the transport current is not too close to $I_c$, thermal coupling operates. An interface divides a fully normal region where $\rho = \rho_n$ and a superconducting region. The normal front advances by thermal diffusion of joule heat $(j^2\rho_n)$ across the interface into the adjacent superconducting region. When the wire is axially magnetized, the azimuthal persistent currents in the superconducting region decay and the attendant magnetic moment disappears as the temperature rises. This decay of the persistent currents and the destruction of the magnetic moment is not a flux avalanche. The collapse does not arise from an instability of the configuration and it is not self-perpetuating and self-generating. The velocities of propagation observed under these circumstances are slow and are governed by the rate of heat diffusion. Furthermore, the collapse of the superconducting state is radially symmetric. This phenomenon has been investigated in type I superconductors and in unmagnetized type II superconductors by other workers.

When the wire is strongly magnetized axially and/or the transport current is near $I_c$, the configuration of the magnetic induction is unstable and true flux avalanches occur. The avalanche and its longitudinal advance feed on the magnetic energy stored in the azimuthal and axial components of the magnetic induction. The collapse of the superconducting state in one place triggers the collapse of the critical magnetic configuration in the adjacent region by electromagnetic induction (electromagnetic coupling). The rate of progress of a disturbance along the wire can then be measured. The disturbance can propagate only because the region it penetrates is an unstable state on the verge of collapse. The collapse of these unstable states is rapid and catastrophic, terminating with the creation of the normal state. The velocities of propagation are large since they are not limited by the rate of thermal diffusion. Furthermore, it is found that, when electromagnetic coupling operates, the flux jumps are azimuthally asymmetric and follow helical trajectories along the wire.

For the thermal and electromagnetic modes of propagation, extensive data are presented on the dependence of the longitudinal velocity of propagation on the transport current I, the longitudinal magnetic field $H_o$ and the initial magnetic moment $\langle M_z \rangle$. The dependence of the helical path followed by the flux jumps on the variables just enumerated is also determined.

An examination of the correspondence between $U_{fj}$, the energy dissipated during the flux jump and its velocity of propagation V is undertaken. In order to calculate the energy dissipated during the avalanche, it is necessary to know the $B_z$ and $B_\theta$ profiles before and after the flux jump. From measurements of the magnitude of the pulses observed during the advance of the flux jump it can be verified that the normal state is the final configuration. The initial $B_z$ and $B_\theta$ profiles are estimated in the spirit of the Bean-London approximation. More specifically, the axial and azimuthal current densities are taken as spatially constant, but to depend only on $H_o$ in the first instance and on both $H_o$ and I in the latter instance. Within the context of this approximation it is found computationally convenient to exploit an empirical expression to determine the azimuthal current density $J_c$ rather than extracting this value directly, step by step, from the experimental curves of $\langle M_z \rangle$ vs. I. This empirical formulation faithfully reproduces the experimentally observed evolution of the axial magnetization $\langle M_z \rangle$ as the current increases to $I_c$ in various $H_o$ and starting with different initial moments. It is however only a tool used to perform a specific task and is not put forward as a model with physical content.

The approach introduces two parameters $I_c'$ and $I_c''$. These two parameters are found to be nearly equal. The latter has a clear physical meaning since it is defined as the transport current which will fill the entire cross-section of the wire. The experimentally observed critical current $I_c$ is found to fall fractionally below $I_c'' \gtrsim I_c'$. It is speculated that the occurrence of a spontaneous flux jump at $I_c$ may account for this behaviour.

In view of the similarity between the observed $V_z$ vs I families of curves and the calculated $U_{fj}$ vs I families of curves this information is combined in graphs which illustrate the functional relationship between $V_z$ (or V) and $U_{fj}$. This representation makes it possible to determine the dependence of the critical threshold energy $U_c$ for the propagation of a flux jump on $H_o$ and on the initial magnetic state. The results indicate that the flux flow resistivity $\rho = \rho_n\, B/H_{c2}(T)$, as well as $U_{fj}$, play an important role in controlling V. Because of this complication and the consequent horizontal spread in the data exhibiting the correlation between V and $U_{fj}$ it has not been deemed meaningful to extract an empirical formula for V vs $U_{fj} - U_c$ from these graphs.

The assumption that the flux jumps follow helical paths corresponding to the average helix of the flux vortices in the cylindrical region occupied by the transport current adjacent to the surface of the wire is explored. To estimate the pitch of these helical paths, a crude arithmetical average of $B_\theta$ and $B_z$ in the region carrying the transport current is used. A comparison of the results of this approach with the present experimental observations on helical propagation indicates that the basic idea appears to be valid.

References

Abrikosov, A.A.

57 Soviet Phys. J.E.T.P. 5, 1174 (1957)

Andronikashvili, E.L.

67 and S.M. Ashimov, D.G. Chigvinadze and J.S. Tsakadze, Phys. Lett. 25A, 85 (1967)

69 and J.G. Chivinadze, P.M. Kerr, J. Lowell, K. Mendelssohn and J.S. Tsakadze, Cryogenics 9, 119 (1969)

Ashimov, S.M.

76 and V.Z. Gabdulin, O.V. Magradze, J.S. Tsakadze and A. Nemoz, Cryogenics 16, 589 (1976)

Barnes, L.J.

66 and H.J. Fink, Phys. Letters 20, 583 (1966)

Bean, C.P.

62 Phys. Rev. Letters 8, 250 (1962)

64 Rev. Mod. Phys. 36, 31 (1964)

64 and J.D. Livingston, Phys. Rev. Letters 12, 14 (1964)

70 J. Appl. Phys. 41, 2482 (1970)

Belanger, B.C.

68 Ph.D. Thesis, University of Southern Calif. U.S.A. (1968)

Bode, H.J.

67 Phys. Letters 25A, 661 (1967)

Broer, L.J.F.

47 Physica 13, 473 (1947)

Broom, R.F.

60 and E.H. Rhoderick, Brit. J. Appl. Phys. 11, 292 (1960)

Bussière, J.F.

72a Proc. 1972 Appl. Superc. Conf. Annapolis, Maryland (U.S.A.)

72b Proc. 13th Int. Conf. Low Temp. Phys. Boulder, Colorado, U.S.A. (1972)

73 Ph.D. thesis, University of Ottawa, Ottawa, Canada (1973)

75 and M.A.R. LeBlanc, J. Appl. Phys. 46, 406 (1975)

76 and M. Suenaga, J. Appl. Phys. 47, 707 (1976)

Campbell, A.M.

72 and J.E. Evetts, Advances in Physics 21, 199-442 (1972)

Chang, C.C.

71 and A.C. Rose-Innes, Proc. 12th Int. Conf. Low Temp. Phys., ed. E. Kando (Academic Press of Japan), p. 381 (1971)

Chang, C.T.M.

67 and M.A.R. LeBlanc, Appl. Phys. Letters 10, 344 (1967)

Cherry, W.H.

60 and J.I. Gittleman, Solid-State Electronics (Pergamon Press) 1, 287 (1960)

Cline, H.E.

66 and B.P. Strauss, R.M. Rose and J. Wulff, J. Appl. Phys. 37, 5 (1966)

Condon, E.U.

49 and E. Maxwell, Phys. Rev. 76, 578 (1949)

Cullen, G.W.

73 and G.D. Cody, J. Appl. Phys. 44, 2838 (1973)

Darby, M.I.

73 and N. Morton, Journal of Computational Physics 13, 35 (1973)

De Sorbo, W.

64 and W.A. Healy, Cryogenics 4, 257 (1964)

Druyvesteyn, W.F.

64 Phys. Letters 13, 195 (1964)

Dunn, W.I.

68 and P. Hlawiczka, Brit. J. Appl. Phys. 1, 1469 (1968)

Ezaki, T.

76a and F. Irie, Jour. of Phys. Soc. Japan 40, 382 (1976)

76b and K. Yamafuji and F. Irie, Jour. Phys. Soc. Japan 40, 1271 (1976)

Faber, T.E.

53 Proc. Roy. Soc. (London) A219, 75 (1953)

Fietz, W.A.

64 and M.R. Beasley, J. Silcox and W.W. Webb, Phys. Rev. 136, A335 (1964)

69 and W.W. Webb, Phys. Rev. 178, 657 (1969)

Fink, H.J.

65 Phys. Rev. Letters 14, 309 (1965)

Friedel, J.

63 and P.G. De Gennes and J. Matricon, Appl. Phys. Letters 2, 119 (1963)

Fritz, J.J.

49 and O.D. Gonzalez and H.L. Johnston, Phys. Rev. 76, 580 (1949)

50 and O.D. Gonzalez and H.L. Johnston, Phys. Rev. 80, 894 (1950)

Fuhrmans, M.

76 and C. Heiden, Cryogenics 16, 451 (1976)

Gauthier R.

76 Ph.D. Thesis, University of Ottawa, Ottawa, Canada (1976)

Gilchrist, J.G.

72 J. Phys. D.: Appl. Phys. 5, 2252 (1972)

Harrison, R.B.

73 and L.S. Wright and M.R. Wertheimer, Phys. Rev. B 7, 1864 (1973)

Hart, H.R. Jr.

67 and P.S. Swartz, Phys. Rev. 156, 403 (1967)

Hauser, J.J.

62 Phys. Rev. Letters 9, 423 (1962)

Irie, F.

75 and T. Ezaki and K. Yamafuji; IEEE Transactions on Magnetics, Vol. Mag-11, No. 2, p. 332-335 (1975)

Iwasa, Y.

68 and J.E.C. Williams, J. Appl. Phys. 39 2547 (1968)

Kim, Y.B.

63 and C.F. Hempstead and A.R. Strnad, Phys. Rev. 129, 528 (1963)

65 and C.F. Hempstead and A.R. Strnad, Phys. Rev. 139, A1163 (1965)

Kramer, E.J.

73 J. Appl. Phys. 44, 1360 (1973)

Lachaine, A.

76 Ph.D. Thesis, University of Ottawa, Ottawa, Canada (1976)

LeBlanc, M.A.R.

64 and F.L. Vernon Jr. Phys. Letters 13, 291 (1964)

65 and W.F. Druyvesteyn and C.T.M. Chang, Appl. Phys. Letters 6, 189 (1965)

66 and E.L. Fletcher, Appl. Phys. Letters 9, 161 (1966)

67 and D.J. Griffiths and H.G. Mattes, Appl. Phys. Letters 11, 143 (1967)

London, H.

63 Physics Letters 6, 162 (1963)

Love, G.R.

66 J. Appl. Phys. 37, 3361 (1966)

Makiej, B.

75 and S. Golab, A. Sikora, E. Trojnar and W. Zacharke, Proc. 14th Int. Conf. on Low Temp. Phys. Otaniemi, Finland, p. 141 (1975)

Milne, I.

72 and D.F. Gibbons, J. Appl. Phys. 43, 1955 (1972)

Mints, R.G.

75 and A.L. Rakhmanov, J. Phys. D: Appl. Phys. 8, 1769 (1975)

Morton, N

73 and M.I. Darby, Cryogenics 13, 232 (1973)

Overton, W.C. Jr.

71 J. Low Temp. Phys. 5, 397 (1971)

Park, J.G.

65 Phys. Rev. Letters 15, 352 (1965)

Pippard, A.B.

50 Phil. Mag. 41, 243 (1950)

Pry, R.H.

52 and A.L. Lathrop and W.V. Houston, Phys. Rev. 86, 905 (1952)

Rollins, R.W.

67 and J. Silcox, Phys. Rev. 155, 404 (1967)

Saint-James, D.

63 and P.G. de Gennes, Phys. Letters 7, 306 (1963)

Schäfer, R.

76 and C. Heiden, Proc. 1976 Appl. Superc. Conf., Stanford, U.S.A.

Schweitzer, D.G.

67a and M. Garber, Phys. Rev. 160, 348 (1967)

67b and M. Garber, Phys. Rev. Letters 18, 206 (1967)

Silcox, J

63 and R.W. Rollins, Appl. Phys. Letters 2, 231 (1963)

64 and R.W. Rollins, Rev. Mod. Phys. 36, 52 (1964)

Swartz, P.S.

62 Phys. Rev. Letters 9, 448 (1962)

65 and H.R. Hart, Phys. Rev. 137, A818 (1965)

68 and C.P. Bean, J. Appl. Phys. 39, 4991 (1968)

Ullmaier, H.A.

66a Phys. Stat. Sol. 17, 631 (1966)

66b and W.F. Gauster, J. Appl. Phys. 37, 4519 (1966)

Walker, M.S.

65 and J.K. Hulm, Appl. Phys. Letters 7, 114 (1965)

66 and J.K. Hulm, J. Appl. Phys. 37, 1015 (1966)

72 and J.K. Hulm, Proc. 1972 Appl. Superc. Conf. p. 446 (1972)

Walmsley, D.G.

72 J. Phys. F.: Metal Phys. 2, 510 (1972)

Wertheimer, M.R.

67 and J. le G. Gilchrist, J. Phys. Chem. Solids 28, 2509 (1967)

Wexler, A.

50 and W.S. Corak, Phys. Rev. 78, 260 (1950)

Whetstone, C.N.

65 and C.E. Roos, J. Appl. Phys. 36, 783 (1965)

Wipf, S.L.

64 Conference Type II Superconductors, Cleveland, Ohio 1964; Westinghouse Scientific Paper 64-1J0-280-P1.

67 Phys. Rev. 161, 404 (1967)

Zahradnitsky, A.

73 M.Sc. Thesis, University of Ottawa, Ottawa, Canada (1973)